Morphological and Numerical Modeling of a Highly Dynamic Tidal Inlet at Shippagan Gully, New Brunswick

Seth James Logan

Submitted under the supervision of

Dr. Ioan Nistor

Dr. Andrew Cornett

Dr. Ousmane Seidou

Partially funded by the Canadian Hydraulics Center, NRC-CNRC

In partial fulfillment of the requirements
for the degree of

Master of Applied Science in Civil Engineering

Department of Civil Engineering

University of Ottawa

March, 2012

ACKNOWLEDGEMENTS

My fascination with coastal engineering began in 2008 upon being introduced to the field in my final year of an undergraduate degree at Queen's University. Perhaps growing up a few short kilometres from the Atlantic Ocean played a role, but something about the sheer power and magnitude of our oceans and seas intrigued me. Being a fairly creative minded person, I was also attracted by the fact that no design code exists for coastal engineers. Instead, every project is unique, and therefore requires an equally unique and creative solution.

In response to my fascination, I quickly sought ways in which I could pursue a graduate degree in coastal engineering. After a series of set-backs and rather unfortunate events, I was extremely lucky to be led to Dr. Ioan Nistor and the University of Ottawa. As a graduate student, one could not ask for a better supervisor than Dr. Ioan Nistor. His level of care and interest in each and every one of his student's endeavours is un-surpassed by anyone I have ever met in academia. For that, I owe him many thanks.

A second strike of good fortune along my academic journey was the opportunity to embark on an outstanding and highly diverse project with the Canadian Hydraulics Center. Not only did this project contain the very concepts which interested me the most, but it also gave me an excellent perspective into the coastal engineering industry. For providing me with such an outstanding thesis topic and for all of their guidance, support and patience along the way, my deepest gratitude must also be extended to Mr. Thierry Faure and Dr. Andrew Cornett of the Canadian Hydraulics Center.

Although not directly related to this study, additional thanks should be given to Baird & Associates, particularly Mr. Derek Williamson, Mr. Graham Frank and Dr. Douglas Scott, for providing me with the opportunity to gain invaluable work experience throughout the course of my graduate studies. Thanks to them I've been able to live a double life over much of the past two years, learning more about coastal engineering then would have ever been possible from academia alone.

Additional gratitude must be given to Dr. Dan Kelley, a lifelong friend and a tremendous source of guidance, particularly in the later stages of this writing. Dr. Kelley graciously volunteered his time and attention to help make this thesis the best it could be, by providing me with invaluable edits and extensive feedback. For that and so much more, I am very grateful.

Finally, my most sincere thanks and appreciation must be given to both my family and my wonderful girlfriend, who have supported me through all of my academic endeavours, regardless of the fact that my stress levels and ensuing poverty spilled over to them. The present study is as much a result of their efforts as it is of my own.

ABSTRACT

Shippagan Gully is a highly engineered, tidal inlet located near Shippagan, New Brunswick, on the Gulf of St. Lawrence. It is a particularly complex tidal inlet due to the fact that its tidal lagoon transects the Acadian Peninsula and is open to the Bay des Chaleurs at its opposite end. As such, two open boundaries with phase lagged tidal cycles drive the flow through the inlet, alternating direction with each tide and reaching velocities which exceed 2 m/s. Over the past century, despite various engineered interventions, shipping activities through the inlet have been threatened due to the increasing encroachment from sediment which has accumulated on the east side of the navigation channel and immediately offshore from the inlet. In addition to these highly asymmetrical sediment deposition patterns, severe down-drift erosion suggests the presence of a prominent westward net longshore transport, further complicating the coastal morphology at the inlet.

Due to the overwhelming requirement for constant maintenance dredging and the long-term degradation of existing coastal structures, a numerical model study of Shippagan Gully has been undertaken in order to identify principal morphology mechanisms and to provide guidance for future coastal works. The numerical models CMS Wave and CMS Flow (USACE) have been applied in a coupled manner to simulate the hydrodynamics, coastal processes and morphology changes at the inlet due to the combined effects of waves and tides. Once calibrated to historical morphologic evolution, the numerical modeling system was used as an analytical tool to identify and understand the hydrodynamic processes responsible for the morphological changes observed at Shippagan Gully. The numerical model was further used to predict future morphologic trends, in a qualitative manner, for both the *status-quo* and a number of engineered alternatives proposed by the author. The methodology and results of this study are presented herein.

This thesis was completed in partnership with the Canadian Hydraulics Center (NRC-CNRC) and with funding provided in part by Public Works and Government Services Canada.

TABLE OF CONTENTS

LIST OF FIGURES

LIST OF TABLES

List of Symbols

A = empirical coefficient typically ranging from 0.1 to 2 (non-dimensional)
A_{cr} = empirical coefficient (non-dimensional)
a = empirical coefficient (non-dimensional)
a_i = amplitude of tidal constituent (m)
b = sediment transport coefficient dependent on Reynolds number (non-dimensional)
= distance between adjacent wave rays (m)
= empirical coefficient (non-dimensional)
C = wave celerity (m/s)
= depth-averaged sediment concentration (volume of sediment over total volume)
= Chezy friction coefficient (non-dimensional)
C_b = empirical bottom-stress (friction) coefficient
C_d = wind drag coefficient (non-dimensional)
C_ε = coefficient determined from an empirical curve (non-dimensional)
C_x = characteristic velocity in wave-action density equation (m/s)
C_y = characteristic velocity in wave-action density equation (m/s)
C_θ = characteristic velocity in wave-action density equation)m/s)
c_f = Darcy-Weisbach friction coefficient (non-dimensional)
c_R = reference concentration in Lund-CIRP formula for suspended load (kg/m^3)
D = characteristic particle diameter (m)
= sediment deposition rate (downward sediment flux) (kg/s)
D_x = diffusion coefficient for the x direction (non-dimensional)
D_y = diffusion coefficient for the y direction (non-dimensional)
d = water depth (m)
d_b = water depth at wave breaking (m)
d_{50} = mean grain diameter (m)
d_* = non-dimensionalized grain size (non-dimensional)
E_{total} = total energy density (J/m^2)
f = Coriolis coefficient (rad/s)
g = gravitational acceleration (m/s^2)
H = nearshore wave height (m)
H_b = breaking wave height (m)
H_o = offshore wave height (m)
H_{sb} = significant breaking wave height (m)
h = total water depth (m)
K_r = refraction coefficient (non-dimensional)
K_s = shoaling coefficient (non-dimensional)

K_x = sediment diffusion coefficient for the x-direction (non-dimensional)

K_y = sediment diffusion coefficient for the y-direction (non-dimensional)

k = wave number (m^{-1})

L = wavelength (m)

MWL = mean water level (m)

MSL = mean sea level (m)

m_b = beach slope (m/m)

N = wave-action density (J·s/m^2)

n = sediment porosity (non-dimensional)

= Manning's roughness coefficient (non-dimensional)

P = sediment pick-up rate (upward sediment flux) (kg/s)

= material placed in sediment budget cell (m^3)

p = sediment porosity (non-dimensional)

Q_k = potential longshore sediment transport (Kamphuis formula) (m^3/yr)

Q_s = longshore sediment transport rate (CERC formula) (m^3/yr)

Q_{sink} = sink term to a sediment budget (m^3)

Q_{source} = source term to a sediment budget (m^3)

q_{bw} = bed load parallel to wave direction (m^3/m·s)

q_{bn} = bed load normal to the wave direction (m^3/m·s)

q_{sb} = bed load rate (m^3/m·s)

$\bar{q}_{sb}$ = gravimetric specific bed-load rate (N/m·s)

q_x = flow per unit width parallel to the x-axis (m^2/s)

q_y = flow per unit width parallel to the y-axis (m^2/s)

q_{tot} = total load (both suspended and bed load) (m^3/m·s)

R = material removed from the sediment budget cell (m)

= hydraulic radius (m)

S_{xx} = wave-driven radiation stress (N/m^2)

S_{xy} = wave-driven radiation stress (N/m^2)

S_{yy} = wave-driven radiation stress (N/m^2)

SWL = still water level (m)

T = wave period (s)

T_{op} = wave period in Kamphuis formula for potential longshore transport (s)

t = time (s)

U = total current velocity (m/s)

U_c = depth averaged current velocity (m/s)

u = depth-averaged current velocity parallel to the x-axis (m/s)

u_b = mean horizontal wave orbital velocity at the sea bed (m/s)

V = fluid velocity (m/s)

V_* = shear velocity (m/s)
v = depth-averaged current velocity parallel to the y-axis (m/s)
W = wind speed (m/s)
w = density of bed material divided by density of water (non-dimensional)
Y = Y-axis in Shields curve (non-dimensional)
Y_{CR} = critical parameter determined from the Y-axis of Shields curve (non-dimensional)
z = water elevation relative to the bed (m)
α = wave crest angle relative to the shoreline (^{0})
α_b = breaking wave angle relative to the shoreline (^{0})
α_i = phase angle of tidal constituent (^{0} or rad)
γ_s = specific gravity (N/m^3)
ΔV = net change in volume within the cell (m^3)
κ = wave diffraction term (non-dimensional)
η = water surface elevation relative to still water level (m)
= relative water depth (z/h)
ρ = fluid density (kg/m^3)
ρ_a = density of air (kg/m^3)
ρ_s = sediment density (kg/m^3)
ρ_w = density of seawater (kg/m^3)
θ = wind direction (^{0})
$\theta_{cw,m}$ = mean Shields parameter for combined waves and currents (non-dimensional)
θ_{cw} = maximum Shields parameter for combined waves and currents (non-dimensional)
τ = shear stress (N/m^2)
τ_b^* = dimensionless shear stress (non-dimensional)
τ_{bmax}^* = maximum shear stress at the bed (non-dimensional)
τ_{cr} = shear stress at incipient sediment motion (N/m^2)
τ_c^* = dimensionless critical shear stress (non-dimensional)
τ_{bx} = bottom stress parallel to the x-axis (N/m^2)
τ_{by} = bottom stress parallel to the y-axis (N/m^2)
τ_{wx} = surface stress parallel to the x-axis (N/m^2)
τ_{wy} = surface stress parallel to the y-axis (N/m^2)
τ_{Sx} = wave stress parallel to the x-axis (N/m^2)
τ_{Sy} = wave stress parallel to the y-axis (N/m^2)
ν = kinematic viscosity (m^2/s)
$\emptyset$ = Einstein's Phi (non-dimensional)
ω_i = angular frequencies of tidal constituent (s^{-1})

1.0 INTRODUCTION

Shippagan Gully is a coastal inlet located on the Gulf of St. Lawrence near Shippagan, New Brunswick. The inlet marks the south-eastern limit of a natural waterway which transects the Acadian Peninsula, providing an alternate route between the Bay de Chaleurs and the Gulf of St. Lawrence (refer to Figure 1.1). The inlet, which is shown in Figure 1.2, has been maintained using man-made coastal structures since the late 1800's as its navigability has proven crucial to the local economy, which is influenced in large part by the fishing industry. Since the initial construction of two 300 metre jetties in the 1880's, sediment accumulation both within and immediately offshore from the inlet has been observed. As such, a number of structural alterations, rehabilitations and dredging activities were undertaken throughout the 20th century in an attempt to stabilize the inlet and promote navigable depths. Regardless of these human interventions however, sediment has continued to deposit both within Shippagan Gully and offshore, greatly limiting its use as a navigable passage between the Bay de Chaleurs and the Gulf of St. Lawrence.

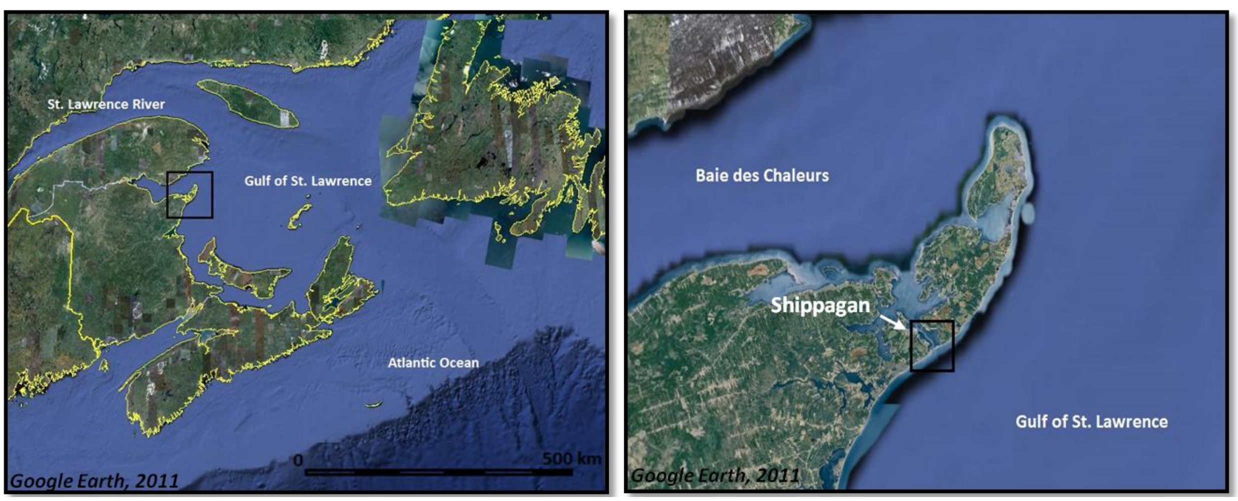

Figure 1.1: Satellite imagery showing the location of Shippagan Gully within Atlantic Canada (left) and the Acadian Peninsula (right) (Google Earth, 2011).

Figure 1.2: Aerial photograph of Shippagan Gully taken in 2007 (PWGSC, 2010).

In the absence of human intervention in recent years, natural morphological changes have taken hold of Shippagan Gully. Safe navigation through the inlet has become increasingly limited due to the continual growth and migration of morphologic features at the site. As such, the Canadian Hydraulics Centre (CHC) of the National Research Council of Canada (NRC) was retained by Public Works & Government Services Canada (PWGSC) to investigate the hydrodynamic and sedimentary processes at Shippagan Gully. This work was performed principally by the present author and in partnership with the University of Ottawa, thereby forming the basis of this thesis.

1.1 Significance of the Study

The contributions of the present thesis are significant in both a practical and technical sense. The practical significance of this study stems from the fact that Shippagan Gully is an important navigation channel which has a long history of being poorly understood and subsequently underutilized. Past coastal works at the site have proven unsuccessful in providing maintainable and navigable depths through the inlet, thereby resulting in great losses to the local economy and community. By developing a proper understanding of the hydrodynamic and sedimentary processes present at the inlet, guidance can be provided from which future decisions regarding coastal works and sediment management can be confidently made. In a practical sense, this work represents a significant contribution to the development of a safe and navigable water way for future generations.

In a technical sense, this thesis is considered to be both significant and novel for a number of important reasons. First, numerical modeling studies of tidal inlet morphology are not a common occurrence in Canada. USA has begun to recognize the importance of such work and has subsequently formed a division within the United States Army Corps of Engineers (USACE) to study such topics, aptly named the Coastal Inlets Research Program (or CIRP). Canada however does not have such a task force to monitor and study the various coastal inlets which scatter our coastlines. As such, a Canadian study regarding tidal inlet morphology is novel, simply because it's Canadian.

A second point which makes the present study novel is the relative complexity of the morphological features present at Shippagan Gully. As is discussed later in this thesis, many morphological characteristics at Shippagan Gully do not fit the typical description of a 'normal' tidal inlet, nor are their dominant processes so easily identified. This is in large part due to the long history of engineering activities at Shippagan Gully, many of which have likely left the site worse off than it would otherwise have been. These historical human interventions further complicate the situation at Shippagan Gully, making it a particularly difficult inlet to fully understand.

Lastly, the most defining feature of Shippagan Gully is that its extensive tidal lagoon transects a peninsula, and is therefore open to tidal forcings from both sides. Due to this fact, much of our conventional knowledge regarding tidal inlet hydrodynamics is no longer applicable, as it is the phase-lagged differential between two water levels which governs the tidal hydrodynamics at the site. As a result, the ebb and flood tides may no longer be approximately equal in length or magnitude, the timing of maximum and minimum flows are likely to be drastically altered, and the relationships which are built on the concept of a tidal prism are no longer valid. These topics are discussed in detail herein. As a result, Shippagan Gully cannot be studied, nor can it be properly understood, based solely upon experience and knowledge of previous tidal inlet works. Shippagan Gully is an example of an inlet which is not typical and contains key features which have never before been extensively studied, nor understood. As such, much of the findings presented herein are the first of their kind, making this study a truly novel one.

1.2 Study Objective and General Approach

The main objective of the present study is to provide a scientific basis to inform and guide decisions concerning the maintenance and future development of the existing infrastructure and navigation channel at Shippagan Gully. Under this main objective, the following sub-objectives were identified:

- Identify the governing hydrodynamic processes responsible for the complex morphological features present at Shippagan Gully;
- Predict future morphological evolution if the status quo is maintained;
- Study and understand the hydrodynamics and sediment transport for alternative arrangements of structures; and
- Predict future morphological evolution for alternative structural arrangements;

A numerical modeling approach was taken in order to fulfil the requirements and general objectives of the study. Two numerical models, CMS-Wave (Lin *et al*., 2008) and CMS-Flow (Buttolph *et al*., 2006) (both developed by the United States Army Corps of Engineers; USACE), were selected and used as together they represent state of the art technology for the simulation of tidal currents, wave-induced currents, wave-induced longshore sediment transport, current induced sediment transport, and morphological change. The models were calibrated to observed hydrodynamics and to historical morphological evolution of the inlet, as documented from historical aerial photographs, dredging records and hydrographic surveys. Once calibrated, the modeling system was applied to study the hydrodynamic and sedimentary processes at Shippagan Gully, ultimately providing a tool with which the above listed study objectives could be fulfilled.

A number of preparatory tasks were undertaken in order to be able to model the hydrodynamics and morphological processes present at Shippagan Gully. These preparatory steps included:

- Site visit and field data collection;
- Meetings with local stakeholders, as well as fishermen and their representatives;
- Study of historical documents including aerial photographs and dredging records;
- Analysis of local sediment properties;
- Analysis of past morphologic change, including erosion and deposition rates;
- Assessment of local water levels;
- Assessment of nearshore wave climate;
- Assessment of longshore sediment transport potential;
- Numerical modeling of combined wave and tidal hydrodynamics;
- Numerical modeling of sediment transport and morphology change;
- Calibration of the numerical model to observed hydrodynamics; and
- Calibration of the numerical model to observed morphology change.

Once these above listed steps were successfully completed, the calibrated numerical model was used as a tool to identify the governing processes responsible for the complex morphology present at Shippagan Gully. Based on the findings of this task, a number of alternative design scenarios were developed in collaboration with colleagues from PWGSC and the Department of Fisheries and Oceans (DFO) to address the navigable requirements of the inlet. The calibrated numerical model was then applied to determine the expected outcome of each of the alternative scenarios including the status quo option, with regards to morphology at Shippagan Gully. Results of these simulations are presented in Section 6.2.

Based on the findings of this numerical model study, guidance was provided to PWGSC concerning the future development of coastal infrastructure and sediment management programs at Shippagan Gully. This thesis thereby serves as a scientific basis on which future engineering and economic decisions can be made concerning coastal works at this highly dynamic tidal inlet.

1.3 Organization of Dissertation

The present thesis has been organized into seven main sections. The first section provides a brief introduction to the topic of the study, including the main objectives, the proposed methodology and the scientific and practical significance of the work presented herein. The second section provides a literature review of coastal-related topics which together form the scientific basis required to perform this study. This section also includes examples of past research and case-studies regarding tidal inlets which together serve to illustrate many of the topics presented in the literature review in a practical context. The third section provides a site description, which summarizes the important geographic and historical features of Shippagan Gully and the surrounding area, both of the built and natural environments. The fourth section of the present thesis includes all non-numerical modeling based analyses completed throughout the course of the study. This includes the collection of pertinent data, the assessment of past and present morphological change, the study of local environmental conditions and the preparatory tasks required for the numerical modeling component of the study. The fifth section documents the numerical modeling of hydrodynamics and morphology at Shippagan Gully. This section includes descriptions of the numerical models and supporting software which were consulted throughout the course of the study. It also includes details of the set-up, simulation and calibration of the numerical modeling system. The sixth section presents the application of the numerical model to fulfill the objectives of the study, thereby the identification of governing morphological processes and the assessment of alternative design scenarios. This section has been referred to as *Analysis and Discussion* as opposed to *Results and Discussion*. This is due to the fact that the numerical model was used as an analytical tool with which coastal processes at Shippagan Gully could be studied as opposed to simply being a numerical system which provides results. The numerical analyses are discussed within the same section such that the individual tasks and modeling scenarios could be analysed and discussed sequentially. The seventh and final main section of this thesis presents conclusions based on the findings of the study as they pertain to the objectives outlined in Section 1.2. Guidance which was provided to PWGSC concerning future development and maintenance at Shippagan Gully is summarized in this section and potential areas for future work are highlighted.

2.0 Literature Review

Coastal inlets are common features of the coastal zone which connect the ocean or sea to an inland body of water. Natural coastal inlets are found all over the globe and are highly dynamic and variable in their nature. Several types of coastal inlets exist, categorized primarily by the hydrodynamic processes responsible for their formation and maintenance. For example, tidal inlets are inlets which are formed and maintained by ebb and flood flows entering and exiting a tidal lagoon. Inlets can also be created by waves, river outflow, or are man-made to serve a navigational or environmental purpose. Another defining feature of coastal inlets is the nature of the connected bodies of water. For example, a coastal inlet could connect the ocean to a tidal lagoon, a river estuary, or a man-made harbour, each having very different hydrodynamic and morphological characteristics.

An important differentiation to make with regards to coastal inlets is whether or not the inlet is serviced by land based flow, or in other words is part of a river system. When no land based flow exists at a coastal inlet, the source of all flow in and out of the inlet is the ocean or the sea. This type of inlet is typically referred to as a tidal inlet, as it is the tides which are responsible for the exchange of water through the inlet. Tidal inlets are common in North America, where vast expanses of sandy shorelines are present in conjunction with significant tidal ranges. Shippagan Gully can be categorized as a tidal inlet and, as a result, the present study and literature review focuses on this topic.

2.1 Tidal Inlets

A typical tidal inlet system is composed of a tidal lagoon and a short flow pathway (the inlet) which connects the lagoon to the open ocean. A tidal lagoon is a protected body of water which fills and drains (partially or fully) with each tidal cycle, via the tidal inlet. Tidal lagoons and inlets are naturally formed in many different environments and for many different reasons. In locations such as North America's eastern seaboard, long expanses of shoreline are subjected to continual coastal sediment migration (referred to as longshore transport). In these environments, tidal lagoons are commonly formed behind morphological features called barrier islands. In this scenario, the tidal inlet transects the barrier island(s) providing a pathway between the ocean and the sheltered lagoon. Shippagan Gully is an example of such an inlet. As such, it is useful to discuss tidal inlets in this context for the present study.

Barrier islands are long spits of sediment formed by years of wave induced longshore coastal sediment transport (a term given to the lateral migration of sediment along a coastline). In the absence of hydrodynamic forcing such as tides, this process could eventually result in the barrier island re-joining the mainland and thus creating a separate, protected body of water in its lee. In the presence of tides however, flow is driven into the back-bay system (behind the barrier island) with every flood tide and returned to the ocean with every ebb tide. Depending on the local tidal range and the volume of the back-bay system, this perpetual inflow and outflow of seawater is often powerful enough to sustain a self scouring inlet, thus halting the barrier island from reaching complete closure. An example of a typical tidal inlet - barrier island system is presented in Figure 2.1.

Figure 2.1: An example of a classical barrier island transected by a natural tidal inlet. Oregon Inlet, North Carolina (Google Earth, 2011).

The width and depth of a tidal inlet depend greatly on the local coastal processes as well as the volume of the back-bay system. In general, large (cross-sectional) inlets are found where either the tidal range is large or where the back-bay system is expansive in volume (or both). Both of these scenarios result in large volumes of water (referred to as a *tidal prism*) entering and exiting the tidal lagoon via the inlet with each tidal cycle. This process can result in a large flow rate through the tidal inlet which in turn scours a larger natural channel. Conversely, narrow and/or shallow tidal inlets are typically found were the tidal lagoon is smaller in volume or the tidal range is minimal.

The previous statements of course exclude the effects of waves, which are extremely important when considering tidal inlet morphology. Waves tend to mobilize coastal sediment and facilitate sediment migration in both the cross-shore and longshore directions. As such, waves are capable of transporting a great deal of sediment to and from the nearshore zone surrounding a tidal inlet and thus further complicating the local morphology. Furthermore, energetic storm waves are capable of producing coastal erosion, particularly when accompanied by a storm surge. In fact, it is often the enormous erosive power of waves which trigger the initial formation of a tidal inlet through a barrier island, a process which is known as a *break-through* (Dean and Dalrymple, 2002).

2.2 Tidal Inlet Hydrodynamics

There are two principal contributors to the hydrodynamics at most tidal inlets; astronomical tides and water waves. Both processes strongly influence flow magnitudes and flow patterns in and around the inlets and their combined effects can be extremely complex, particularly with respect to inlet morphology. Prior to examining these complexities however, it is essential to have a basic understanding of each hydrodynamic mechanism separately.

2.2.1 Astronomical tides

Astronomical tides are caused by a combination of forces acting on individual water particles. These forces include the gravitational attraction of Earth, the centrifugal force generated by the rotation of the Earth and the gravitational pull from other celestial bodies such as the Moon and the Sun (Kamphuis, 2000). Of these factors, the gravitational pull of the Moon and the Sun are the most significant. These two primary celestial tidal forcings create what are often referred to as equilibrium tides, since they result from the assumption that they act on water particles for a very long time such that equilibrium is achieved between their resulting force and Earth's gravity (Kamphuis, 2000).

The gravitational pull from the Moon results in a small horizontal force on water particles. On the side of the planet which faces the Moon, water particles are pulled in its direction. At this, the location on Earth which is closest to the Moon, the gravitational pull is at its maximum. Conversely, on the opposite side of Earth, water particles are pushed away from the Moon. This occurs due to the fact that the gravitational pull induced by the moon is the weakest at this location. The end result is two bulges in the water surface profile on opposite sides of the planet and in line with the position of the Moon. If the whole Earth were covered with water, this phenomenon would result in an elliptical water surface profile, with the long axis of the ellipse in line with the location of the Moon (illustrated in Figure 2.2). The combined effect of Earth's rotation and the orbit of the Moon results in a relative frequency of 24.84 hours. Since the water surface profile is elliptical and thus possesses two bulges with respect to a spherical Earth, the resulting tidal period is in fact 12.42 hours.

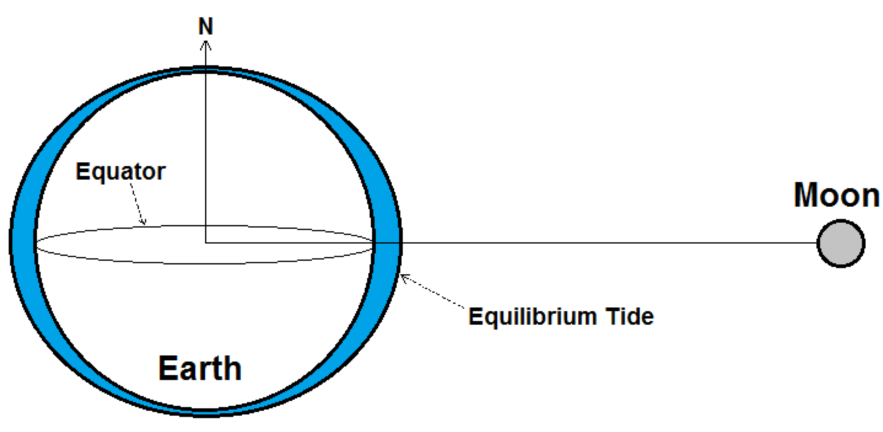

Figure 2.2: Lunar equilibrium tide, creating an elliptical water surface profile over a spherical, water-covered Earth with a period of 12.42 hours.

The Sun creates a similar gravitational pull on the Earth resulting in a second, smaller set of bulges on opposite sides of the conceptual water-covered Earth. Since our day is measured with respect to the Sun, the period of the tidal cycle generated by the Sun is 12 hours.

Since both of these tidal forcings act continually, their combined effects are important. When the Moon and the Sun are aligned (at new Moon and full Moon) the tides will be higher than usual as both gravitational pulls will operate together. This occurrence is referred to as a spring tide. Conversely, at quarter Moon the forces of the Sun and Moon will act at 90^0 to each other, thus limiting each other's gravitational pull and subsequently resulting in lower than normal tides. This occurrence is called a neap tide. Since the Moon orbits the Earth monthly (29.3 day period), two springs and two neaps are incurred per month.

These two recurring tidal forcings are referred to as tidal constituents. A tidal constituent is an independent tidal forcing which can be attributed a frequency (12.42 hours for the Moon and 12 hours for the Sun) and amplitude (Dronkers, 1964). If the planet were in fact covered in water of uniform depth, and the Earth's rotation and celestial orbits were strictly circular and two-dimensional (in plane), the amplitude of the equilibrium tidal constituents would be consistent along any latitude. This is not the case however. Staying with the assumption that the Earth is covered in water of uniform depth, the Sun and the Moon are seldom in plane with the Earth's equator, nor is their motion strictly two-dimensional or circular. In fact, the Moon and Sun generally have a north or south declination with respect to the equator as pictured in Figure 2.3. Thus, an observer traveling at constant latitude would experience two tides per day of unequal height. This phenomenon is referred to as daily inequality and is represented as its own constituent (one for solar and one for lunar). Daily inequality is most dramatic when the Sun or Moon is furthest north or south of the equator. Both lunar and solar inequality are harmonic processes with the lunar cycle repeating itself every lunar month (29.3 days) and the solar cycle every calendar year. In addition to daily inequality, there are dozens of other secondary effects which are each attributed a tidal constituent of their own (Dean and Dalrymple, 2002).

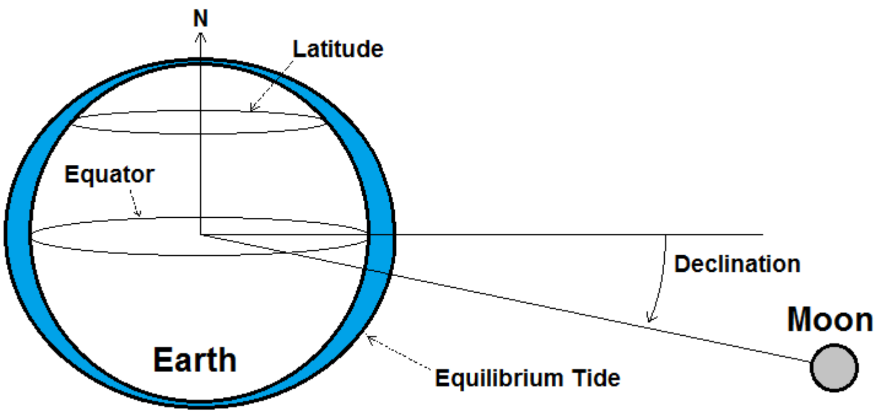

Figure 2.3: Lunar daily inequality, caused by north or south declination of lunar orbit with respect to the equator.

The previous paragraphs have of course been based entirely on a spherical Earth which is covered in water of uniform depth. This assumption is obviously incorrect as the various landmasses present on our planet interrupt the idealized tidal model. In fact, the only place on the planet in which true equilibrium tides can theoretically exist is in the southern hemisphere where an uninterrupted band of water circles the globe encompassing several different oceans. Even in this part of the world however, equilibrium tides take time to progress through the various water bodies. As such, actual water levels lag behind the theoretically determined constituents (Kamphuis, 2000).

Another large factor in the propagation of tides around the globe is the presence of seas, bays and estuaries. Certain tidal constituents tend to resonate in these partially closed water bodies, thus further complicating local tidal predictions. In certain locations some tidal constituents are amplified while others simply disappear. Often, the shape of a bay will have a funnelling effect on water levels resulting in spatial amplification. The Bay of Fundy is a prime example of this, where the local tidal constituents are amplified such that tides of up to 17 metres are observed, giving the Bay of Fundy the largest tidal range in the world (Sankaranarayanan and McCay, 2003).

Daily inequalities are often strongly influenced in resonating bays, with the difference between larger and smaller daily tides being increased by the local resonance to the point at which the smaller tide becomes non-existent. When this occurs, the typical semi-diurnal (twice per day) tide becomes what is known as a diurnal (once per day) tide (Kamphuis, 2000).

2.2.1.1 Tidal Analysis

The basic principal of performing a tidal analysis is to separate a measured water level record into as many of its constituents as possible. The tide can then be represented as a harmonic summation as shown in Equation 1 (Dronkers, 1964).

$$\eta_{\mathrm{T}}(t) = \sum_{i=1}^{I} a_i \cos\left(\omega_i t + \alpha_i\right) \tag{1}$$

where $\eta_{\mathrm{T}}(t)$ is the water level at time t, a_i and α_i are the respective amplitudes and phase angles of the tidal constituents, and ω_i is their angular frequencies. Since angular frequencies are already known, tidal analysis is therefore the task of determining values for a_i and α_i from measured data sets. Since there are many tidal constituents acting at a given location, separating and analysing the different tidal signals can be a very difficult task. As such, only the most significant constituents are typically considered.

Several numerical models have been developed to facilitate the analysis of tides. These models include (but are not limited to) MIKE 21 (DHI, 2011), ADCIRC (Luettich and Westerink, 2011) and an un-named tidal analysis package developed by Mike Forman at the University of British Columbia (DFO, 2009).

Once amplitudes and phase angles of the significant constituents have been deciphered for a given location, Equation 1 can be applied to predict future tidal levels at any given time. This process has been undertaken for most major ports and navigable waterways around the world, thus providing operators with reasonable estimates of navigable depths (Kamphuis, 2000). In fact, many previously analysed tidal constituents from around the globe have been documented and published and are publically available.

2.2.1.2 Tidal Currents

Naturally, substantial currents are induced by the perpetual raising and lowering of water levels around the globe. These currents can be considered extremely long water waves which are hundreds of kilometres in length. Since the depths in the nearshore zone (where water level fluctuations are important) are relatively shallow (order of metres), small amplitude wave theory (first discussed by Airy in 1845 and discussed further in Section 2.2.2 below) can be applied by use of the shallow water long-wave velocity equation (where $d/L < 0.05$). This equation is presented below as Equation 2.

$$C = \sqrt{gd} \tag{2}$$

where C is the velocity of propagation, g the gravitational acceleration and d the water depth. The wave length of an equilibrium tide is therefore:

$$L = CT \tag{3}$$

where T is the wave period, which in this case is 12.42 hours for the semi-diurnal lunar constituent and 12 hours for the semi-diurnal solar constituent. From Equations 2 and 3 it is seen that as a tidal current propagates into shallower water (decreasing depth), both the velocity of propagation and the wave length will decrease.

Given that tidal currents possess wave lengths of hundreds of kilometres, their propagation is dramatically influenced by the rotation of the Earth. As such tidal currents do not propagate in straight lines through the Earth's numerous connected water bodies. Instead, tides tend to propagate in circular patterns, forming extremely large eddies. One such eddy exists in the Gulf of St. Lawrence, where tides propagate in a counter-clockwise manner with the center of rotation (referred to as an amphidromic point) some 100 kilometres northeast of Prince Edward Island, near the Iles de la Madeleine (Forrester, 1983). At the center of rotation, water levels remain approximately constant. Figure 2.4 shows this rotation of tidal flow for the Gulf of St. Lawrence, where dashed lines represent lines of equal tidal range and solid lines show lines in which the tide has the same phase (arrives at the same time).

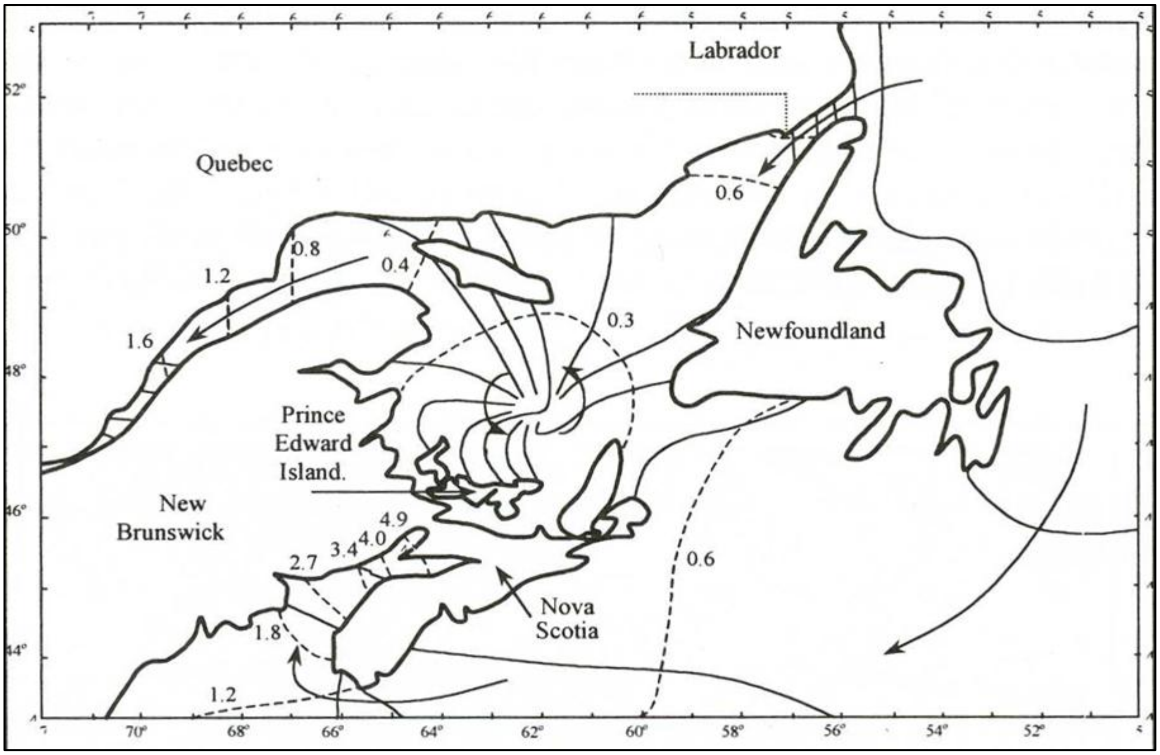

Figure 2.4: Semi-diurnal tide in the Gulf of St. Lawrence, illustrating lines of similar amplitude, lines of similar phase and the center of rotation, referred to as an amphidromic point (Kamphuis, 2000).

The presence of a counter-clockwise tidal circulation in the Gulf of St. Lawrence is important in the context of the present study, as it directly affects the propagation of currents near Shippagan Gully. Since the New Brunswick coastline runs approximately north-south and is located to the west of the center of tidal rotation in the Gulf of St. Lawrence, a weak tidal current is incurred from the north to the south along the Acadian Peninsula coast. Thus, in the absence of waves, a small longshore current is present at Shippagan Gully as water levels arrive at the inlet from the northeast and are propagated down shore.

In addition to the counter-clockwise tidal-circulation in the Gulf of St. Lawrence is the presence of a significant outflow jet from the St. Lawrence River. This outflow forms an estuarine plume which generates a weak southerly surface current due to the geometric properties of the estuary mouth and the relative buoyancy of the fresh water outflow (Sheng, 2001). This current follows closely the Gaspé Peninsula shoreline and subsequently passes the eastern shore of the Acadian

Peninsula in a southerly direction. This process strengthens the existing tide-induced current which is present in this region (Sheng, 2001).

2.2.1.3 Tidal Flow through an Inlet

As tides arrive at a shoreline, the water level along that shoreline will rise and fall in phase with the water level offshore (along lines of similar phase). However, in the presence of a partially closed bay such as those which are found behind barrier islands, the rising water levels in the sea will cause a current to flow into the bay, thus raising its water level. This inflow of water is referred to as the flood, while the subsequent outflow that comes with the falling water levels is called the ebb. If the bay is small enough and the entrance to the bay (tidal inlet) is large enough, the rise and fall of the water level in the bay will be precisely in phase with that of the ocean. As such, when both water bodies reach high tide, flow through the inlet will be zero (called the high water slack tide). Similarly, zero flow will be experience at low tide (low water slack tide). Following this pattern, the maximum flows through a tidal inlet will theoretically occur at the halfway point between high and low tides, where the mean water level is reached.

When a tidal inlet is narrow, or where the tidal lagoon is large, the filling of the lagoon will be slowed during the flood tide. As such, the maximum water level in the tidal lagoon will occur later than in the ocean or sea, and thus flow will continue to progress into the bay for some time after high tide has been reached in the sea. Similarly, the maximum currents flowing through the inlet will no longer occur at the mean water level (half way between high and low tides). Instead, the currents will lag behind depending on the geometric characteristics of the tidal inlet and lagoon (Dean and Dalrymple, 2002).

A useful tool in analysing flow through tidal inlets is called the *tidal prism*. The tidal prism is the total volume of water that must flow in and out of a tidal lagoon with every tidal cycle (D'Alpaos *et al*., 2010). It can be calculated by determining the differences between the high and low water levels throughout the tidal lagoon and multiplying them by the surface area. By calculating the tidal prism for a tidal inlet, average flow rates and current velocities through the inlet can be calculated based on the geometric properties of the inlet itself. Furthermore, tidal prisms provide a means by which inlets can be classified and compared in a quantitative manner (D'Alpaos *et al*., 2010).

For inlets with large tidal prisms, or for inlets in which the channel cross-section is relatively small, extremely large currents can be experienced both entering (flood) and exiting (ebb) the inlet. The erosive forces which accompany these high velocity flows can create a great deal of sediment transport in and around a tidal inlet. As such, tidal inlets are typically highly dynamic with respect to their long-term morphology. Sediment transport through tidal inlets will be discussed further in Section 2.3.

2.2.2 Nearshore Waves

2.2.2.1 Background on Wind Waves

In order to comprehend the complex nearshore hydrodynamics which occur in proximity to tidal inlets, some basic background on water waves is required. Furthermore, a basic understanding of the principal transformations which occur as waves propagate towards the shoreline must be discussed and understood.

Surface water waves are fluctuations in water levels which can be grouped into several different categories. In essence, any mechanism that creates a disturbance in a water body will ultimately create water waves. Water waves are commonly classified by their frequency (the inverse of wave period), with long period waves such as tides and tsunamis at one end of the frequency spectrum, and capillary waves (ripples) at the other. In the middle of the wave frequency spectrum lies a classification referred to as *gravity waves*, which are waves with periods typically between 1 and 30 seconds and wave heights which rarely exceed 10 m (Kamphuis, 2000). This wave classification receives its name from the restoring force which works to restore the still water level. Gravity waves are typically created by winds which blow over large expanses of open water, inducing shear stress at the air-water interface. This shear stress displaces the water in the direction in which the wind is blowing subsequently creating *wind waves*. The height of wind waves is directly related to three important variables: the wind speed, the distance over which the wind blows (referred to as the fetch) and the duration for which the winds are sustained (Kamphuis, 2000).

Wind waves can be classified into two categories referred to as sea and swell. Sea waves are locally generated wind waves and are highly variable in both height and period. These waves tend to propagate more or less in the prominent wind direction and tend to create extremely rough seas where strong winds are present. Storm systems are typically accompanied by high local winds and subsequently large sea waves (Goda, 2000).

On large bodies of water, locally generated wind waves will continue to travel beyond the area in which they are generated. As they propagate across open water, their profile becomes more regular as individual waves separate and waves of similar frequency group together. The result of this process is well defined groupings of regular waves commonly referred to as *wave sets*, which continue to propagate over areas in which there is no-longer a generating wind. These waves are referred to as *swell waves* and are experienced on most ocean-bordering coastlines around the world (Goda, 2000).

Generally speaking, sea and swell waves occur simultaneously at a given location, as waves which have arrived from elsewhere are subjected to local winds. In these situations, the sea and swell wave components can be separated by period, with swell waves having a much lower frequency than sea waves (Goda, 2000).

There are numerous numerical models available to model the generation and propagation of water waves. These models can be loosely divided into two groups; phase-averaged models and phase-resolving models. Phase resolving models calculate the entire wave height profile (crest to trough) as the waves propagate across the model domain, thereby providing a realistic simulation of individual waves and wave trains in motion. Phase-averaged models on the other hand neglect changes in wave phase and instead calculate the wave action density for given wave spectra, from which characteristic wave parameters are inferred (Aquaveo, 2011). The most common wave parameter to be calculated in a phase-averaged wave model is referred to as the significant wave height, which is by definition, the average of the highest one third of the wave heights. Significant wave height is an important parameter which is used in the majority of conventional coastal engineering practises due to the fact that it has been shown to closely approximate the highest wave height observed by a trained observer (USACE, 1984). As such, many classical formulations have been based on significant wave height, making it the basis of many coastal engineering calculations which are still used today.

Largely due to the significant reduction in computational time required by phase-averaged models over phase resolving models, phase-averaged models are the more practical model for simulating large domains or large temporal scales. SWAN (Ris,, 1997), STWave (Smith *et al*., 2001), MIKE21 (DHI, 2011) and CMS-Wave (Lin *et al*., 2008) are all examples of widely used phase-averaged wave models.

In smaller domain applications, particularly where nearshore wave transformations (discussed in the following section) and wave reflection are of importance, phase-resolving wave models are likely to be the better suited model. Although computationally more demanding, these models can produce much better solutions for transient wave data. An example of a typical application in which a phase-resolving model will likely provide better results is studying the wave agitation inside a sheltered harbour or marina. Examples of widely used phase-resolving wave models are CG-Wave (Demirbilek and Panchang, 1998) and BOUSS-2D (Nwogu and Demirbilek, 2001).

2.2.2.2 Nearshore Wave Transformations

As both sea and swell waves propagate towards a shoreline and advance into shallower waters, they begin to feel the presence of the sea-floor. This transition occurs when the depth is approximately half of the wave length (Airy, 1845). At this point, several changes to the water surface profile begin to occur and are hence referred to as *nearshore wave transformations*. The four principal nearshore wave transformations are shoaling, refraction, diffraction, and breaking and are discussed in the following sections as they pertain to tidal inlets.

Once waves begin to feel the bottom ($d/L > 0.5$) they will begin to shoal. Shoaling is the process by which both wave lengths and wave speeds are decreased while wave heights are increased.

The result is a progressive steepening of the wave profile. This process continues as the wave propagates into shallower water until the wave profile becomes steep enough that it loses stability and breaks (discussed further below). Due to the process of wave shoaling, nearshore waves are typically much higher than they once were offshore. As such, waves arriving at a tidal inlet will have an increased height relative to the nearshore depths surrounding the inlet (assuming they remain un-broken). Similarly, their propagation through the tidal inlet (assuming the wave direction is perpendicular to the inlet mouth) will be determined largely by the available depths.

Analytically, wave shoaling is typically represented by a local shoaling coefficient (K_s), which is simply the ratio of the wave height at any given nearshore location to its offshore wave height. There are several theoretical and empirical methods available to predict K_s, which generally relate the offshore wave height (H_o) and period (T) to the local water depth (d). The most common of these methods is derived from small amplitude wave theory (first discussed by Airy in 1845) and is as follows:

$$K_s = \frac{H}{H_o} = \sqrt{\frac{1}{2n}\frac{1}{\tanh kd}} \tag{4}$$

Where H is the nearshore wave height at the location of interest, H_o is the offshore wave height, k is the wave number (2π divided by the wave length, L), d is the local water depth and:

$$n = \frac{1}{2}\left(1 + \frac{2kd}{\sinh 2kd}\right) \tag{5}$$

Equation 4 is a linear approximation of wave shoaling, where K_s is 1.0 in deep water, decreases with water depth to 0.91 and then rises to infinity as the water depth approaches zero (Kamphuis, 2000). Of course, the nearshore wave height will not grow to infinity in reality, as a practical limitation on wave growth is imposed by the process of wave breaking (discussed below).

The above paragraphs are of course based on the idealized situation, in which a wave approaches the shoreline at an angle precisely normal to the depth contours. In this situation, shoaling will occur simultaneously along the entire length of the wave in the longitudinal direction (shore parallel). However, this is rarely the case as shorelines and bathymetric contours do not typically form straight lines and waves rarely approach the shoreline at exactly 90^0. The result is that one end of the wave crest will reach shallower water first and begin to shoal prior to the opposite end of the wave crest. Since shoaling slows the wave speed and steepens the wave profile, the portion of the wave in shallower water will slow prior to the portion of the wave which is in deeper water, creating a bend in the wave crest (in plan-view). This process is referred to as refraction and ultimately results in wave crests bending as they propagate towards the shoreline in order to align themselves with the bathymetric contours. This process is illustrated in Figure 2.5 below.

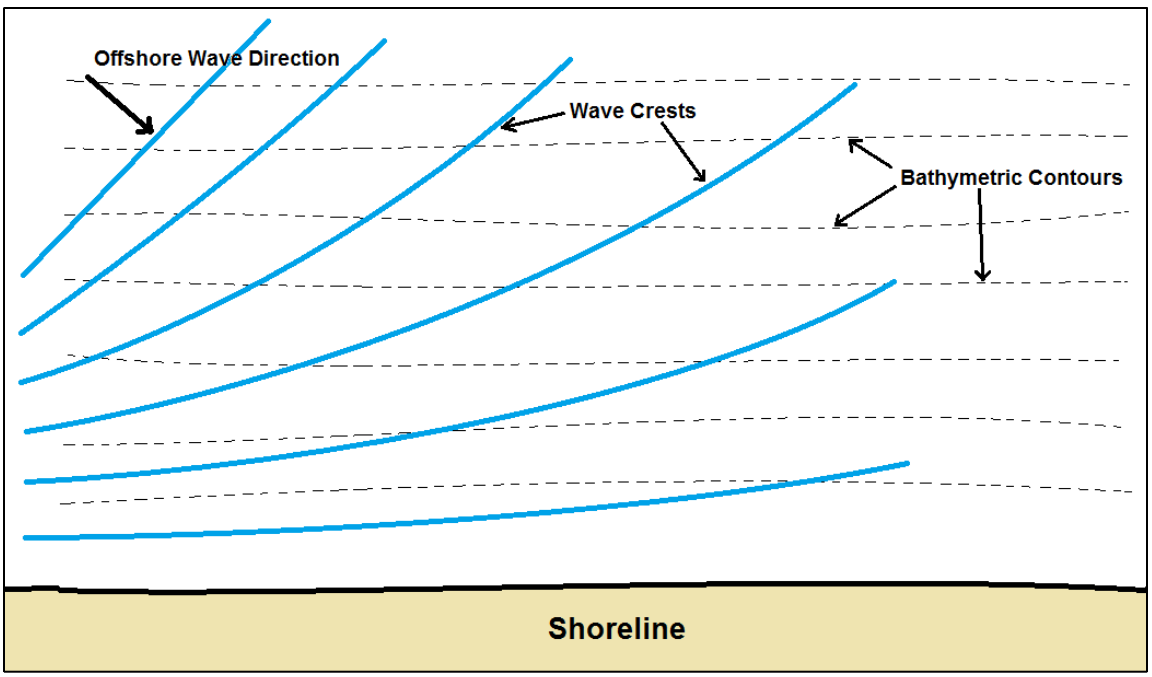

Figure 2.5: Wave crests refracting as they propagate towards the shoreline over approximately parallel bathymetric contours.

Similar to wave shoaling, wave refraction is represented analytically as a local refraction coefficient (K_r), which is a ratio of the distance between adjacent wave rays (b) at the offshore location to the location of interest in the nearshore zone. This distance can be approximated as the cosine of the angle formed between the wave crest and the shoreline, thus resulting in the refraction coefficient being written as follows:

$$K_r = \sqrt{\frac{b_0}{b}} = \sqrt{\frac{\cos\alpha_0}{\cos\alpha}} \tag{6}$$

where α is the wave crest angle relative to the shoreline and b is the distance between adjacent crests. In order to predict what K_r will be given the characteristics of an offshore wave, an estimation must therefore be made for the value of α at the location of interest. This is typically done using Snell's law, which is shown in Equation 7 below (Kamphuis, 2000).

$$\frac{\sin\alpha}{\sin\alpha_0} = \tanh\frac{2\pi d}{L} \tag{7}$$

where d is the local water depth and L the wave length at the given water depth. As such, d must first be known and L estimated from linear wave theory (or a higher order theory).

Once K_r and K_s have been approximated using the above formulations (or other), the offshore wave height can be multiplied by both coefficients to determine the nearshore wave height at the location of interest. This process is shown below as Equation 8:

$$H = K_s K_r H_0 \tag{8}$$

Due to the existence of refraction, waves propagating in the nearshore zone will bend and conform to the local depth contours, which can be particularly complex especially where offshore bars or ebb-shoals exist. As such, waves which reach the mouth of a tidal inlet are likely to be propagating in an altered direction to those which are present offshore. It is the plan-view orientation of local bathymetric contours surrounding a tidal inlet which will depict the directional range from which waves will arrive at the inlet mouth.

Similar to refraction, diffraction refers to the bending of a wave crest. Diffraction however is not induced by the gradual change in bathymetry but is instead induced by the presence of an obstruction. For example, waves propagating perpendicular to an offshore breakwater will diffract around the ends of the breakwater, thus creating a bend in their wave crests which will cause them to wrap around the structure and continue to propagate inwards directly in its lee. In an engineered coastal inlet, diffraction plays an important role as waves will bend around the inlet headlands or inlet jetties and subsequently propagate towards to the interior edges of the inlet or navigation channel. The concept of wave diffraction is shown in Figure 2.6 for both an idealized offshore breakwater and a typical engineered tidal inlet.

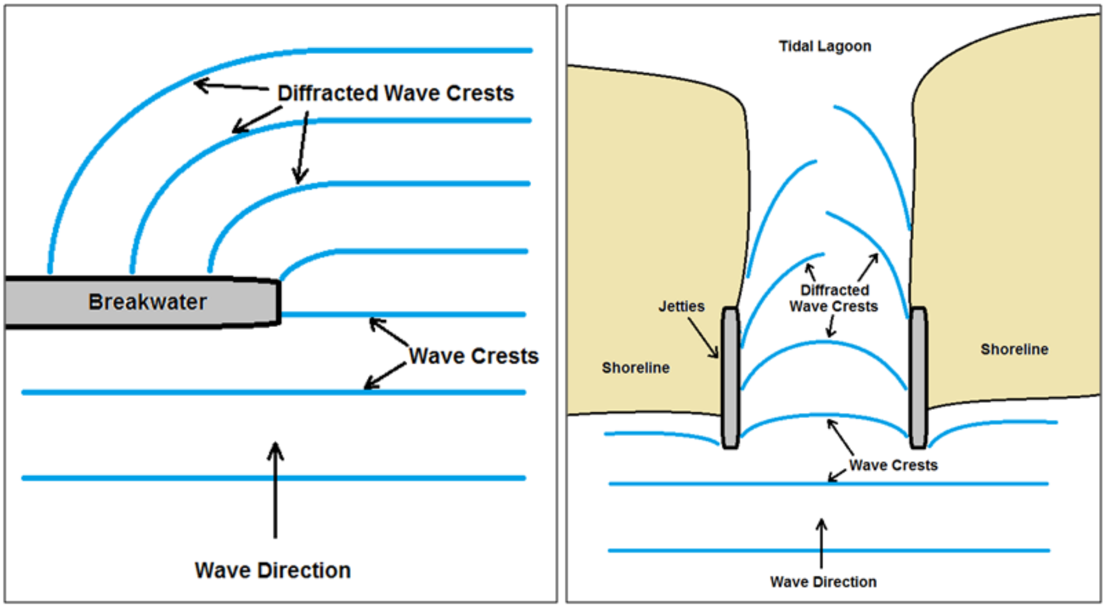

Figure 2.6: Wave diffraction around an offshore breakwater (left) and through a tidal inlet with engineered jetties (right).

Perhaps the most important nearshore wave transformation with respect to nearshore hydrodynamics and coastal morphology is wave breaking. As was previously mentioned, a wave will continue to shoal as it propagates over increasingly shallow waters until it becomes too steep and de-stabilizes. At this point the wave will break, a process by which a great deal of energy is expended and ultimately dissipated, creating highly turbulent flow. Since wave breaking occurs when the shoaling process has reached its physical limit, it too is a function of water depth. Often, large waves will break further offshore, while secondary breaking of smaller waves will occur in shallower depths or along the shoreline. Increased depths due to high tides or storm surge will however permit larger waves to propagate further and break closer to the shore. For the case of a tidal inlet, these elevated water levels can result in much larger waves propagating into the confines of the inlet un-broken than would normally be possible.

There are dozens of accepted formulas to predict breaking wave heights and breaking wave depths given the offshore characteristics for a given wave. This has been the subject of numerous studies due to the fact that breaking waves create large forces on coastal structures (Rattanapitikon and Shibayama, 2000). Furthermore, the hydrodynamic effects of a breaking wave are a primary driving force behind coastal sediment transport. The simplest and oldest widely used breaking wave formula was first presented by McCowan in 1894 and relates breaking wave height to breaking wave depth as follows:

$$H_b = 0.78d_b \tag{9}$$

where H_b is the breaking wave height and d_b is the breaking wave depth. When plotted in conjunction with a shoaling formula such as the one which was presented in Equation 4 above, the line created by McCowan's formula will intersect the shoaling curve at the theoretical location of breaking. An example of this is shown in Figure 2.7, which also includes the breaking formulation of Goda (1970), Weggle (1972) and Komar & Gaughan (1972) for comparison.

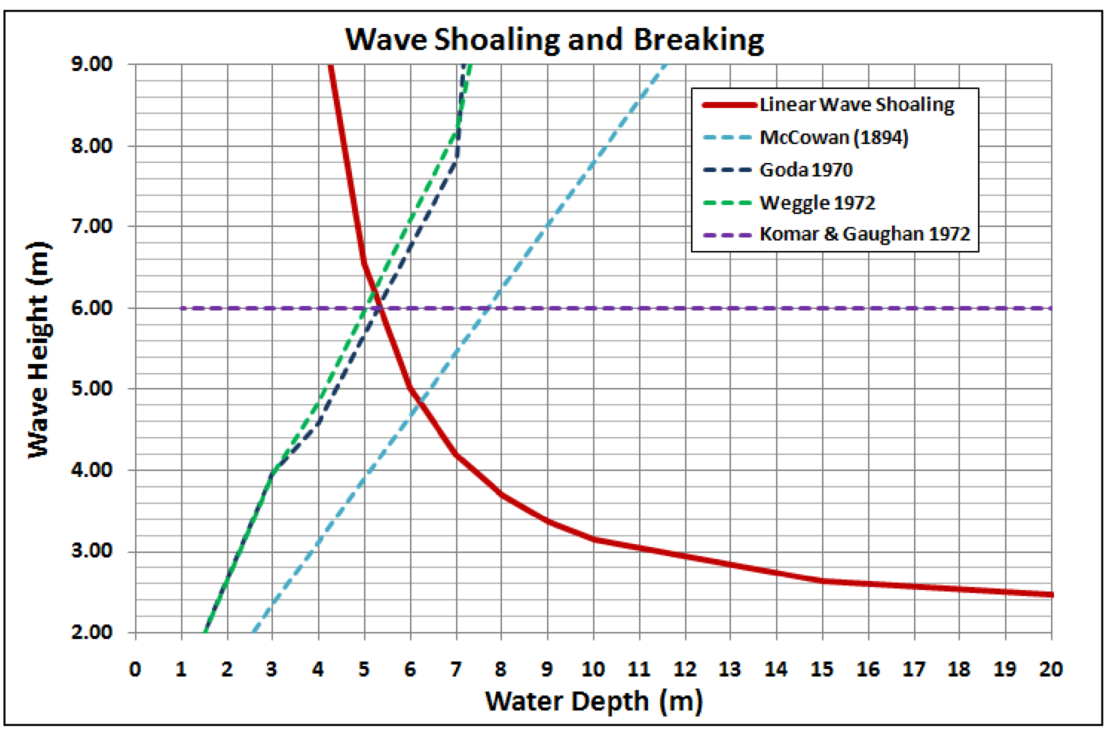

Figure 2.7: Plot of theoretical shoaling profile and limitations on wave height posed by wave breaking, as per four classical wave breaking formulations (H_{m0} = 4.2 m, T_p = 17 s, α_0 = 75^0).

The breaking wave criterion presented in Equation 9 is a relatively old and highly approximate method. Dozens of more recent researchers have shown breaking wave heights and depths to be influenced by other variables such as wave length and beach slope (Goda (1970), Weggle (1972), Komar and Gaughan (1972), Battjes (1974) and Smith and Krause (1990)). However, the method presented by McCowan still serves as a reasonable approximation in many cases (Rattanapitikon and Shibayama, 2000). More widely accepted and well validated formulas include the three additional formulations presented in Figure 2.7.

2.2.2.3 Wave Induced Currents

As waves propagate towards the shoreline, there is a mean transport of water in the direction of propagation. This phenomenon is referred to as *mass transport* and is not accounted for by linear wave theory (first discussed by Airy in 1845). Linear wave theory assumes that water particles subjected to surface waves will travel in *closed* elliptical orbits. This has been shown however to be untrue, as in reality the elliptical orbits move in the direction of wave propagation. As such, the elliptical orbits overlap and therefore do not close. This phenomenon is illustrated in Figure 2.8. The process is explained by the fact that the portion of the ellipse in which water particles move forwards occurs under the wave crest. Conversely, the backwards motion of water particles corresponds to the wave trough. Since the total depth at the wave crest is larger than at the trough, this portion of the elliptical orbit is also slightly larger, and thus results in the net forward movement of water particles. It follows that mass transport is larger for more energetic waves, or in other words waves with larger wave heights (Dean and Dalrymple, 2002).

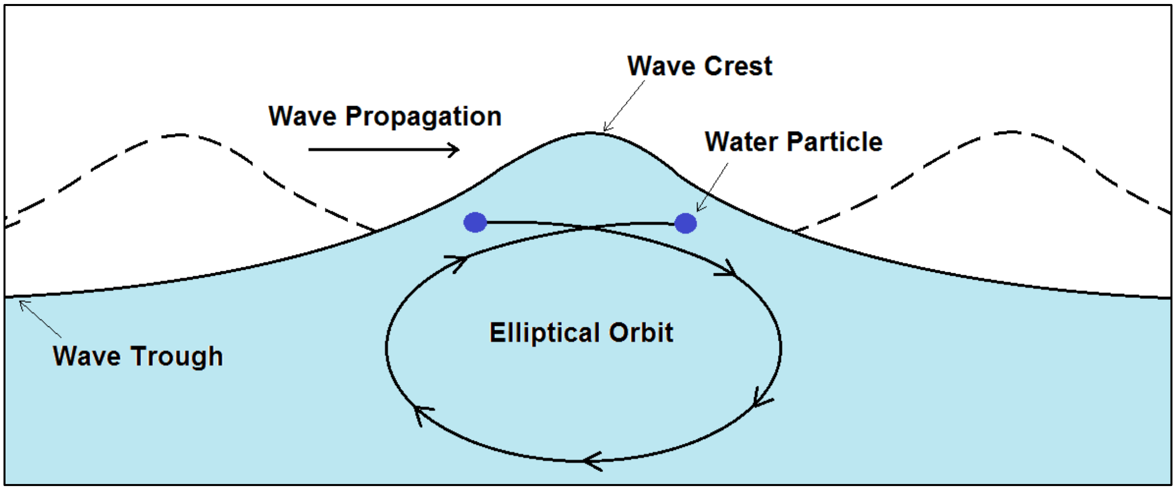

Figure 2.8: Overlapping elliptical orbit of water particles under surface waves.

As with any dynamic mechanism, mass transport has a momentum component. Following Newton's second law, forces must be generated whenever momentum changes in either magnitude or direction. In recognition of this, Longuet-Higgins and Stewart (1963) introduced the concept of wave momentum flux, designating the sum of the momentum flux and the mean pressure as the *radiation stress*. Radiation stress is a vector quantity which drives water currents in the nearshore zone in the general direction of wave propagation.

At the moment in which a wave breaks, the momentum flux significantly decreases as wave energy is dissipated. This change in momentum flux must be balanced, which is achieved by inducing large forces in the surf zone (nearshore zone in which waves break) in the direction of wave propagation. These forces magnify the existing radiation stresses; ultimately creating large currents in the nearshore zone, particularly where breaking waves exist. The by-product of these processes is a relative increase in water level due to the surge of water in the direction of the shoreline. This phenomenon is known as wave set-up (Dean and Dalrymple, 2002).

Wave induced currents can be divided into two categories based on direction. Currents which act normal to the coastline are referred to as cross-shore currents, while currents acting parallel to the coastline are called longshore currents. In reality, currents generally posses components in both the longshore and cross-shore directions and thus their direction is truly represented by the resultant vector. Since mass transport creates a current primarily in the shoreward direction, it can be considered a cross-shore process. The shoreward transport of water induced by mass transport must however be returned to the sea. On a long, uniform beach this process is referred to as *undertow* (refer to Figure 2.9). Undertow is a cross-shore return current (in the seaward direction) which propagates along the sea floor, thus counteracting mass transport and rendering the net cross-shore flow to zero (as must logically be the case). When the shoreline is non-uniform, *rip currents* can be formed in which converging currents exit together through the entire water column (as opposed to along the bottom as is the case for undertow). On most coastlines around the world, undertows and rip currents are found in combination. These processes return the shoreward transport of water to the sea and thus balance the theoretical cross-shore hydrodynamic model (refer to Figure 2.9).

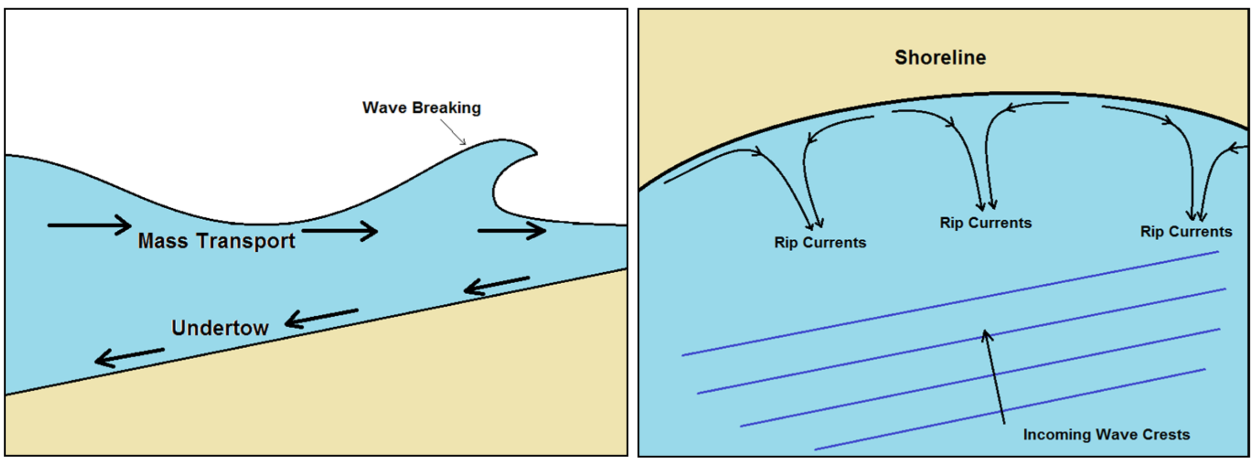

Figure 2.9: Profile and plan-views of nearshore zone showing mass transport and undertow (left), and rip currents (right).

Longshore currents are generated when waves approach the shoreline at an angle. As waves are refracted towards the shoreline, the induced momentum flux (radiation stresses) have a longshore vector component. As such, the elliptical orbits of water particles become helixes, thus propagating in three dimensional space with a longshore component. The result is a longshore current whereby the direction is governed by the angle of incoming waves. Waves approaching from > 90^0 relative to the coastline will cause longshore currents in one direction, while waves approaching from < 90^0 will cause currents in the opposite direction. On most coastlines around the world, one longshore direction typically outweighs the other, resulting in a net longshore current in one direction along the coastline. Not surprisingly, this current is typically accompanied by sediment transport (discussed in Section 2.3.1). As such, its direction and magnitude can often be inferred from local morphological characteristics along the shoreline. This topic is discussed in the following sections.

2.3 Tidal Inlet Morphology

All of the coastal processes which were described in the previous sections have the ability to move sediment. This is due to the fact that they create currents which induce shear stresses capable of picking up sediment and moving it in the direction of flow through the tidal inlet or within the nearshore zone. Given that many of the above-described processes occur simultaneously at or near tidal inlets, the interaction between the various sediment transport mechanisms is extremely complex and is a partial subject of the present study. However, basic principals can be derived from previous research and case studies which are summarized in the following sections.

2.3.1 Sediment Transport Mechanisms

Coastal inlets are generally extremely dynamic in nature and are often inherently unstable. This is due to the complex cross shore and longshore sediment transport mechanisms which exist in these regions. Not surprisingly, cross shore and longshore sediment transport are directly related to their hydrodynamic counterparts which were discussed in the previous sections. It is useful to describe these processes independently, while recognizing that they in fact occur simultaneously at a coastal inlet.

As was described above, cross shore coastal processes are those which occur at an angle approximately normal to the shoreline, while longshore coastal processes are those which occur parallel to the shoreline. This is of course a generalized statement as coastal processes will never be strictly 2-dimensional. As such, the classification of a cross-shore or longshore processes is often used in reference to the shore-perpendicular and shore- parallel components of a vector process.

The most important hydrodynamic processes at a tidal inlet are of course tides and waves. As was previously discussed, both tides and waves induce strong currents in the nearshore zone and into a tidal inlet/lagoon system. These processes generate shear stresses along the bed which are capable of inducing sediment motion. If the shear stress exerted by the passing current exceeds the critical shear stress of the bed material (sediment), the bed material will begin to move in the direction of the current. The classical numerical representation of the requirement for incipient sediment motion is known as the Shields parameter and was originally presented by A. Shields in 1936. The Shields parameter is a non-dimensionalization of a shear stress which represents the ratio of fluid force on a given particle to the weight of that particle (Shields, 1936). The Shields parameter is presented below as Equation 10.

$$\tau_* = \frac{\tau}{(\rho_s - \rho)gD} \tag{10}$$

where τ is a dimensional shear stress, ρ_s is the density of the sediment, ρ is the density of the fluid (water), g is gravitational acceleration and D is the characteristic particle diameter of the sediment. In order for sediment motion to begin, the following relationship must therefore be met:

$$\tau_b^* = \tau_c^* \tag{11}$$

where τ_b^* is the dimensionless shear stress and τ_c^* is the dimensionless critical shear stress. Shields (1936) demonstrated that the criterion depicted by Equation 11 above can be empirically plotted as curve on a chart with the following axes:

$$X = \frac{V_* D}{\nu} \qquad\qquad Y = \frac{\rho V_*^2}{\gamma_s D} \tag{12, 13}$$

where V_* is the shear velocity, ν is the kinematic viscosity and γ_s is the specific gravity of the bed material (product of density and acceleration due to gravity). The ensuing curve is referred to as the Shields curve. It can be seen that the X-axis is essentially a particle Reynolds number. It is also noted that both axes possess the shear velocity parameter V_* thereby requiring iterations on an initial assumed value.

2.3.1.1 Bed Load

Once incipient sediment motion has been reached, the mobile sediment will be transported in one of two possible ways. These are referred to as *bed load* and *suspended load*. *Bed load* is the term given to sediment which is moving along the bed, either by rolling, sliding and/or hopping. Numerous researchers have studied *bed load* resulting in the existence of multiple formulas for the calculation of *bed load rate*. The classical methods involve a term referred to as Einstein's Phi which is shown in Equation 14 (Einstein, 1942).

$$\emptyset = \frac{q_{sb}\rho^{1/2}}{\gamma_s^{1/2} D^{3/2}} \tag{14}$$

Where $\emptyset$ is Einstein's Phi, and q_{sb} is the bed load rate (in m^2/s). The formula shown in Equation 14 can be re-arranged to solve for q_{sb}, however Einstein's Phi must first be known. Consequently, many researchers have proposed empirical or semi empirical formulas for this purpose, namely:

Einstein's Generalized Form (1942):

$$\emptyset = 8(Y - Y_{CR})^{3/2} \tag{15}$$

Meyer Peter and Müller (1948):

$$\emptyset = 8(\tau_* - 0.041)^{3/2} \tag{16}$$

R.A. Bagnold (1968):

$$\emptyset = bY^{1/2}(Y - Y_{CR}) \tag{17}$$

M.S. Yalin (1963):

$$\emptyset = 0.635 \times S\sqrt{Y}\left[1 - \frac{1}{aS}\ln(1 + aS)\right] \qquad S = \frac{Y - Y_{CR}}{Y_{CR}} \qquad a = \frac{2.45Y_{CR}^{1/2}}{W^{0.4}} \tag{18}$$

Van Rijn (1984):

$$\emptyset = 0.053\Xi^{-0.3}(\frac{Y}{Y_{CR}} - 1)^{2.1} \qquad \Xi = (\frac{\gamma_s D^3}{\rho\nu^2})^{1/3} \tag{19}$$

Where Y and Y_{CR} are determined from the Y-axis component of Shields Curve (equation listed above), V is the fluid velocity, b is a coefficient depending on the Reynolds number ($b \approx 4.25$ for rough turbulent flow) and W is the density of the bed material divided by the density of water.

2.3.1.2 Suspended Load

The second form of sediment transport, referred to as *suspended load*, is the transport of sediment (or bed material) which is entrained in the water column (i.e. not moving along the bed). Calculating the *suspended load* rate is a more difficult endeavour then calculating *bed load* due to the fact that it requires integration through the entire water column. As such, *suspended load* formulations are generally computationally complex. Similar to *bed load*, multiple researchers have proposed empirical or semi-empirical formulas to calculate the *suspended load* throughout the water column. A classical example of one such formulation is the Rousse-Einstein (1937, 1954) formulation which is presented as Equations 20 and 21 below:

$$\phi_{SS} \int_{\eta_a}^{\eta_b} = C_\varepsilon \frac{2.5 \ln \dfrac{h}{K_s} + B_s}{(\dfrac{1}{\eta_\varepsilon} - 1)^m} \int_{\eta_a}^{\eta_b} \eta^{1/7} (\frac{1}{\eta} - 1)^m d\eta \tag{20}$$

$$\bar{q}_{ss} \int_{\eta_a}^{\eta_b} = V_* h \gamma_s \phi_{ss} \tag{21}$$

where η is the relative water depth (z/h where z is measured from the bed), C_ε is determined from an empirical curve (where $\varepsilon = 2D \times Y/Y_{CR}$), m is equal to $2.5\omega/V_*$ and ω is also determined from an empirical curve.

Another common equation for suspended load, particularly in numerical modeling applications is the Advection-Diffusion (AD) equation. The AD equation is particularly useful for situations where the suspended sediment concentration is subjected to rapid changes in both time and space. This is often the case for applications at a river mouth, inlet entrance, in a navigation channel or in the vicinity of coastal structures, thus making it particularly useful for the present topic of numerical modeling at a tidal inlet. The AD equation for suspended load is obtained from the continuity of depth-averaged suspended sediment transport and is written as follows (Buttolph *et al.*, 2006):

$$\frac{\partial(Cd)}{\partial t}+\frac{\partial(Cq_x)}{\partial x}+\frac{\partial\left(Cq_y\right)}{\partial y}=\frac{\partial}{\partial x}\left(K_x d\frac{\partial C}{\partial x}\right)+\frac{\partial}{\partial y}\left(K_y d\frac{\partial C}{\partial y}\right)+P-D \tag{22}$$

where:

- C = depth-averaged sediment concentration
- d = total depth ($h + \eta$)
- h = still water depth
- η = deviation of the water-surface elevation from the still-water level
- t = time
- q_x = flow per unit width parallel to the x-axis (ud)
- q_y = flow per unit width parallel to the y-axis (vd)
- u = depth-averaged current velocity parallel to the x-axis
- v = depth-averaged current velocity parallel to the y-axis
- K_x = sediment diffusion coefficient for the x-direction
- K_y = sediment diffusion coefficient for the y-direction
- P = sediment pick-up rate (upward sediment flux)
- D = sediment deposition rate (downward sediment flux)

2.3.1.3 Combined Load and Total Load

In practice, bed load and suspended load can be calculated using separate formulations and added, which results in the *combined load*, a term which describes the complete sediment transport rate for a given set of parameters and at a given location. Alternatively, the term *total load* refers to stand-alone formulations which approximate both bed and suspended load together. *Total load* formulations are often employed in sediment transport numerical models due to their comparative computational simplicity. An example of a classical total load formulation is the Watanabe (1987) total load formulation. This formulation is shown as Equation 23:

$$q_{tot}=A\left[\frac{\left(\tau_{b,max}-\tau_{cr}\right)U_c}{\rho_w g}\right] \tag{23}$$

where:

- q_{tot} = total load (both suspended and bed load)
- $\tau_{b,max}$ = maximum shear stress at the bed
- τ_{cr} = shear stress at incipient sediment motion
- U_c = depth-averaged current velocity

- ρ_w = density of water
- g = acceleration of gravity
- A = empirical coefficient typically ranging from 0.1 to 2

It can be seen from the above sections that numerous sediment transport models exist for the calculation of both bed load and suspended load, which can often be employed as stand-alone formulations, or in combination with other formulae. It can be seen that key parameters in all formulations are derived from the original work completed by Shields in 1936. As such, the concept of sediment transport can be more or less simplified to be a function of shear stress. To understand how sediment transport occurs at a tidal inlet, we must therefore look at the processes which produce shear stresses.

2.3.1.4 Cross-Shore Sediment Transport at Tidal Inlets

The most prominent cross-shore sediment transport mechanism at most tidal inlets is the hydrodynamics accompanied by tides. As was discussed in Section 2.2.1, a rising tide causes flow to enter a tidal inlet and subsequently fill the back-bay system, a process which is called the flood tide. Conversely, as the water level falls in the ocean, the back-bay system will drain subsequently forcing flow to exit the tidal inlet, referred to as the ebb tide. This inflow and outflow of water can result in large currents through the inlet, where the magnitude of the current is governed by the tidal prism and the cross-sectional area of the inlet. As was discussed in the previous sections, large currents are accompanied by large shear stresses at the bed, which can induce sediment motion if the critical shear stress of the bed material is exceeded. Once this criterion is exceeded, sediment will move in the direction of flow, which in the case of a flood tide means sediment will enter the tidal lagoon. Following this logic, sediment which is mobile during the ebb tide will be transported sea-ward.

As the ebb-flow exits a tidal inlet, the currents will weaken as the cross-sectional area becomes very large in the open ocean. Similarly, the flood-flow currents will weaken as the flow enters the tidal lagoon. As can be seen from the equations presented in the previous sections for bed load and suspended load, sediment transport rates are directly related to velocity (shear stress). As such, both bed load and suspended load rates will diminish as current velocities become smaller. As such, the governing criteria for sediment motion may no longer be met and sediment will begin to be deposited. In the case of the ebb flow, sediment deposition will occur directly offshore where the ebb flow enters the ocean, thus creating what is commonly referred to as an ebb-shoal. Conversely the flood tide will transport sediment into the tidal lagoon, subsequently depositing the sediment in the confines of the sheltered back-bay system in the form of a flood-shoal. An example of this cross-shore morphology is illustrated in Figure 2.10 below.

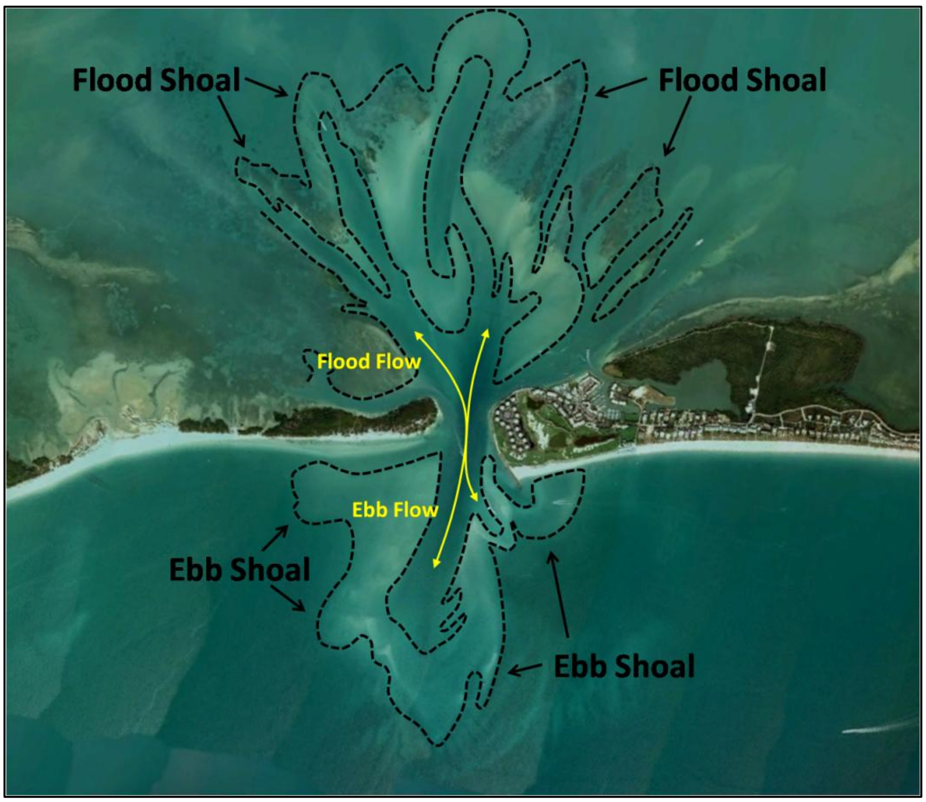

Figure 2.10: Satellite imagery of Red Fish Pass, Florida, illustrating well defined ebb and flood shoals (modified from Google Earth, 2011).

The second process contributing to cross-shore sediment transport is nearshore waves. As was discussed in Section 2.2.2, waves are capable of producing strong currents in the near-shore zone. This is particularly true during the wave breaking process where the presence of a large momentum flux results in the generation of radiation stresses, driving currents in the direction of wave propagation. Similarly to tidal currents, the wave induced currents are capable of producing shear stresses which exceed the critical shear stress for incipient sediment motion and thus induce sediment transport in the direction of wave propagation.

In the absence of any obstruction, waves propagating normal to the shoreline will break uniformly, eroding the bed at the breaking point (where the largest shear stresses induce the maximum sediment motion). The entrained sediment will then be deposited in one of two locations where the wave induced currents diminish; either in the swash zone (area immediately inshore of the breaking point), or immediately offshore and adjacent to the breaking point where it is transported by the undertow. The first of these scenarios results in the creation of a morphological beach feature referred to as a berm, while the second results in the creation of a feature which is called a bar (refer to Figure 2.11).

In the winter, waves are typically larger than they would be in the summer due to the increase in relative storm frequency and intensity. As such, more frequent and larger waves will break further offshore, thus shifting the primary breaking and subsequent erosion zone further from the shoreline. As is shown in Figure 2.11 below, this seasonal variance can create a multi-tiered beach profile with two berms and two bars, corresponding to the winter (high energy) and summer (low energy) seasons.

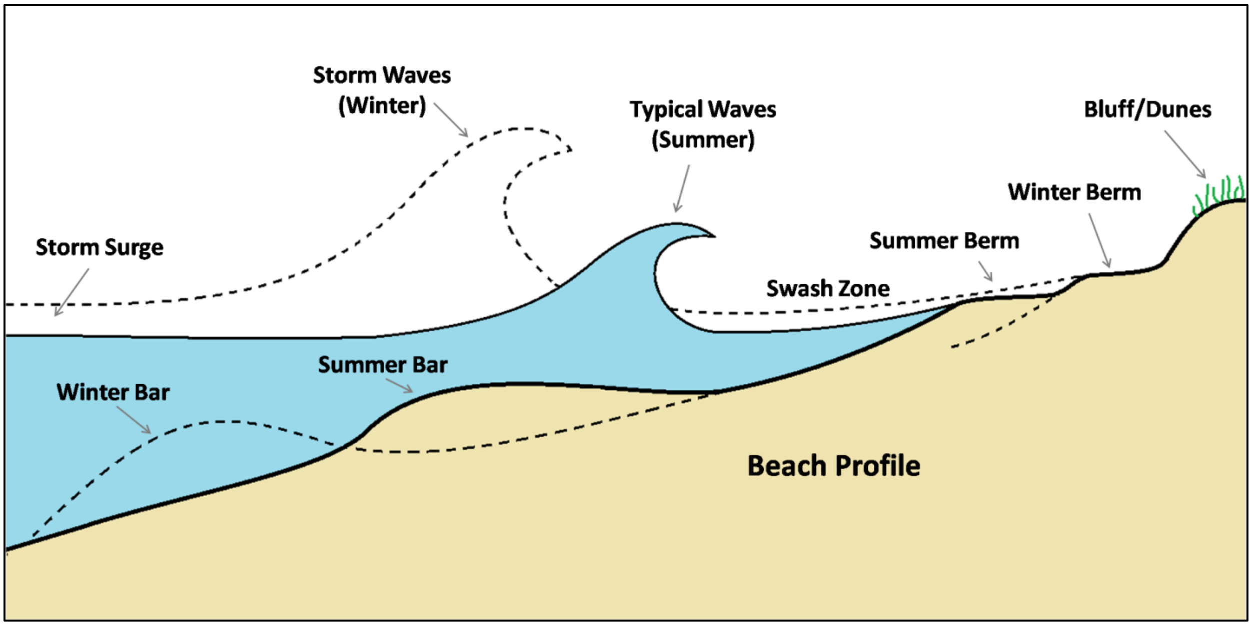

Figure 2.11: Definition sketch illustrating seasonal variations in beach profile caused by the relative intensity of winter and summer waves.

When storm waves arrive at a coastline they are often accompanied by storm surge. Storm surge is an increase in water level at the shoreline due to a combination of low atmospheric pressure and wind set-up, a process by which wind-induced shear stress tilts the water surface profile in the direction of the wind. As storm surge creates deeper water in the nearshore zone it allows storm waves to propagate further inshore then would otherwise be possible. The morphologic result of this phenomenon is that the larger waves are able to propagate further inshore, often resulting in increased erosion of the beach face or dune-system.

As waves approach a tidal inlet, a portion of the wave energy will propagate through the inlet and into the tidal lagoon. If these waves are energetic enough they are capable of transporting sediment through the inlet and into the back-bay system. Waves entering an inlet will also diffract around the inlet entrance and refract along the inner banks of the channel. As such, waves will be re-directed towards the sides of the inlet where they will break resulting in the potential for morphologic change (illustrated in Figure 2.12).

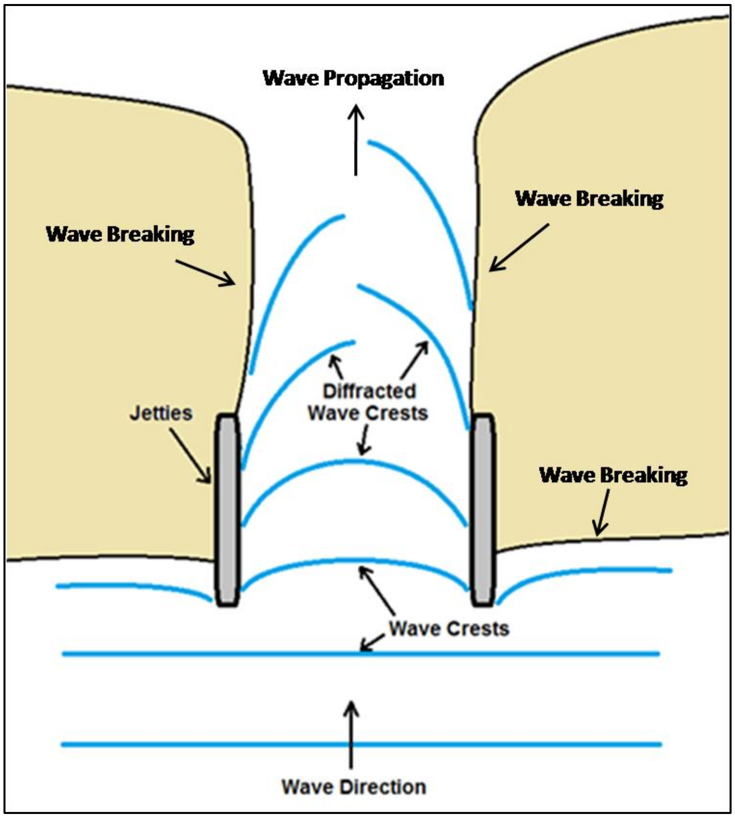

Figure 2.12: Wave propagation through an idealized, engineered inlet, illustrating wave breaking on inlet banks.

As is seen in Figure 2.12, the combination of refraction/diffraction inside the tidal inlet and the breaking process can induce large erosive forces along the inlet banks. This process can subsequently result in the widening of a tidal inlet; however this widening is often accompanied by a shallower inlet cross-section. It is important to understand that this can alter the cross-sectional area of the tidal inlet, thus having an effect on tidal currents through the inlet and further complicating the cross-shore inlet morphology.

2.3.1.5 Longshore Sediment Transport at Tidal Inlets

Longshore sediment transport is transport which is induced by longshore hydrodynamic processes. As was discussed in Section 2.2.2, longshore currents are created by waves which approach the shoreline at an oblique angle. The wave induced currents are accompanied by shear stresses, which are capable of meeting the criterion for incipient sediment motion. Once incipient sediment motion occurs, the sediment will be transported in the direction of the wave-induced currents (radiation stresses) which in this case have a longshore vector component. As such, sediment will be moved down the coastline.

There are two well known longshore transport formulae available to estimate potential longshore sediment transport rates. The first and best known equation for estimating bulk longshore sediment transport rate, Q_s, is published in CERC (1984), and is written as follows:

$$Q_{s=} \frac{I_s}{(\rho_s - \rho)(1-n)g} \tag{24}$$

where:

$$I_s = 0.39 P_{asb} \tag{25}$$

$$P_{asb} = \frac{1}{16} \frac{\rho g^{3/2}}{\gamma_{sb}^{1/2}} H_{sb}^{5/2} sin2\alpha_b \tag{26}$$

The CERC formula takes into account the effects of sediment density (ρ_s), water density (ρ), sediment porosity (n), significant breaking wave height (H_{sb}), breaking wave depth (d_b) and breaking wave angle relative to the shoreline (α_b).

The second well known formula was developed and published by Kamphuis (1991) and is presented below as Equation 27. This formula was developed based on small-scale hydraulic model tests and was found to be valid for available field data (Kamphuis, 1991). As a supplement to the CERC formula parameters, the Kamphuis formula includes the effects of wave period (T_{op}), beach slope (m_b) and mean sediment grain diameter (D). As such, it is likely the more accurate formula for use with a highly variable wave climate propagating over a shallow beach slope.

$$Q_k = 6.4 \times 10^4 H_{sb}^2 T_{op}^{1.5} m_b^{0.75} D^{-0.25} sin^{0.6} 2\alpha_b \tag{27}$$

It is important to note that the presented longshore transport formulas produce theoretical *potential* longshore sediment transport rates. This assumes that there is an infinite amount of sediment available for transport along an infinitely long beach. Of course this is not necessarily the case in coastal regions and thus a distinction must be made between the *potential* transport rate and the *actual* transport rate.

As was discussed previously, longshore currents are typically more frequent in one direction along a coastline, thus resulting in a net longshore current. The same can therefore be said of longshore sediment transport, where a net longshore transport direction is typically observed along a coastline. This direction can often be readily identified where abrupt changes in coastline are present, such as near coastal structures or natural headlands, as sediment will begin to build up on one side of the obstruction. An extremely important concept to understand with regards to longshore sediment transport is that when sediment is deposited on one side of an obstruction, the sediment supply is depleted in its lee (down-drift of the structure). As such, the presence of obstructions in the longshore sediment transport pathway will often lead to severe erosion further down the coastline. These processes are illustrated in Figure 2.13.

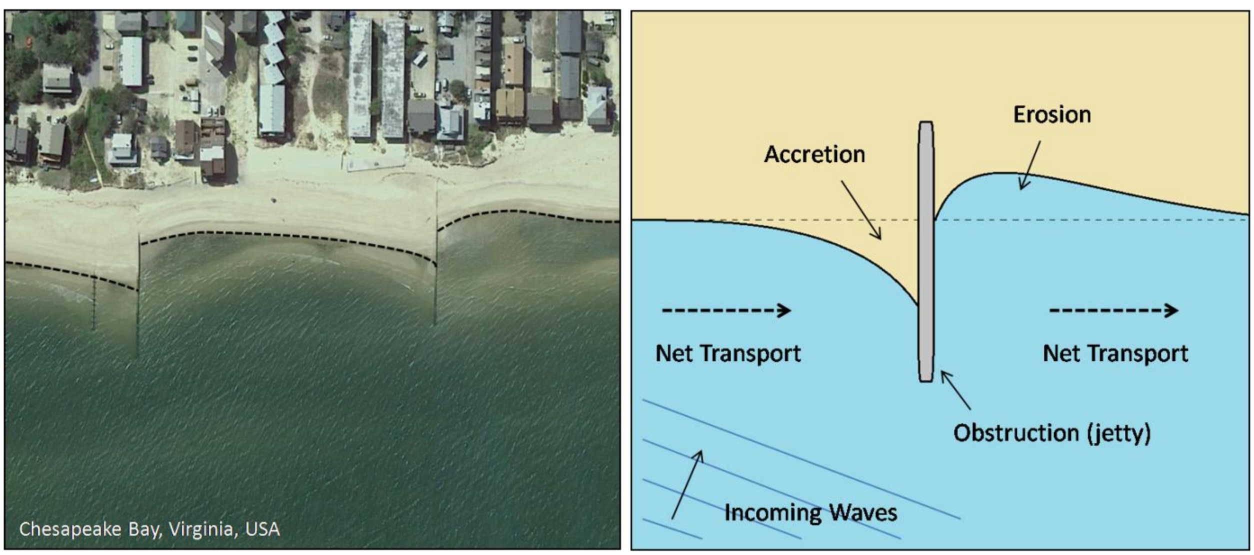

Figure 2.13: Definition sketch (right) and an example from Chesapeake Bay, Virginia, illustrating the effects that an obstruction (a groyne in this case) can have on longshore sediment transport and subsequent coastal morphology (modified from Google Earth, 2011).

Longshore sediment transport in the presence of a natural (non-engineered) tidal inlet is a highly complex topic and one that has been the subject of a great deal of research. In essence, a tidal inlet presents an obstruction to the natural course of the net sediment transport down a coastline; however the obstruction is dynamic in that it is itself a morphologic feature capable of movement and migration. Furthermore, the presence of the tidal inlet introduces cross-shore currents (ebbs and floods) which present a hydrodynamic obstruction to longshore sediment transport capable of altering its pathway.

In the most simplistic scenario, sediment will amass on the up drift side of a tidal inlet, as its passage across the inlet mouth is obstructed by deeper water and cross-shore currents. This in turn will result in erosion on the down drift side of the inlet, resulting in an offset inlet, where the up drift and down drift shorelines do not precisely align. However, at a coastal inlet with significant tidal flows, sediment arriving at the inlet will typically interact with the ebb and flood currents. The transported coastal sediment will enter the inlet from the up drift side where it is subsequently transported into the tidal lagoon with the flood current or offshore to the ebb-shoal with the ebb current. This represents an interaction between longshore and cross-shore processes, an immensely complex topic which is discussed in the following section.

In the presence of an extensive ebb-shoal complex (system of ebb-shoals), longshore sediment transport will often follow the shallow waters of the shoal(s), therefore passing around the tidal inlet and being deposited at the conclusion of the shoal once deeper waters are encountered. This process causes the ebb-shoal to expand in the longshore direction and can ultimately result in what is known as an attachment bar; where the ebb shoal has re-joined with the coastline down drift. Once an attachment bar is formed, partial longshore sediment transport will resume around the coastal inlet, thus reinstating a supply of sediment to the down drift shoreline. This process is referred to as sediment by-passing and is an important component of tidal inlet morphology (Bruun, 1987). An example of a location in which sediment bypassing occurs is at Corson Inlet, New Jersey, pictured in Figure 2.14. The aerial photograph on the left of Figure 2.14 reveals the presence of an extensive ebb-shoal system including a partial attachment bar. The photograph on the right shows the inlet during intense wave action, where waves can be seen breaking along the ebb-shoal and thus providing the hydrodynamic requirements for sediment bypassing to occur.

Figure 2.14: Corson Inlet, New Jersey, USA, showing extensive ebb-shoal complex (left) and waves breaking along the ebb-shoal (right). The sediment bypassing pathway is shown in red (modified from Google Earth, 2011).

The above paragraphs are of course a simplistic overview of a highly complex series of interrelated processes. Sediment bypassing is in fact much more complicated and is dependent on a number of factors including the relative strength of the ebb and flood currents, the local wave climate, the properties of the local sediment including its availability, and the plan view alignment of the inlet and surrounding shoreline. For further information on the topic, FitzGerald *et al.* (2000) presents an excellent summary of different classifications for sediment bypassing at a coastal inlet.

When stabilizing a coastal inlet by means of engineered structures, special attention must be given to factors concerning longshore sediment transport and sediment bypassing. For example, if impermeable shore-perpendicular jetties are constructed extending seaward on either side of a coastal inlet, longshore sediment transport will be further interrupted resulting in the creation of a large beach on the up drift side of the inlet and the potential for massive down drift erosion. In the past, coastal inlets were engineered with improper knowledge of the negative effects of interrupting natural sediment transport processes with the results often being the dramatic loss of shoreline adjacent to coastal inlets. It is the engineer's responsibility to exercise due diligence in ensuring minimal negative impacts on areas adjacent to a coastal project. As such, advances are being made through research (including the present study) in which engineered solutions to coastal inlet projects are tailored such that interruptions to naturally occurring sediment pathways are minimized.

As is pointed out in Seabergh and Kraus (2003), there are a number of techniques available to ensure that adequate sediment bypassing is obtained, through artificial means. These techniques generally include some form of controlled sediment trap, where accretion rates are predictable and can be artificially transferred to the down drift shoreline via dredging or pumping. A weir-jetty system is one such method in which sediment is contained ensuring an adequate beach on the up drift side of the inlet, while spill-over sediment is mechanically bypassed to the down drift shoreline (Seabergh and Kraus, 2003). This method controls and facilitates the artificial bypassing of sediment while maintaining a stabilized inlet mouth using coastal structures. Precise and well educated alignment of coastal jetties can also be effective in stabilizing a coastal inlet while streamlining sediment flow along a pathway by which it can bypass the inlet (Bruun, 1986). These techniques and topics will be addressed in the present study based on the findings of an analysis of longshore sediment transport at Shippagan Gully.

2.3.1.6 Combined Sediment Transport at Tidal Inlets

As eluded to in the previous sections, cross shore and longshore sediment transport processes are not explicitly independent and it is their complex interaction which produces the ultimate coastal morphology observed at tidal inlets. Morphology at a tidal inlet is in fact a combination of all the processes discussed thus far in this literature review. Although these processes are highly complex, a simple look at the typical morphological characteristics exhibited by a tidal inlet can be taken, revealing the net effects of each of the underlying factors governing tidal inlet morphology. These factors can be summarized as follows:

- The geometry and size of the tidal lagoon,
- The local tidal range (which combined with the lagoon geometry determines the tidal prism),
- Channel width and depth (cross-sectional area),
- Geologic controls such as sediment type and the presence of a non-erodible bottom,

- The sediment supply,
- Local wave climate,
- The relative strength of wave action to tidal flow,
- The net and gross longshore sediment transport rates,
- Engineered activities in the channel, estuary and adjacent beaches (including dredging),
- The presence and configuration of jetties, and
- Other factors.

Figure 2.15 presents a definition sketch of typical tidal inlet morphology for a natural inlet in which there has been no human intervention.

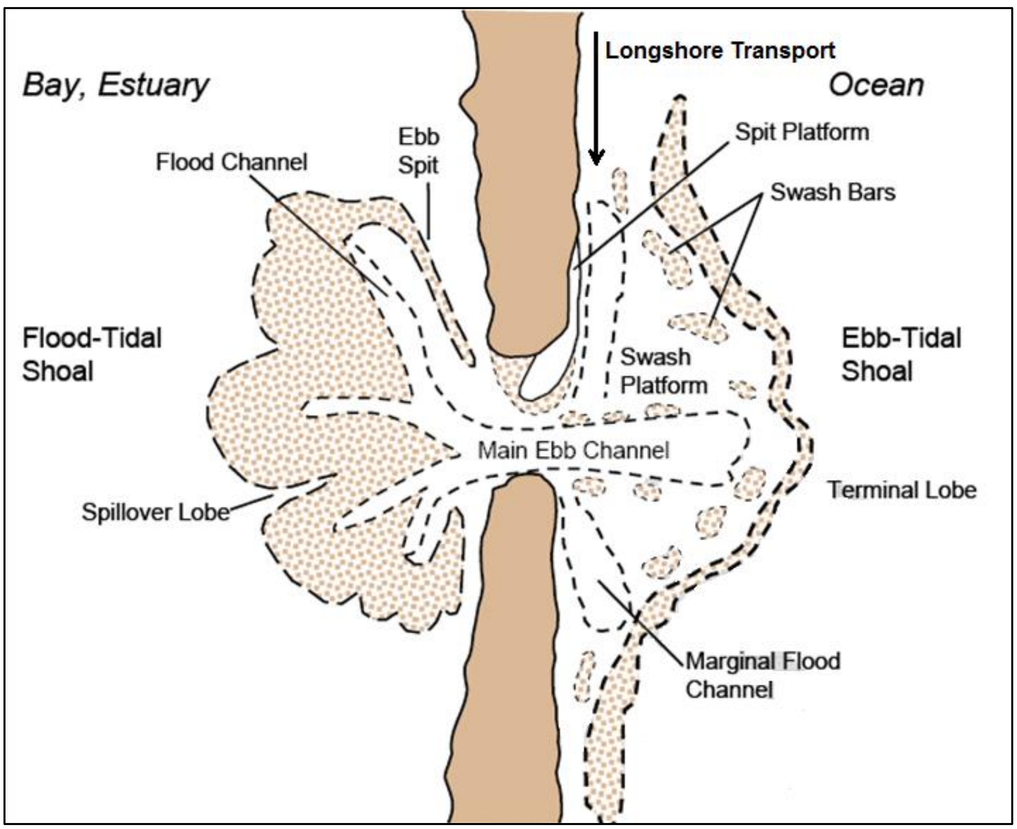

Figure 2.15: Definition sketch of typical tidal inlet morphology for an idealized inlet free of human intervention (Davis and Fitzgerald, 2004).

The main ebb and flood-induced features are outlined in Figure 2.15, including the ebb and flood shoals which were discussed in Section 2.3.1. Wave-induced features are also depicted such as the *spit platform* (induced by longshore sediment transport) and the various components of the swash platform, which are formed as incoming waves break over the ebb-shoal and carry sediment into the relative shelter in its lee.

The inlet depicted in Figure 2.15 is an example of an idealized inlet where morphological processes are fully developed, approximately symmetrical and well balanced. Most inlets however do not exhibit such well defined characteristics and are instead the morphologic result of the relative strength of the various processes at play. The relative strength of the longshore sediment transport rates along a coastline for example plays a large role in depicting the geometry of a tidal inlet. If there is a strong net transport direction (one direction largely outweighs the other), the inlet will take a much different geometric shape then for the case of an inlet with relatively balanced longshore transport (similar transport rates in both directions). The effects of the relative strength in longshore sediment transport on inlet morphology are presented in Figure 2.16 below, after Galvin (1971).

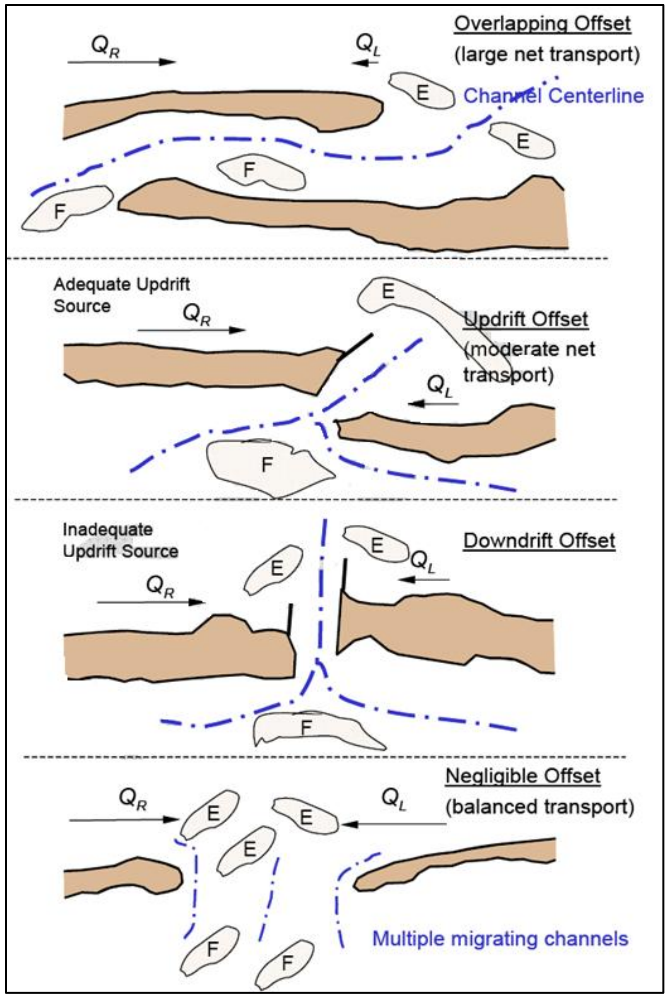

Figure 2.16: The effects of relative strength in longshore sediment transport on the morphology of a tidal inlet (Galvin, 1971).

Coastal inlet morphology can also be classified in terms of the relative strength of the tidal forcing and the wave forcing. Davies and Hayes (1984) showed that inlets where the mean tidal range is significantly greater than the mean wave height can be classified as tide-dominated inlets, while inlets where the mean wave height is much larger are generally considered to be wave-dominated. The precise relationship between these processes was defined by a series of curves and is shown in Figure 2.17. Researchers have more recently acknowledged that the tidal morphology should rather be based on the tidal prism as opposed to the mean tidal range, as the magnitude of the tide-induced hydrodynamic forces through an inlet are also dependent on the volume of the back-bay system (D'Alpaos *et al*., 2010).

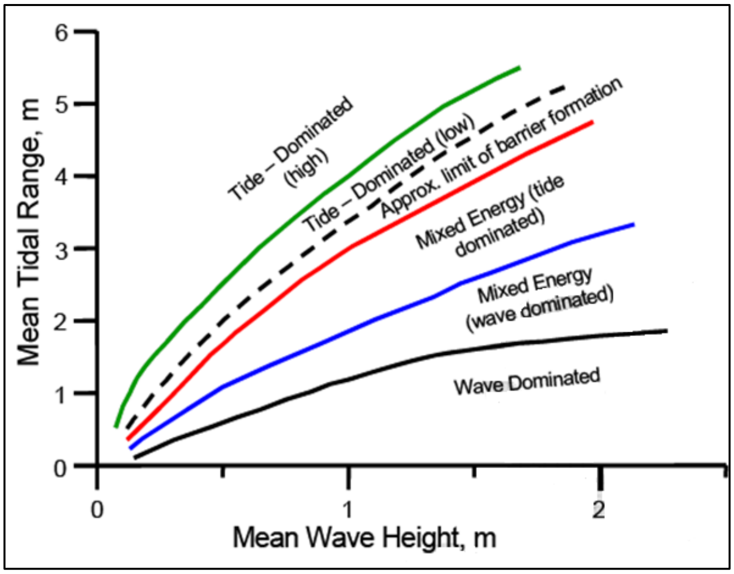

Figure 2.17: Classification of tidal inlet morphology based on relative strength of the wave related and tide related energy (Davies and Hayes, 1984).

Whether a tidal inlet is wave-dominated or tide-dominated has a particularly large effect on both the plan form geometry of the inlet and the sediment bypassing pathways. This is due to the alterations in the location and geometry of the various shoals which vary depending on the relative strength of their governing processes. The simplified effects of the relative strength of tides versus waves on inlet morphology and sediment bypassing are illustrated in Figure 2.18, where the transitional/mixed case is approximately that which is presented in Figure 2.15 above for the idealized tidal inlet.

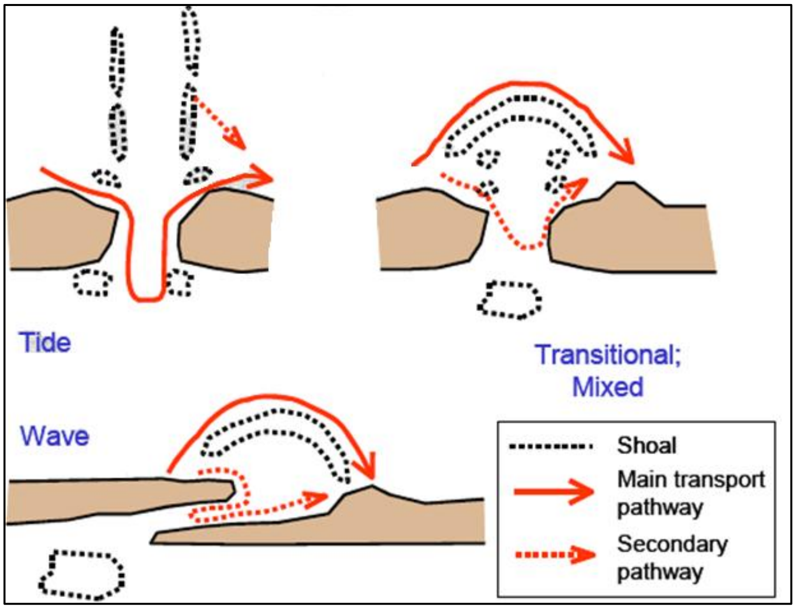

Figure 2.18: Representative plan-form morphology and main modes of sand-bypassing for tide-dominated, wave-dominated and transitional natural inlets (Davies and Hayes, 1984).

The above paragraphs represent generalized qualitative classifications for tidal inlet morphology due to a combination of inter-related factors. It is however much more difficult to classify tidal inlet morphology in a quantitative way. Common engineering practice with regards to quantitative analyses of tidal inlet morphology involves the use of a sediment budget. A sediment budget is a tallying of sediment gains and losses (sources and sinks) within a specified control volume, typically referred to as a cell. Sediment budgets provide a conceptual and quantitative model of sediment-transport magnitudes and pathways for a given volume and time period (Rosati and Kraus, 1999). By estimating a sediment budget for a given location under current conditions, the relative and quantitative effects of engineering activities can be approximated.

Although there are a number of methods in which a sediment budget can be formulated, the underlying equation is typically expressed as follows (Shore Protection Manual, 1984):

$$\sum Q_{source} - \sum Q_{sink} - \Delta V + P - R = Residual \tag{28}$$

where the terms must be expressed consistently as either volumes or as the volumetric rate of change. Q_{source} and Q_{sink} are the sources and sinks to the control volume respectively; ΔV is the net change in volume within the cell; P and R are the amounts of material placed in and removed from the cell respectively; and *Residual* is a measure of which the cell is balanced. A perfectly balanced cell would have a *Residual* of zero (Rosati and Kraus, 1999). Examples of sources include longshore sediment transport (entering the cell), erosion of bluffs or dunes, transport of sediment to the coast by rivers, artificial beach fill and dredged spoil. Sinks on the other hand include longshore sediment transport (leaving the cell), accretion along the shoreline and dredging of the beach or nearshore zone (Rosati and Kraus, 1999).

The application of a sediment budget to a coastal engineering project typically involves introducing engineered sources and sinks to an otherwise natural system and often includes the mechanical placement (P) and removal (R) of sediment from the cell. The effects of such changes to the natural sediment budget can then be quantified using the conceptual model presented in Equation 28.

For a long straight shoreline, the application of a sediment budget can be fairly straight forward. For the case of a tidal inlet however, the conceptual model is much more complicated. The increased complexity is due to a variety of reasons, namely the inherent difficulty in defining sediment transport magnitudes and pathways at a coastal inlet, the presence of flood and ebb currents, the combined effect of currents and waves, and the additional refraction and diffraction due to the presence of the inlet (Rosati and Kraus, 1999). The process has become somewhat more accurate however, with the introduction of sediment transport numerical models, which can be used in place of a sediment budget, or as a tool to provide input to the sediment budget (Rosati, 2005).

2.3.2 Morphological Numerical Modeling of Tidal Inlets

A morphological numerical model generally consists of a hydrodynamic numerical model which has been equipped with sediment transport calculation schemes such as those presented in Section 2.3.1 above. The hydrodynamic numerical model therefore feeds the calculated hydrodynamics into the sediment transport formulations, thus providing the user with an estimation of sediment transport directions and rates. Many morphological numerical models are furthermore capable of simulating bed change as a function of the sediment flux through a given model grid (in a finite difference model) or triangulated mesh (in a finite element model). As such, numerical models with morphologic capabilities can be used as a tool not only to predict sediment budget parameters (longshore sediment transport rates for example), but also to predict expected morphologic changes such as erosion of an inlet channel, or the formation of ebb and flood shoals.

Examples of morphological numerical models include MIKE 21 (DHI, 2011), ADCIRC (Luettich and Westerink, 2011) and CMS-Flow (Buttolph *et al*., 2006). These numerical models are perhaps better known as being strictly hydrodynamic models; however, they all possess the ability to incorporate sediment transport thus making them morphological models as well. It is important to note however, that as we have seen, tidal inlet morphology is an extremely complex concept which results from the interaction between numerous individual coastal processes, many of which are difficult to accurately assess. We have also seen that many of the available sediment transport formulations are computationally demanding, thereby adding to the overall complexity of the numerical model. Therefore, it cannot be expected that morphological numerical modeling will provide an initially accurate result or that it can be applied with a high degree of confidence. Morphological models must therefore be carefully calibrated and ideally validated prior to being used to support engineering analysis. In order to calibrate and validate a numerical model however, reliable data must first be available. As such, a numerical modeling study of tidal inlet morphology can only be considered accurate if it is supported by an extensive field data acquisition campaign.

2.4 Field Investigations at Tidal Inlets

Field investigations at tidal inlets are a crucial endeavour which must be completed in order to obtain data from which engineering analyses and good judgement can be properly exercised. The nature of the data, the level of precision of the data and the temporal range in data are all dependent on the requirements for the given project. Field data are often obtained simply to gain a better understanding of the nature of the coastal processes present at a site. For example, it may be desired to obtain a sufficient time series of wave data such that a qualitative assessment of net longshore transport direction can be made. Conversely, detailed field data such as a time series of current magnitudes or suspended sediment transport rates may be required for the calibration and validation of a numerical model.

There are several types of data which may be of interest for an engineering project related to tidal inlets. Pratt *et al*. (2000) provides a good summary of parameters for which data acquisition may be necessary. These parameters are as follows:

- Water levels,
- Salinity,
- Suspended sediments,
- Wave related parameters,
- Meteorological data (wind, temperature, pressure, etc.),
- Currents,
- Bathymetry,
- Sediment properties.

A great deal of guidance regarding the acquisition of each of the above listed parameters at a coastal inlet is provided in Pratt *et al*. (2000). The guidance is based on common methods for data acquisition and is by no means a summary of all available methods.

Water levels are perhaps the most important parameter to obtain with regards to tidal inlets. Without water level data, hydrodynamic characteristics due to tidal flow cannot be accurately assessed or modeled. Typical methods by which water level elevations can be recorded involve using a solid-state electronic instrument, typically containing a strain gauge or pressure transducer which records the absolute pressure of the water column above the instrument. These pressure type gauges are often affected by local changes in barometric pressure, particularly if they are not vented. This can be easily corrected however with a second dry gauge, which independently measures the required barometric correction (Pratt *et al*., 2000). Common practice with water level data is to measure a given period of time covering at least one lunar cycle, and to extrapolate the data by analysing the tidal constituents. This process was described above in Section 2.2.1.1.

Salinity measurements are often required for environmental and ecological purposes, as well as to guide analyses which are sensitive to water density (vessel draft for example). Salinity is typically measured using a water quality data logger which provides additional measurements of conductivity and temperature.

Suspended Sediment data may be required where numerical modeling of sediment transport is to be performed. The data may then be used as a tool for calibration and validation of the numerical model. A number of electronic and manual samplers are available to measure suspended sediment, each capturing a pre-defined sample of water and measuring its sediment content. Measuring suspended sediment transport rates is however a highly approximated task, as suspended sediment transport is a process which is highly variable both temporally and spatially (Pratt *et al*., 2000).

Wave related parameters are an extremely important form of data particularly for the case of coastal inlets. As has been previously discussed, waves play a very large role in the morphology of the shoreline including that present at a tidal inlet. As such, a good understanding of the local wave climate is required for most coastal inlet-related projects. Wave parameters are typically determined from one of two types of gauges. The first type of wave gauge is similar to a water level gauge, in that it sits at depth (typically on the seabed) and measures the absolute pressure of the water column above it. The second form of wave gauge is referred to as a buoy gauge, and unlike the pressure gauge it sits on top of the water surface like a buoy. This form of wave gauge is typically tethered to the bottom by means of an elastic shock cord. Accelerometers measure the motion of the buoy as waves pass below, thereby providing a data set of wave heights and periods. Many wave gauges are manufactured to incorporate velocity sensors such that the wave direction can be assessed. Newer wave gauges are variations on the above listed principals, by which acoustic instruments are incorporated such that waves and currents are measured through the entire water column (Pratt *et al*., 2000).

Meteorological data, such as wind speed, wind direction, temperature and barometric pressure, are recorded by weather stations. Weather stations are located either on land or offshore and are typically placed at an elevation of 10 m (following American Meteorology Society standards). Most advanced weather stations are self-operating and contain a microcomputer with a real-time clock to log measurements. These devices are typically powered by solar-powered batteries (Pratt *et al*., 2000).

Currents are typically measured using an acoustic current meter, allowing for fast and accurate profiling of current velocities and directions (Pratt *et al*., 2000). Acoustic Doppler Current Profiler's (ADCP) are common current meters which transmit sound bursts into the water column which are then scattered back to the instrument by particles suspended in the flow. Velocity and depth values are then calculated based on the return time and change in frequency caused by the moving particles (referred to as the Doppler shift).

Bathymetry is an extremely important parameter in any coastal related engineering project. It is the bathymetry which controls local water depths and nearshore wave transformations. Bathymetry can be measured in a number of ways, the most common being using an acoustic depth sounder which measures the travel time of a sound wave which is reflected off the bed. In addition to acoustic depth sounders, a number of newer survey methods are becoming popular due to either their improved accuracy or the reduction in the time required to survey a given area. These methods include (but are not limited to) multi-beam swath systems and LiDAR (light detection and ranging) devices (Pratt *et al*., 2000).

Sediment properties are a commonly required data set for any civil or coastal related project. Particularly where sediment transport calculations are to be carried out, a good understanding of properties is required. Sediment is typically drawn from the seabed in small volumes and analyzed in a laboratory to determine properties such as grain sizes (typically represented by a sample gradation curve), density and porosity (Pratt *et al*., 2000). Often a simple visual inspection of the bed and adjacent beach material is enough to perform a qualitative assessment of sediment transport tendancies.

2.5 Case Studies

In order to support the information documented in this literature review, a number of case studies have been examined, three of which are presented herein. Although more recent studies were reviewed, the following three were selected for discussion due to the fact that they follow closely the information presented in this literature review, and are therefore the most helpful in support of the present study. The reviewed studies are as follows:

- Sebastian Inlet, Florida – Zarillo *et al*., 2003,
- Beaufort Inlet, North Carolina – Olsen Associates Inc., 2005,
- Ocean City Inlet, Maryland – Buttolph *et al*., 2006,

2.5.1 Sebastian Inlet, Florida

A paper entitled "Morphological Analysis of Sebastian Inlet, Florida: Enhancements to the Tidal Inlet Reservoir Model" was published in *Proceedings, Coastal Sediments '03*. The authors of this paper are G.A. Zarillo, N.C. Kraus and R.K. Hoeke. The paper summarizes a study in which geomorphic analysis was conducted to re-formulate an analytical model of shoal evolution and sediment bypassing. Figure 2.19 shows an aerial photograph of Sebastian Inlet, taken in 2008.

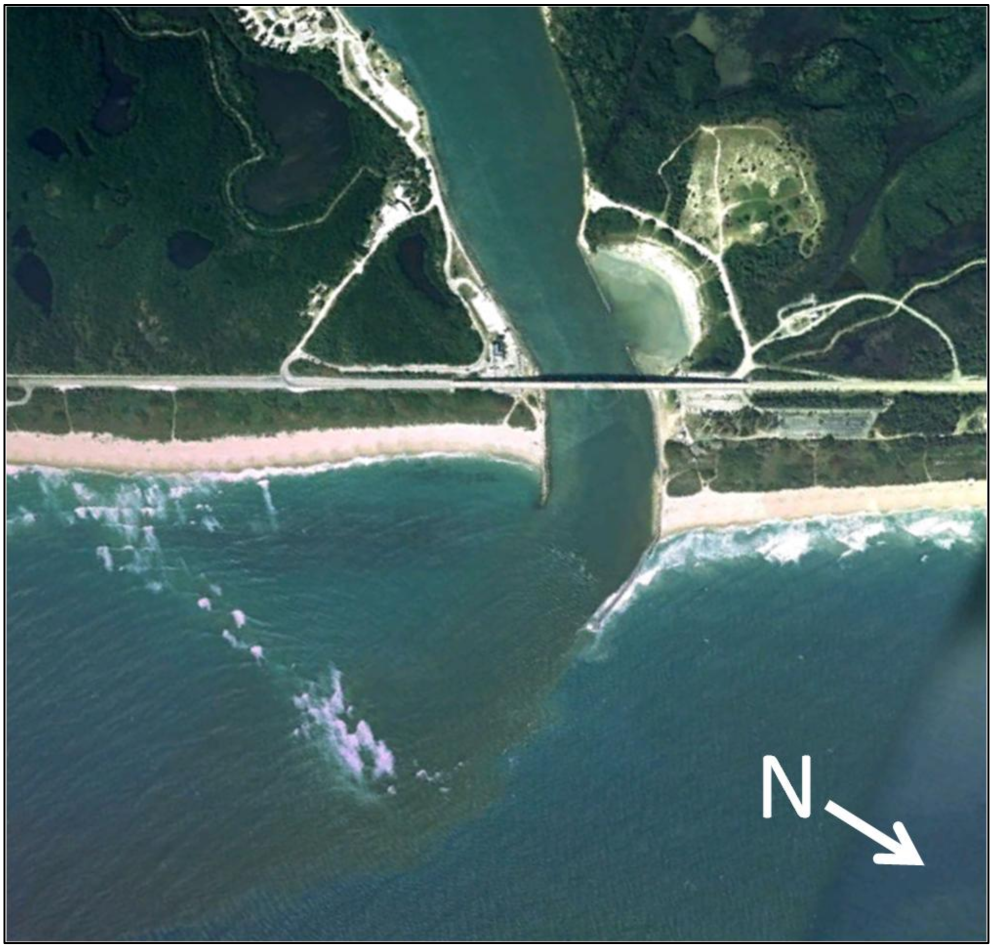

Figure 2.19: Aerial photograph of Sebastian Inlet, Florida, taken in 2008 (Google Earth, 2011).

Sebastian Inlet is an example of an *engineered* tidal inlet as it has been stabilized with offset jetties. Further human intervention includes a man-made sediment trap which has been dredged on the seaward side of the flood shoals, near the entrance to the tidal lagoon. The purpose of the sediment trap is to provide a deep, calm area where sediment which is transported into the lagoon (with the flood tide) will settle, thus creating a manageable borrow site. This sediment supply can then be used as beach nourishment material or mechanically bypassed to the down-drift shoreline.

Waves at this location along the coast of Florida have a mean annual height of 0.6 m, while the tidal range is in the order of one metre. According to the empirical curves developed by Davies and Hayes (1984) and shown in Figure 2.17, this makes Sebastian Inlet a mixed-energy, wave-dominated inlet.

The most frequent waves arrive at Sebastian inlet from an azimuth which is greater than 90^0 to the shoreline. These waves therefore create longshore sediment transport from the south to the north. The relative frequency of these waves is however offset by the greater power of less-frequent storm waves which arrive from angles less than 90^0, thus creating north to south sediment transport along the coastline. This corresponds well with observed morphological features, which show the net longshore transport to be clearly from north to south. This is most notably seen from the relative historical positions of the shoreline on either side of the inlet, which are shown in Figure 2.20 below.

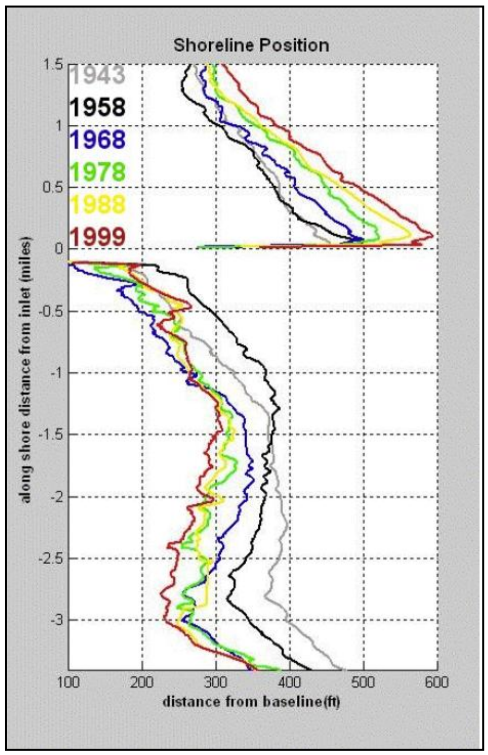

Figure 2.20: Comparison of shorelines mapped from aerial photography between 1943 and 1999 (Zarillo *et al.*, 2003).

Figure 2.20 shows that the shoreline position to the north of Sebastian Inlet has been generally accreting since 1943, while the south shoreline position has been receding. This observation shows that the inlet has not yet reached an equilibrium state.

The objective of the Sebastian Inlet study was to develop an analytical model which was capable of simulating the sediment transport pathways and morphological volumes, such that the effects of engineered sediment management plans (mechanical removal and re-location of sediment) could be predicted. The analytical model in this case is a model developed by Kraus (2000, 2002), which is based on the conservation of sediment volume, where different morphological features are represented as beakers containing a finite volume of sediment. The individual beakers are then interconnected by various sediment transport pathways, with rates and directions of transport associated to each path. The model is therefore essentially a combination of several sediment budgets, linked together to form a system. An aerial photograph showing the various morphological features and a sample illustration of the methodology employed in the model are illustrated below in Figure 2.21.

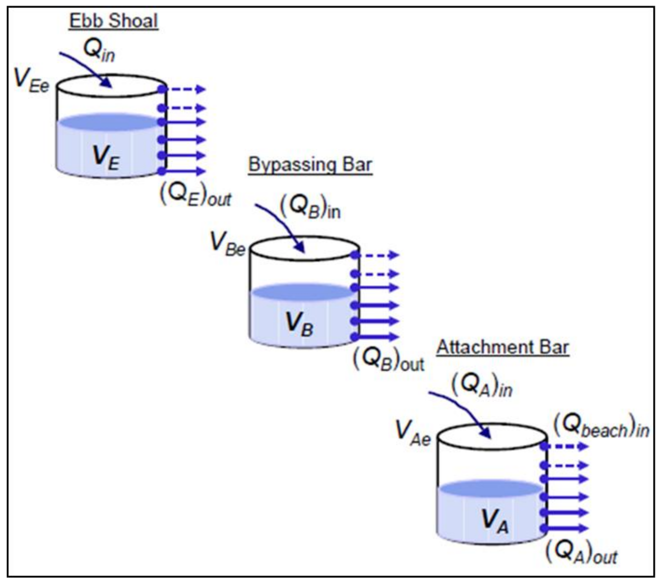

Figure 2.21: Aerial photograph of Sebastian Inlet showing morphological features included in the analytical model (left) and a sample of the methodology employed in the model (right) (Zarillo *et al.*, 2003).

The analytical model was first calibrated to historical surveyed or estimated volumes for each of the morphological features. This was done by adjusting the rates of transport along the various known sediment transport pathways until a balanced model was achieved. A schematic of the various modeled sediment pathways is shown below in Figure 2.22, where E = ebb shoal, B = bypass bar, A = attachment bar, C = channel, T = sand trap, F = flood shoal, Ss = south fillet and In = north fillet.

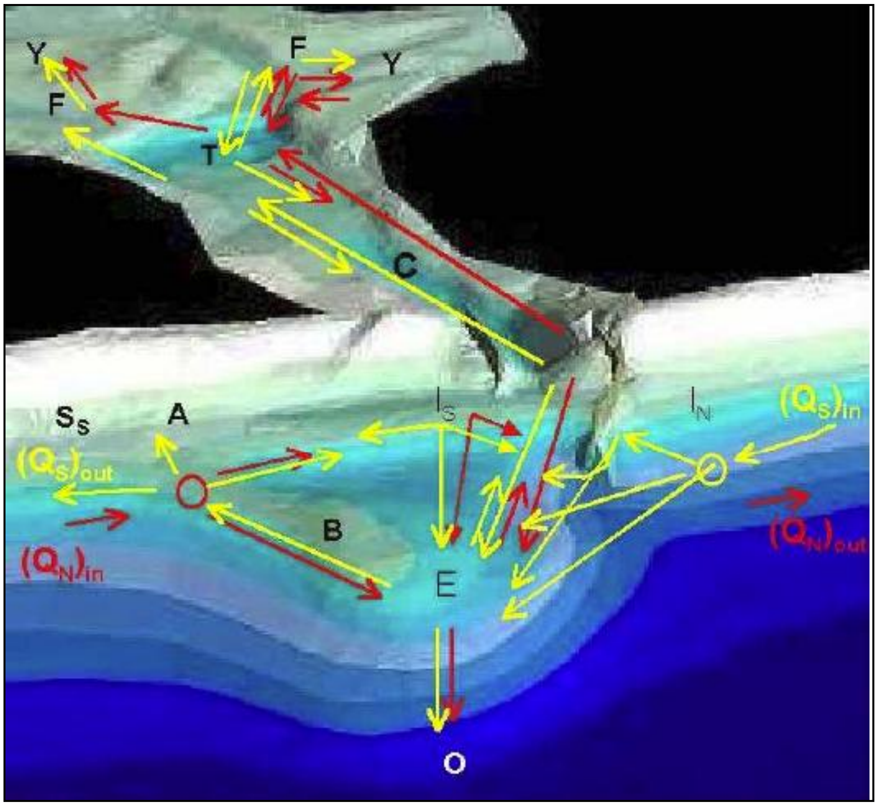

Figure 2.22: Sediment pathways described in the analytical model, superimposed on Sebastian Inlet morphological components (Zarillo *et al.*, 2003).

With the analytical model balanced, the total rate of change for each of the morphological features could be estimated. These rates were then extrapolated until the model reached a state of equilibrium, thus representing morphological equilibrium of the tidal inlet. The equilibrium volume of the ebb shoal was found to be 3 million m^3 while the flood shoal equilibrium volume was 4.5 million m^3. The model was also used to estimate the longshore transport rates at Sebastian Inlet, which were found to be 125,000 m^3 from the north to south and 50,000 m^3 from the south to north, thereby corresponding to a net longshore transport rate from north to south of 75,000 m^3. The model was further applied to estimate the relative rate of transport due to the ebb and flood tides respectively, which revealed that the flood tide is accompanied by a higher sediment transport rate, thus resulting in the rate of growth of the flood shoal being slightly larger in comparison to that of the ebb. Lastly, the model allowed for a quantitative assessment of sediment bypassing at Sebastian Inlet, a value which can often be very difficult to estimate.

It was concluded in the study that the analytical model was successful in simulating a simplistic picture of sediment transport and long-term morphology at Sebastian Inlet. The model now provides engineers with a tool to help guide decisions concerning sediment management at Sebastian Inlet.

2.5.2 Beaufort Inlet, North Carolina

A technical report was produced in 2005 by Olsen Associates Inc., documenting an assessment of inlet morphology at Beaufort Inlet, North Carolina. Beaufort Inlet, is a relatively large (over a kilometre wide at the mouth) tidal inlet which services a very large tidal lagoon comprised of several bays. The city of Morehead City, North Carolina, is located on the tidal lagoon, not far from the inlet itself. Beaufort Inlet is therefore a highly navigated channel which connects Morehead City Harbour to the Atlantic Ocean.

Beaufort Inlet has been subjected to regular dredging activities since 1936 in an effort to maintain a relatively deep and highly navigable channel. Since the commencement of said engineering activities, the morphological characteristics of the inlet have changed drastically. In an effort to define the morphological changes which have occurred since 1936 and to gain an understanding of the morphology which is to be expected in coming decades, Olsen Associates Inc. completed an extensive study of the existing and historical morphological features. This study began with the acquisition of highly accurate bathymetry by way of a 2005 multi-beam survey of the inlet and immediate offshore area. The results of this survey is presented as a bathymetry map in Figure 2.23 below, alongside an aerial photograph of Beaufort inlet which was taken in 2002.

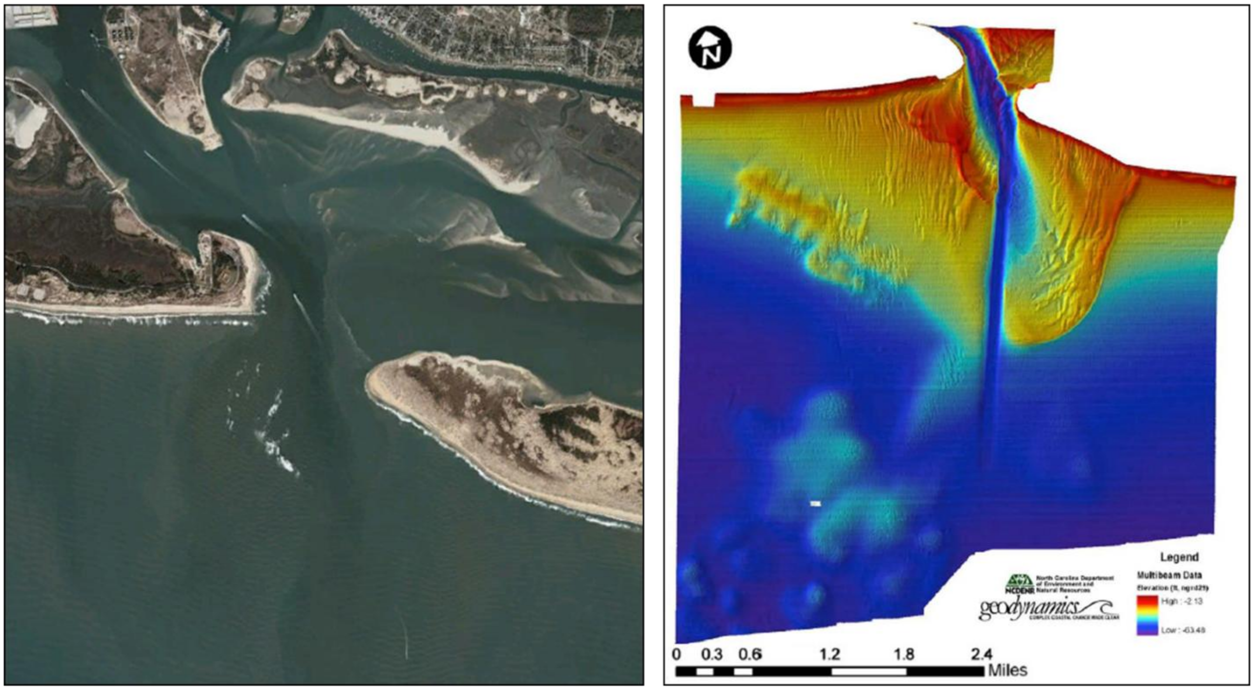

Figure 2.23: Aerial photograph of Beaufort Inlet, circa 2002 (left)(Google Earth, 2011) and a bathymetric contour map of the inlet and immediate nearshore zone, produced from data obtained in a 2005 multi-beam survey (right)(Olsen Associates Inc., 2005).

From the bathymetric survey shown in Figure 2.23 above, several important morphological characteristics were deciphered. Perhaps the most obvious feature is the dredged navigation channel, which clearly severs the ebb shoal platform and thereby precludes any significant sediment bypassing across the inlet. Sediment transport from the adjacent beaches (called Bogue Banks to the west and Shackleford Banks to the east) is also noted to be entering the inlet from both sides. Two sediment disposal mounds (large accretion areas) are evident, one immediately to the west of the channel mouth and one further offshore, along the western limit of the ebb shoal complex. Finally, evidence of a strong ebb jet is apparent, whereby the ebb-jet is directed slightly to the south east, pushing accreted sediment seaward along the east edge of the navigation channel.

A primary objective of the reviewed study was to assess the differences in pre-engineered morphology (pre-1936) and post-engineered inlet morphology (post-1936). To do this, historical bathymetry was acquired from numerous bathymetric surveys and nautical charts and was subsequently compared. Figure 2.24 presents bathymetric contours from bathymetric surveys undertaken in 1900 and 2004 respectively. The difference between these two contour maps is therefore representative of over a century of natural and unnatural morphologic change.

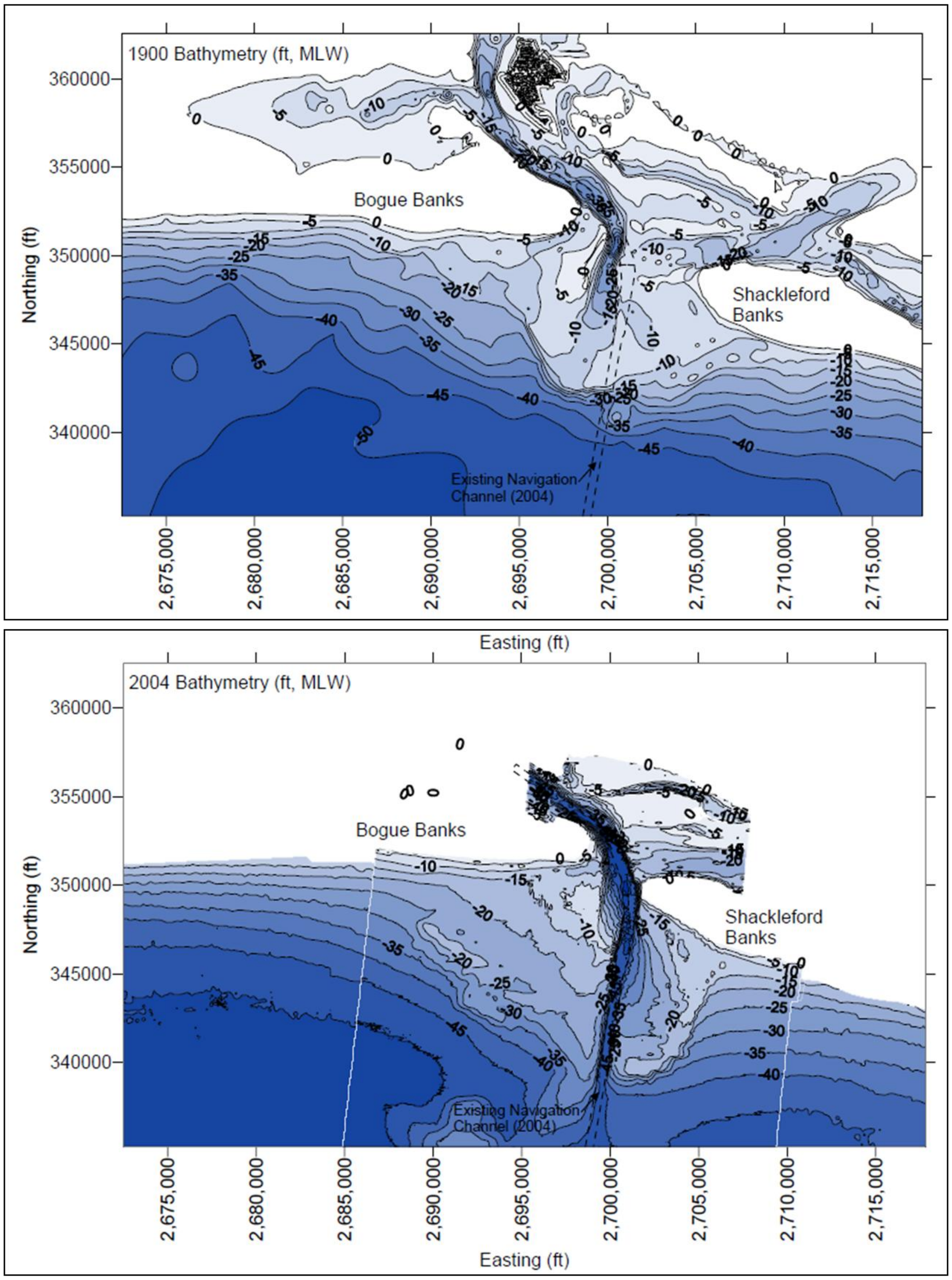

Figure 2.24: Bathymetric contours representing conditions near Beaufort Inlet in 1900 (upper) and 2004 (lower).

From Figure 2.24 above, several key conclusions can be drawn regarding morphology at Beaufort Inlet over the century spanning the two contour maps. There is an extensive ebb-shoal complex present in both images, however the ebb-shoal observed in 1900 is approximately symmetrical, while the ebb-shoal in 2004 is highly asymmetrical. Furthermore, depths throughout the ebb-shoal complex and inlet channel are considerably deeper in 2004 than they were in 1900. The former indicates that the ebb-shoal complex has been depleted in the time elapsed since the 1900 bathymetric survey. The depth change in the navigation channel on the other hand is largely due to dredging activities, which have deepened the channel to -45 ft MLW (mean low water). The ebb-shoal is also noted to have been pushed much further offshore between 1900 and 2004. A final key observation from the contour maps shown in Figure 2.24 is the location of the barrier islands to either side of the inlet, primarily Shackleford Banks to the east, which has migrated significantly in the direction of the inlet. The result is a much narrower inlet in 2004 than was present in 1900.

The above listed observations were checked for numerous time periods throughout the past century (where bathymetric data was available) and it was generally found that morphological trends presented above were ongoing and consistent from the time at which dredging activities began (1936) onward. As such, morphological trends which are currently active at Beaufort Inlet have been occurring with a certain degree of consistency for over 70 years.

In order to assess changes which occurred as a result of engineering activities, a closer look was given to morphology which occurred prior to 1936 in comparison to morphology which has occurred since 1936. In particular, volumes were calculated for the morphological features which exist at the inlet and subsequently compared throughout the inlet's history. The following observations summarize the pre-1936 condition of Beaufort Inlet:

- Interior flood shoals exhibited minor net volume change,
- East end of Bogue Banks was advancing eastward (towards the inlet), gaining +43,800 m^3/yr above the low water line, while the west end of Shackleford Banks was retreating eastward at a similar rate,
- The ebb-tidal shoal was gaining sand at an average rate of about +159,030 m^3/yr, and
- The entire inlet complex (including ocean shorelines within 4.4 km to the west and 3.4 km to the east of the inlet) exhibited a net gain of about +158,000 m^3/yr.

Subsequently, the following observations were made concerning the post-1936 condition of Beaufort Inlet:

- Interior flood shoals changed from weakly accretional to highly erosional (-41,750 m^3/yr),
- The east end of Bogue Banks reversed from advancement to retreat (-31,580 m^3/yr),
- The west end of Shackleford Banks halted its retreat and advanced significantly toward the inlet (+63,610 m^3/yr),
- The ebb-tidal shoal reversed from accretion to erosion (-222,180 m^3/yr), and
- Overall, the inlet complex changed from net gains of +157,800 m^3/yr to net losses of -231,890 m^3/yr, on annual average.

The above listed observations can be summarized by stating that essentially all of the inlet's volume changes were reversed post-1936.

Considering the ebb tidal shoal volumes specifically, the portion of the shoal to the west of the navigation channel was observed to have incurred losses over four times greater than the shoal to the east of the channel, in the time since the initiation of dredging works (1936). If losses and gains along Bogue Banks and Shackleford Banks are to be included, virtually all of the net inlet volume losses can be attributed to the west side of the inlet.

Given the numerous morphological observations presented in the study, the authors presented the conclusion that the continual dredging of the navigation channel has virtually severed all sediment supply to the west side of the inlet. It is this removal of the inlet's ability to bypass sediment that has led to a complete reversal of all morphological features, and severe erosion to all features located to the west of Beaufort Inlet. It is concluded that if current averaged annual rates continue, the ebb shoals to the west of Beaufort Inlet will have completely disappeared in approximately 40 years time. At this point it is speculated that erosion will be increased along Bogue Banks, resulting in potentially massive losses of sediment and a significant retreat of the barrier island.

The study conducted at Beaufort Inlet does well to reveal how sensitive the tidal inlet system can be to engineering activities and human intervention. As has been shown by the authors, relatively minor dredging activities to deepen the existing navigation channel has entirely altered the morphological characteristics of Beaufort Inlet and led to an enormous and ongoing loss of sediment from the inlet system, particularly on the down drift side (west). This case is a good illustration of why it is crucial for the morphological effects of engineering activities to be well understood prior to human intervention of any scale.

2.5.3 Ocean City Inlet, Maryland

A paper was published in the proceedings of the 30th Coastal Engineering Conference (2006) summarizing a study of tidal inlet morphology at Ocean City Inlet, Maryland. The paper was entitled "Natural Sand Bypassing and Response of Ebb Shoal to Jetty Rehabilitation, Ocean City Inlet, Maryland, USA", and the athors were A.M. Buttolph, W.G. Grosskopf, G.P. Bass and N.C. Kraus. A 2010 aerial photograph of Ocean City Inlet is shown in Figure 2.25 below.

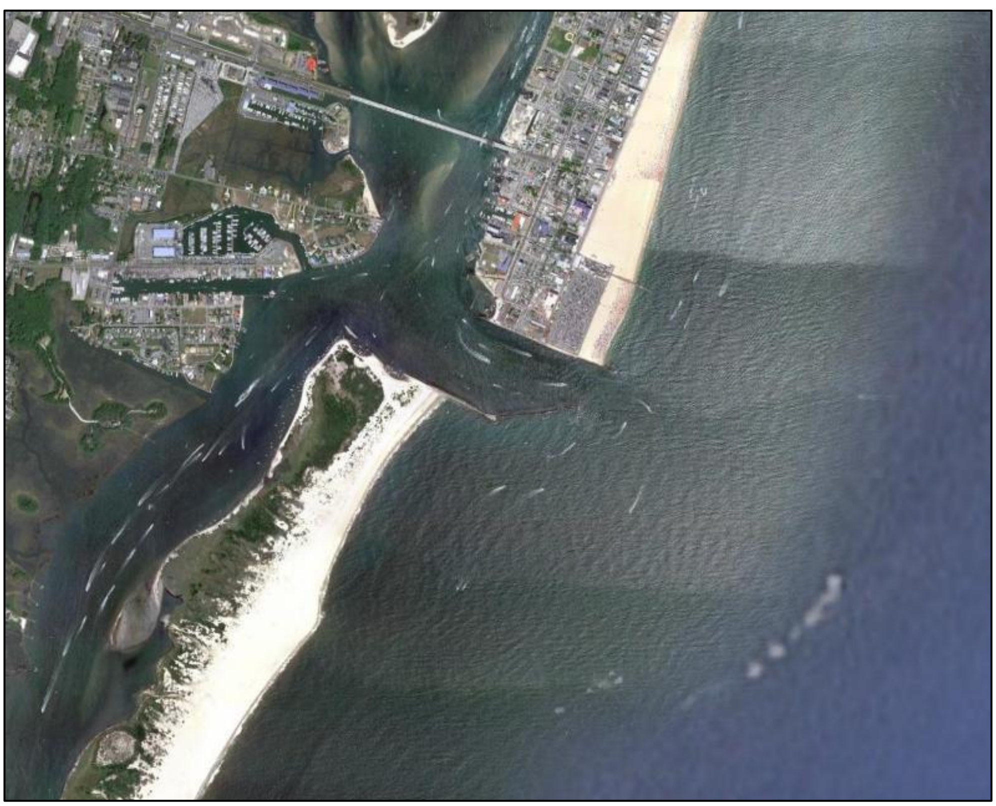

Figure 2.25: Aerial photograph of Ocean City Inlet, Maryland, taken in 2010 (Google Earth, 2011).

Ocean City Inlet was formed by natural means in 1933 when a severe hurricane broke through the barrier island which protects the Maryland coast. This breakthrough created a passage from Chincoteague Bay to the south and Isle of Wight Bay to the north, through the barrier island and into the ocean. The bays therefore became what is now an expansive tidal lagoon, serviced by Ocean City Inlet.

After the 1933 break through, it was decided that the newly formed inlet should be stabilized for commercial navigation interests. A 600 m jetty was constructed on the north side of the inlet and a 750 m elbow jetty (a bend in plan-view orientation) was constructed on the south side of the inlet. Both jetties were built as rubble-mound structures. In addition to the construction of the jetties, the inlet was dredged in order to increase its navigational capacity.

Within three years of the construction of the new jetties, Ocean City beach to the north of the inlet had accreted to the maximum extent of the north jetty, at which point sediment had begun to pass around (and through) the structure and into Ocean City Inlet. This was clear evidence that a net longshore transport of sediment was moving sediment from the north to the south down the coastline. In response to this, the north jetty was raised, extended and sand tightened in 1936. Throughout this same time period, severe erosion was incurred along the southern beach (south of Ocean City Inlet). As such, mechanical bypassing of sediment was commenced, transferring accreted sediment from the north side of the inlet to the eroded coastline to the south. The mechanical bypassing of sediment was however unable to halt the erosion entirely, and by the mid 1970's the shoreline to the south of Ocean City Inlet had receded by over 500 m. The ongoing erosion resulted in concern that the barrier island to the south would be overtopped or even breached in the event of a large storm, thus sacrificing the shelter of Chincoteague Bay and its marine navigators and residents.

By the mid 1970's an attachment bar had formed on the southern side of Ocean City Inlet. This morphologic feature illustrated that partial natural sediment bypassing around the inlet had resumed, thus re-instating a supply of sediment to the down drift shoreline. The attachment bar had an unforeseen negative effect however, as waves were observed to refract along the bar, thus creating occasional longshore sediment transport from the south to the north (opposite to the direction of net transport), where it passed through the permeable southern jetty and into Ocean City inlet. In response to this, the inshore section of the south jetty was raised and sand-tightened to prevent further sediment intrusion in the inlet. Figure 2.26 illustrates the refraction of waves along the attachment bar and the original (pre-1933) shoreline position, overlaid on a shaded bathymetric map of the nearshore area surrounding Ocean City Inlet.

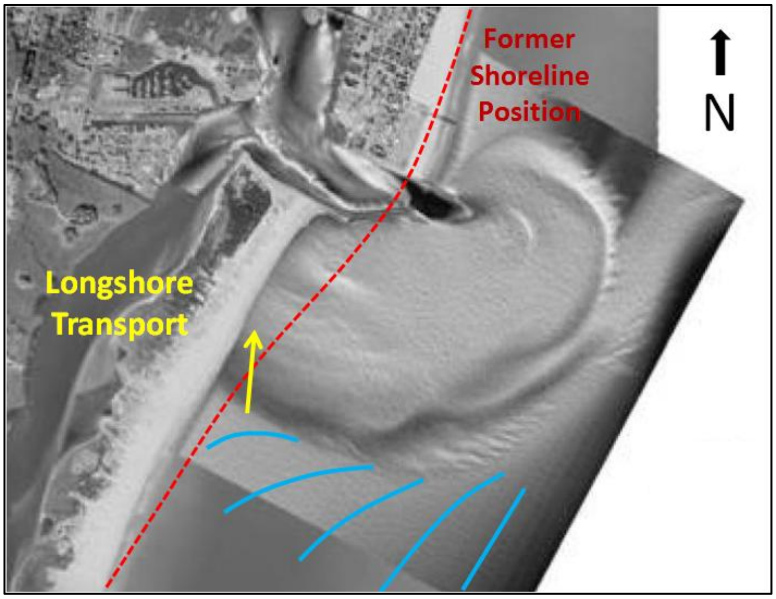

Figure 2.26: Map of Ocean City Inlet nearshore zone, showing shaded bathymetry, refraction of incoming waves along the attachment bar and the former shoreline position, prior to 1933 (Buttolph *et al.*, 2006).

Numerous data collection campaigns have been carried out at Ocean City Inlet in an effort to monitor the dramatic morphological changes which have taken place since its original stabilization in 1933. Pre and post-1933 beach surveys were conducted, which do well to illustrate the changes to the shoreline incurred by the 1933 storm. Periodic surveys of the beach profile both to the north and south of Ocean City Inlet have continued since these original datasets were acquired. Furthermore, detailed dredging records exist for Ocean City Inlet, quantitatively documenting all dredging activities at the site since 1933.

More recently, an offshore directional wave gauge was deployed in 1994, documenting hourly wave data which can then be transformed to the site using a numerical model. Finally, 9 high resolution multi-beam bathymetric surveys have been completed at Ocean City Inlet since 2004, carried out by the United States Army Corps of Engineers (USACE). These more recent and accurate surveys have revealed characteristics of the morphological features which were never previously observed. For example, the ebb-shoal possesses an elongated crescentric shape that ultimately concludes at the attachment bar. The northern extent of the ebb-shoal possesses a unique shape which is uncharacteristic for ebb-shoals, in that it has clearly been flattened and pushed to the north, against the direction of net longshore transport. This formation is referred to in the study as the ebb-shoal tongue. In addition to the ebb shoal tongue, an extremely deep scour pit is revealed at the inlet mouth, directly between the offset jetties. The aforementioned morphologic features are shown in Figure 2.27 below, which is a 3-dimensional representation of a 2005 multi-beam survey.

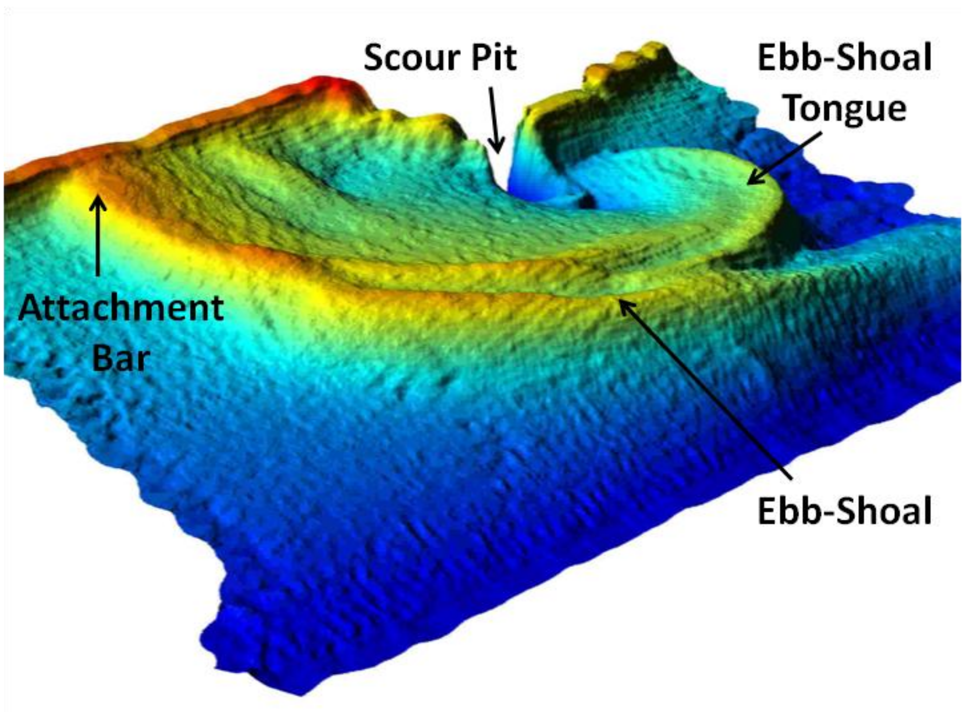

Figure 2.27: 3D representation of a 2005 multi-beam survey showing prominent morphological features of the ebb-shoal complex (Buttolph *et al.*, 2006).

Another interesting feature of Ocean City Inlet which was revealed due to the extensive data collection campaigns over the past several years was the existence of a scour zone along the back side (north side) of the outer portion of the south jetty. By 2002 the scour was so severe that the structural stability of the jetty was on the verge of being compromised. It was determined that the scour was due to the unique flow path taken by the ebb-current as it exits between the offset jetties. This flow path follows the southern bank of the inlet and passes directly along the lee side of the jetty. In order to prevent the jetty from being undermined, a 2002 project was undertaken to install a rubble scour blanket along lee-side foot of the south jetty. Additionally, the jetty itself was entirely rehabilitated, sand-tightened and raised. The unique flow path responsible for this morphology and subsequent engineering activities is illustrated below in Figure 2.28.

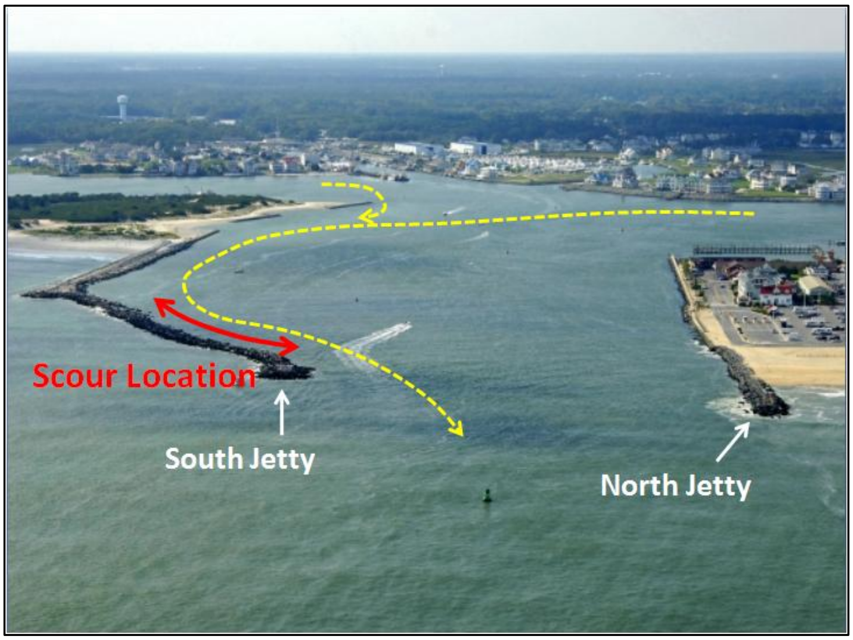

Figure 2.28: Photograph of Ocean City Inlet showing ebb-flow pathway through the inlet (photo courtesy of SBYNews, 2011).

The reviewed study was composed of three main objectives:

- Identify the driving process behind the formation and maintenance of the ebb-shoal tongue,
- Identify sand bypassing pathways under both typical and storm conditions, and
- Determine the hydrodynamic and morphodynamic effects of the 2002 south jetty rehabilitation.

The above listed study objectives were fulfilled by utilizing a hydrodynamic and morphological numerical model. The model used was in fact a combination of two models, one being a circulation model and the other being a spectral wave model. Both numerical models were developed by the USACE Coastal Engineering Laboratory.

CMS-Flow is a 2-dimensional, finite difference circulation model which computes hydrodynamics and sediment transport. The input to the model is a time series of water level elevations, or a series of tidal constituents from which the input transient water level is inferred at the specified model boundaries. CMS-Flow can also be considered a morphological model due to the fact that it is outfitted with the ability to calculate sediment transport and subsequent bed morphology. CMS-Wave is the spectral wave model which was used in the study. CMS-Wave is a 2-dimensional, finite difference propagation and transformation model, which transforms inputted wave spectra from the offshore boundary over the inputted model bathymetry to the project site. CMS-Wave accounts for all major wave transformations including shoaling, diffraction, refraction and breaking.

For the reviewed study the models CMS-Flow and CMS-Wave were combined through the use of a steering module. The steering module allows information to be shared between the models at a user specified interval. For example, wave induced currents (radiation stresses) are transferred from the wave model and subsequently accounted for in the circulation model (added to the existing currents). Conversely, water levels and currents calculated by the circulation model are transferred to the wave model such that their effects on wave propagation are accounted for. Following this methodology, both the effects of nearshore waves and tidal circulation currents are accounted for in the ultimate calculation of sediment transport and bed morphology. Further detail regarding the specifications of both CMS-Flow and CMS-Wave is not given in the present literature review due to the fact that both models are used in the present study (Shippagan Gully) and are therefore well described in Section 5.0.

For the reviewed study, 2000 survey bathymetry was used as the initial bathymetry in both the CMS-Flow and CMS-Wave model domains. The south jetty was represented based on 2002 construction drawings, such that the effects of the 2002 rehabilitation and alterations could be assessed. As such, the area in lee of the south jetty was given a hard bottom in the numerical model to account for the presence of the newly installed rubble scour blanket.

The numerical models which were used for the reviewed study are both variable grid, finite-difference models. Therefore their calculations are conducted over a rectangular grid of variable size. The cell sizes (computational resolution) utilized in the reviewed study ranged from 38 m in the center of Ocean City Inlet to 183 m at the offshore boundary and throughout the large back-bay system. The CMS-Wave model covered a relatively small area including the inlet and the ebb-shoal complex, extending to a distance of approximately 10 km offshore (deep water). The CMS-Flow grid covered a much larger domain however, encompassing the entirety of the back-bay system which stretches approximately 20 km to the north, 50 km to the south and 20 km inland of Ocean City Inlet. The CMS-Flow domain was required to be this large due to the fact that the entire volume of the back-bay system must be accounted for in order to properly simulate the full tidal prism at Ocean City Inlet. If the full tidal prism were not accounted for, flows through the inlet would be representative of a fraction of the actual flow which is experienced at the site.

A full year of water level data was input to the circulation model boundaries by using tidal constituents from the CIRP (Coastal Inlets Research Program – USACE) constituent data base. A full year of annually averaged wave data was input at the offshore boundary of the wave model. Morphological changes were then set to be updated every 15 minutes, while the steering interval between the two models was chosen to be 3 hours.

The coupled model was run for a full simulated calendar year. The results from this simulation were then analyzed to fulfill the objectives of the study. From this analysis it was found that sediment bypassing from the north to the south occurs regularly, but only for above average waves originating from the NE. Small waves are shown to propagate over the shallow waters of the ebb-shoal complex and into the inlet mouth prior to breaking. As such, sediment is carried into the inlet under these conditions as opposed to across the ebb-shoal bar.

The numerical model shows that the ebb-jet (ebb-flow current as it exits the inlet mouth) was strengthened by the 2002 rehabilitation of the south jetty. This is due to the fact that prior to the jetty rehabilitation, its permeability allowed flow to exit through the structure. This strengthening of the ebb-jet subsequently pushed the ebb-shoal further offshore. The ebb-jet was also noted to exit the inlet with a southward direction at the beginning of the ebb-tidal cycle, and to sweep northward throughout the course of the tide. This unique sweeping of the ebb-jet is deemed to be responsible for the formation and maintenance of the ebb-shoal tongue as sediment is pushed northward in the final stages of each ebb-tide. This process is illustrated in Figure 2.29 below; with sub-figures A through D showing numerical model results as they progress through a single ebb-tide.

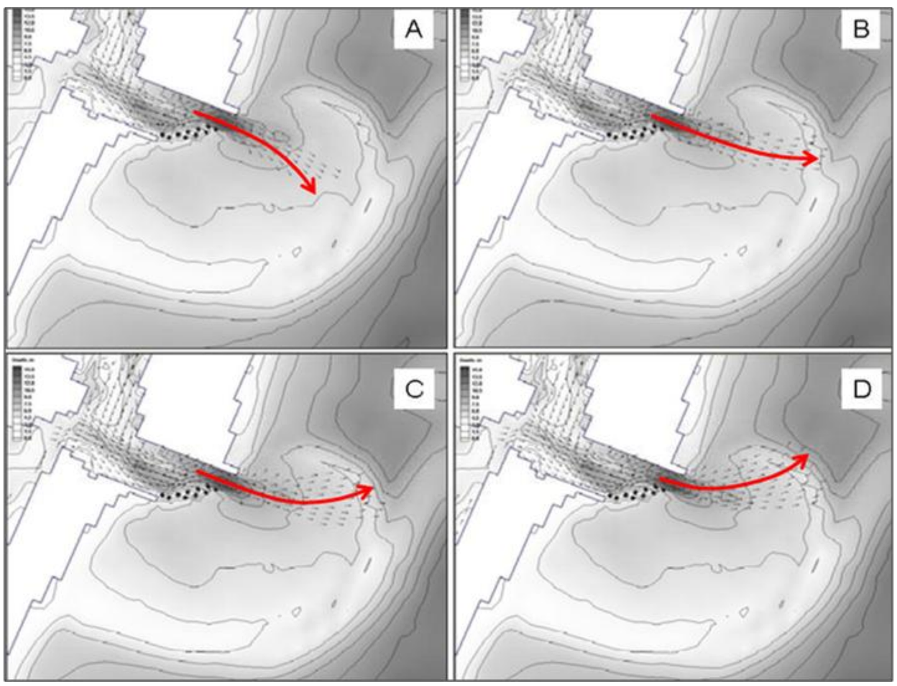

Figure 2.29: Numerical model output showing the sweeping motion of the ebb-jet from south to north during a single ebb-tide (Buttolph *et al*. 2006).

In addition to the occasional southward longshore transport across the ebb shoal, the numerical model showed the occurrence of northward transport under small waves originating from the SE. These waves were shown to refract around the attachment bar prior to breaking, thus resulting in the creation of northward radiation stresses. This sediment is then deposited along the beach immediately adjacent to the inlet and along seaward face of the south jetty. The 2002 rehabilitation of the south jetty was shown to be successful in abating the intrusion of this sediment into the inlet from the south.

Conclusions from the reviewed study were that the driving process behind the formation and maintenance of the ebb-shoal tongue is in fact the sweeping motion of the ebb-jet, and is therefore entirely tide-related and independent of wave action. This makes the ebb-shoal tongue a good borrow site for mechanical bypassing of sediment and beach nourishment due to the fact that it will be quickly refilled by the perpetual sweeping of the ebb-jet. A further conclusion of the authors was that the 2002 rehabilitation was successful in abating both the intrusion of sediment into the inlet from the south and the scouring along the lee-side toe of the south jetty. Lastly, it was concluded that natural sediment bypassing (from north to south) does occur, however it only occurs under large north-easterly wave conditions. Therefore the natural supply of sediment to the down drift shoreline can be infrequent at times and varies largely in magnitude based on the local wave climate.

The reviewed study regarding morphology at Ocean City Inlet is a good example of a case in which a numerical model has been applied to a highly complex system in order to gain a better understanding of the processes at play. Even though a large amount of data was available for calibration and validation of the numerical model, the authors did not attempt to provide quantitative predictions for morphological change based on the model results. This study does well to illustrate the difficulty in using a numerical system to accurately describe a process as complex as tidal inlet morphology, yet it highlights the potential use of the model as an analytical tool. The reviewed study is also a good example of a case in which CMS-Flow and CMS-Wave were coupled together to simulate tidal inlet morphology. This is significant in the present context due to the fact that the same two numerical models will be used in the present study to simulate the even more complex inlet morphology present at Shippagan Gully.

2.6 Discussion

Several relevant topics have been presented and discussed in this literature review, from the very basics of coastal engineering, to the highly complex classification of tidal inlet morphology. The topics which were discussed are crucial in creating a basis of knowledge for the study of inlet morphology at Shippagan Gully. Without the information presented herein, this study could not have been completed, nor could this thesis be properly understood.

It is apparent from the literature review presented herein that coastal processes which are related to tidal inlet morphology are abundant and complex. It is also apparent that coastal engineering is a relatively new branch of engineering, as researchers have only recently begun to be able to quantify many coastal phenomena in a quantitative manner. Coastal processes which drive the morphology at a tidal inlet are inherently complex; however it is the complexity of their interaction that makes them so difficult to study. Although we are beginning to develop a good understanding of each of the processes individually, much more research is required before we will be able to confidently predict their net and long-term effects.

Each of the presented case studies supports the topics discussed in the previous sections. Much can be learned from these previous works, both in terms of what we know as coastal engineers, and what we must not pretend to know when performing such a study. It is clear from the review of these studies that tidal inlet morphology is not a process that can be easily predicted. Sediment transport mechanisms at tidal inlets are too numerous, too diverse, and too sensitive to be entirely understood at present. Even with a substantial amount of quality field data, neither analytical nor numerical models can be expected to provide an accurate quantitative result when assessing tidal inlet morphology. When applied in conjunction with a good understanding of coastal processes and a certain degree of caution, these numerical models can however serve as extremely useful tools in assessing past trends and making responsible and educated engineering decisions for the future.

Although there are hundreds of coastal inlets located in North America and many hundred more around the world, very few studies have been completed and documented regarding tidal inlet morphology. Properly understanding the mechanics which form, maintain, and alter the geometry of a tidal inlet is an ongoing mission which does not have a long history. The majority of coastal works constructed at tidal inlets up until the mid 19^{th} century were completed with little to no knowledge of the effects the human intervention would have on the surrounding natural environment. As a result, these projects often resulted in (and continue to result in) extensive recession or loss of shoreline, navigation channels which are unsafe for navigation and large continual maintenance costs. Now that coastal science has advanced to a point at which we are beginning to understand the complex coastal processes responsible for tidal inlet morphology, it is our responsibility as engineers to appropriately assess the impacts of our actions and exercise good engineering judgment. The present study is one more step in this direction.

3.0 Site Description

Shippagan Gully is located at the south-eastern limit of a natural waterway which transects the Acadian Peninsula. The waterway serves as a navigation channel between the Bay de Chaleurs to the NW and the Gulf of St. Lawrence to the SE (see Figure 3.1). Shippagan Gully is therefore an unusual inlet as it connects two parts of the same body of open water and is thus subjected to tidal forcing from both directions. Water level fluctuations at each end of the waterway are however not precisely in phase. In fact, there is sufficient difference in the phase and amplitude of the tide in the two regions (sometimes diurnal, sometimes semi-diurnal) to force a strong bi-directional tidal current through the inlet at Shippagan Gully. Currents through Shippagan Gully, particularly during the ebb-tide, have been observed to reach velocities of over 2 m/s, while the tidal range at the inlet is generally on the order of 2 m or less.

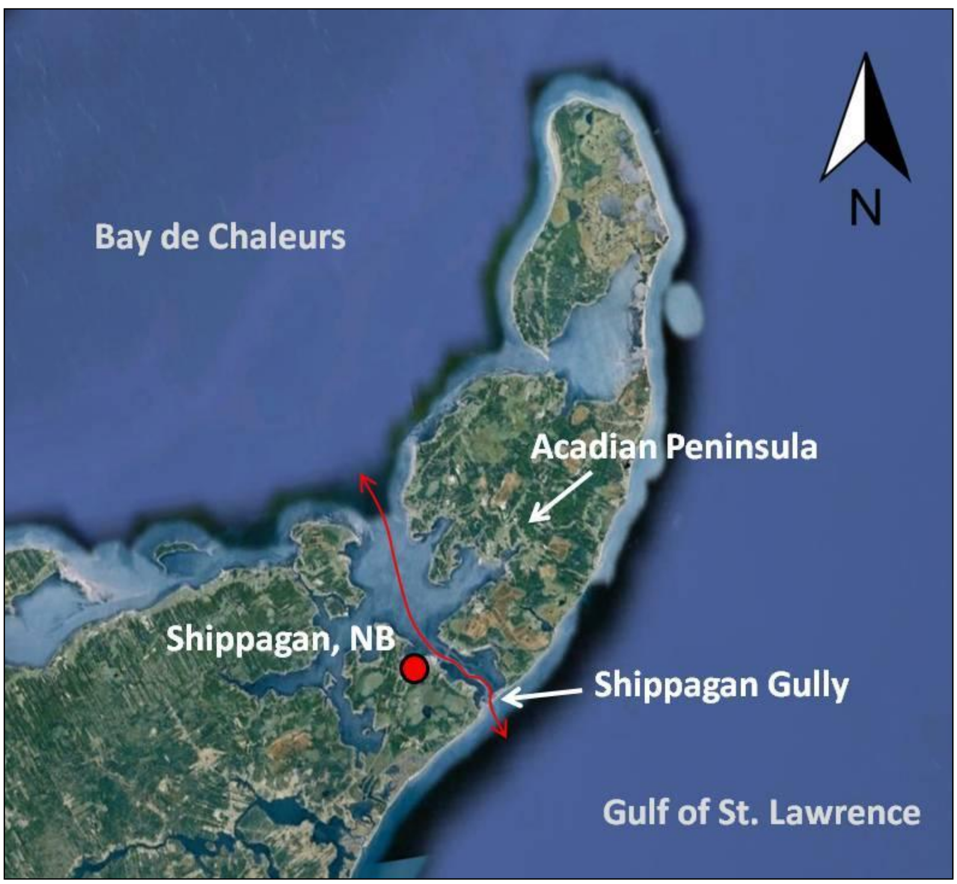

Figure 3.1: Map of the Acadian Peninsula, with the Bay de Chaleurs to the NW and the Gulf of St. Lawrence to the SE. The natural waterway which exits at Shippagan Gully is denoted in red (modified from Google Earth, 2010).

The local shoreline along the Gulf of St. Lawrence is approximately linear, and is oriented along the bearing from SW to NE. Local morphology and the presence of moderate (0 to 4 m high) multi-directional waves originating in the Gulf of St. Lawrence suggest the existence of significant littoral (longshore) transport, caused by waves breaking along the sandy shoreline. There is clear evidence that the net longshore sand transport at Shippagan Gully is from NE to SW, hence there is a net supply of sediment arriving at the inlet from the NE. This indicates that the local wave climate is likely governed by waves approaching from the east. Waves also approach the site from the south and southeast, but these are less frequent and/or tend to be less energetic.

Shippagan Gully has been maintained by man-made coastal structures since the late 1800's in an effort to stabilize its position and promote its navigability. The earliest documented coastal works at the site was the construction of two 300 m jetties in the 1880's, on either side of the inlet. Late 19th century engineering drawings show periodic extensions to the east jetty, as sediment was accumulating on its east face and ultimately passing around its sea-ward limit and into Shippagan Gully. This accumulation of sediment on the east side of the inlet, along with severe erosion which was observed to the west of the inlet, supports the hypothesis that a net longshore transport exists from NE to SW. It further indicates that natural sediment bypassing was interrupted at Shippagan Gully by the introduction of these original coastal structures in the late 19th century.

Throughout the mid 20th century, several engineering works were completed at Shippagan Gully, most notably during the 1960's and 1970's. A new jetty was constructed on the east side of the inlet near the inlet mouth (see Figure 3.2). This new structure was built on the inlet side (west) of the older east jetty, its angle differing such that it was nearly parallel to the shoreline. The new jetty stretched 90 metres to the south west, across the inlet mouth, effectively reducing the inlet width. The second major coastal works undertaken in the 1960's and 1970's was the two phase construction of a 600 m long curved, vertical sheet pile breakwater within the inlet. This structure was constructed off the inner tip of the west jetty, progressing inland (north) and into the tidal lagoon. The structure was built with the purpose of maintaining a self-scouring navigation channel between the two jetties. As a result of this new construction, a sheltered small craft harbour was created in its lee, known locally as Le Goulet. All coastal works constructed in the 1960's and 1970's are shown in Figure 3.2.

Figure 3.2: Aerial photograph taken in 1980 showing coastal works completed in late 1960's and early 1970's (PWGSC, 2010).

No significant coastal works have been undertaken at Shippagan gully since the 1970's. Furthermore, no dredging has been completed in Shippagan Gully since 1983 (although the small craft harbour was dredged in 1989 and 1993). As such, natural morphologic processes have taken hold of the inlet over the past 28 years, resulting in its present state. Severe degradation of the existing coastal structures has become apparent, most notably characterized by a complete collapse of the outer 40 m of the newer east jetty sometime between 1998 and 2004. The northern part of the curved breakwater is also severely corroded. Presently, navigation through Shippagan Gully is limited due to the presence of a large volume of sediment on the east side of the navigation channel, within the confines of the inlet. This sediment continues to accumulate, pushing the navigation channel increasingly further to the west against the curved breakwater. Furthermore, navigable depths in the offshore region are highly variable and often dangerously low due to the presence of a highly dynamic crescentric ebb shoal, which is skewed to the SW. A 2010 bathymetric contour map is presented in Figure 3.3, illustrating depths in the channel and nearshore zone, as interpolated from bathymetric survey data.

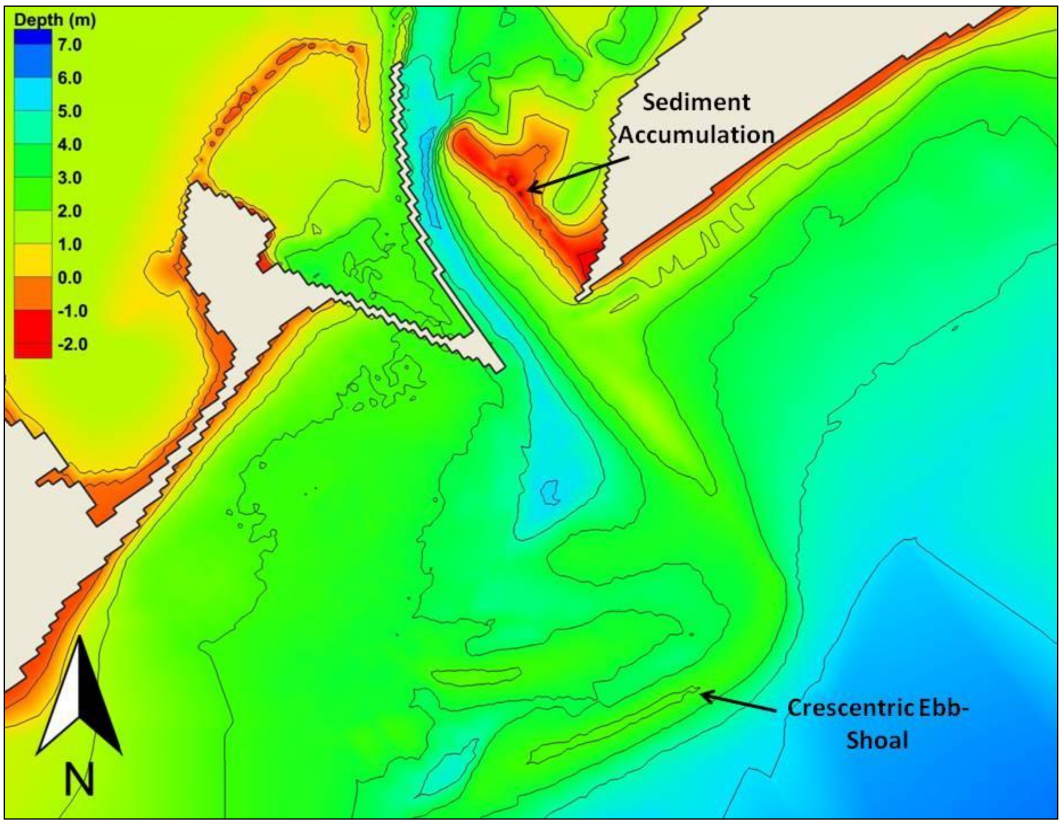

Figure 3.3: 2010 bathymetric contours at Shippagan Gully, showing sediment accumulation on the east side of the navigation channel and the crescentric ebb-shoal in the shallow nearshore region.

4.0 MORPHOLOGICAL AND HYDRODYNAMIC INVESTIGATIONS

4.1 Site Visit and Field Data Collection

A site visit to Shippagan Gully was completed in August 2010 during which field work was performed and historical information gathered from local sources. The field team, which consisted of representatives from both the Canadian Hydraulics Centre and the University of Ottawa, spent three days taking field measurements and meeting with stakeholders, including members from Public Works and Government Services Canada (PWGSC), Department of Fisheries and Oceans (DFO-SCH) and the Comité Brise-lames de Le Goulet. During these encounters, local concerns were voiced in order to help steer the direction of the project. Furthermore, historical information was gathered from local sources in order to aid in creating a basis of understanding for the conditions and complex hydrodynamic and sedimentary processes present at Shippagan Gully.

Current velocity measurements were taken at Shippagan Gully during both ebb and flood tides using an electromagnetic current meter (see Figure 4.1) while measurement positions were mapped using a Global Positioning System (GPS). Documenting the precise timing and position of the current velocity measurements was crucial, as the measurements were later used for calibration of the hydrodynamic numerical model (discussed in Section 5.1.5). Approximate depths of each measurement were also logged, such that depth-averaged velocities could be approximated from the measurements using empirical relationships for velocity profiles in open flow channels. Depth-averaged values were required due to the fact that the numerical modeling system employed in the present study was two-dimensional.

Sediment samples were extracted at various locations both up-drift and down-drift from the project site, as well as from within the inlet. Similar to the current velocity measurements, the location from which the sediment samples were obtained was logged using a Global Positioning System (GPS). Sediment samples were subsequently analysed in a laboratory setting in order to obtain sediment properties for input into the numerical model (discussed in Section 4.2). Sediment sample and velocity measurement locations are shown in Figure 4.2

Figure 4.1 Electromagnetic current meter used for measuring current velocities at Shippagan Gully during both ebb and flood tides (left). Members of the field team taking measurements from a boat, August 12th 2010 (right).

Figure 4.2: Current velocity measurement and sediment sample locations from August 2010 field study, documented using GPS (photograph provided by PWGSC, 2010).

4.2 Sediment Analysis

A laboratory analysis of sediment samples obtained during the August 2010 field investigation was completed in order to determine local sediment properties at Shippagan Gully. Eleven sediment samples were collected from beaches both up-drift and down-drift from the inlet, as well as from the spit which has formed within the inlet.

Prior to analysing the sediment properties, all 11 samples were placed in an oven for at least 4 hours in order to remove moisture. The dry samples were then sieved using a shake table and sieves of variable size ranging from 0.125 mm to 12.5 mm. Sediment trapped in each sieve was weighed independently in order to determine the % finer (in sediment size) from the total sample mass. Gradation curves were then plotted for each sediment sample, illustrating the percentage of the sample (by mass) which is finer than a given grain size. From the gradation curves, the mean diameter (d_{50}) of each sample was determined, followed by the mean diameter from all samples, which was used in sediment transport calculations (Section 4.6) and as input to the numerical model. A sample gradation curve for sediment samples taken from within Shippagan Gully is shown in Figure 4.3.

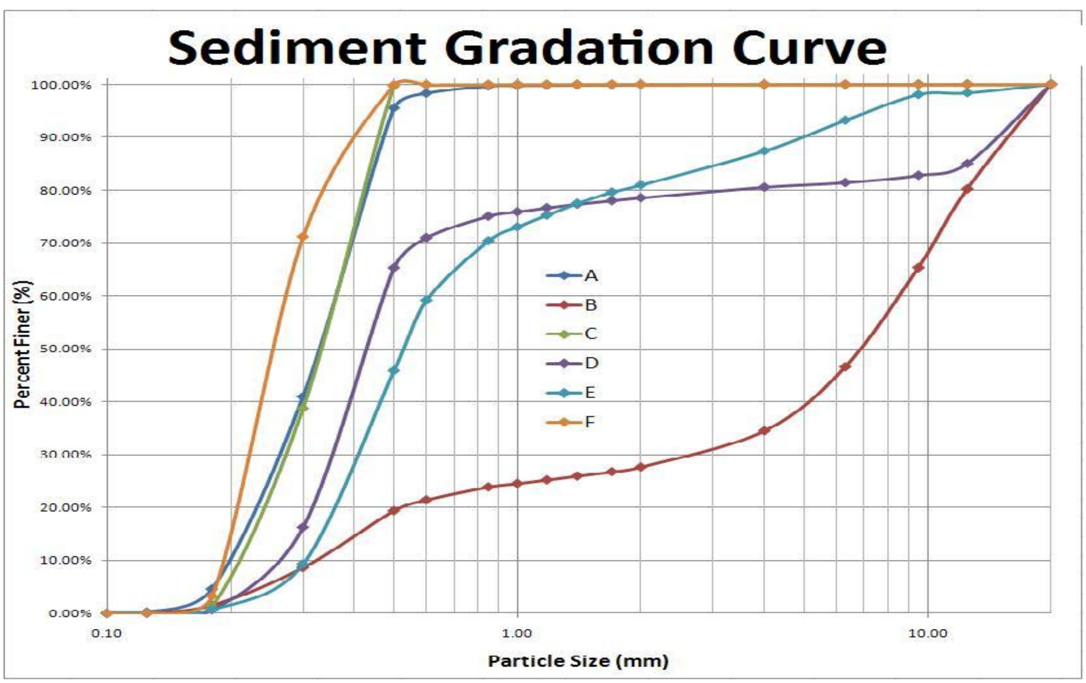

Figure 4.3: Sample sediment gradation curve, analysed from sediment samples extracted from deposition zones within Shippagan Gully.

Once gradation curves had been constructed from the sieve analysis, the sediment samples were re-assembled and weighed again in their entirety. The total dry volume of each sample (volume of sediment + volume of voids) was then estimated using a measuring cylinder. The samples were then placed in a second measuring cylinder with a known volume of water, in order to determine the sediment volume and the volume of voids for each sediment sample. From these findings, sediment porosity and density were calculated to be used as input to the numerical model. The results of the above described analyses, averaged over 8 of the 11 samples (3 were excluded due to sampling location or inaccuracies in the analysis), resulted in a mean diameter (d_{50}) of 0.40 mm, a mean porosity of 0.42 and a mean density of 2610 kg/m^3. A complete table of results from the sediment sample analysis is found in Appendix A.

4.3 Detailed Study of Historical Morphologic Changes

A great deal of information concerning past morphologic change and the effects of historical human intervention at Shippagan Gully can be deduced from historical engineering documents and aerial photographs. The earliest such documents are a series of plan view engineering drawings from the late 1800's which indicate coastal works and subsequent morphological details inherent to the time period (see Figure 4.4). These drawings illustrate the construction of the original east and west jetties in the late 1880's and early 1890's. Moreover, the initial effects these jetties had on the local morphology are also noted. To the west of Shippagan Gully, previous low and high water lines (1895 and 1898) are indicated on the drawings, revealing that a substantial retreat of the shoreline (20 to 25 m per year) occurred to the west of the inlet in the years following the construction of the original jetties. This observation reveals several important facts regarding morphology at Shippagan Gully. First, it demonstrates that active littoral drift (longshore sediment transport created when waves arrive at an oblique angle to the shoreline and break in the sandy shallow waters) is present in the region, with a strong net direction from the east to the west. Furthermore, it is apparent from these drawings that natural bypassing of sediment along the coastline was interrupted by the construction of the original jetties. As such, the region to the west of Shippagan Gully was depleted of its sediment source, and subsequently subjected to dramatic erosion. A sample engineering drawing produced in 1899 is presented in Figure 4.4.

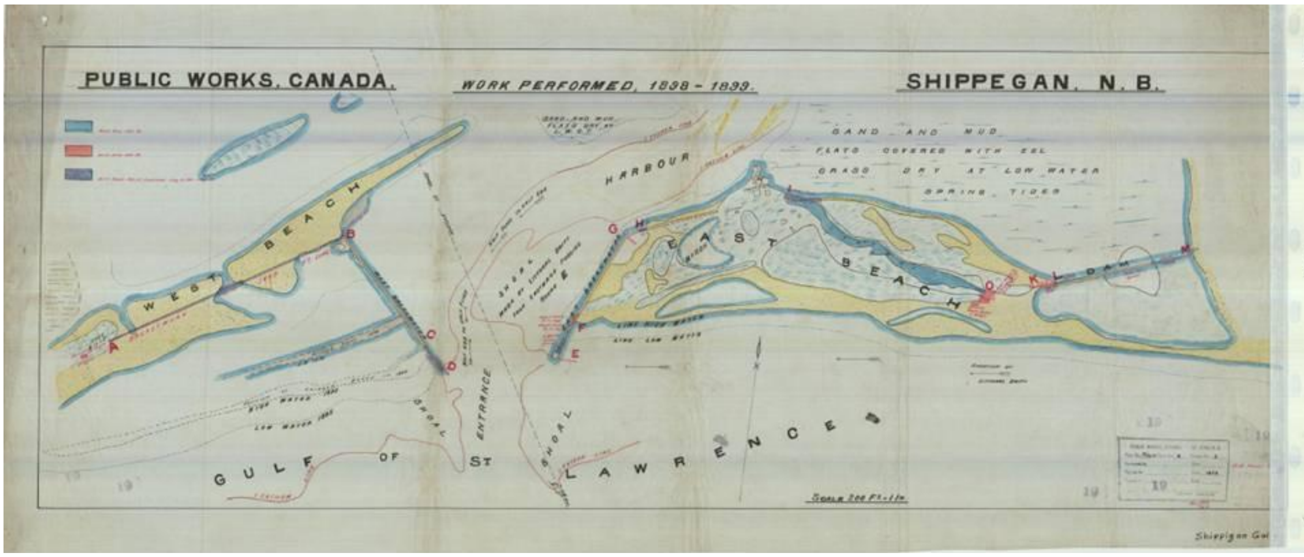

Figure 4.4: Engineering drawing dated 1899 showing original coastal works and subsequent morphological response (courtesy of PWGSC, 2010).

In addition to shoreline erosion, bathymetric contour lines denoting depths of 1 fathom (1.83 m) are included in the historical drawings. These contours indicate the presence of several shoals. Ebb-shoals are shown to exist in the nearshore region, both on the east and west sides of the channel mouth, thus indicating the presence of a strong ebb-current. A third shoal is denoted within the confines of the inlet, occupying the eastern side of the navigation channel, in lee of the east jetty. This shoal is labelled in the drawings as littoral drift (longshore transport) which is deposited after passing around the tip of the east jetty (see Figure 4.4). Likely based upon this observation, the east jetty was extended several times in the late 19th and early 20th centuries, in an attempt to limit the amount of sediment entering the inlet. As such, it is apparent that littoral drift was at least partially responsible for sediment accumulation within Shippagan Gully at the turn of the century.

Due to the continual accumulation of sediment on the east side of Shippagan Gully, the navigation channel which passes through the inlet on route from the Bay de Chaleur to the Gulf of St. Lawrence was pushed increasingly further to the west as it was forced to flow around the deposited sediment. This westerly migration of the channel resulted in a curved flow path just prior to exiting the inlet mouth into the Gulf of St. Lawrence. In an attempt to stabilize the position of the navigation channel and to create deeper, more navigable depths between the two jetties, a "pierhead" groyne was constructed at the end of the west breakwater, extending eastward towards the navigation channel. It is presumed that this new structural addition was implemented to constrict flow at the inlet mouth from the west, thus promoting self scour and counteracting the westerly migration of the channel.

The first half of the 20th century did not see a great deal of coastal works at Shippagan Gully, aside from mechanical dredging operations which are discussed further in Section 4.3.1. As such, natural morphological trends can be deciphered from aerial photographs taken during this period. The inner shoal located on the east side of the inlet is clearly visible in photographs from 1944, 1958, 1964 and 1966 (see Figure 4.5), and is seen to be expanding in both the westerly (towards the navigation channel) and northerly (into the tidal lagoon) directions. The unique plan-form shape of the shoal illustrated in Figure 4.5b, c and d indicates that although the sediment source may be at least partially longshore transport entering the inlet from the east, complex hydrodynamic conditions (due to a combination of waves and tidal-currents) likely have a strong influence on its formation and maintenance.

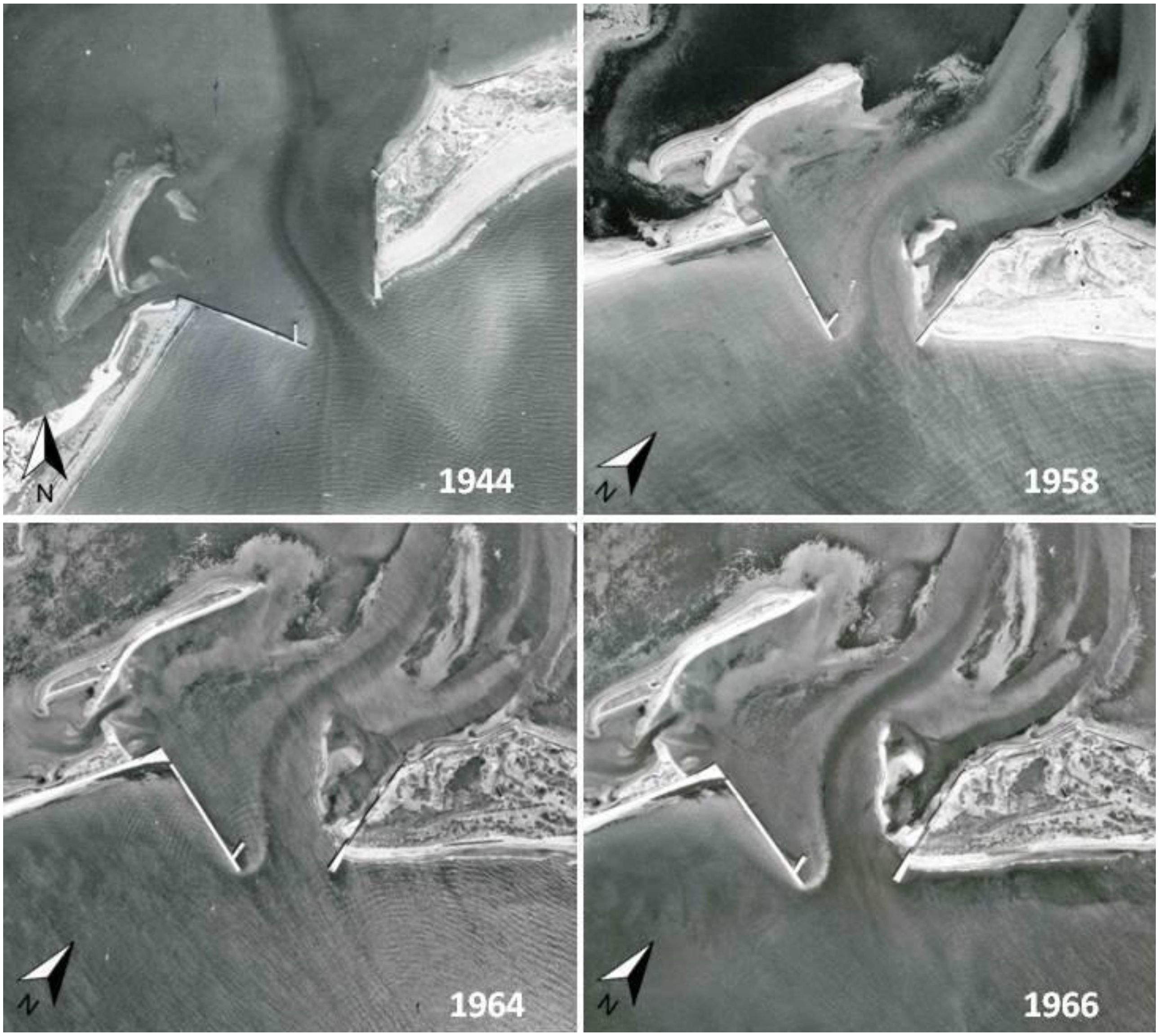

Figure 4.5: Aerial photographs of Shippagan Gully taken in 1944 (a), 1958 (b), 1964 (c) and 1966 (d) respectively, showing coastal structures, flow pathways and sediment deposition on the east side of the inlet (courtesy of PWGSC, 2010).

A great deal of change occurred at Shippagan Gully during the 1960's and 1970's with the construction of a new jetty on the east side of the inlet mouth and a 600 m long curved sheet-pile breakwater along the western edge of the navigation channel (as discussed in Section 3.0 and presented in Figure 3.2). From aerial photographs taken in 1970, 1980, 1987 and 1995 (see Figure 4.6), it can be seen that although the location of the curved navigation channel appears to be approximately stabilized by the new curved breakwater, significant sediment accumulation is still apparent on the inside of the channel bend, on the east side of Shippagan Gully. This observation indicates that although the new east jetty may have slowed the intrusion of littoral drift into the inlet, it did not provide a solution to the sediment deposition which continued to occur in its lee in the decades after its construction.

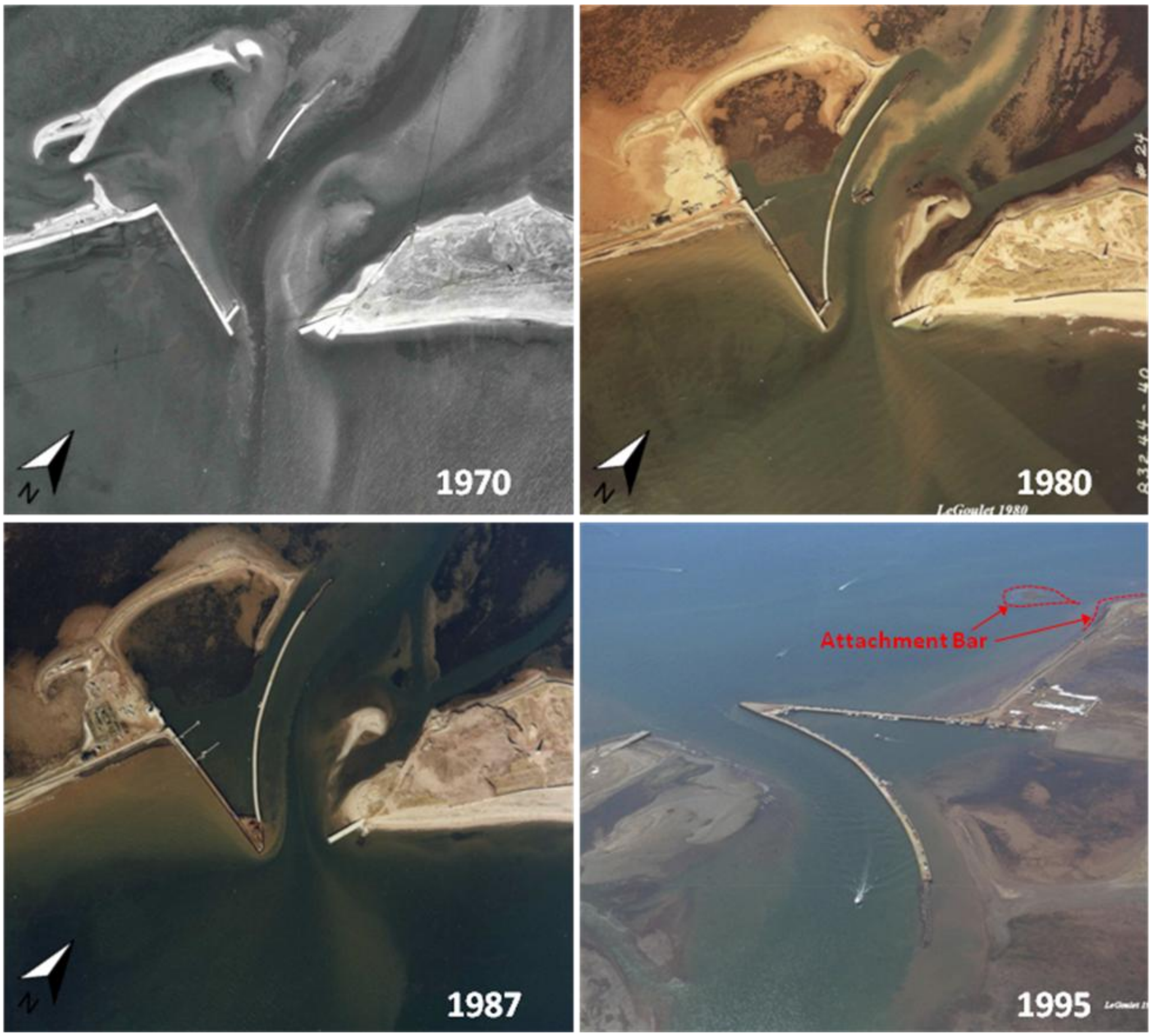

Figure 4.6: Aerial photographs of Shippagan Gully taken in 1970 (a), 1980 (b), 1987 (c) and 1995 (d) respectively, showing coastal structures, flow pathways and sediment deposition on the east side of the inlet (PWGSC, 2010).

By 1995 it appears as though partial natural sediment bypassing of Shippagan Gully had resumed. This is revealed by the presence of an attachment bar nearly a kilometre to the west of

Shippagan Gully (as seen in Figure 4.6d). An attachment bar is formed when longshore sediment transport is carried along the ebb shoal in the direction of net transport, causing the ebb-shoal complex to expand in a similar direction. The ebb-shoal expands until it re-attaches itself to the downdrift shoreline, thus allowing sediment to bypass the inlet and continue onward as littoral drift. This phenomenon is often characterized by a seaward protrusion in the shoreline or a nearshore bar downdrift from the inlet (both of which are visible in Figure 4.6d). Natural sediment bypassing should be maintained whenever possible, as it is this process by which sediment is supplied to the downdrift shoreline. An interruption in this process removes the downdrift sediment supply, and often results in severe shoreline erosion (Dean and Dalrymple, 2002).

It is important to note that up until the late 1990's, ebb-flows exiting Shippagan Gully followed two separate flow paths through the inlet, which are depicted in Figure 4.7. The majority of flow exiting the tidal lagoon followed the primary navigation channel to the south and along the curved breakwater prior to exiting at the inlet mouth. However, a secondary flow path existed in which ebb-flow arrived at the inlet from the east (inside the tidal lagoon) and was permitted to exit Shippagan Gully directly behind and parallel to the original east jetty. In the late 1990's, continual sediment deposition on the east side of the main navigation channel resulted in the closure of this secondary flow path, likely influencing the hydrodynamic and morphologic processes at Shippagan Gully.

Figure 4.7: 1987 aerial photograph with primary and secondary ebb-flow pathways denoted (PWGSC, 2010).

To further complicate this time period, at some point between 1998 and 2004, dramatic structural failure of the newer east jetty occurred, resulting in the collapse of the outer 40 m of the structure. The precise reason for the collapse is unknown; however it is highly likely that the collapse had a strong influence on the local hydrodynamics and sedimentary processes, possibly triggering the closure of the secondary flow path from the east. Both of these topics are investigated in Section 6.1.1 below.

Over the past decade, substantial sediment deposition within Shippagan Gully has continued, and is illustrated in Figure 4.8 which shows aerial photographs from 2004, 2007 and 2008. Most notably, the inner shoal on the east side of the navigation channel has expanded to the NW, greatly reducing the width of the navigation channel near the centre of the curved breakwater. Furthermore, the inner shoal has greatly increased in height, with vegetated dunes at its centre rising nearly 2 m above the mean water level (MWL). Since the tidal range at Shippagan Gully rarely exceeds 2 m, it is likely that this sediment is deposited during storm events accompanied by significant surge. This topic will be discussed further in Section 6.1.3.

Figure 4.8: Aerial photographs of Shippagan Gully taken in 2004 (a), 2007 (b), and 2008 (c) respectively, showing coastal structures, flow pathways and sediment deposition on the east side of the inlet (PWGSC, 2010).

A point-form history of documented morphological change and human interventions at Shippagan Gully is provided in Appendix B.

4.3.1 Dredging History

A complete dredging history for Shippagan Gully was made available by PWGSC, highlighting years in which dredging occurred, the location in which dredging was completed, and the amount of material that was removed. Much of the relevant information is however missing from several entries, particularly specific locations in which dredged material was removed. An abbreviated version of the dredging history for Shippagan Gully which includes all operations relevant to the current project is presented in Table 4.1.

In comparing the dredging records presented below to the aerial photographs presented in Section 4.3, it can be seen that natural sediment transport was continually counteracting historical dredging efforts in Shippagan Gully. Even though sediment was removed from the navigation channel on several occasions over the past century, natural sedimentary processes were replacing the removed material with continual deposition in the inlet, most notably on the east side of the navigation channel.

Table 4.1 Abbreviated dredging history.

1912 – 1913	2,013 m^3 removed (location unknown)
1917 – 1918	19,620 m^3 removed from four different sections of navigation channel
1918 – 1919	14,188 m^3 removed from original harbour (north of east jetty)
1954 – 1955	9,717 m^3 removed from two areas in Shippagan Gully
1955 – 1956	21,884 m^3 removed from two shoal areas on the sides of the channel
1980 – 1981	Dredging completed with land-based equipment (location and quantity unknown)
1981 – 1982	1,900 m^3 removed (location unknown)
1982 – 1983	59,520 m^3 removed from channel entrance and harbour basin area
1988 – 1989	3,190 m^3 removed from harbour and disposed along existing sandbar in western end of harbour

The dredging record at Shippagan Gully shows that no dredging within the inlet has been conducted since 1983 (the small craft harbour was dredged in 1988 and 1993, although the latter is not clearly documented). It has been stated that the above water deposition in lee of the east jetty was occasionally used as a borrow site for aggregates, however, this did not affect the morphology within the inlet. As such, natural processes in the inlet have continued uninterrupted for nearly three decades, resulting in the bathymetry and topography currently present at Shippagan Gully.

4.3.2 Quantification of Historical Morphologic Change

Many of the morphological changes identified in Section 4.3 can be quantified in terms of shoreline recession rates or annual deposition volumes. By analysing these rates we can achieve a better understanding of the relative magnitude and speed at which morphological changes have occurred.

All aerial photographs and historical engineering drawings were georeferenced using ArcGIS. The most recent aerial photograph (2008) was first georeferenced to an available topographic map of the Acadian Peninsula which was obtained from PWGSC. The topographic map was previously georeferenced in the Universal Transverse Mercator coordinate system (zone 20), and gives an approximate indication of shoreline locations. Once the 2008 aerial photograph was georeferenced, all subsequent historical photographs (and historical engineering drawings) were georeferenced to the 2008 image. A minimum of 7 control points was used for the aerial photographs with a maximum RMS error of less than 1 m deemed to be generally acceptable. Historical engineering drawings (1889 – 1907) were however much less accurate due to a lack of reasonable control points, and resulted in an RMS error of up to 5 m.

Once all available images had been georeferenced, historical shoreline positions were digitized for each available year. This process required a great deal of engineering judgement as the water levels (high tide versus low tide) at the time in which the photographs were taken were unknown. As such, digitized shoreline positions are an approximation only of the low water line.

4.3.2.1 Shoreline Erosion

Based upon digitized shorelines from 1889 to 1907, an expansive beach existed (or was perhaps formed) off the tip of the west jetty immediately after its construction. This beach was approximately in line with the existing shoreline to the east of the inlet. The beach was however the subject of dramatic erosion which occurred immediately to the west of the newly engineered inlet in the years following the construction of the west jetty. As is shown in Figure 4.9, this erosion was characterized by a shoreline recession of 20 to 25 m per year (approximately 250 m total from 1895 to 1907). As was previously discussed, this shoreline retreat is due to the fact that natural sediment bypassing in the form of longshore transport was cut-off by the construction of jetties at Shippagan Gully in the late 1800's. Further evidence to this phenomenon is the accumulation of sediment on the east side of the east jetty, which is labelled in the original engineering drawing presented in Figure 4.9. Several extensions to the east jetty were undertaken in the late 1800's in order to keep up with this accumulation of sediment on its eastern side. These jetty extensions are visible in Figure 4.9.

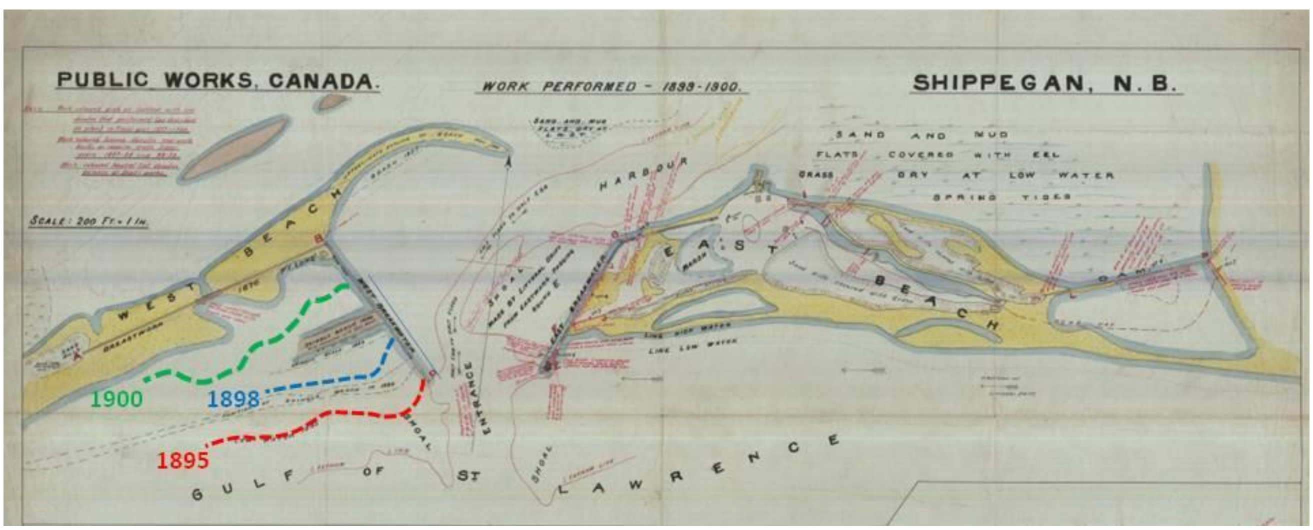

Figure 4.9: Historical engineering drawing dated 1900, illustrating low water lines to the west of Shippagan Gully during 1895, 1898 and 1900 (PWGSC, 2010).

4.3.2.2 Sediment Deposition within the Inlet

In recent years, the most notable morphologic change at Shippagan Gully has been the growth and migration of the sediment spit which has formed within the inlet, on the east side of the navigation channel. As such, polygons were created in ArcGIS from the digitized low water lines on the eastern side of the navigation channel, bounded by the original east jetty. A sample of digitized polygons representing deposition areas is illustrated in Figure 4.10. The change in the area of each polygon from one aerial photograph to the next therefore depicts the change in the two-dimensional area of sediment deposited above the estimated low water line (LWL) inside the inlet over the time period between successive aerial photographs. To capture more sediment deposition in the analysis, beach profiles were extrapolated such that the analysis extended to an elevation of -1 m (Geodetic Datum, GD). By introducing approximate elevations for the morphological features (estimated from aerial photographs and in accordance with photographs and measurements from the August 2010 field investigation), volumetric deposition rates above the -1 m contour (GD) can be estimated.

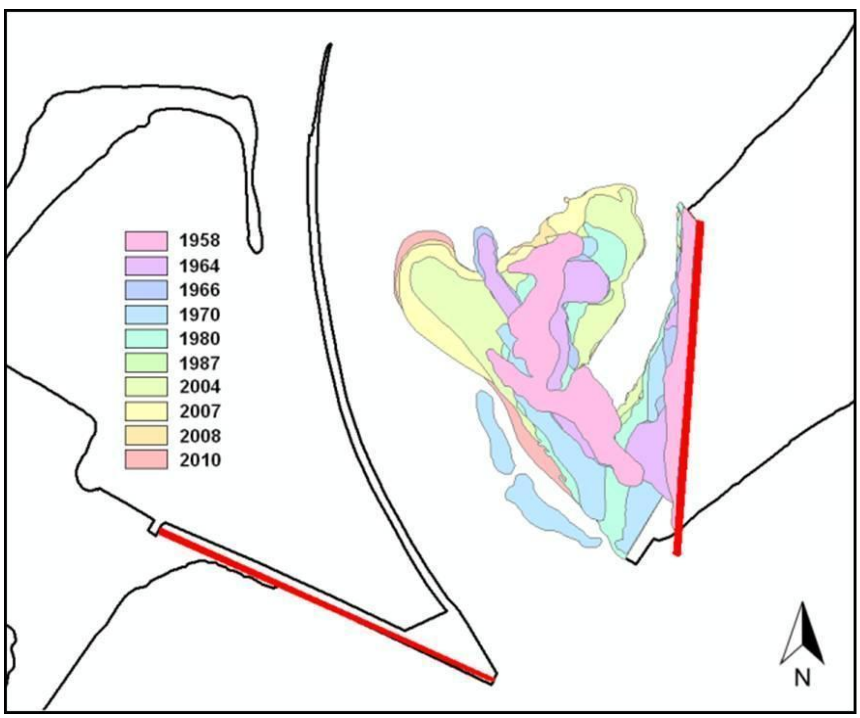

Figure 4.10: Polygons representative of two-dimensional sediment accretion areas, as digitized from aerial photographs using ArcGIS.

By plotting the estimated volumes of deposited sediment (above -1 m GD) versus the date in which the aerial photographs were taken, the rate of deposition can be estimated graphically. This plot is presented in Figure 4.11, where vertical lines represent human interventions at

Shippagan Gully, such as the construction of coastal structures (green and purple lines) and the dredging of material from the inlet (red lines).

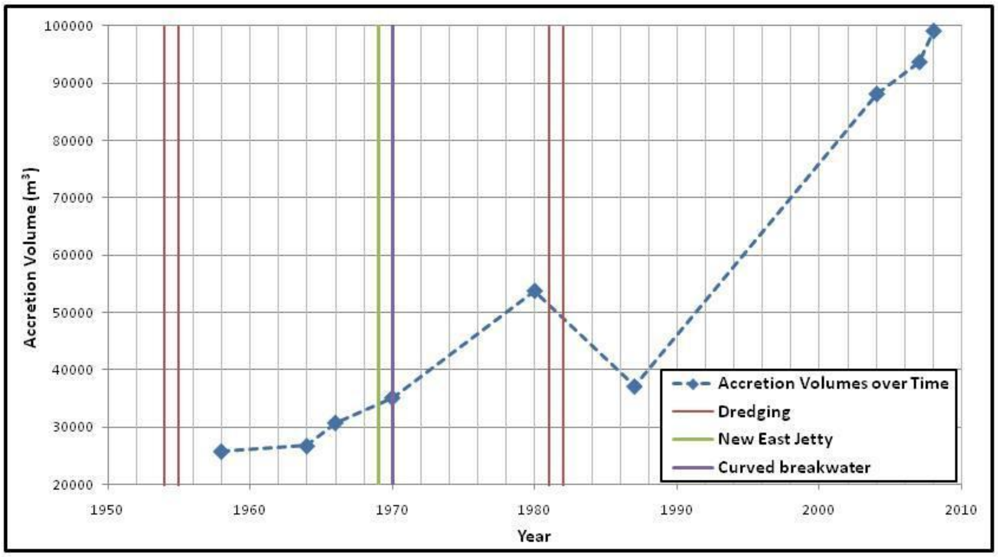

Figure 4.11: Historical sediment deposition volumes (above low water line) within Shippagan Gully as estimated from georeferenced water lines and aerial photographs.

From Figure 4.11 it can be seen that the amount of sediment present above the -1 m contour (GD) within Shippagan Gully has been steadily increasing since the earliest available aerial photographs depicting above water deposition. The sole exception to this trend is the period between 1980 and 1987, during which time substantial dredging operations were undertaken in the inlet. Also of note is that the rate at which deposition has occurred (slope of the dashed lines) is relatively consistent for all years, particularly since 1987. This graph also indicates that above -1 m GD, deposition rates on the eastern side of Shippagan Gully may have increased after the construction of the curved breakwater and new east jetty in the late 1960's and early 1970's. Ignoring the time period from 1980 to 1987 in which sediment was removed from the site, the average above -1 m GD deposition rate from 1958 to 2008 was calculated to be 2200 m^3/year, with a current volume of sediment of nearly 100 000 m^3 present above the -1 m GD contour within Shippagan Gully. A table of values obtained from the accretion analysis is presented in Appendix A.

4.3.2.3 Migration of Navigation Channel

A major morphological change which has been observed at Shippagan Gully is the continual westward migration of the navigation channel, which forces navigators to pass increasingly close to the curved sheet pile breakwater to the west. It has also been observed that although the navigation channel is becoming narrower due to this increased constriction, navigable depths are not increasing. As such, the observed westward migration of the navigation channel poses a real threat to safe navigation through Shippagan Gully.

Navigable depths have been closely monitored at Shippagan Gully over the past two decades by means of nearly-annual bathymetric surveys along the entire navigation channel (1992 to 2009 inclusive). Navigation channel cross-sections were subsequently created from the periodic bathymetric survey data, thus providing a visual means by which to quantify the westward migration of the navigation channel. Figure 4.12 shows bottom elevations at three channel cross-sections, and the location of each of the three cross-sections. In this figure, the x-axis originates at the curved breakwater face.

From Figure 4.12 it can be seen that the position of the east (right) bank of the navigation channel has continually migrated further to the west (left). The most severe migration can be found in cross-section 2 and corresponds to a shift of more than 20 m over the 17 years from 1992 to 2009 (approximately 1 m per year). In addition to the westward movement of the east bank, erosion on the west bank near the curved breakwater face (left side of the cross-sections) is apparent at all three cross-sections. If this erosion continues, it could pose a substantial threat to the structural integrity of the eastern wall of the curved breakwater.

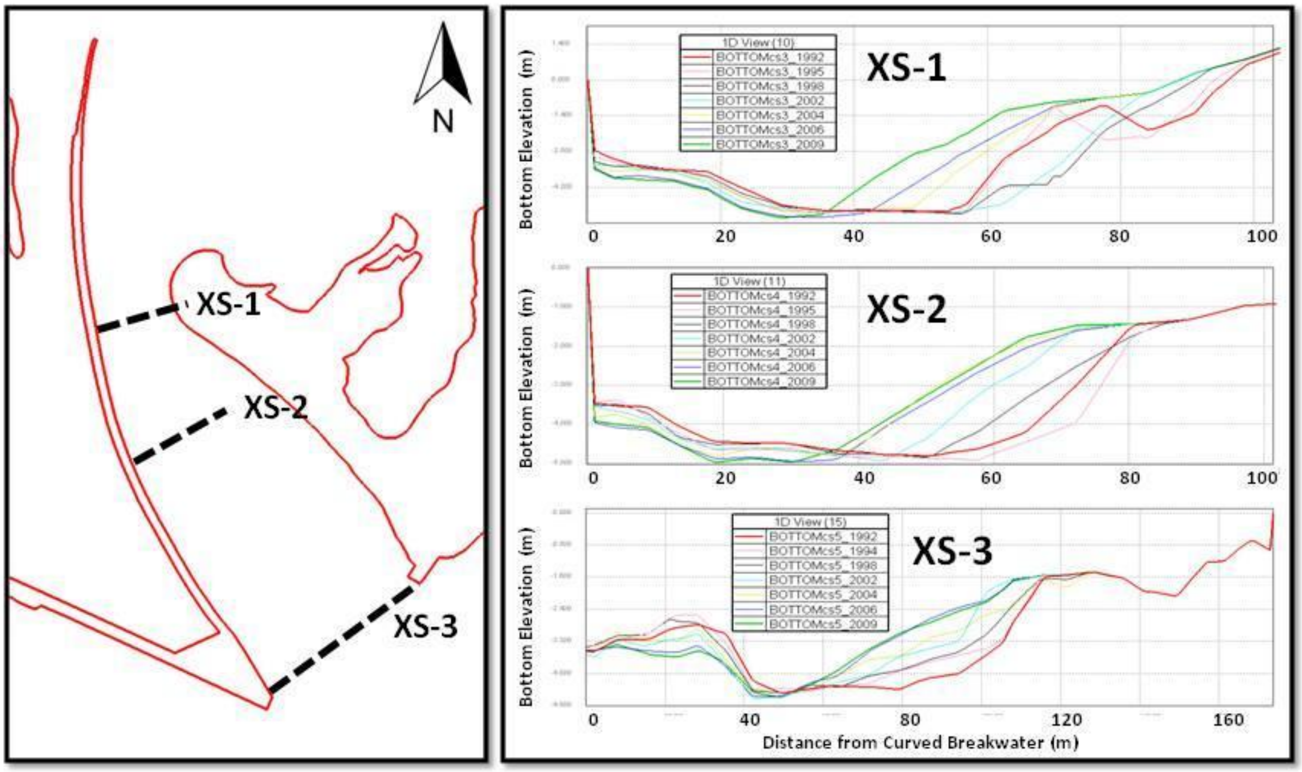

Figure 4.12: Navigation channel cross-sections (1992-2009) and cross-section locations.

4.4 Analysis of Water Levels

The flows through Shippagan Gully are forced mainly by the difference in water levels between the Bay de Chaleurs and the Gulf of St. Lawrence. Good information on these water levels, and their variations with time, is essential to simulate the flows through the Gully. Due to the fact that no long term water level measurements were available in close proximity to Shippagan Gully, an alternative approach had to be taken in order to obtain a time series of water level variations (tides) suitable for use as input to the hydrodynamic numerical model, CMS-Flow (discussed in Section 5.0). The alternative approach involved developing a second hydrodynamic model, covering a larger area, to simulate and predict the tides throughout the region. The second model was developed using the Telemac2D modeling system (Hervouet and Lang, 2000), and was used to establish appropriate water level fluctuations at the boundaries of the CMS-Flow model.

4.4.1 The Telemac2D Model

The Telemac2D software is a fully dynamic, finite element, depth-averaged two-dimensional hydrodynamic model. The physical system (in this case, the seawater bounded by the seabed and shoreline) is discretized into an unstructured mesh of triangular elements, seen in Figure 4.13. Each node is assigned an elevation corresponding to the local elevation of the seabed or shore. The water depth and the depth averaged velocity vector at each node are computed as function of time, subject to boundary conditions applied at the edges of the computational domain.

The Telemac2D model covered an area including the entire tidal lagoon (from the bridge at Shippagan to the inlet), as well as a zone stretching 8 km offshore along the Gulf of St. Lawrence. This coastal zone extended approximately 44 km, from Tracadie (26 km to the south of Shippagan Gully) to a location approximately 18 km to the north of Shippagan Gully. Because of its wide extent, the model was able to reproduce the mean counter clockwise ocean circulation along the East coast of the Acadia Peninsula, as well as the tidal propagation from northeast to southwest along this coast. The Telemac2D numerical model domain is shown in Figure 4.13.

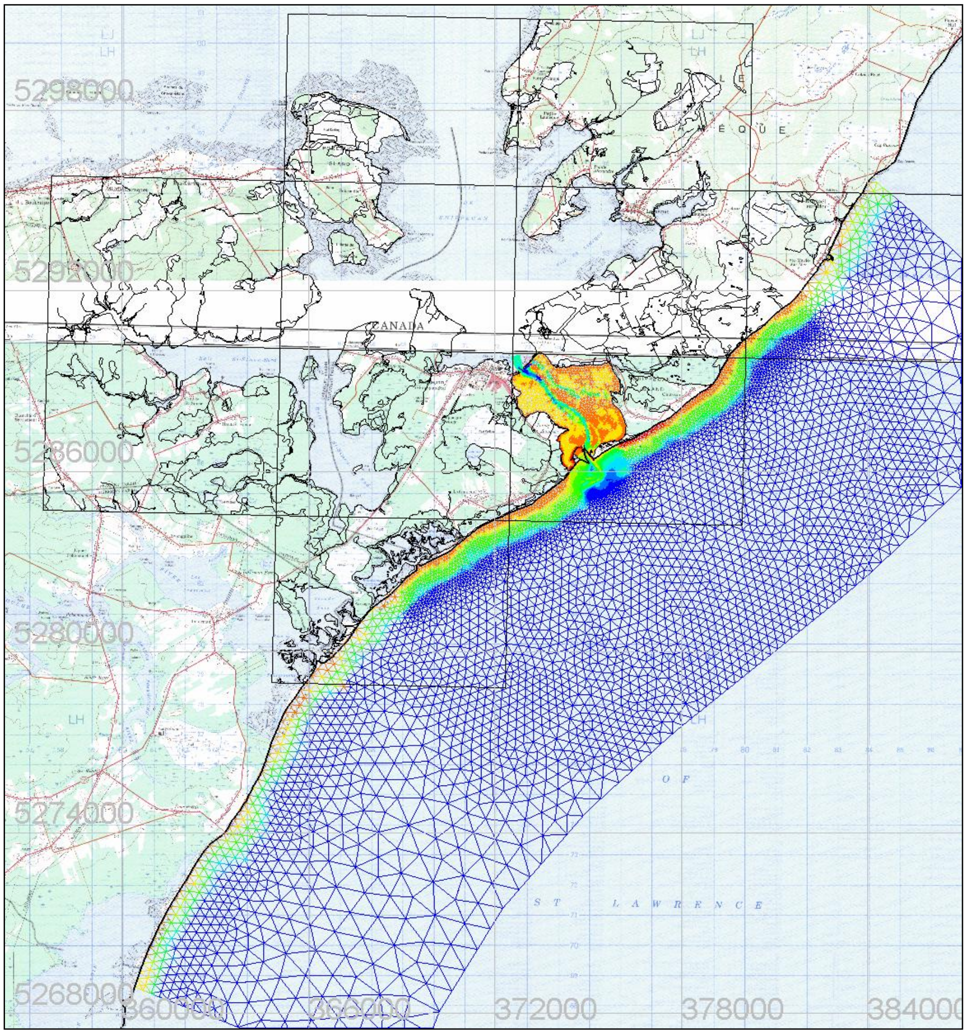

Figure 4.13: Extent of the Telemac2D hydrodynamic model used to simulate tidal propagation.

4.4.2 Model Bathymetry

The bathymetry for the Telemac2D model (and the CMS model) was developed by merging data from several sources, including:

- Navigation channel bathymetry inside the tidal lagoon and offshore from Shippagan Gully, surveyed annually from 1992 to 2009. Provided by PWGSC (red zone in Figure 4.14),
- 2010 bathymetric survey of the tidal lagoon and nearshore zones not covered by the navigation channel surveys. Provided by PWGSC (green zone in Figure 4.14),

- 2010 topographic survey of sediment deposition above the low water line and on the east side of the navigation channel, within Shippagan Gully. Provided by PWGSC (light blue zone in Figure 4.14),
- 2010 bathymetric survey of the small craft harbour known as Le Goulet. Provided by PWGSC (dark blue in Figure 4.14),
- Offshore bathymetry (coarse resolution) obtained from Canadian Hydrographic Services navigation charts (not pictured),
- Top of bank locations and important bathymetric features, estimated from aerial photographs (brown lines in Figure 4.14).

The coverage of the various surveys near Shippagan Gully is mapped in Figure 4.14.

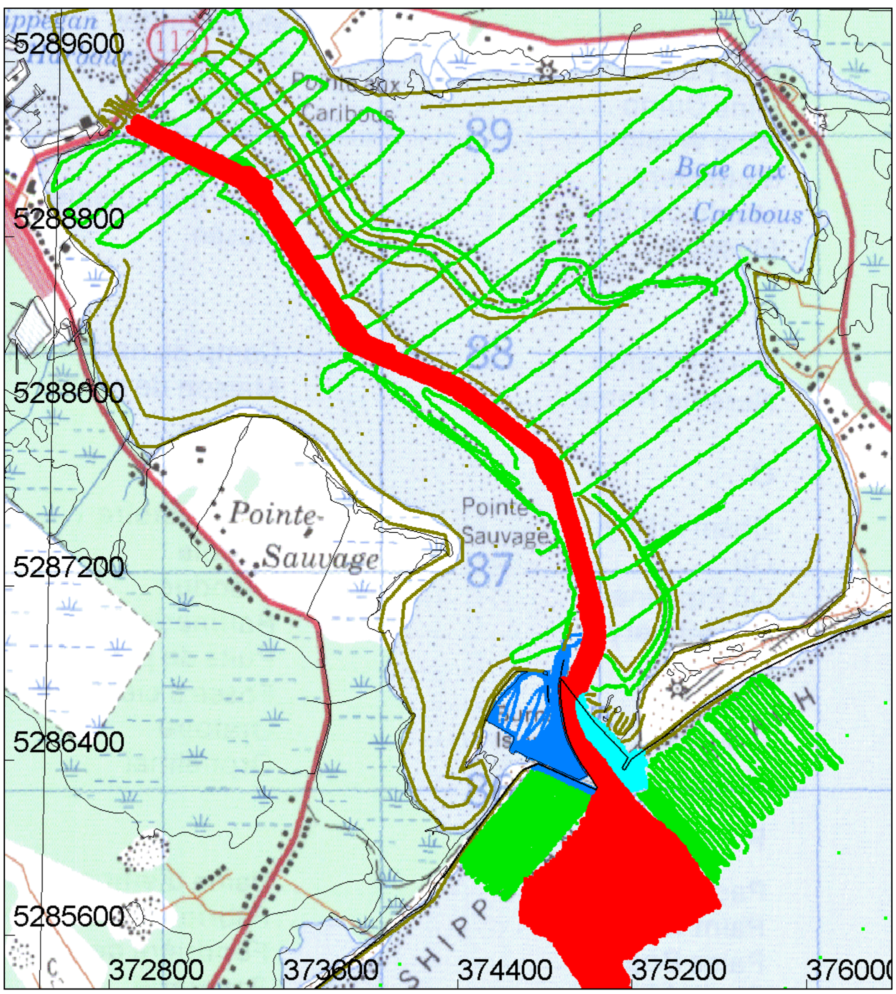

Figure 4.14: Locations of available bathymetric survey data.

All bathymetric data was converted with Telemac2D, from Chart Datum (CD) to Geodetic Datum (GD) using linear interpolation, with the corrections shown in Table 4.2 (provided by the Department of Fisheries and Oceans).

Table 4.2: Corrections to convert from Chart Datum to Geodetic Datum.

Location	**Correction CD to GD**
Shippagan Harbour	0.75 m
Le Goulet - 250 m north of north end of existing breakwater	0.65 m
Le Goulet – 60 m south of south end of existing breakwater	0.53 m
Tracadie tidal station	0.60 m

4.4.3 Water Levels during Site Visit – Aug. 11th–13th, 2010

In order to simulate the precise hydrodynamic conditions present during the August 2010 site visit, the local water level elevations for that month were required. Estimated water levels at Tracadie and Shippagan tidal-stations were obtained from Canadian Hydrographic Services (CHS) tide tables for the entire month of August 2010 and prescribed at the northwest and southwest boundaries of the Telemac2D model. These water levels are shown in Figure 4.15.

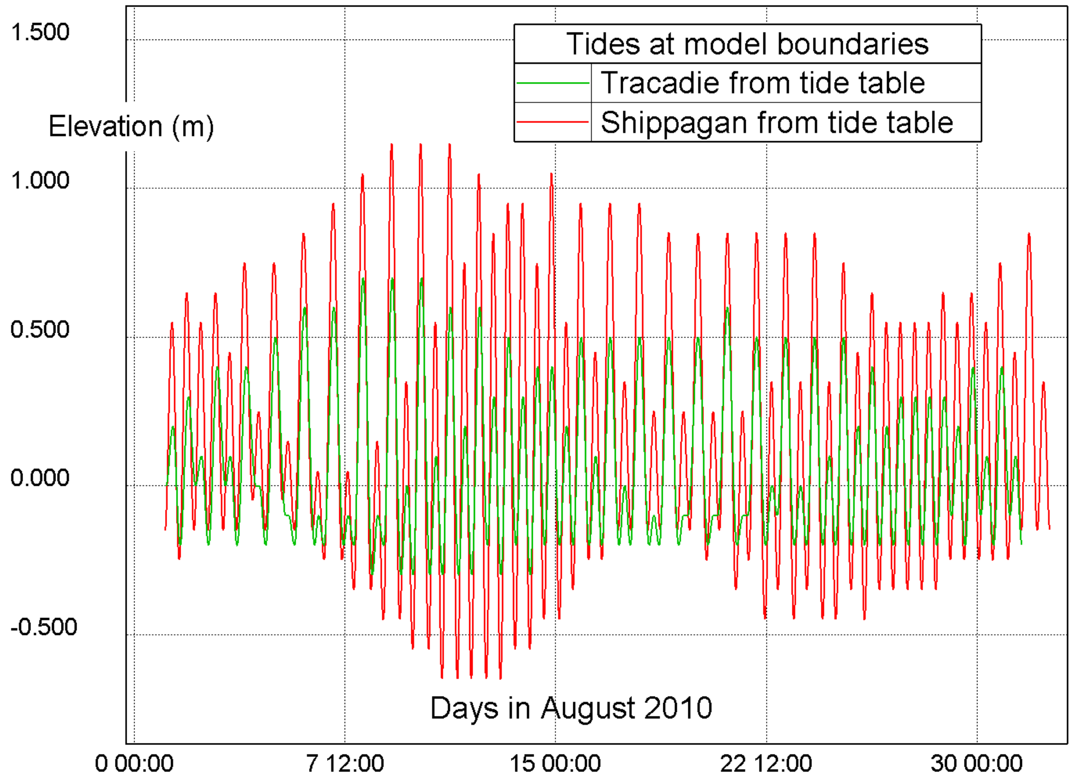

Figure 4.15: Water surface elevations for the month of August 2010, from tide tables, at two of the model boundaries.

The closest tidal station to the northeast boundary was located at Miscou; however tide tables from this station could not be used since they are affected by the tides within the Bay des Chaleurs. Instead, tidal predictions from the WEBTIDE tidal prediction system (developed by researchers with Fisheries and Oceans Canada) were used to assess the difference in water surface elevation and the phase shift between Tracadie and this boundary location (18 km northeast of Shippagan Gully). With this information it was then possible to create a tide signal corresponding to the month of August 2010 for the northeast boundary of the Telemac2D model. This difference in the timing of high and low tides at the southwest and northeast boundaries of the Telemac2D model (44 km apart) is illustrated in Figure 4.16, which shows water level fluctuations for August 12th, 2010 (when current velocity measurements were taken).

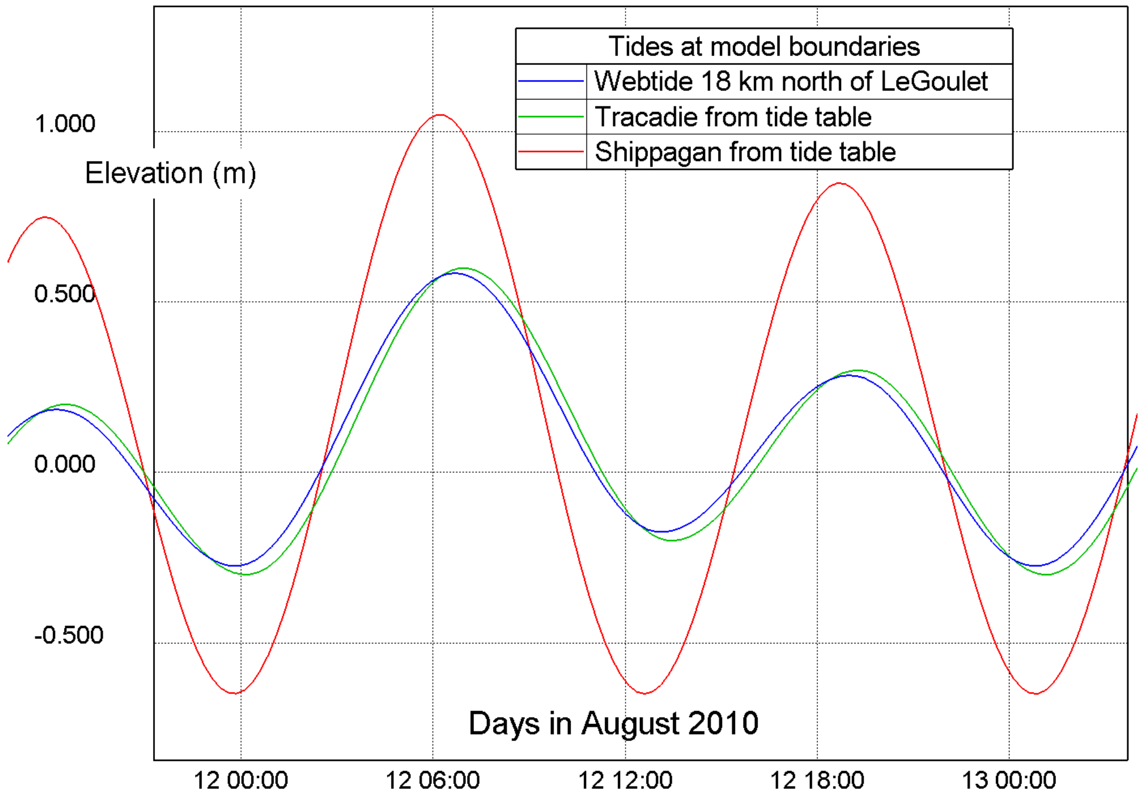

Figure 4.16: Water surface elevations at all three Telemac2D boundary locations for August 12th, 2010.

Figure 4.17 (below) illustrates modeled water level output at three locations; immediately offshore from Shippagan Gully (shown in green), near the centre of the inlet channel (440 m north of the southern limit of the curved breakwater – shown in red) and inside the small craft harbour (shown in blue). Additionally, water levels obtained from a DFO-CHS tide table corresponding to "Shippagan Goulet" are overlaid for the same time period (shown in black). The exact location of this water level prediction is not clearly documented and is therefore unknown. The coordinates associated with the tide table place the prediction on the southern-most quay wall of the small craft harbour; however these coordinates refer to the benchmark and not the actual water level location. Regardless, Figure 4.17 serves as a means by which the modeled water levels can be qualitatively validated against tide table predictions local to Shippagan Gully. Note that all water levels were converted from CD to GD using the corrections provided in Table 4.2.

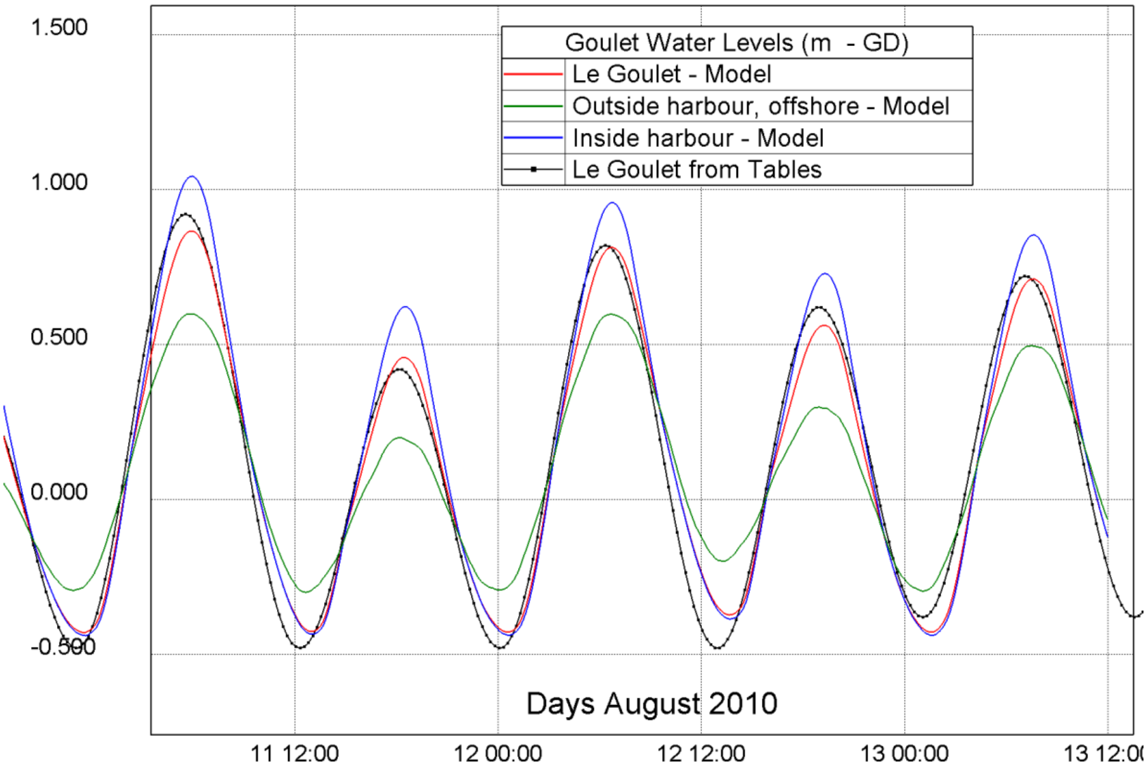

Figure 4.17: Modeled water surface elevations at locations immediately offshore from Shippagan Gully, within the navigation channel and inside the small craft harbour, compared to tide table predictions for "Shippagan Goulet", for which the location of origin is unknown.

From Figure 4.16, the difference in elevation between Shippagan (NW extent of the tidal lagoon) and the Gulf of St-Lawrence (offshore from Shippagan Gully) is clearly visible. It is this difference which drives large currents through the inlet at both high and low tides. The current exits into the Gulf when the water level at Shippagan is highest, while the current reverses and enters the tidal lagoon when the water level at Shippagan is lowest. Maximum currents are observed to occur immediately after the peaks in the tidal signal (high and low). However, due to the phase difference in tidal signals, the ebb and flood flows are not equal in magnitude. In fact, the ebb flow is in general approximately twice as strong as the flood flow, meaning that an asymmetry exists in currents and subsequently sediment transport through the inlet. As such, these coastal inlet processes are weighted heavily in the direction of the Gulf. This unique feature of Shippagan Gully represents an important attribute which is likely to prove crucial to understanding the local sedimentary processes.

The Telemac2D model was calibrated and then used to predict water surface variations at locations much closer to the project site, corresponding to the boundaries of the CMS-Flow morphologic model, which is described in detail in Section 5.0.

4.4.4 Generic Water Levels

In order to perform long term hydrodynamic and morphological simulations at Shippagan Gully (simulations of several years), a simplified representation of tides for a typical year was required. Since using tide tables for this task was not practical, the tide signals were constructed from a numerical model of the St-Lawrence estuary, developed by the Canadian Hydrographic Service (CHS). This model provides 30 tidal constituents over the entire Gulf of St. Lawrence at a 5 km grid spacing.

The locations closest to Tracadie and to the northeast boundary were chosen and the model extent was slightly modified to correspond to these CHS data points. For the Shippagan tide in the Bay des Chaleurs, the closest data point located at 3.4 km from the model boundary was chosen.

Using these 30 tidal constituents, a full year of water level fluctuations was generated at each of the three Telemac2D model boundaries. These records were then analysed to identify the range in amplitude for the spring (maximum 2 m) and neap (minimum 0.5 m) tides. The Telemac2D model was used to obtain corresponding water level fluctuations at the three locations corresponding to the boundaries of the CMS-Flow model. From these new datasets, 14 day periods encompassing the maximum spring and minimum neap tides were identified and combined to produce a set of 28 day water level signals which were considered representative of the tides throughout a typical year. This 28 day tidal cycle is shown in Figure 4.18. These 28 day tidal signals could be repeated to simulate the tidal fluctuations over longer durations.

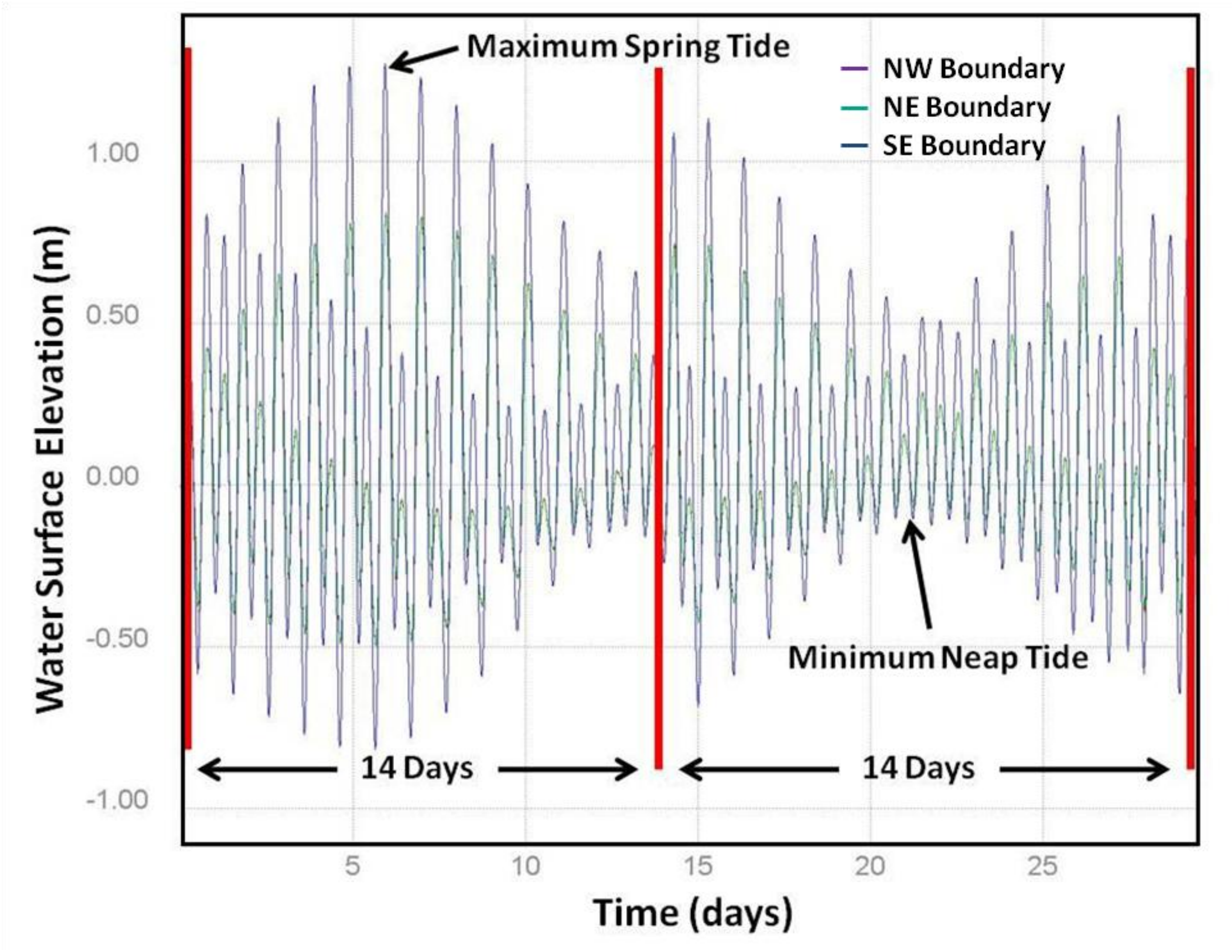

Figure 4.18 Combined generic 14 day tidal cycles at all three CMS-Flow model boundaries.

4.5 Wave Climate Study

Since longshore sediment transport is caused by oblique wave energy dissipation along a shoreline, a comprehensive understanding of the local wave climate is required for any study regarding coastal morphology. As previously discussed, the coastal morphology at Shippagan Gully indicates that there is a strong net longshore transport from northeast to southwest. Therefore it is highly likely that the dominant wave direction is from the east. However, the relative heights, periods and frequency of significant waves at Shippagan Gully were unknown. Good information on the local wave climate was required in order to properly assess the coastal processes, both hydrodynamic and sedimentary, present at Shippagan Gully. Furthermore, a representative data set of wave heights, periods and directions is required for input to any hydrodynamic model in which coastal processes will be studied.

Data from the MSC50 Wave Hindcast Study (Swail *et al*., 2006) was used as the best estimate of historical wave data for the Gulf of St. Lawrence off the coast of the Acadian Peninsula. A wave hindcast is a means by which historical wave data (which is often unknown) can be estimated from historical wind data (which is much more common). The MSC50 Hindcast was commissioned and provided by Environment Canada and is an improvement upon the former AES40 North Atlantic hindcast (Swail *et al*., 2006.). The hindcast provides hourly estimates of significant wave height, peak period and dominant direction as well as wind speed and wind direction at a 0.1 degree resolution across the entire Gulf of St. Lawrence. The hindcast is based on NCEP/NCAR 10-metre wind fields and covers a time period of 54 years from 1954 to 2008 inclusive. The MSC50 hindcast has been calibrated against available buoy data from the Gulf of St. Lawrence and was further validated by NRC-CHC for the present study. A sample plot of MSC50 significant wave height versus available buoy data (buoy number C44153) is presented in Figure 4.19 for a 90 day period in 1995. (The buoy data was obtained from the DFO-ISDM website.) Data in this figure represents the wave climate at a location approximately 90 km to the east of Shippagan Gully (approximate location of the buoy). From Figure 4.19 it can be seen that a reasonable correlation exists between measured and hindcast wave data, thus affirming its quality for use in this study.

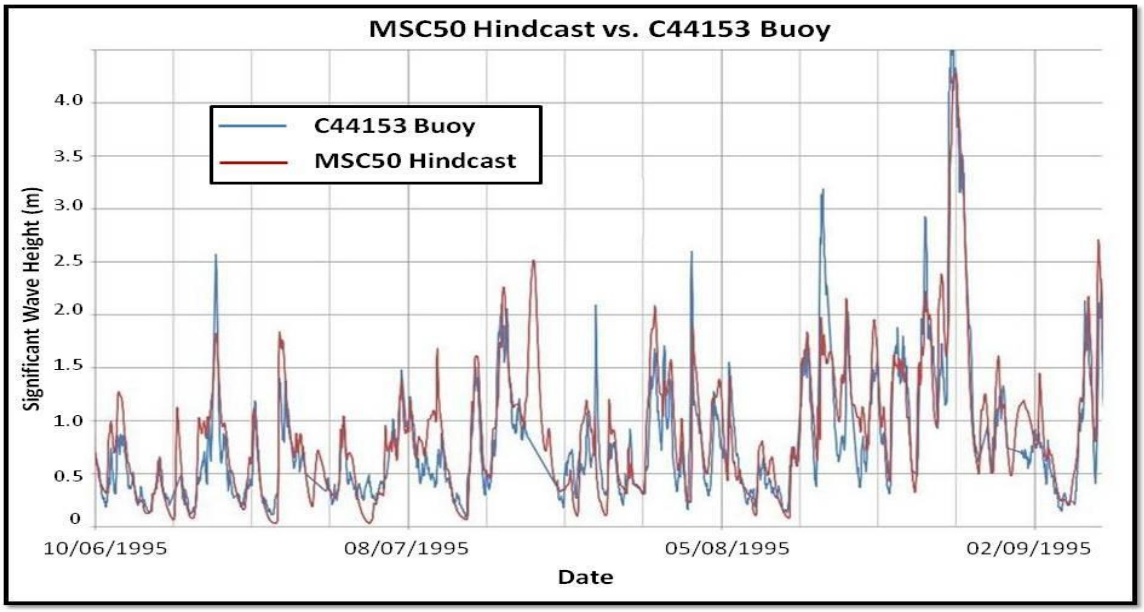

Figure 4.19: Comparison of measured significant wave height (DFO-ISDM buoy data) with MSC50 hindcast significant wave height for a 90 day period in 1995, at a location approximately 90 km east of Shippagan Gully.

4.5.1 Statistical Analysis of Wave Data

After successful validation of the MSC50 hindcast data, all 54 years of hourly data were extracted from the nearest hindcast grid point, located 5 km offshore and immediately to the east of Shippagan Gully at 16 m depth (see Figure 4.20). A detailed statistical analysis of this wave data was then completed. Wave roses were plotted for both significant wave height and peak wave period. A wave rose is a data analysis method in which specified wave parameters are sorted into directional bins and subsequently plotted on a compass, based on their magnitude and relative frequency of occurrence. Figure 4.21 below presents wave roses for both significant wave height and peak wave period for the full 54 years of wave data at the location 5 km offshore from Shippagan Gully. In this figure, the direction of the contour bars represents the direction *to* which the waves are travelling, the radial length of the contour bar represents the relative frequency of waves falling within that directional bin, while the colours represent the magnitude of the specified parameter, in this case significant wave height (left) and peak period (right).

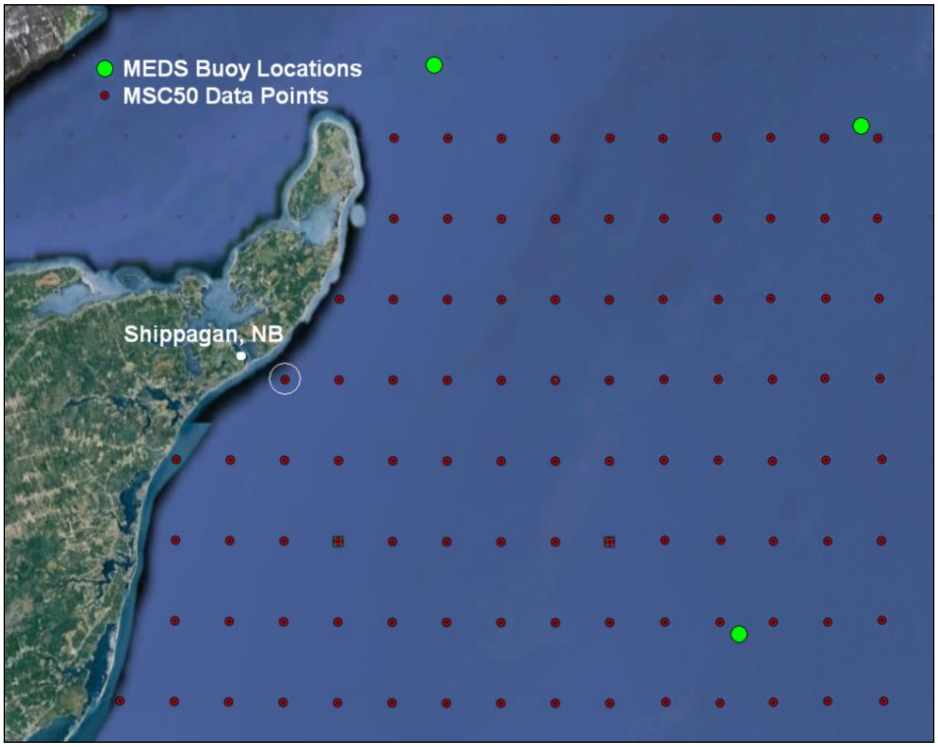

Figure 4.20: Output grid points from MSC50 hindcast covering the Gulf of St. Lawrence at a 0.1 degree resolution. Grid point 5 km offshore from Shippagan Gully is denoted along with three buoy locations from which measured data was obtained for validation.

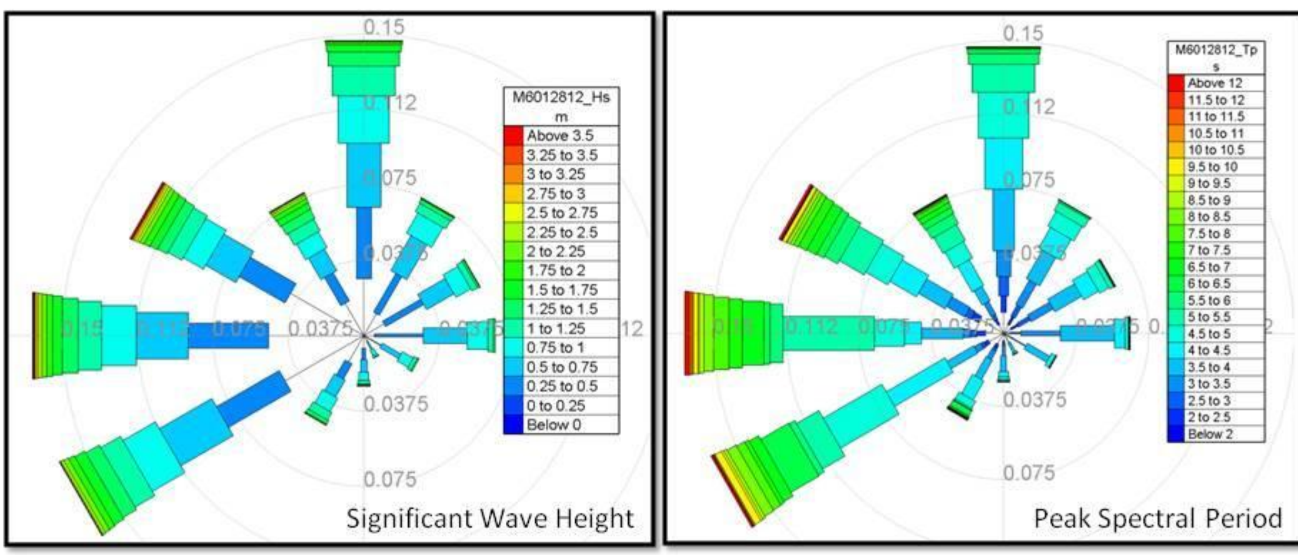

Figure 4.21: Wave roses of significant wave height (left) and peak spectral period (right) at a location 5 km offshore from Shippagan Gully (1954 to 2008). Direction corresponds to the direction of wave propagation.

A number of conclusions can be drawn from the wave roses presented in Figure 4.21. It is apparent that the largest wave heights, largest wave periods (swell waves) and waves with the highest frequency of occurrence generally approach Shippagan Gully from the east (from ESE to ENE), with a significant but smaller frequency of large waves approaching from the South. Five principal directions of wave propagation can be identified from Figure 4.21 for Shippagan Gully:

- 240^0
- 270^0 (waves from east)
- 300^0
- 330^0
- 360^0 (waves from south)

As such, further statistical analysis of wave parameters was limited to these five directional bins. Since waves at this location (5 km offshore) which are travelling in a westerly or southerly direction are travelling away from Shippagan Gully, these directional bins can be ignored.

A great deal of insight can also be obtained from the wave roses with respect to sediment transport, prior to performing any further analyses. With the shoreline in the vicinity of Shippagan Gully oriented at approximately 60^0 due north, waves approaching from the south will create longshore transport from southwest to northeast, as they refract towards the shoreline and break in the sandy nearshore zone. Waves approaching Shippagan Gully from the east on the other hand will drive sediment transport along the coast from northeast to southwest. Since the largest and highest frequency waves are generally found to be approaching from the east (240^0, 270^0 and 300^0), a net longshore transport of sediment can be expected, moving sediment from northeast to southwest, as was indicated in historical engineering drawings and aerial photographs (discussed in Section 4.3).

In order to model the coastal processes at Shippagan Gully using numerical methods, a more detailed statistical analysis of the offshore wave climate was required for each previously selected directional bin. As such, five separate datasets were carried forward for further statistical analysis, corresponding to the 240^0, 270^0, 300^0, 330^0 and 360^0 directional bins. Each directional bin was attributed an overall frequency, representative of the total percentage of waves which travel within the defined direction (bin direction +/- 15^0) through the 54 years of data. Within each bin, two separate analyses were then completed; a full statistical analysis of typical wave conditions (full data set) and an extreme value analysis.

4.5.1.1 Typical Wave Conditions

Data-sets from each of the five predominant directional bins were independently sorted by both period and wave height. Prior to sorting however, the sea and swell components of each data point were separated, thus creating twice the amount of data from which to build the frequency tables. This separation also creates a better representation of the sea and swell components of the wave climate. With these new data sets, a frequency table of significant wave height versus peak wave period was created for each of the five predominant wave directions. A sample table for the 270^0 directional bin is presented in Table 4.3. Frequency tables for the remainder of the directional bins are found in Appendix C. The frequencies within the tables indicate the percentage of time that a wave within that directional bin will have the specified combination of wave height and period. Frequency tables of this nature present a simple means by which to identify common combinations of wave conditions from each predominant direction.

Table 4.3: Frequency table of significant wave heights and peak wave periods for all waves travelling within the 270^0 directional bin, analysed from the 54 years of MSC50 hindcast data at a location 5 km offshore from Shippagan Gully.

Directional Frequency Table

		Hs (m)							
	TOTAL	0 to 1	1 to 2	2 to 3	3 to 4	4 to 5	5 to 6	Total %	Cum. %
Tp (s)	0 to 2	7.54%	0.01%	0.00%	0.01%	0.02%	0.00%	7.58%	7.58%
	2 to 4	18.01%	0.38%	0.00%	0.00%	0.00%	0.00%	18.39%	25.97%
	4 to 6	35.62%	5.09%	0.03%	0.00%	0.00%	0.00%	40.74%	66.72%
	6 to 8	8.52%	9.66%	1.28%	0.02%	0.00%	0.00%	19.47%	86.19%
	8 to 10	2.75%	4.10%	1.92%	0.44%	0.04%	0.00%	9.24%	95.43%
	10 to 12	2.32%	0.11%	0.20%	0.13%	0.02%	0.00%	2.77%	98.20%
	12 to 14	0.98%	0.03%	0.00%	0.00%	0.00%	0.00%	1.02%	99.22%
	14 to 16	0.53%	0.04%	0.00%	0.00%	0.00%	0.00%	0.57%	99.79%
	16 to 18	0.17%	0.01%	0.00%	0.00%	0.00%	0.00%	0.19%	99.98%
	18 to 20	0.02%	0.00%	0.00%	0.00%	0.00%	0.00%	0.02%	99.99%
	20 to 22	0.00%	0.00%	0.00%	0.00%	0.00%	0.00%	0.01%	100.00%
	22 to 24	0.00%	0.00%	0.00%	0.00%	0.00%	0.00%	0.00%	100.00%
	Total %	76.47%	19.43%	3.43%	0.60%	0.08%	0.00%	100.00%	
	Cum. %	76.47%	95.89%	99.33%	99.92%	100.00%	100.00%		100.00%

In this study, the numerical wave propagation model CMS-Wave was used to model the propagation and transformation of waves from the MSC50 grid point (located 5 km offshore) into the coastline at Shippagan Gully. Representative wave conditions which were used in the numerical model were ultimately determined from an analysis of the scatter tables for each directional bin (see Table 4.3). Further details on the wave modeling are presented in Section 5.0.

4.5.1.2 Extreme Value Analysis

A second form of statistical wave analysis, referred to as an extreme value analysis, was completed for each of the 5 dominant directional bins. The purpose of this analysis is to define the magnitude and frequency of large storm events approaching Shippagan Gully within each of the defined directional bins (240^0, 270^0, 300^0, 330^0 and 360^0). To begin this process, the peak-over threshold method is employed, in which a threshold wave height is introduced below which all data points are removed from the analysis. The selection of this threshold is somewhat subjective and is dependent on the relative wave heights featured in the data set. Presently, a threshold of 2 metres was chosen for the MSC50 hindcast data.

The next step in the analysis was to select a minimum event duration and to introduce criterion which separate individual events. A minimum event duration of three hours was chosen (wave heights must remain above the 2 metre threshold for at least three consecutive hours) and events occurring within 24 hours of each other were considered to be the same event. Once the data had been filtered according to these criteria, the peak wave height and period from each storm event were selected as the representative parameters for that event. Additionally, the total duration of each event was determined and added to the dataset.

The final result of these steps was a list of large events (with maximum Hs > 2m) occurring within each directional bin over the 54 years of coverage, each with a representative Hs, Tp and duration. This new dataset is called a storm list. To complete the extreme value analysis, each storm list (one for each direction of wave propagation) is fit to any number of statistical distributions (normal, log-normal, Pearson, Weibull and Gumbel distributions were all applied for the present study) which define their magnitude in terms of a given return period. For the case of the MSC50 hindcast data 5 km offshore from Shippagan Gully, the Weibull statistical distribution produced the highest correlation coefficient and was therefore the best fit for all five directional bins. The end result of this analysis is a statistical plot from which a table of significant wave heights and peak wave periods is extracted, each corresponding to a given return period (an event with a 5 year return period corresponds to an event which statistically occurs once every 5 years). The results of the extreme value analysis for the 240^0, 270^0 and 360^0 directional bins (highest frequency directions) are presented below in Table 4.4. Extreme value analysis results for the remainder of the directional bins are found in Appendix C. For the case of the 270^0 bin, the 50 year storm event (from the east) would statistically feature a significant wave height of 5.1 m and a peak period of 11.3 s (refer to Table 4.4).

Table 4.4: Tables of storm events within the 240^0, 270^0 and 360^0 directional bins, as determined from an extreme value analysis of 54 years of hindcast data at a location 5 km offshore from Shippagan Gully.

240^0 Directional Bin

9.34%

Weibull Distribution

Correlation:	0.994	0.993

Tr	Hs (m)	Tp (s)
1	2.40	9.10
1.5	2.51	9.36
2	2.63	9.58
5	3.01	10.15
10	3.30	10.51
20	3.60	10.83
25	3.70	10.92
50	4.00	11.21
100	4.30	11.47
500	5.01	12.02
1000	5.32	12.23

270^0 Directional Bin

11.04%

Weibull Distribution

Correlation:	0.993	0.990

Tr	Hs (m)	Tp (s)
1	3.20	9.25
1.5	3.32	9.33
2	3.50	9.55
5	4.02	10.16
10	4.37	10.55
20	4.71	10.91
25	4.81	11.01
50	5.12	11.33
100	5.42	11.63
500	6.07	12.26
1000	6.34	12.51

360^0 Directional Bin

9.86%

Weibull Distribution

Correlation:	0.995	0.976

Tr	Hs (m)	Tp (s)
1	2.00	6.20
1.5	2.07	6.38
2	2.18	6.86
5	2.45	7.72
10	2.63	8.20
20	2.80	8.61
25	2.85	8.74
50	3.00	9.10
100	3.15	9.44
500	3.47	10.15
1000	3.61	10.43

With frequency tables and extreme value tables of wave height and wave period defined for a location 5 km offshore of Shippagan Gully, both typical (high frequency, low magnitude) wave conditions and rare (low frequency, high magnitude) storm conditions can be selected for input into the nearshore numerical model and desktop sediment transport calculations. Typical (high frequency) wave conditions may drive slow but steady morphologic change over the long term, while storm waves may create large changes in coastal morphology over short durations and at infrequent intervals. Both types of processes are likely to be important at Shippagan Gully.

4.6 Assessment of Longshore Sediment Transport

With the offshore wave climate characterized, the numerical model CMS-Wave (USACE) was used to transform the waves from their input location, 5 km offshore, to the shoreline in the vicinity of Shippagan Gully. CMS-Wave is a phase-averaged spectral wave model, which accounts for the major shallow water wave transformation mechanisms, including refraction, shoaling and breaking. CMS-Wave will be discussed further in Section 5.0.

Starting from a bathymetric grid interpolated from the 2010 bathymetric survey data described in Section 4.4, the most common offshore (daily) wave parameters from each directional bin (as determined in Section 4.5 above) were input into the numerical wave model (CMS-Wave) and propagated to the shoreline. The nearshore (transformed) wave parameters were then outputted at their breaking point and at three separate locations approximately 250 metres apart in the longshore direction. Two separate longshore sediment transport formulas were then used at each of the three locations in order to determine the rate of longshore sediment transport created by the breaking waves and more importantly the direction in which the transported sediment moves. The results from each of the three locations were then averaged to produce an estimated *potential* longshore transport rate for the representative 750 metres of coastline subjected to typical wave conditions from each of the five directional bins.

Two well known longshore transport formulas were employed in this preliminary analysis of potential transport rates near Shippagan Gully, both of which were presented in detail in Section 2.3.1.5. For convenience, both formulations are repeated below in Equations 29 - 32. The first and best known equation for estimating bulk sediment transport rate, Q_s, is published in CERC (1984), and can be written as:

$$Q_{s=} \frac{I_s}{(\rho_s - \rho)(1-n)g} \tag{29}$$

where:

$$I_s = 0.39 P_{asb} \tag{30}$$

$$P_{asb} = \frac{1}{16} \frac{\rho g^{3/2}}{\gamma_{sb}^{1/2}} H_{sb}^{5/2} sin2\alpha_b \tag{31}$$

The CERC formula takes into account the effects of sediment density (ρ_s), water density (ρ), sediment porosity (n), significant breaking wave height (H_{sb}), breaking wave depth (d_b) and breaking wave angle relative to the shoreline (α_b).

The second formula was developed and published by Kamphuis (1991) and is presented below as Equation 32. This formula was developed based on small-scale hydraulic model tests and was found to be valid for available field data (Kamphuis, 1991). As an addition to the CERC formula parameters, the Kamphuis formula includes the effects of wave period (T_{op}), beach slope (m_b) and mean sediment grain diameter (D). As such, it is likely the more accurate formula for use with a highly variable wave climate propagating over a very shallow beach slope, as is the case for Shippagan Gully.

$$Q_k = 6.4 \times 10^4 H_{sb}^2 T_{op}^{1.5} m_b^{0.75} D^{-0.25} sin^{0.6} 2\alpha_b \tag{32}$$

It is important to note that both of the applied sediment transport formulas produce theoretical *potential* longshore sediment transport rates. This assumes that there is an infinite amount of sediment available for transport along an infinitely long beach. Of course this is not necessarily the case in coastal regions and thus a distinction must be made between the *potential* transport rate and the *actual* transport rate.

By applying the two previously described longshore sediment transport equations with the breaking wave parameters predicted by the numerical wave model CMS-Wave, *potential* longshore sediment transport rates were determined under typical wave conditions from each of the five principal wave directions. A frequency factor was then applied to each calculated transport rate based on the relative frequency of waves travelling within each directional bin. The net sediment transport rate and direction is then calculated by summing the weighted transport rates from each of the five directions of wave propagation.

The process was repeated using storm waves from each of the directional bins. Breaking wave parameters (determined from simulations of nearshore wave propagation conducted with the numerical model CMS-Wave) corresponding to the yearly event, the bi-yearly event and the 5-year event for each of the five dominant wave directions were added to the analysis. An artificial year was then created by summing the yearly transport rates due to five one-year events, two and a half two-year events and one five year event, and subsequently dividing the result by five. This value was then added to the previously calculated yearly transport rate due to typical wave conditions in order to produce an estimation of the gross and net (*potential*) longshore sediment transport rates due to a combination of typical and storm-induced waves. The resulting annual net transport rate predicted using the CERC formula is 2036 m^3/yr, while the Kamphuis formula gives a potential transport rate of 2658 m^3/yr, both from northeast to southwest. The result of this analysis thus supports the presence of net longshore sediment transport from northeast to southwest at Shippagan Gully, as was interpreted from the aerial photographs and historical changes in coastal morphology. A summary table of calculated values for gross and net transport rates is presented in Table 4.5 below.

Table 4.5: Calculation of gross and net *potential* longshore sediment transport rates near Shippagan Gully.

						GROSS Potential - 5 Years		GROSS Potential - 1 Year	
Direction (°)	Return Period (yrs)	CERC (m^3/hr)	Kamphuis (m^3/hr)	Duration (hrs)	Mult Fact (5yr)	CERC (m^3)	Kamphuis (m^3)	CERC (m^3)	Kamphuis (m^3)
240	Daily	12	1	818.184	5	49091	4091	9818	818
	1	233	23	10	5	11650	1150	2330	230
	2	305	28	10	2.5	7625	700	1525	140
	5	465	44	10	1	4653	440	931	88
270	Daily	29	2	967.104	5	140230	9671	28046	1934
	1	572	45	10	5	28600	2267	5720	453
	2	738	55	10	2.5	18450	1375	3690	275
	5	1133	87	10	1	11330	867	2266	173
300	Daily	7	1	770.004	5	26950	3850	5390	770
	1	355	35	10	5	17767	1733	3553	347
	2	494	44	10	2.5	12350	1100	2470	220
	5	759	69	10	1	7590	690	1518	138
330	Daily	-21	-1	649.992	5	-68249	-3250	-13650	-650
	1	-77	-11	10	5	-3867	-533	-773	-107
	2	-97	-13	10	2.5	-2417	-325	-483	-65
	5	-112	-17	10	1	-1123	-167	-225	-33
360	Daily	-55	-2	863.763	5	-237535	-8638	-47507	-1728
	1	-148	-10	10	5	-7383	-483	-1477	-97
	2	-175	-12	10	2.5	-4367	-308	-873	-62
	5	-226	-18	10	1	-2257	-183	-451	-37
							NET Potential Transport Rate (m^3/yr) =	2036	2658

5.0 Numerical Modeling

5.1 Hydrodynamic Modeling

The numerical models CMS-Flow and CMS-Wave were used in the present study to simulate tidal inlet and nearshore hydrodynamics, sediment transport and morphology change at Shippagan Gully. Both models are developed by the United States Army Corps of Engineers (USACE) under the Coastal Inlets Research Program (CIRP) and have therefore been developed for the primary purpose of modeling coastal inlet hydrodynamics and morphology. A brief description of both models is provided herein.

5.1.1 CMS-Flow

CMS-Flow is a two-dimensional, finite-volume, depth-averaged circulation model. It performs hydrodynamic calculations over a variable size, finite difference (rectangular) grid by solving the two-dimensional depth-integrated continuity and momentum equations for water motion, where velocity components are calculated in two horizontal directions. The hydrodynamic calculations are performed at a user specified interval and for each grid cell in the numerical model domain. The two-dimensional depth-averaged continuity and momentum equations are written as follows:

$$\frac{\partial(h+\eta)}{\partial t}+\frac{\partial q_x}{\partial x}+\frac{\partial q_y}{\partial y}=0 \tag{33}$$

$$\frac{\partial q_x}{\partial t}+\frac{\partial u q_x}{\partial x}+\frac{\partial v q_x}{\partial y}+\frac{1}{2}g\frac{\partial(h+\eta)^2}{\partial x}=\frac{\partial}{\partial x}D_x\frac{\partial q_x}{\partial x}+\frac{\partial}{\partial y}D_y\frac{\partial q_x}{\partial y}-f q_x-\tau_{bx}+\tau_{wx}+\tau_{Sx} \tag{34}$$

$$\frac{\partial q_y}{\partial t}+\frac{\partial u q_y}{\partial x}+\frac{\partial v q_y}{\partial y}+\frac{1}{2}g\frac{\partial(h+\eta)^2}{\partial y}=\frac{\partial}{\partial x}D_x\frac{\partial q_y}{\partial x}+\frac{\partial}{\partial y}D_y\frac{\partial q_y}{\partial y}-f q_y-\tau_{by}+\tau_{wy}+\tau_{Sy} \tag{35}$$

where:

h = still-water depth relative to a specific vertical datum

η = deviation of the water-surface elevation from the still-water level

t = time

q_x = flow per unit width parallel to the x-axis

q_y = flow per unit width parallel to the y-axis

u = depth-averaged current velocity parallel to the x-axis

v = depth-averaged current velocity parallel to the y-axis

g = acceleration due to gravity

D_x = diffusion coefficient for the x direction

D_y = diffusion coefficient for the y direction

f = Coriolis parameter

τ_{bx} = bottom stress parallel to the x-axis

τ_{by} = bottom stress parallel to the y-axis

τ_{wx} = surface stress parallel to the x-axis

τ_{wy}= surface stress parallel to the y-axis

τ_{Sx} = wave stress parallel to the x-axis

τ_{Sy} = wave stress parallel to the y-axis

Component velocities u and v in Equations 34 and 35 are related to the flow rate per unit width as follows:

$$u = \frac{q_x}{h + \eta} \tag{36}$$

$$v = \frac{q_y}{h + \eta} \tag{37}$$

Circulation induced shear stresses (independent of waves) are then given by:

$$\tau_{bx} = C_b u |U| \tag{38}$$

$$\tau_{by} = C_b v |U| \tag{39}$$

where U = total current speed and C_b = empirical bottom-stress (friction) coefficient. The total current speed is the resultant of the two-dimensional current components and is therefore given by:

$$|U| = \sqrt{u^2 + v^2} \tag{40}$$

The bottom-stress (friction) is a key parameter in hydrodynamic numerical model calibration. It is this parameter which is adjusted in order to properly calibrate the numerical model to measured or observed data (discussed in Section 5.1.5). The bottom-stress coefficient is calculated by:

$$C_b = \frac{g}{C^2} \tag{41}$$

where C = Chezy coefficient, which is given by:

$$C = \frac{R^{1/6}}{n} \tag{42}$$

in which R = hydraulic radius and n = Manning's roughness coefficient.

In the presence of waves, a different approximation is used for the calculation of the bottom-shear stresses based on the work of Nishimura (1988). The approximation is based on a time-averaged bottom stress under combined currents and waves, and although computationally demanding, the formulation is much more efficient then explicitly calculating the values at every grid point and for each time step. Supplemental information regarding the calculation of wave induced bottom stresses in CMS-Flow is found in Nishimura (1988).

Surface stresses included in Equations 34 and 35 are a result of the wind blowing over the water surface and are calculated as follows:

$$\tau_{wx} = C_d \frac{\rho_a}{\rho_w} W^2 \sin \Theta \tag{43}$$

$$\tau_{wy} = C_d \frac{\rho_a}{\rho_w} W^2 \cos \Theta \tag{44}$$

where:

C_d = wind drag coefficient

ρ_a = density of air

ρ_w = density of water

W = wind speed

Θ = wind direction

Finally, wave stresses are calculated from spatial gradients in radiation stresses as:

$$\tau_{Sx} = -\frac{1}{\rho_w}\left(\frac{\partial S_{xx}}{\partial x} + \frac{\partial S_{xy}}{\partial y}\right) \tag{45}$$

$$\tau_{Sy} = -\frac{1}{\rho_w}\left(\frac{\partial S_{xy}}{\partial x} + \frac{\partial S_{yy}}{\partial y}\right) \tag{46}$$

where S_{xx}, S_{xy} and S_{yy} are wave-driven radiation stresses, which were previously discussed in Section 2.2.2.3. In CMS-Flow these values are passed to the model from a spectral wave model, which for this study is the numerical model CMS-Wave (discussed below) (Buttolph *et al*., 2006).

Hydrodynamic input to the numerical model is in the form of water surface elevations at each of the specified *open* model boundaries. There are two possible formats in which the boundary conditions can be applied, the first being as a series of tidal constituents. Tidal constituents were discussed in detail in Section 2.2.1.1. The second available format for inputting boundary conditions to CMS-Flow is as a simple time series of water levels. This is the format that was used for the present study as boundary conditions for the CMS-Flow model were in time series format as taken from the regional Telemac2D model (refer to Section 4.4).

For supplemental information regarding the hydrodynamic model CMS-Flow, Buttolph *et al*., (2006) should be consulted and can be found in Section 8.0.

5.1.2 CMS-Wave

CMS-Wave is a two-dimensional spectral wave model which calculates wave propagation and transformations through the nearshore zone. It simulates the steady-state spectral transformation of directional random waves, co-existing with ambient currents in the coastal zone. The model is applicable for the propagation of random waves over complicated bathymetry, as it accounts for all major nearshore transformations, including refraction, diffraction, reflection, shoaling and breaking. The model operates on a half-plane numerical propagation scheme, thereby implying that waves can only propagate from the seaward boundary towards the shore, within a 180^0 directional envelope (ie. waves cannot travel backwards) (Lin, *et al*., 2008).

CMS-Wave is formulated from a parabolic approximation equation with energy dissipation and diffraction terms. This formulation is referred to as the wave-action balance equation, first presented by Mase (2001), and is written as follows:

$$\frac{\partial(C_x N)}{\partial x} + \frac{\partial(C_y N)}{\partial y} + \frac{\partial(C_\theta N)}{\partial \theta} = \frac{\kappa}{2\sigma}\left[\left(CC_g cos^2\theta N_y\right)_y - \frac{CC_g}{2}cos^2\theta N_{yy}\right] - \varepsilon_b N - S \tag{47}$$

where:

$$N = \frac{E(\sigma,\theta)}{\sigma} \tag{48}$$

Where N is the wave-action density to be solved and is a function of frequency (σ) and direction (θ), and C is the characteristic velocity. κ in Equation 47 is the wave diffraction term, which is formulated from a parabolic approximation wave theory (Mase, 2001). For $\kappa = 0$, the model omits all diffraction effects. Conversely, for $\kappa = 4$ (maximum value), strong diffraction will be incorporated in the wave-action balance equation. The selected value for κ is dependent on the ratio of the wave length to the length of structures and specific structural layout characteristics. For example, to simulate wave diffraction at an extremely long breakwater or through a very narrow gap where the wavelength is greater than the gap opening, maximum diffraction ($\kappa = 4$) should be selected. A maximum value of 4 was chosen for simulations at Shippagan Gully, based on the relative distance across the channel mouth (approximately 160 m) and the maximum observed wave length (approximately 220 m).

CMS-Wave operates on a finite-difference, variable size grid, in the same manner as CMS-Flow. This allows for higher resolution to be achieved at points of specific computational interest (ie. inside Shippagan Gully), while larger cells are maintained throughout the remainder of the domain. This greatly improves the computation speed of the model.

CMS-Wave has the ability to account for interactions between the waves and currents, where the characteristic velocities C_x, C_y and C_θ from Equation 47 can be expressed as:

$$C_x = C_g cos\theta + U \tag{49}$$

$$C_y = C_g sin\theta + V \tag{50}$$

$$C_\theta = \frac{\sigma}{sinh2kh}\left(sin\theta\frac{\partial h}{\partial x} - cos\theta\frac{\partial h}{\partial y}\right) + cos\theta sin\theta\frac{\partial U}{\partial x} - cos^2\theta\frac{\partial U}{\partial y} + sin^2\theta\frac{\partial V}{\partial x} - sin\theta cos\theta\frac{\partial V}{\partial y} \tag{51}$$

where U and V are the depth-averaged horizontal current velocity components along the x and y axes, k is the wave number and h is the water depth.

Additional wave transformations which are not explicitly included in the wave-action balance equation include wave reflection, which is approximated in CMS-Wave as:

$$N_r = K_r^2 N_i \tag{52}$$

where K_r is a reflection coefficient (0 for no reflection, 1 for full reflection) which is defined as the ratio of reflected to incident wave height (Dean and Dalrymple, 2002).

Wave breaking is approximated in CMS-Wave by a number of available (user selected) formulations. Available formulations include Miche (1951), Goda (1970), Battjes and Janssen (1978) and Chawla and Kirby (2002). Detailed information regarding each of the above listed breaking formulations can be found in the respective references, or in Lin *et al*. (2008). For the present study, the formulation of Goda (1970) was employed due to its relative stability and extensive history of application.

Bottom friction loss is calculated in CMS-Wave by applying a drag law model which was first described by Collins, (1972). This model can be written as follows:

$$S_{ds} = -c_f \frac{\sigma^2}{g} \frac{\langle u_b \rangle}{g sinh^2 kh} N \tag{53}$$

where:

$$\langle u_b \rangle = \frac{1}{2} \sqrt{\frac{g}{h} E_{total}} \tag{54}$$

where u_b is the mean horizontal wave orbital velocity at the sea bed, E_{total} is the total energy density at a given grid cell and c_f is the Darcy-Weisbach friction coefficient, which is related to Manning's friction coefficient as follows:

$$c_f = \frac{g n^2}{h^{1/3}} \tag{55}$$

As was discussed in the previous section, the governing equations in CMS-Flow (Equations 34 and 35) rely on wave-induced radiation stresses which are passed from CMS-Wave. Radiation stress calculation within CMS-Wave is therefore completed by using linear wave theory, where S_{xx}, S_{xy} and S_{yy} are expressed as follows:

$$S_{xx} = E(\sigma, \theta) \int \left[n_k (cos^2\theta + 1) - \frac{1}{2} \right] d\theta \tag{56}$$

$$S_{xy} = E(\sigma, \theta) \int \left[n_k (sin^2\theta + 1) - \frac{1}{2} \right] d\theta \tag{57}$$

$$S_{yy} = \frac{E}{2} n_k sin2\theta \tag{58}$$

where:

$$n_k = \frac{1}{2} + \frac{kh}{sinhkh} \tag{59}$$

Spectral wave input to CMS-Flow is in the form of a series of wave data, including significant wave height (H_s), peak spectral period (T_p), wave direction and directional spreading. The individual wave cases are input in series, although these series do not necessarily carry a time component. The concept of time is only introduced when coupling the models CMS-Flow and CMS-Wave, where the user specified steering interval becomes the time step between individual wave cases. Otherwise, CMS-Wave results are simply given as individual phase-averaged (non-transient) cases containing no element of time. Inputted wave data is applied at the offshore model boundary and propagated towards the shoreline from the direction(s) specified in the input file.

5.1.3 Supplementary Software

The hydrodynamic and wave models were coupled together through the use of a steering model, which permits the models to share calculated information at a user specified interval. By coupling the two models in this manner, wave propagation and transformation calculations (CMS-Wave) account for variable water levels and updated bed morphology which are calculated by CMS-Flow. Conversely, wave induced currents (in the form of radiation stresses) are passed from CMS-Wave to CMS-Flow. Currents used in the sediment transport calculations performed by CMS-Flow are therefore the combined effect of tide-induced and wave-induced circulation (Militello *et al*. 2003). This method of coupling the two models is ideal for modeling a highly dynamic coastal inlet such as Shippagan Gully, where complex interactions between tide induced currents and nearshore waves are likely to influence local sediment transport patterns.

For this study the numerical models and steering module were accessed via the Surface Water Modeling System (SMS). The SMS is a user friendly interface which allows for simple creation and updating of model grids, supporting data sets and boundary conditions, while simultaneously providing a tool through which the models can be run and the results visualized. Further information on the SMS interface is found online at Aquaveo.com

NRC-CHC`s spatial data analysis software BlueKenue (CHC-NRC, 2011) was additionally used as a supplemental analysis tool for the present study. BlueKenue is a tool with which spatial and transient data sets can be created, viewed, managed and analyzed. For the present study the BlueKenue software was enhanced such that it was able to interpret SMS output files, which are in HDF5 file format. BlueKenue was used primarily for the interpolation and analysis of channel cross-sections and graphical representations of water level and bed level time-series which are presented herein.

5.1.4 Numerical Model Set-Up

The CMS-Wave model grid was set-up such that it extended approximately 5 km offshore from Shippagan Gully and 2 km inside of the tidal lagoon. The offshore boundary of the computational domain traversed the location where the offshore wave climate was determined from analysis of the MSC50 hindcast dataset (see Section 4.5). This allowed the representative wave conditions developed in Section 4.5 (both typical and storm waves) to be input directly at the offshore boundary of the CMS-Wave model. In the longshore direction, the CMS-Wave model domain extended 6 km to the southwest of Shippagan Gully, and 8 km to the northeast, up the Gulf coast. The grid was oriented such that the offshore boundary was approximately parallel to the 16 m depth contour. Cell sizes were variable, ranging from 80 m at the offshore and longshore boundaries, to 10 m over the ebb-shoal and within Shippagan Gully. The CMS-Wave model domain is shown in Figure 5.1.

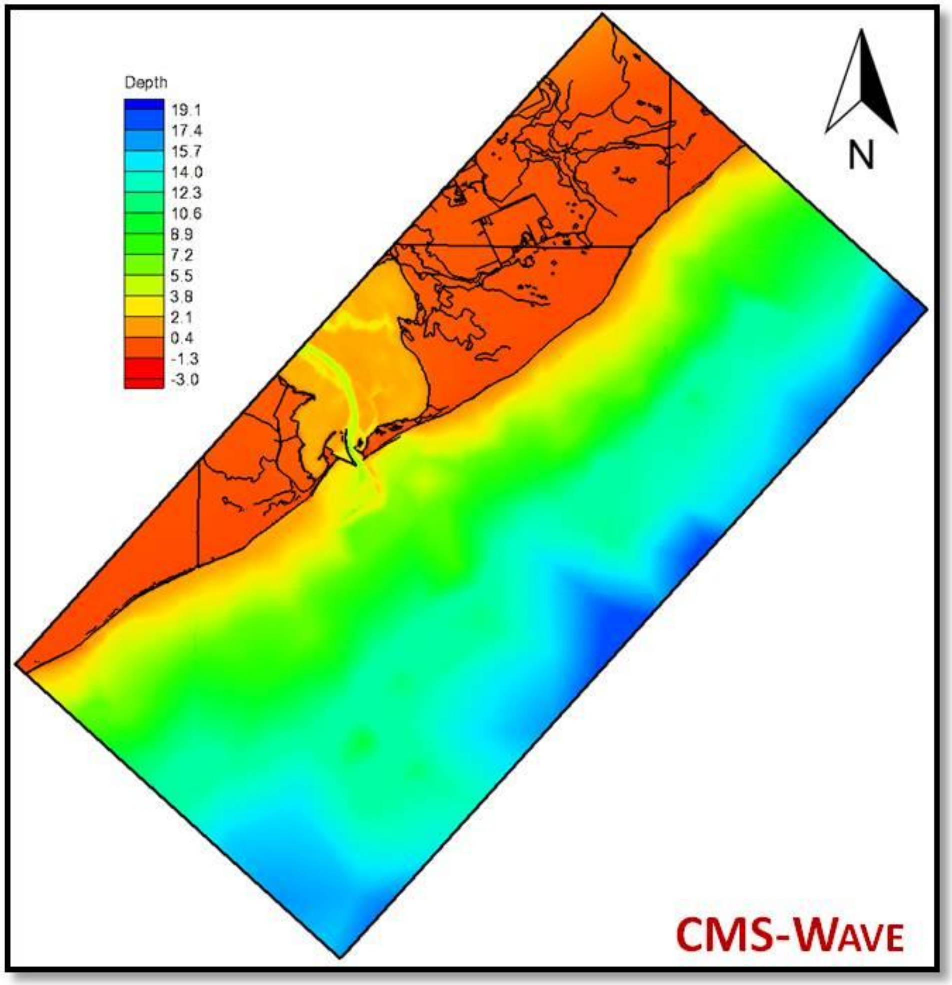

Figure 5.1: CMS-Wave numerical model domain, stretching 5 km offshore from Shippagan Gully and covering 14 km of the Gulf coast.

The CMS-Flow model domain was set-up such that it covered the entire tidal lagoon, all the way to the bridge at Shippagan, and stretched offshore to a distance of approximately 3 km and a depth of 12 m. This extent was deemed to be far enough from the shoreline such that the longshore currents induce by tidal flow through the inlet and breaking waves in the nearshore zone would be negligible at the offshore boundary. In the longshore direction the CMS-Flow grid covered 6 km of coastline with Shippagan Gully at its approximate centre, thus providing ample shoreline to either side of the inlet for the calculation of longshore sediment transport. The CMS-Flow model had three model boundaries where water level fluctuations were specified. The boundaries were defined as the northwest limit of the tidal lagoon (250 m northwest of the bridge at Shippagan) and each of the longshore limits of the numerical model (the northeast and southwest boundaries of the model domain). The offshore (southeast) boundary of the numerical model was set to be a closed boundary. This forced currents to travel in the longshore direction, thus re-creating the tide-induced longshore current which has been shown to exist around the Gulf of St-Lawrence. The CMS-Flow grid cell sizes ranged from 80 m at the offshore boundary to 10 m within Shippagan Gully and the immediate nearshore area. The CMS-Flow model domain is shown in Figure 5.2.

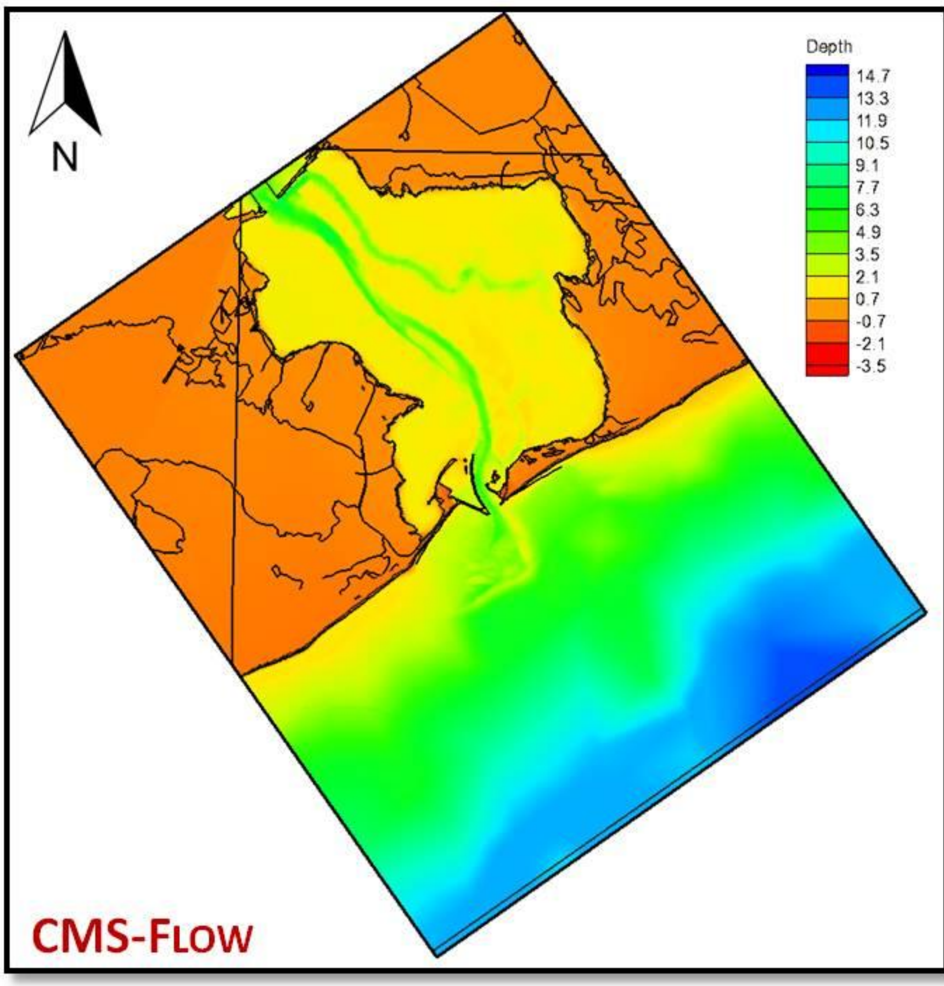

Figure 5.2: CMS-Flow numerical model domain, stretching 3 km offshore from Shippagan Gully and covering 6 km of the Gulf coast.

5.1.4.1 Boundary Conditions

For the CMS-Wave model, boundary conditions were specified along the offshore boundary in the form of a series of two-dimensional wave spectra. Short term simulations with constant wave conditions were run in some cases. In other cases, where long term simulations were conducted, the wave conditions were varied with time (through the use of the steering module) in a manner which replicated, in a statistical sense, the average wave climate offshore from Shippagan Gully. Based on the analysis described in Section 4.5 above, a year-long synthetic time history of wave conditions was constructed to represent the average wave climate at the offshore model boundary. The synthetic wave time history included both normal and extreme wave conditions approaching from the five pre-defined directions of importance. Calm periods (without waves) were also included. The synthetic wave time history honoured, in a statistical sense, the occurrence frequency of daily waves and storm waves (monthly and annual events) from each principle direction and for each month of the year. The year- long synthetic time history of wave conditions was repeated as necessary, depending on the simulation duration. Table 5.1 below shows the statistically accurate representation of hourly wave conditions throughout the year-long synthetic wave climate, as derived from the wave climate analysis described in Section 4.5.

Table 5.1: Table of statistical hourly wave conditions (daily, monthly and yearly conditions) for the year-long synthetic wave time history. Entries represent the number of hours in which each specified wave condition is represented in the calendar year.

		January	February	March	April	May	June	July	August	September	October	November	December	Totals
	CALM	416	416	416	416	416	416	416	416	416	416	416	388	4964
Daily	240	48	60	60	60	60	60	60	60	48	48	48	48	660
	270	60	72	72	72	72	72	72	72	60	60	60	60	804
	300	48	48	48	60	60	60	48	48	48	48	48	48	612
	330	36	36	36	48	48	48	48	48	36	36	36	36	492
	360	60	60	60	60	60	60	60	60	60	60	60	48	708
Monthly	240	8	8	8	8	8	8	8	8	8	8	8	8	96
	270	8	8	8	8	8	8	8	8	8	8	8	8	96
	300	8	8	8	8	8	8	8	8	8	8	8	8	96
	330	8	8	8	8	8	8	8	8	8	8	8	8	96
	360	8	8	8	8	8	8	8	8	8	8	8	8	96
Yearly	240	0	0	0	0	0	0	0	0	0	0	0	8	8
	270	0	0	0	0	0	0	0	0	0	0	0	8	8
	300	0	0	0	0	0	0	0	0	0	0	0	8	8
	330	0	0	0	0	0	0	0	0	0	0	0	8	8
	360	0	0	0	0	0	0	0	0	0	0	0	8	8
	Hours	708	732	732	756	756	756	744	744	708	708	708	708	8760
	Days	29.5	30.5	30.5	31.5	31.5	31.5	31	31	29.5	29.5	29.5	29.5	

As discussed in Section 5.1.4, the CMS-Flow model was driven using three different water level time histories, one for each water boundary of the model domain. (No water levels were prescribed along the offshore boundary.) For all long term numerical simulations, the synthetic 28-day water level time histories discussed in Section 4.4 and plotted in Figure 4.18 were used and repeated as often as necessary. This set of water level time series included both the maximum spring and minimum neap tides that occur in a typical year. Since this time series repeated itself every 28 days, it could easily be extended to cover any desired simulation duration.

5.1.5 Hydrodynamic Calibration

The hydrodynamic model (CMS-Flow) was calibrated so that it was able to replicate the flow conditions (levels and current speeds) observed during the August 2010 field investigation with good accuracy. The calibration involved making small adjustments to the friction factor used in the model in order to minimize the differences between the model's predictions and the observations made during the site visit.

Current velocity measurements were taken in the inlet during both ebb and flood tides using an electromagnetic current meter. The global position of each measurement was documented using GPS and the times at which the measurements were taken were noted. Velocities were measured at various depths (documented) as well as on the surface. Velocities measured below the water line were estimated to be representative of the depth-averaged velocity while an empirical coefficient of 0.85 was applied to estimate depth-averaged velocity from the surface velocity measurements (based upon several published empirical values).

The numerical model was run using 2010 bathymetry and estimated water levels from August 11th to August 13th, 2010 (dates of the field investigation). 2010 bathymetric survey data was available for the entire navigation channel, tidal lagoon, small craft harbour and nearshore region. Additionally, topographic data of the sediment deposition zone within Shippagan Gully was available. As such, the only artificial bathymetry required for the 2010 model grid was top of bank elevations along the coastline and throughout the tidal lagoon to mitigate unwanted flooding in the numerical model. Smooth bathymetric grids were then interpolated using the SMS interface for use in both the CMS-Flow and CMS-Wave simulations.

The numerical model was run without any input from waves. As such, CMS-Flow was run independent of CMS-Wave for the hydrodynamic calibration of the model. Depth averaged velocities were output from the numerical model at the closest grid points to the current velocity measurement locations and at times corresponding to the time at which the measurements were taken. Measured and modeled depth-averaged velocities were then compared for both the ebb and flood tides. A mean statistical error from all measured data points was then calculated in order to assess the accuracy of the hydrodynamic numerical model.

In order to calibrate the model, adjustments to the friction coefficients were made. The friction coefficient is a spatially variable factor which quantifies the drag on the water due to the roughness of the seabed. For example, water flowing through vegetated tidal flats or over large cobble would encounter much higher frictional resistance than water flowing over a smooth sandy bed. As such, spatially variable friction coefficients can be adjusted to either increase or decrease the resistance encountered by flow and subsequently the velocity at which the water will propagate. Adjustments were therefore made to the spatially variable friction in the numerical model, re-assessing the mean statistical error between measured and modeled velocities after each adjustment. This process was repeated until an acceptable agreement was reached between the numerical model and the measured current velocity data. It was determined by sensitivity analysis that the timing of flow (and more importantly the timing at which the currents reversed) through Shippagan Gully was controlled by the friction coefficient at the northern limit of the model domain (near the bridge at Shippagan). Conversely the current velocity through Shippagan Gully was generally controlled by the local friction in the inlet.

The final mean statistical error achieved in the hydrodynamic calibration of the numerical model was +0.03 m/s (RMS error = 0.18 m/s). This means that the model predicts current velocities that are, on average, 0.03 m/s too fast. This statistical error was deemed acceptable as it represents a deviation of less than 2% from maximum observed current velocities in Shippagan Gully (approximately 2.0 m/s). A complete table of hydrodynamic calibration results can be found in Appendix D.

5.2 Sediment Transport Modeling

In addition to calculating hydrodynamics, CMS-Flow has several integrated representations for the computation of sediment transport, thus making it a morphological numerical model in addition to being a hydrodynamic model. Sediment transport in CMS-Flow can be calculated using the three following transport rate formulations:

- Watanabe (1987) total load formulation,
- Lund-CIRP (Camenen and Larsen, 2005, 2006) total load formulation (combined suspended and bed load), and
- Advection-diffusion (AD) transport for suspended load, coupled with either the van Rijn (1998) or the Lund-CIRP formulation for bed load. The AD equation applies the reference concentration and sediment diffusivity from either the van Rijn or Lund-CIRP formulation as a user option (Buttolph *et al*., 2006).

All of the above listed equations, with the exception of the Lund-CIRP formulation were previously described in Section 2.3.1. As such, they will not be repeated herein. The Lund-CIRP formulation however was ultimately chosen as the formulation for the present study, in combination with the AD equation for suspended load. The reason for choosing the Lund-CIRP and AD combined formulation is that it is a direct result of recent research into sediment transport at tidal inlets due to the combined effects of waves and currents (Camenen and Larsen, 2007). Furthermore, the Lund-CIRP and AD combined formulation was specifically tailored to function in the CMS-Flow environment and is therefore the most stable of the available formulations. For this reason it is the default formulation in CMS-Flow.

The Lund-CIRP formulation for calculating bed-load is written as follows (Camenen and Larsen, 2005):

$$\frac{q_{bw}}{\sqrt{(s-1)gd_{50}^3}} = a_w\sqrt{\theta_{net}\theta_{cw,m}}exp\left(-b\frac{\theta_{cr}}{\theta_{cw}}\right) \tag{60}$$

$$\frac{q_{bn}}{\sqrt{(s-1)gd_{50}^3}} = a_n\sqrt{\theta_{cn}\theta_{cw,m}}exp\left(-b\frac{\theta_{cr}}{\theta_{cw}}\right) \tag{61}$$

where subscripts w and n refer to the wave direction and the direction normal to the waves, respectively, a and b are coefficients and $\theta_{cw,m}$ and θ_{cw} are the mean and maximum Shields parameters for waves and currents combined, respectively. For a more detailed description of the calculation of Equations 60 and 61, Camenen and Larsen (2007) should be consulted.

Suspended load in the numerical model was calculated as per the advection-diffusion equation (which was presented in detail in Section 2.3.1), with input from the Lund-CIRP formulation for suspended load. Using the Lund-CIRP – AD combined formulation, the pick-up and deposition rates (P and D in Equation 22) are influenced by reference concentrations determined from the Lund-CIRP formulation for suspended load, which is written as follows:

$$q_s = U_c c_R \frac{\varepsilon}{\omega_s}\left(1 - exp\left(-\frac{w_f d}{\varepsilon}\right)\right) \tag{62}$$

where the reference concentration c_R is given by:

$$c_R = A_{cR}\theta_{cw,m}exp\left(-b\frac{\theta_{cr}}{\theta_{cw}}\right) \tag{63}$$

where A_{cR} is a coefficient determined from the following relationship:

$$A_{cR} = 3.5\text{x}10^{-3}\text{exp}\,(-0.3d_*) \tag{64}$$

where d_* is a non-dimensionalized grain size. Further information regarding the calculation of the Lund-CIRP formulation for suspended load and the combined Lund-CIRP – AD formulation can be found in Camenen and Larsen (2006) and in Buttolph *et al*. (2006).

In addition to calculating sediment transport, CMS-Flow calculates morphology (bed level change) through the application of the sediment continuity equation. This equation is written as follows:

$$\frac{\partial h}{\partial t} = \frac{1}{1-p}\left(\frac{\partial q_{bx}}{\partial x} + \frac{\partial q_{by}}{\partial y} + P - D\right) \tag{65}$$

where p is the sediment porosity and P and D are the pick-up and deposition rates respectively.

Bed morphology is calculated in CMS-Flow at a user specified time-step. This time-step is independent of the time-step used in the hydrodynamic and sediment transport calculations. Since morphology is generally a long-term process, it is common practice to employ a rather large time-step, of the order of days or even months. For the present study however a time-step of 30 minutes was selected, such that the morphology associated with individual tides could be properly assessed.

In order to simulate long-term morphological changes, CMS-Flow has the capability of incorporating a *morphologic acceleration factor* into the numerical model simulations. This multiplication factor is applied to the morphological change calculated at each time step, thus accelerating the rate at which the changes occur. As such, a one month simulation with a morphological acceleration factor of 12 would result in one year of morphological time, thus greatly reducing the time required for a one year simulation (USACE, 2011). This tool can of course only be used with confidence if the numerical model input is idealized and/or repetitive data. For example, to simulate a full year of morphology change using only one month of hydrodynamic simulation time, a statistically correct year of wave spectra would also have to be condensed into the single month of hydrodynamic computation.

For the present study, results using morphological acceleration factors of up to 16 were compared to results from simulations covering the same time scale without any morphological acceleration. The results proved to be highly similar, with only minimal changes occurring to sediment deposition and erosion patterns (of the order of centimetres). As such, morphological acceleration factors of up to 16 were used in the long-term numerical model simulations in order to reduce the required computational time.

5.2.1 Sediment Transport Calibration

Following the successful hydrodynamic calibration of the numerical model, a morphologic calibration was performed in order to ensure that the coupled model was capable of reproducing the historical morphologic evolution observed at Shippagan Gully. Not surprisingly, optimizing the model's ability to simulate morphology change at this complex and dynamic site proved to be far more challenging and time-consuming than calibrating the hydrodynamics alone. It should be noted that all water levels and bottom elevations referred to hereafter are presented as metres above or below the Geodetic Datum (as per Table 4.2).

Hydrodynamic conditions, particularly flow velocities, are highly variable at Shippagan Gully, both temporally and spatially. As such, it is very likely that the sediment found at Shippagan Gully is well sorted, and thus spatially variable. Although no appropriate field data is available to verify this hypothesis, zones with high velocity flows, such as the narrow sections of navigation channel near the inlet mouth, are likely to be naturally armoured with much larger bed material then that which is present in low velocity zones such as throughout the rest of the tidal lagoon. Furthermore, wave dominated areas (the shoreline and the ebb shoal) are likely to posses different sediment characteristics than tide dominated areas (tidal lagoon). As such, several overlapping zones with highly variable sediment properties are likely present at Shippagan Gully.

In order to successfully model the sedimentary processes and observed morphologic changes at the site, the spatially varying bed material must be represented within CMS-Flow. CMS-Flow has the ability to account for variable grain size by allowing the user to create a variable d_{50} (mean sediment diameter) bed. This dataset is consulted in sediment transport calculations when determining the local hiding/exposure coefficient, which directly influences the calculated value for critical shear stress and subsequently the requirement for incipient sediment motion (USACE, 2011). As such, the spatial hydrodynamic requirements necessary for the occurrence of bed erosion can be controlled by adjusting the spatially variable d_{50} dataset.

Once the threshold for incipient motion is reached for a given location in the numerical model domain, sediment becomes mobile and is subsequently transported as either bed load or suspended load. Unfortunately the present version of CMS-Flow is unable to employ multiple transport calculations for each grain size throughout the model domain. As such, a global transport value must be specified, which is applied to all transported sediment, regardless of its location of origin within the model domain (USACE, 2011). Two approaches must therefore be taken when calibrating sediment transport in CMS-Flow. The spatially variable d_{50} dataset must be adjusted in order to reproduce natural armouring of high velocity regions while allowing incipient motion to exist where required. Simultaneously, the global transport value must be adjusted in order to control the rates of sediment transport and deposition.

It was determined experimentally that adjustments made to the d_{50} bed dataset were effective in altering the spatial deposition and erosion patterns throughout the model domain, while changes to the global transport value have a stronger influence on the rate at which these patterns progress. These two parameters however are not entirely independent, since transported sediment assumes the local bed value once it is deposited. As such, an iterative approach was taken in calibrating the sediment transport and morphology change at Shippagan Gully. First, the spatially variable d_{50} bed dataset was adjusted until the numerical model was able to approximately reproduce the general erosion and deposition patterns observed over a two year period. Once this spatial calibration was deemed satisfactory, the global transport grain size was adjusted in order to alter the rate at which the morphological changes progressed. Historical channel cross-sections were consulted during this process, with the goal of this temporal calibration being to approximately match the navigation channel's rate of westerly migration. The spatial and temporal approaches to morphologic calibration were performed iteratively in an attempt to reproduce both deposition patterns and deposition rates, based on the available historical data.

5.2.1.1 Variable Bed Dataset Adjustments

The numerical model was first run using 1992 channel bathymetry and a constant grain size corresponding to the mean diameter determined from the sediment sample analysis (d_{50}=0.45 mm). 1992 was selected as the starting point for the morphological calibration for two reasons. Firstly, the earliest available bathymetric survey data for the navigation channel is from 1992. Secondly, no major changes to coastal structures were observed in the years immediately following 1992, nor were there any dredging activities in the inlet. As such, morphologic changes at Shippagan Gully occurring in the mid 1990's were natural and uninterrupted. The drawback to using 1992 bathymetry as a starting point is that there is no available data for bathymetry outside of the navigation channel. As such, 2010 tidal lagoon and offshore bathymetry were used, with topography for the deposition area on the east side of the channel estimated from a 1987 aerial photograph. Each of these bathymetric data sets were combined and interpolated to create an artificial 1992 bathymetry for use in the numerical model. Boundary conditions for the morphological calibration included the synthetic time history of wave spectra described in Section 4.5, which approximated the local wave climate, and the repeating 28 day synthetic tidal cycle described in Section 4.4, which approximated the variability in the tidal forcing.

From the preliminary numerical model results obtained using a constant grain size throughout the model domain (d_{50}=0.45 mm), three critical zones were identified each with different d_{50} requirements. These three zones are shown in Figure 5.3 overlaid on a 1987 aerial photograph and are labelled zone A, zone B and zone C. Zone A, which covers the navigation channel as it passes through Shippagan Gully, experienced substantial erosion for constant grain size simulations due to the strong ebb-tide currents. As such, a much larger value for the bed grain size was required in this region, particularly near the inlet mouth, in order to counteract the erosive forces and replicate the natural armouring of the bed which is hypothesised to exist in this region. Zone B covers the area of sediment deposition within the inlet, to the east of the navigation channel. The mean bed grain size in this region must be small enough such that the sediment is mobile, yet large enough such that accumulation of sediment is favoured as opposed to erosion. Zone C is the most complicated of the three zones as it is nourished primarily by longshore sediment transport (littoral drift) which arrives from the northeast (discussed further in Section 6.1). At this location the d_{50} must be such that littoral drift is either deposited at the inlet mouth or moved along the ebb shoal depending on the relative magnitude of the waves. Furthermore, sediment deposited at the inlet mouth must be small enough to be transported offshore to the ebb shoal by the strong ebb-tide flows, and thus not over-constrict flow entering and exiting Shippagan Gully.

Transitions between the three zones must be progressive and smooth, in order to avoid abrupt artificial changes in sediment transport patterns and morphologic change. The transition between zones A and C is particularly important as erosion must be limited in zone A where the ebb flow reaches high velocities, while accretion must be limited in zone C where longshore transport is deposited in significant volumes. This transition is further complicated due to the fact that its location is highly variable, dependent on the direction and magnitude of incoming waves and longshore currents.

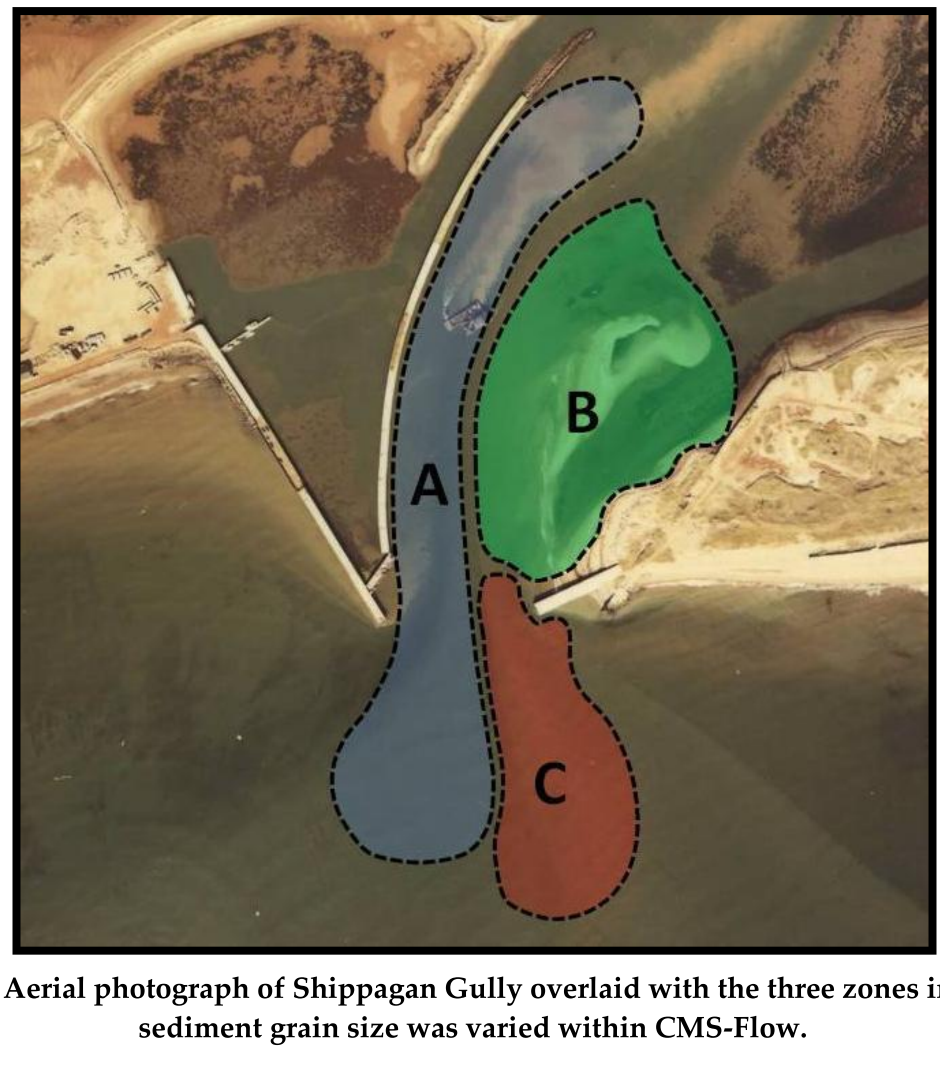

Figure 5.3: Aerial photograph of Shippagan Gully overlaid with the three zones in which the sediment grain size was varied within CMS-Flow.

After numerous variable bed d_{50} datasets were tested for two year simulations starting from the 1992 channel bathymetry, appropriate d_{50} ranges were identified for the three zones outlined in Figure 5.3. The relative water depth in Zone A is historically shown to remain approximately constant since channel cross-sections were first documented in 1992. This zone was therefore determined to require a bed grain size (d_{50}) of 7.0 to 15.0 mm in order to prevent the navigation channel from eroding and becoming deeper. Zone B was determined to require a mean bed grain size of 2.0 to 7.0 mm in order to promote the accretion of sediment on the east side of the navigation channel. Zone C was determined to require a relatively small bed grain size (d_{50}) of less than 2.0 mm in order to allow sediment deposited here by littoral drift to be carried to the ebb shoal during the strong ebb-tide flows, thus respecting the historical depths at this location. Figure 5.4 shows an example of the poor results that were obtained when a bed d_{50} value exceeding 2.0 mm was specified in zone C. In this case, the model predicted excessive accretion in zone C, which served to further constrict flow through the inlet mouth, subsequently increasing velocities and altering the d_{50} requirements in zone A. It is important to note that this behaviour occurs due to the fact that in the numerical model, sediment (once deposited) assumes the d_{50} value given in the spatially variable bed d_{50} dataset. If this value is too large, deposited sediments will not be re-mobilized once high flows resume (on the next large ebb flow). Figure 5.5 shows an example of the spatially variable bed grain size map developed through the calibration process.

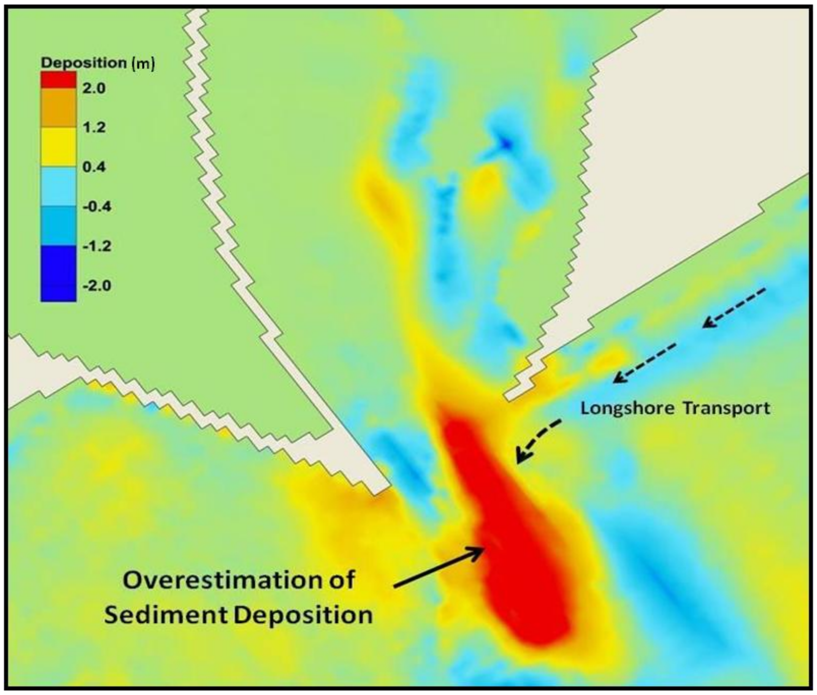

Figure 5.4: Example erosion/deposition map from numerical simulations in which spatial variation of the bed d_{50} dataset leads to excessive deposition at the inlet mouth.

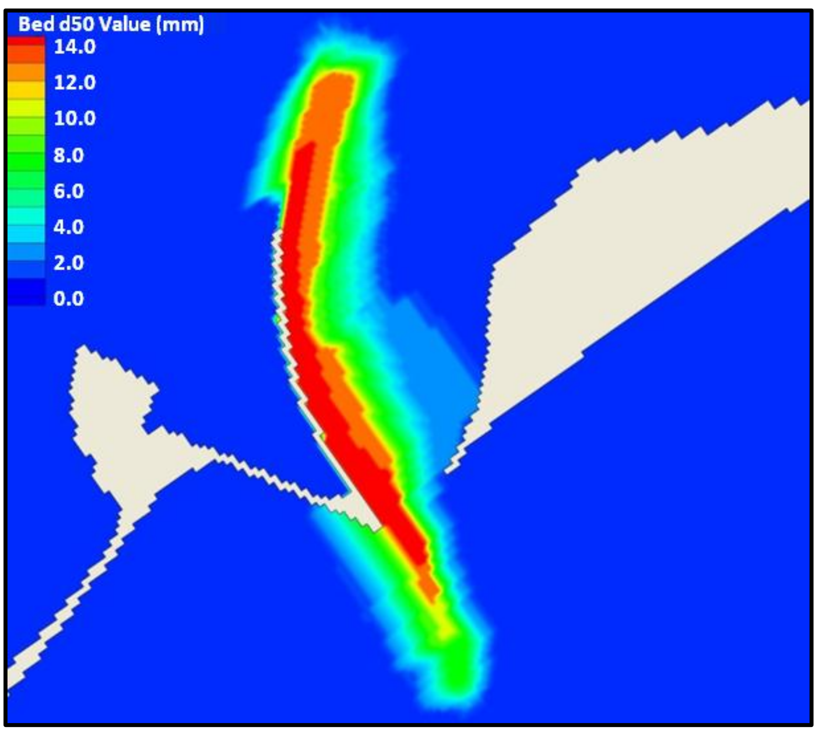

Figure 5.5: Sample variable bed d_{50} dataset used in CMS-Flow.

Numerical model results obtained using the bed d_{50} dataset shown in Figure 5.5 are presented below in Figure 5.6 and Figure 5.8. Figure 5.6 shows modeled bathymetric contours at Shippagan Gully at the beginning (1992 channel bathymetry) and at the end of a two year simulation. Figure 5.8 is an erosion/deposition map showing changes in bed elevation (positive represents deposition) over the course of the two-year simulation. The erosion/deposition map is obtained by subtracting the bed surface at the start of the simulation from the surface at the end of the simulation. Figure 5.7 illustrates the same erosion/deposition map for *measured* bathymetry; however it has been produced from 7 years of morphology (1992 to 1999) (measured erosion/deposition maps throughout the 1990's are presented in Appendix E). Finally, Figure 5.9 shows aerial photographs taken in 1987 and 1996 denoted with major deposition patterns which occurred throughout this time period.

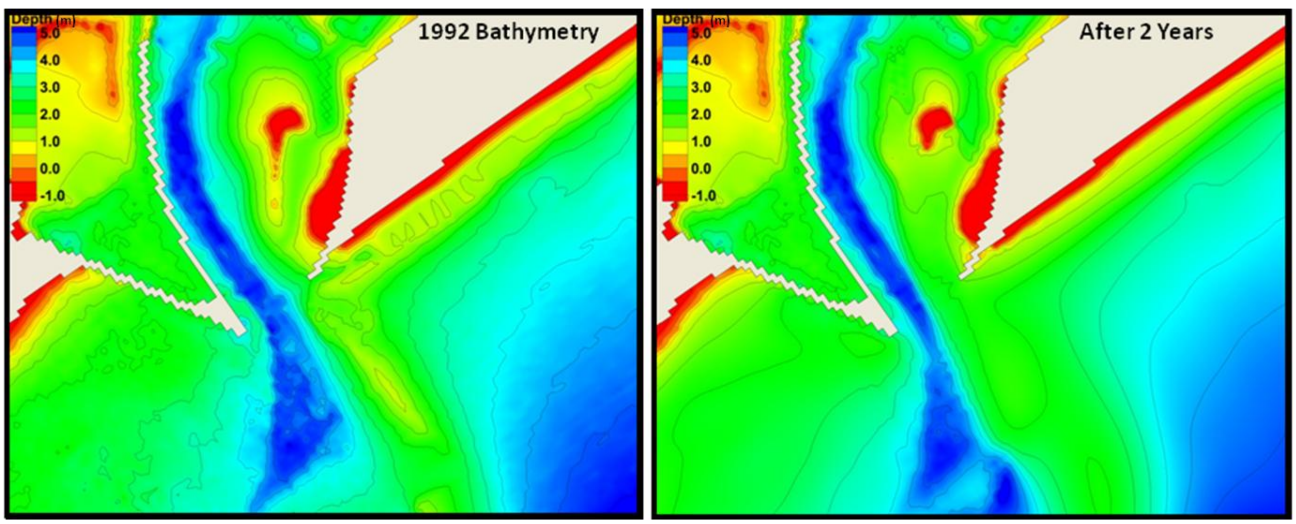

Figure 5.6: Bathymetry before and after a 2 year simulation. Note westward migration of navigation channel and smoothing of ebb-shoal. Navigation channel depths remain approximately constant.

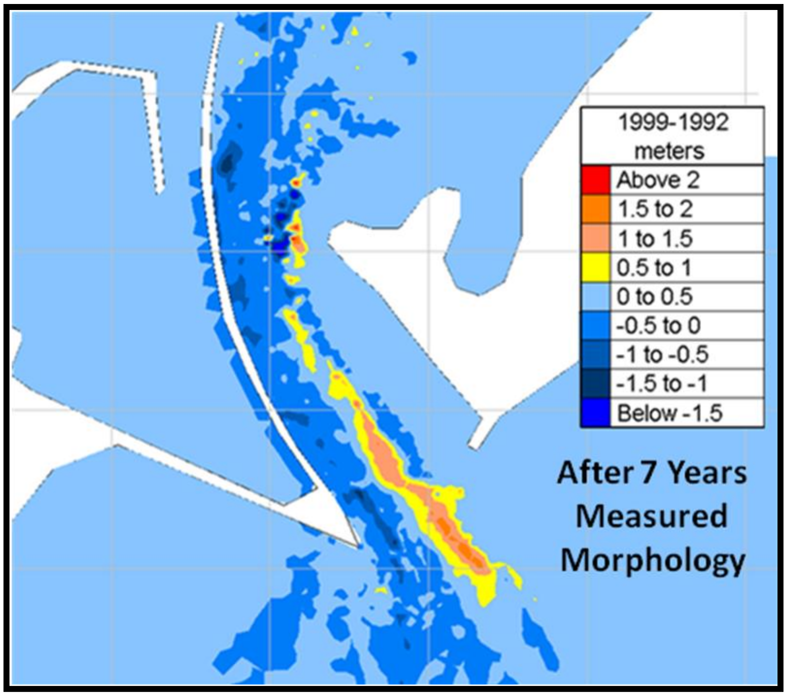

Figure 5.7: Deposition/erosion map after seven years of measured morphology. Note deposition within inlet on eastern edge of navigation channel.

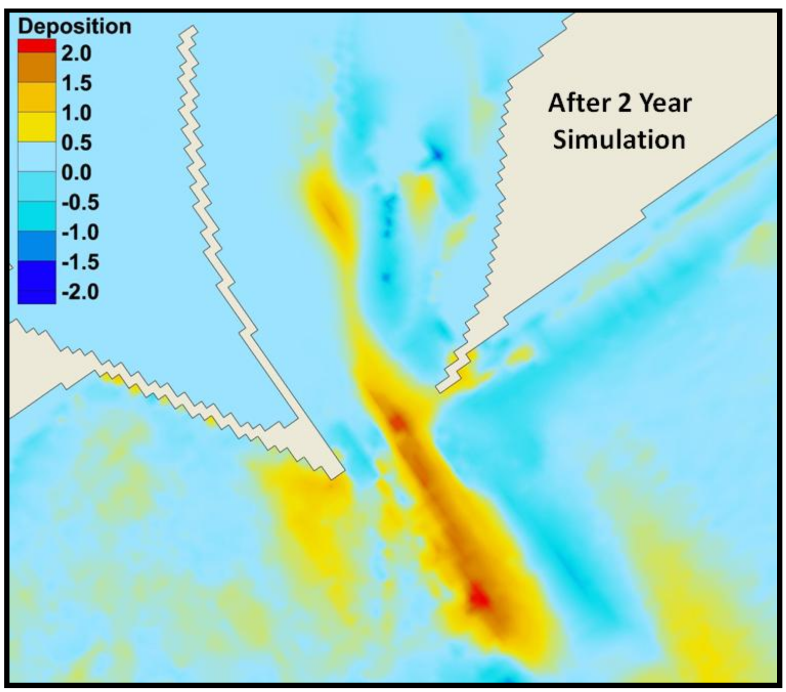

Figure 5.8: Deposition/erosion map after two year simulation, showing deposition within inlet on eastern edge of navigation channel and modest accretion in Zone C, immediately offshore from the inlet mouth.

Based on the results presented in Figure 5.6 and Figure 5.8, it is apparent that the westerly migration of the navigation channel observed in Shippagan Gully can be successfully simulated using a spatially variable bed d_{50} dataset. In comparing Figure 5.7 with Figure 5.8, it can be seen that observed erosion and deposition patterns are generally well simulated by the numerical model. The rate of deposition however appears to be accelerated in places by the numerical model as the observed deposition illustrated in Figure 5.7 is over a 7 year period compared to the 2 years of simulated morphology shown in Figure 5.8. This topic is addressed in Section 5.2.1.2 below. Finally, comparing Figure 5.8 and Figure 5.9, it can be seen that the spatially calibrated numerical model is able to simulate deposition in the primary deposition zone identified in Figure 5.9 (1996).

Figure 5.9: Aerial photographs from 1987 and 1996 showing deposition patterns within Shippagan Gully. Observed primary deposition zone corresponds well to modeled deposition shown in Figure 5.8.

5.2.1.2 Global Transport Grain Size Adjustments

Although discussed separately in this thesis, the global transport grain size was adjusted iteratively with the variable bed d_{50} dataset in an attempt to simulate observed deposition rates at Shippagan Gully. It was determined that the global transport grain size value has a very strong influence on the rate at which morphologic change occurs. This is due to the fact that for the same hydrodynamic conditions, the rate of sediment transport is a strong function of the sediment grain size. Larger sediment particles are harder to mobilize and more likely to be deposited while smaller sediment particles are easier to mobilize and tend to travel further before settling. As such, the pace of morphologic change is observed to increase with decreasing global transport grain size, and vice versa. There is however a limit to the realistic increase in global transport values, as once the value is increased enough, particles will only be transported very short distances before being deposited, thus resulting in an under-representation of the sediment transport patterns observed at Shippagan Gully.

Six years of modeled navigation channel migration (starting from 1992 channel bathymetry with intact east jetty) obtained using a global transport grain size of 2.0 mm is illustrated in Figure 5.10 at a channel cross-section located at the inlet mouth. Here the modeled cross-sections are compared to measured historical cross-sections taken from 1992 to 1998. It can be seen from this comparison that the numerical model is effective in reproducing the westward migration of the navigation channel, with a good representation of sediment accumulation on the east (right) bank and slight erosion on the west (left) bank. Furthermore, the rate at which these morphological changes progress is reproduced reasonably well by using a global transport grain size of 2.0 mm, as both the observed and modeled maximum channel migration over the 6 year period is approximately 20 m (at -4 m elevation).

It should be noted that simulating the sedimentary processes and long-term morphological changes at Shippagan Gully is an extremely challenging task. Our ability to model these processes with high precision is limited by many factors, including: the complexity of the processes at the site; a lack of data pertaining to bed grain sizes and other parameters, the limited capabilities of the best-available modeling tools and the many underlying simplifications and assumptions. Hence, it is unreasonable to expect the model to be able to reproduce the sedimentary processes and the morphological changes precisely. For example, representing such a complex site with a single global transport value is a gross oversimplification of reality, since in nature, a large range of sediment sizes are likely to be mobile at Shippagan Gully due to the highly variable spatial and temporal hydrodynamics which have been shown to exist. Given this reality, the model was judged to be adequately well calibrated when it was able to reproduce the main trends in morphology change, such as the sediment accumulation on the eastern side of the main channel and the westward migration of the main channel. Hence the results presented in Figure 5.6 - Figure 5.10 indicate that the model was successfully calibrated for predicting trends in morphological change starting from the 1992 bathymetry.

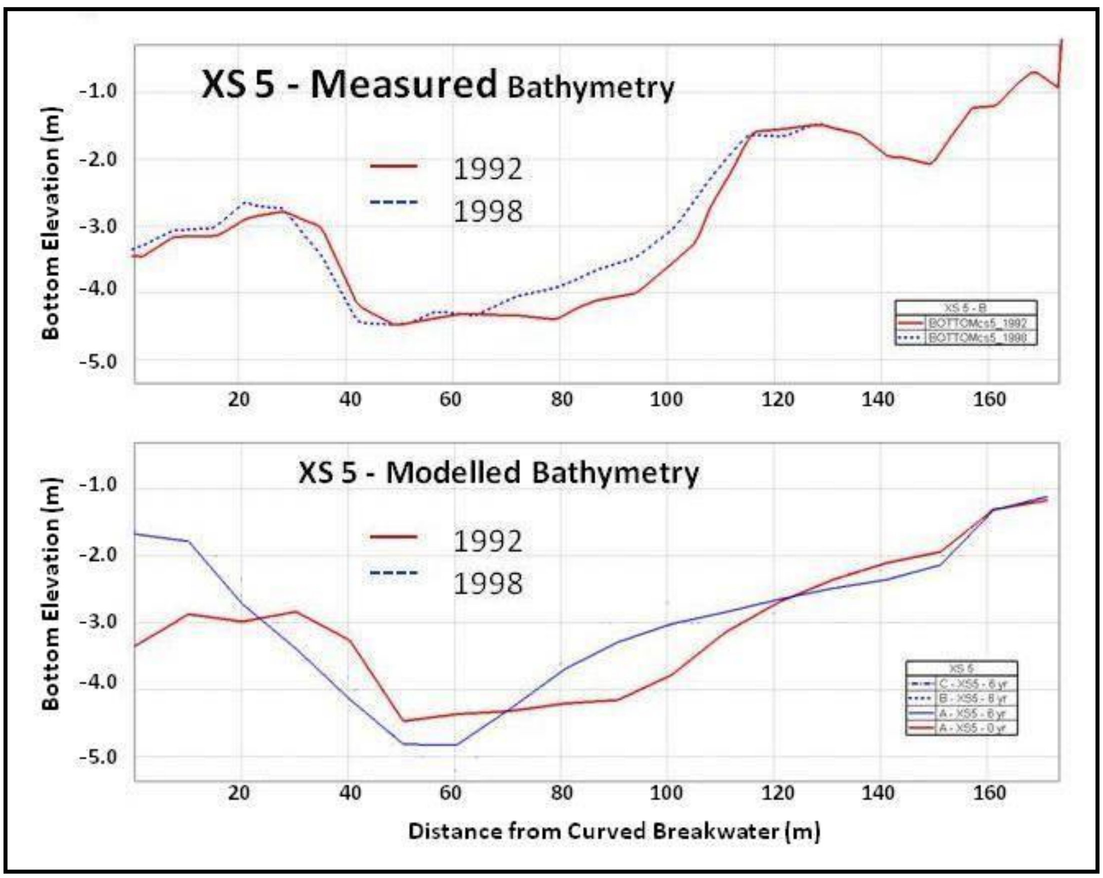

Figure 5.10: Modeled westerly migration of navigation channel (bottom) compared to measured channel migration (top) at the inlet mouth.

5.2.1.3 2010 Variable Bed Dataset Adjustments

With the numerical model successfully calibrated to the 1992 bathymetry with respect to morphology change, a variable bed grain size (d_{50}) map had to be created for future simulations which would be based upon the current 2010 bathymetry. The ranges in sediment size which were identified in Section 5.2.1.1 were deemed to hold true for the 2010 bathymetry, however the spatial distribution of the sediment sizes was altered to account for differences in the bathymetry and in the hydrodynamics between 1992 and 2010. As such, the optimized spatial bed grain size dataset for the 1992 bathymetry was adjusted such that the sediment size contours approximately matched the velocity magnitude contours in Shippagan Gully, during a peak ebb-flow event and over the 2010 bathymetry (simulated). This meant that the largest sediment sizes determined from the 1992 calibration were applied in areas where the 2010 ebb-flows were strongest. The optimized variable bed grain size map which was ultimately used in all numerical simulations starting with the 2010 bathymetry is presented in Figure 5.11 below. For comparison, the optimized bed grain size map for the 1992 bathymetry is presented in Figure 5.5.

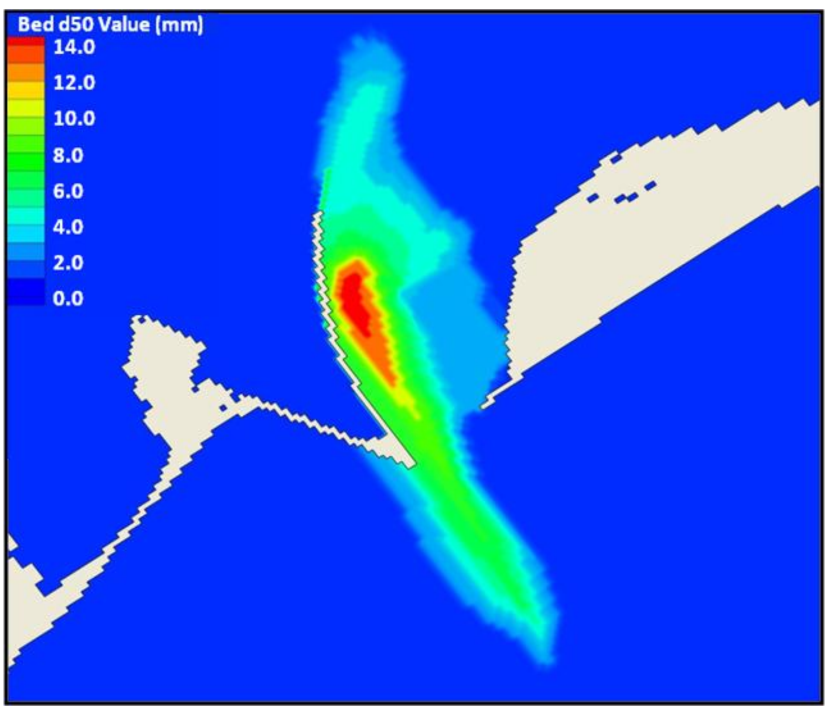

Figure 5.11: Variable bed d_{50} dataset used in 2010 simulations, spatially adjusted from 1992 calibration based on velocity magnitude contours at the maximum ebb-tide.

6.0 ANALYSIS AND DISCUSSION

6.1 Analysis of Governing Morphological Processes

Once the numerical model had been successfully calibrated with respect to both hydrodynamics and morphological trends, the calibrated model was used as a tool to help identify governing coastal processes responsible for sediment deposition at Shippagan Gully. First, the model was applied to help understand the effects of the most recent significant changes which have occurred at the inlet, namely the collapse of the outer portion of the east jetty and the closure of the secondary flow path in the late 1990's (both discussed in Section 4.3).

6.1.1 Effects of East Jetty Failure and Secondary Flow Path Closure

Three separate 6-year simulations were run starting from the same partially artificial 1992 bathymetry which was created for the morphological calibration (see Section 5.2.1). Each simulation (and all long term simulations referred to hereafter in this report) was run with the boundary conditions described in Section 5.1.4.1. These three simulations were setup in order to study the effects of significant changes which occurred at Shippagan Gully in the late 1990's. The simulation scenarios were as follows:

- Simulation 1: Fully intact (undamaged) east jetty
- Simulation 2: Collapsed outer 40 metres of east jetty
- Simulation 3: Artificial closure of the secondary flow path on the east side of the inlet (jetty intact)

Each simulation was run for 6 years, and subsequent morphological changes were compared and assessed. Figure 6.1 below shows morphology change maps at the end of each of the three simulations. These morphology change maps use colour to indicate areas of sediment deposition (red) and erosion (blue), while the intensity of the colour denotes the amount of sediment (in vertical metres) which has been deposited or eroded.

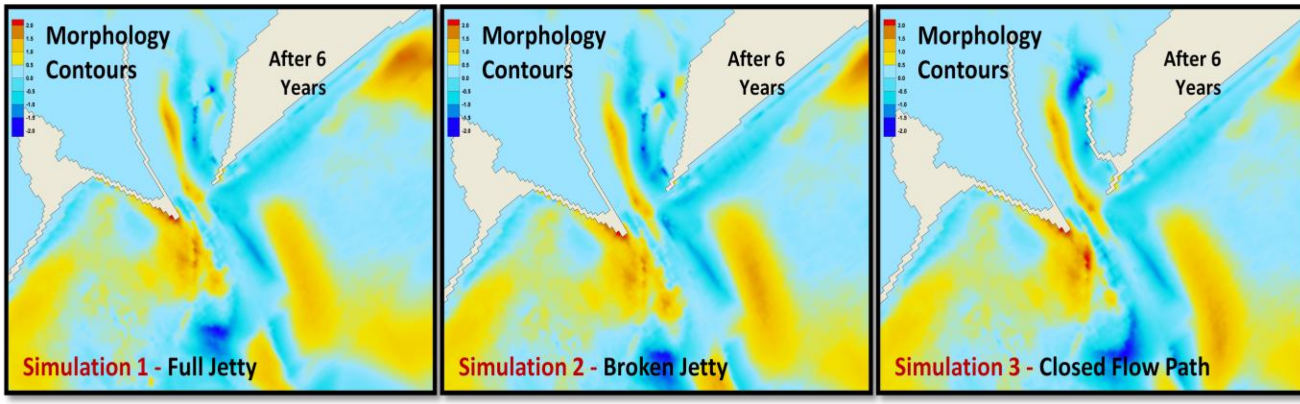

Figure 6.1: Morphology change maps for three simulation scenarios in which the effects of dramatic structural and morphological changes at Shippagan Gully in the late 1990's are observed.

From Figure 6.1 it is apparent that all three simulation scenarios produce highly similar erosion and deposition patterns after 6 years, particularly with respect to the accumulation of sediment on the east side of the navigation channel at the centre of the inlet (which creates the westerly migration of the navigation channel). For a closer look at the effects of these three simulation scenarios on navigation through the inlet, channel cross-sections at various locations within the inlet were analysed at the end of the 6 year period for each of the three runs. A sample comparison of cross-sections is presented in Figure 6.2 for a location at the inlet mouth, between the tips of the east and west jetties.

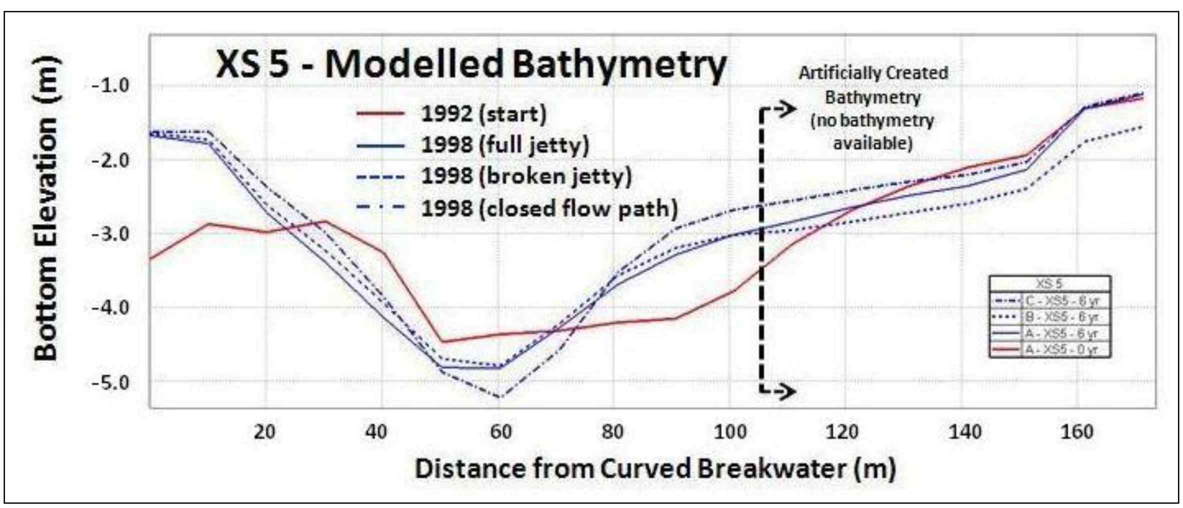

Figure 6.2: Modeled navigation channel cross-sections for three scenarios, at the end of the 6 year simulations period, compared to the starting bathymetry (1992 channel bathymetry).

From Figure 6.2, it can be seen that all three simulations produce sediment deposition on the east side of the navigation channel (right) and erosion on the west side (left) as was discussed in Section 4.3.2.3. The difference in modeled morphology change at the inlet mouth between simulation 1 and simulation 2 (fully intact east jetty versus collapsed east jetty) is relatively small. This suggests that the failure of the east jetty did not have a large influence on the migration of the navigation channel. Closure of the secondary flow path (simulation 3) had a slightly larger, but still modest, influence on the morphology of the navigation channel. This simulation predicts slightly more deposition than either simulations 1 or 2, particularly at the -3 m elevation and on the east side of the channel. It also shows slightly more erosion in the centre of the navigation channel, approximately 60 m from the curved breakwater wall (left extent of Figure 6.2). This is likely due to the additional flow which has been forced to follow the primary flow path at Shippagan Gully once the secondary flow path had been closed.

It should be stated that although sediment deposition in the navigation channel is effectively reproduced, none of these three simulations shows any sediment deposition on the accumulated beach (above the LWL) which is clearly visible in recent aerial photographs on the east side of the inlet. Since so much of the deposition in this area is above the water line, processes outside the typical tidal range and not included in these simulations must be influencing its formation. As such, sediment deposition in this zone is addressed in Section 6.1.3.

6.1.2 Mechanisms Responsible for Sediment Deposition

The calibrated numerical model can be used to provide answers to three very important questions in understanding the morphological process present at Shippagan Gully:

- When is sediment being deposited?
- Why is sediment being deposited?
- Where is the sediment coming from?

To answer these questions, time series of predicted morphological change at specific points of interest were examined. Results from simulation 1 above (6 year run, starting from 1992 artificially created bathymetry and with fully intact east jetty) were consulted for this task, and three grid points were chosen from which to analyse the time varying bed elevation. The three selected grid points are pictured in Figure 6.3, overlaid on 1992 bathymetric contours representative of the numerical model bathymetry at the start of the 6 year simulation.

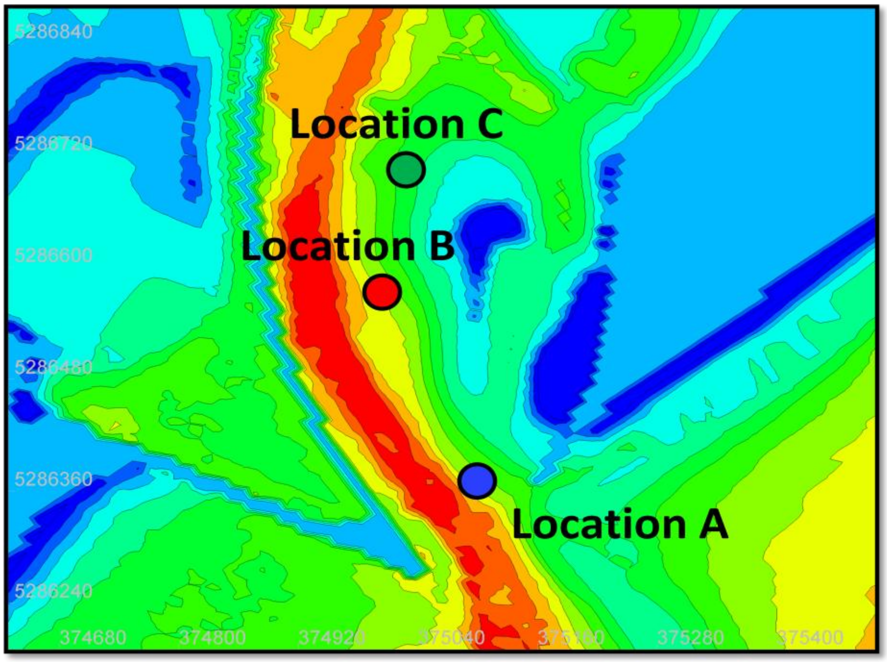

Figure 6.3: Three locations at which time series were extracted for further analysis, overlaid on the 1992 bathymetry as was the starting bathymetry for the numerical model simulation.

A time series of bed elevations was plotted for each of the three locations depicted in Figure 6.3. From these plots, morphological trends at each of the three locations can be deciphered as they pertain to other time varying parameters such as tides and waves. The three locations shown in Figure 6.3 were chosen as they are representative of three different deposition/erosion zones. Location A corresponds to a highly dynamic deposition zone at the inlet mouth. Location B corresponds to the migrating eastern bank of the navigation channel at a point approximately 300 metres from the inlet mouth. Location C corresponds to the northern limit of observed deposition within Shippagan Gully. Time series of modeled depths (below MWL) for each of the three locations are presented in Figure 6.4, accompanied by a time series of water surface elevations for the entire 6 year simulation. It should be noted that a morphological acceleration factor of 16 was used in this simulation (see Section 5.2). As such, hydrodynamics were simulated for a total of 137 days, which results in 2192 days of morphological time, or 6 years.

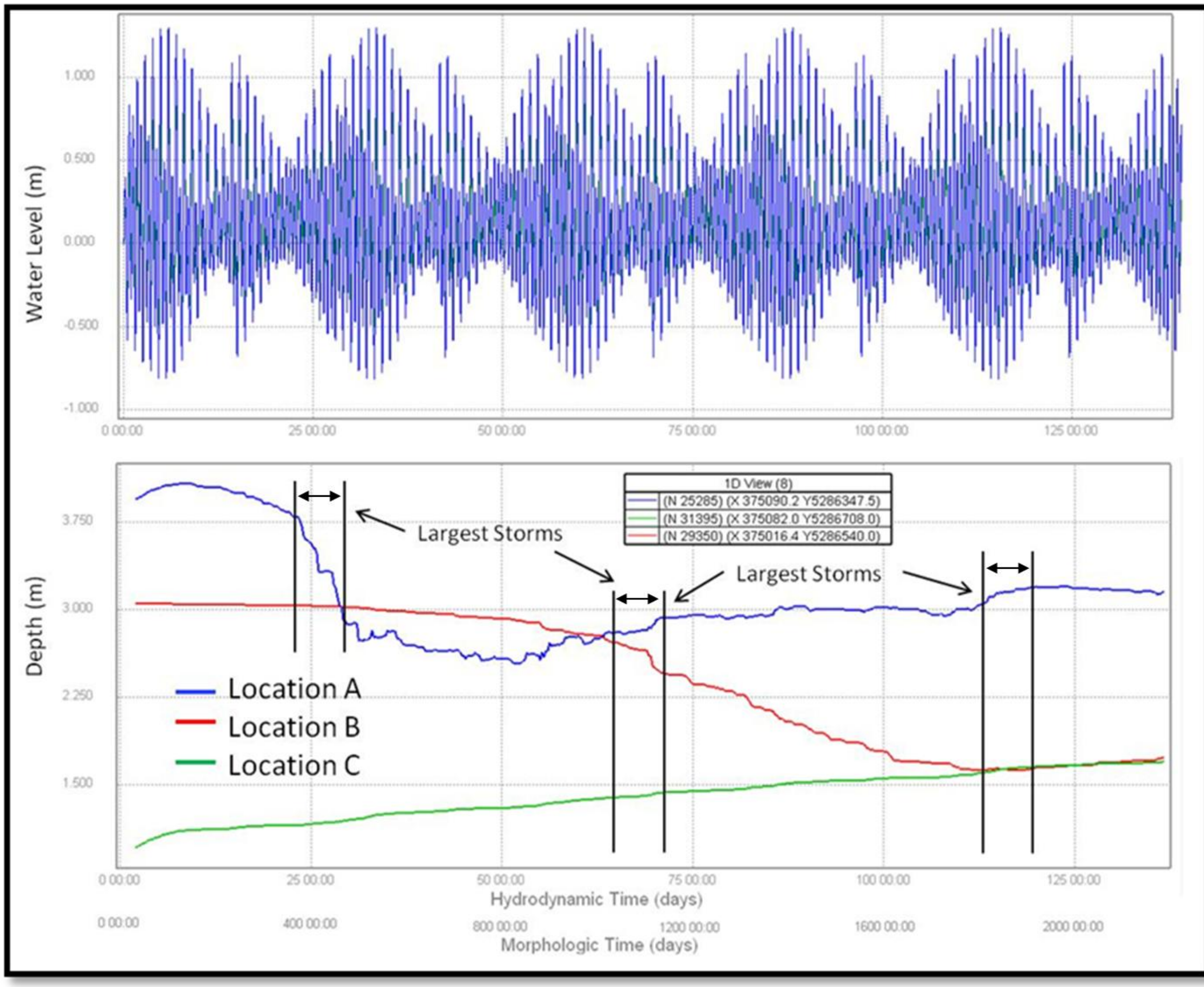

Figure 6.4: Bed elevation time series at three locations defined in Figure 6.3 above, for a 6 year morphological simulation starting from 1992 bathymetry and with a fully intact east jetty.

From Figure 6.4 several important observations can be made. First, from looking at the temporal morphology change at location A, it is apparent that both deposition and erosion occur at this location, and are highly variable with no apparent long term trend. Furthermore, significant changes in depth (below MWL) are observed at location A during periods of intense wave action, such as during the stormy periods highlighted in Figure 6.4 (these highlighted temporal ranges correspond to the winter months in which the largest storm events are grouped). These observations indicate that at this location at the inlet mouth, sediment deposition is wave-dominated. Conversely, locations B and C depict relatively smooth long term trends and are not subject to the variability demonstrated at location A. Furthermore, locations B and C do not seem to be overly influenced by periods of intense wave action. Hence, the numerical model results indicate that morphology changes at locations B and C are tide-dominated.

By inspecting at the same bed elevation time series at a higher temporal resolution, another important observation is made. It can be seen from Figure 6.5 that at both location B and location C, morphology change occurs primarily during the ebb-flows (tide exiting), while little to no change is observed during the flood-flow (tide entering). As such, not only does the numerical model show that deposition/erosion zones B and C are tide-dominated, but it indicates more specifically that they are *ebb*-tide dominated.

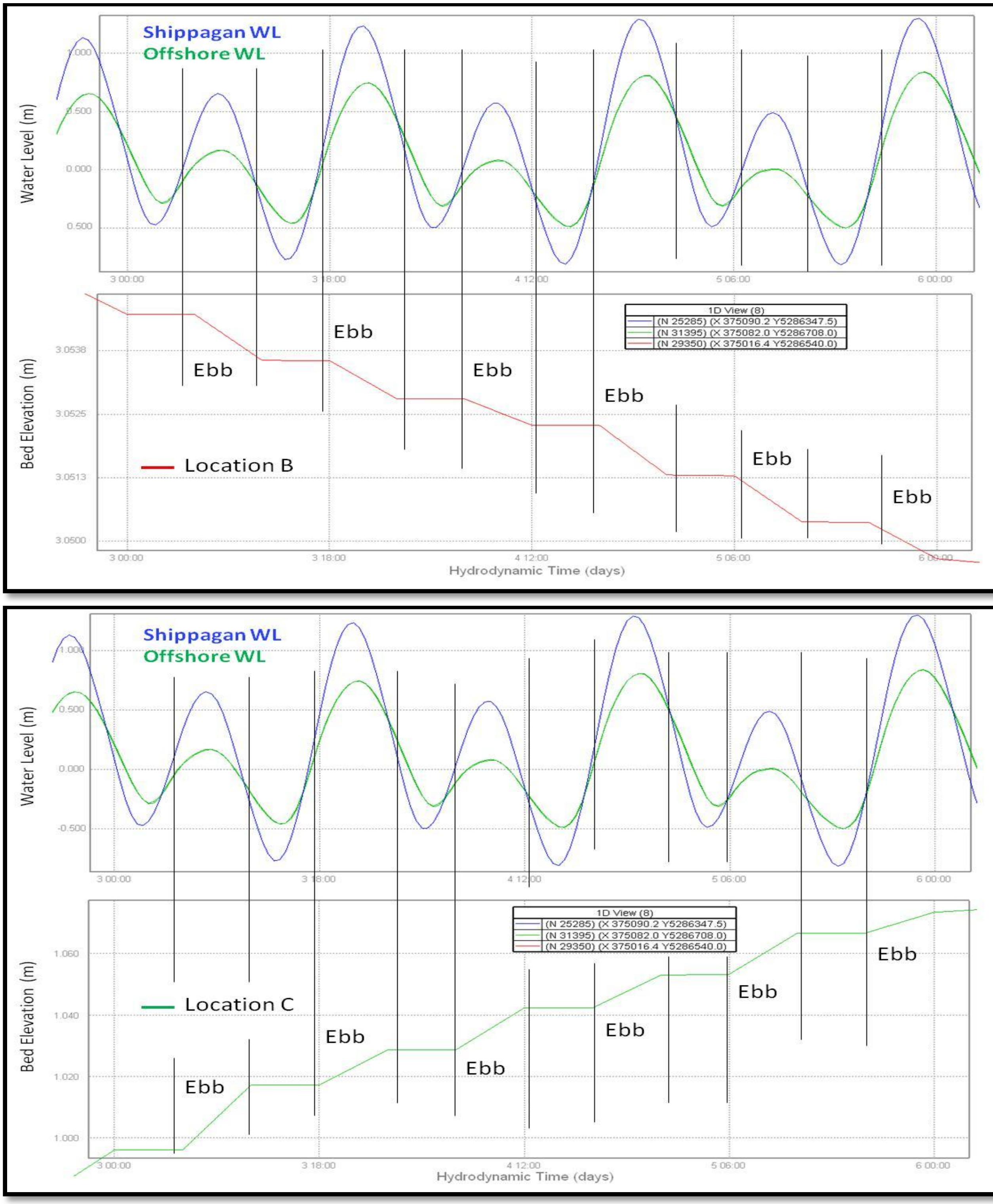

Figure 6.5: High temporal resolution plot of bed elevation at locations B and C as they compare to the time-varying water levels at the numerical model boundaries.

Once the governing processes for morphology change were identified within Shippagan Gully, a justification for this deposition was sought. Wave-induced deposition occurring at the inlet mouth is easily explained by the previously discussed presence of a net longshore transport of coastal sediment from northeast to southwest. Sediment arrives at Shippagan Gully from the northeast and is subsequently deposited in the sheltered confines of the ebb-shoal near the inlet mouth or is transported offshore and along the ebb-shoal by the combined effects of easterly waves and the strong ebb-current.

Tide-dominated deposition within the inlet on the east side of the navigation channel is however slightly more difficult to explain. The likely reason for this sediment deposition and subsequent migration of the navigation channel is the fact that water passing through Shippagan Gully must flow around a large bend, guided by the curved breakwater. As such, the highest current velocities are found on the outside of the bend (near the curved breakwater's sheet pile wall), while comparatively lower velocities are present on the inside of the bend. This phenomenon results in erosion of the outer bank, while sediment deposition is promoted along the inner bank. This process is analogous with that which creates a meandering river. Small river bends tend to expand radially outwards, eroding the outer bank and creating shallow sloping deposition banks on the inside of the bends. This process often continues until the formation of an oxbow (see Figure 6.6) and typically occurs faster when the flow is higher (in this case during the ebb-flow). Figure 6.6 and Figure 6.7 illustrate this phenomenon and its manifestation at Shippagan Gully.

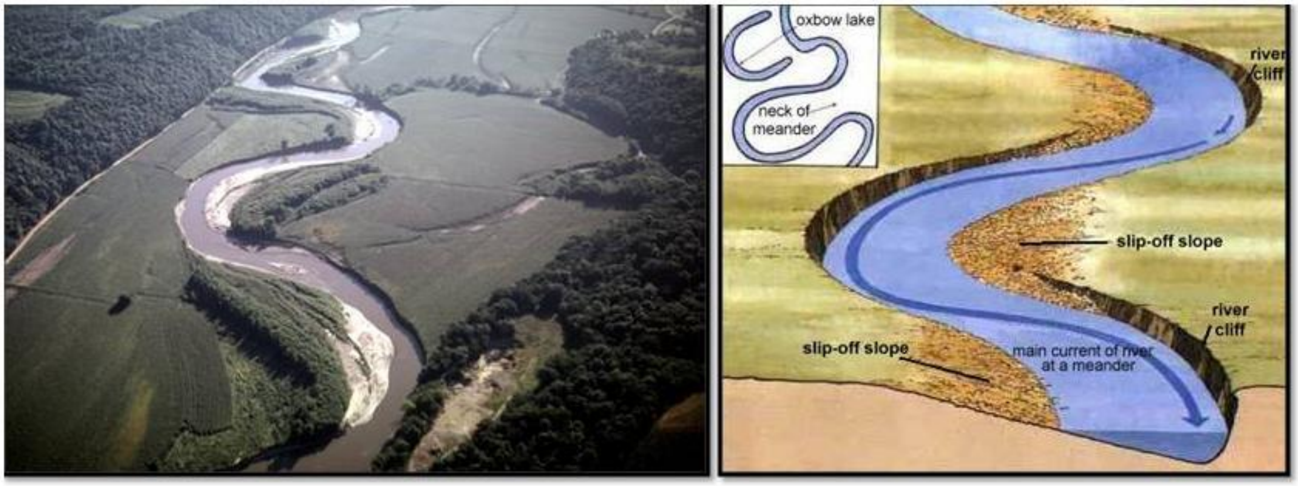

Figure 6.6: A meandering river showing steep, eroded outer banks and shallow sloping sediment deposition on the inner banks (left) and an illustration of the main flow path through a river meander, with the formation of an oxbow shown in the inset (right) – (University of Wisconsin, 2011).

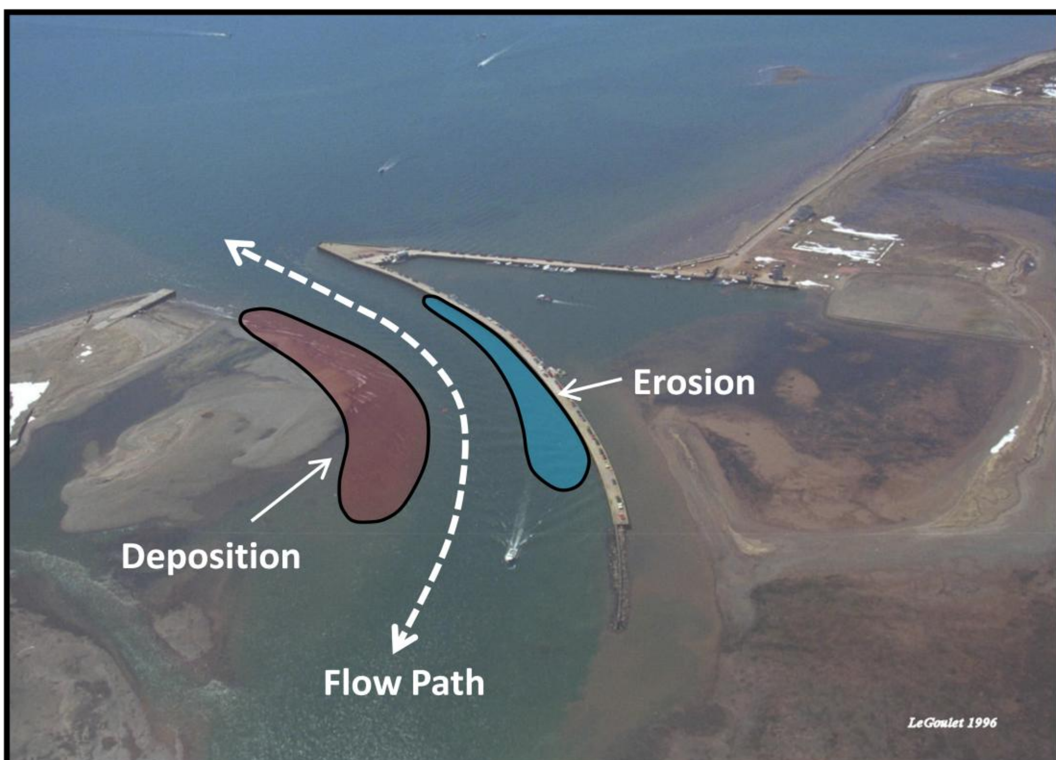

Figure 6.7: Aerial photograph of Shippagan Gully taken in 1996 showing the curved flow path followed by the strong ebb-current as it exits the inlet.

A morphology change map illustrating modeled deposition and erosion after 6 years of simulation time (starting from the 1992 bathymetry) is presented in Figure 6.8 below. Indicated on the morphology change map are the ebb-tide-dominated deposition and wave-dominated deposition zones discussed above, as well as the location of the navigation channel and approximate 2010 water line position on the east side of the inlet.

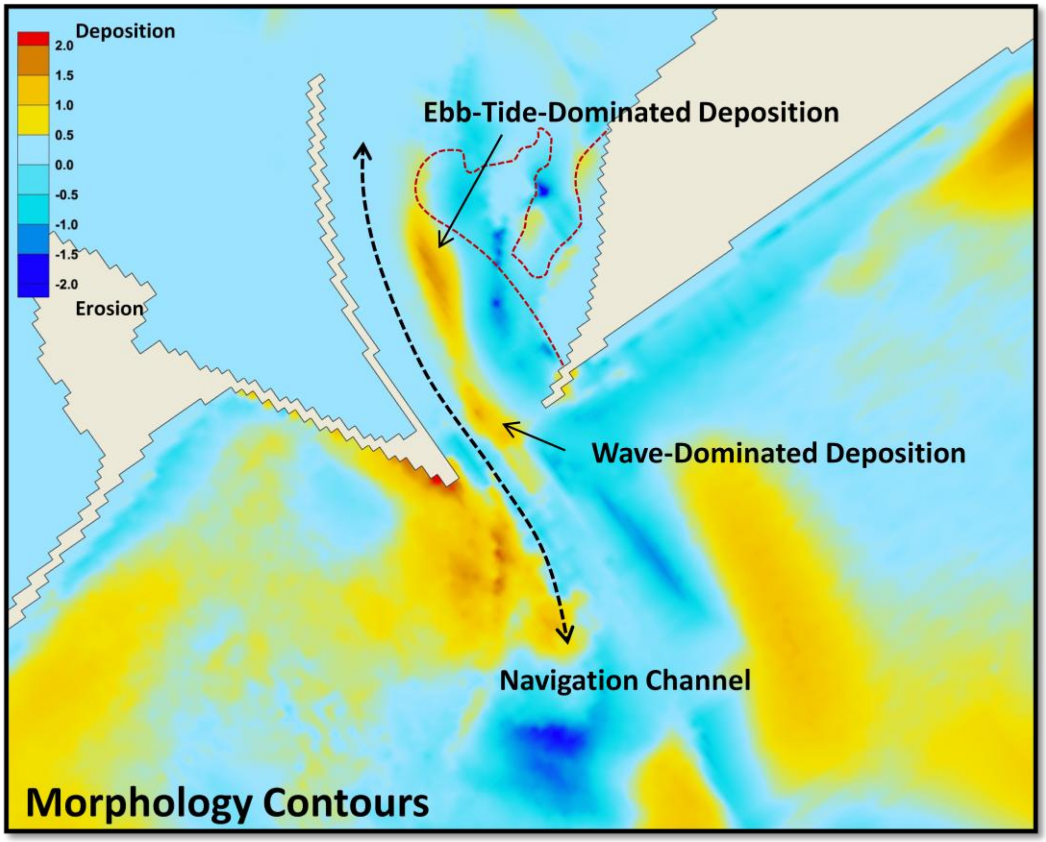

Figure 6.8: Summary image showing sediment deposition zones within Shippagan Gully after a 6 year morphology simulation beginning with the 1992 assumed bathymetry.

6.1.3 Storm Surge

Although the mechanisms responsible for both the deposition at the inlet mouth and along the eastern bank of the navigation channel (resulting in the westerly migration of the channel) are successfully modeled and discussed in Section 6.1.2, the numerical model was unable to reproduce any of the deposition on the eastern side of the inlet which is so apparent in aerial photographs. It was determined in Section 4.3.2.2 that approximately 2150 m^3 of sediment is deposited in this region above the -1 m (GD) contour each year. Furthermore, deposition in this area reaches elevations of over 2 m above the LWL. As such, it is likely that a hydrodynamic process occurring above the typical tidal range is responsible for this substantial amount of deposition. The effects of elevated water levels due to storm surge were therefore investigated using the numerical model.

Unfortunately, no measured storm surge data are available for the Gulf Coast surrounding Shippagan Gully. As such, an estimated water surface elevation adjustment of 1 m was used, based on anecdotal information from locals. A 12 hour period encompassing the maximum spring tide was simulated with the addition of this 1 m to the water surface elevation at all three model boundaries and for a variety of storm conditions. 2010 bathymetry was used as the starting bathymetry for the storm surge simulations and is identical to that which is described in Section 5.1.5 above. Wave parameters corresponding to annual storm events from 270^0, 330^0 and 360^0 were input to the numerical model and each 12 hour storm was simulated individually. Results from these simulations were compared to results from identical simulations without the additional surge, in order to determine the relative effects that this increased water level has on local morphology change during large storm events. Figure 6.9 below presents colour contour plots of significant wave height for simulations without (left) and with (right) 1 m storm surge. These results correspond to an annual storm event approaching from the 330^0 directional bin. Waves during this event had an offshore significant wave height of 2.65 m with a peak spectral period of 8.25 s.

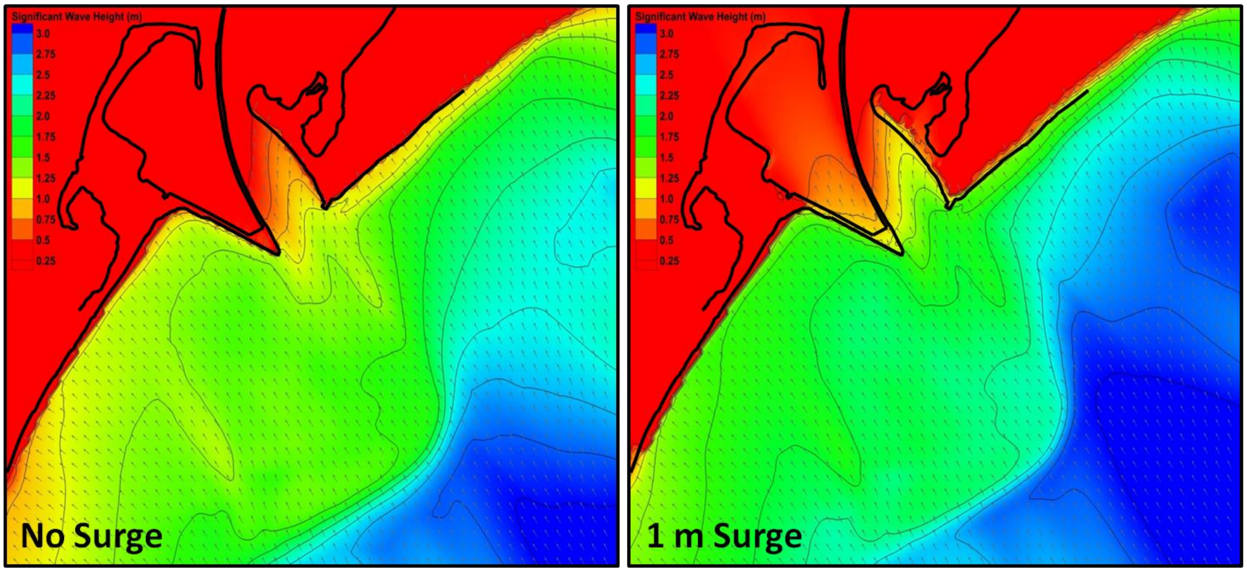

Figure 6.9: Contour plots of significant wave height during an annual storm event from the 330^0 directional bin, for both normal water levels (left) and with the addition of a 1 m storm surge (right).

It can be seen from Figure 6.9 that with the addition of a 1 m storm surge, much larger waves are able to propagate well into Shippagan Gully. For this particular event, the largest waves to reach the eastern shoreline inside of the inlet without storm surge are on the order of 1 m. With the addition of a 1 m surge however, waves with significant wave heights of nearly 1.5 m are observed at the same location within the inlet, thus resulting in a 50% increase in wave energy.

Figure 6.10 below illustrates morphological changes predicted to occur over the course of the same 12 hour storm event, with annual storm waves approaching from the 330^0 directional bin. It can be seen from this figure that for this particular annual storm, significant changes in ebb-shoal morphology are apparent regardless of the additional surge. This is due to the sediment transport created by waves breaking over the shallow ebb-shoal. Within the inlet however, a great deal of erosion and deposition is apparent along the beach on the eastern side of the navigation channel for the simulation including storm surge, while no morphology change is predicted in this region without storm surge (as was observed in previous long term simulations). Figure 6.11 provides a closer look at the deposition and erosion patterns within the inlet due to the annual storm from the 330^0 directional bin combined with a 1 m storm surge.

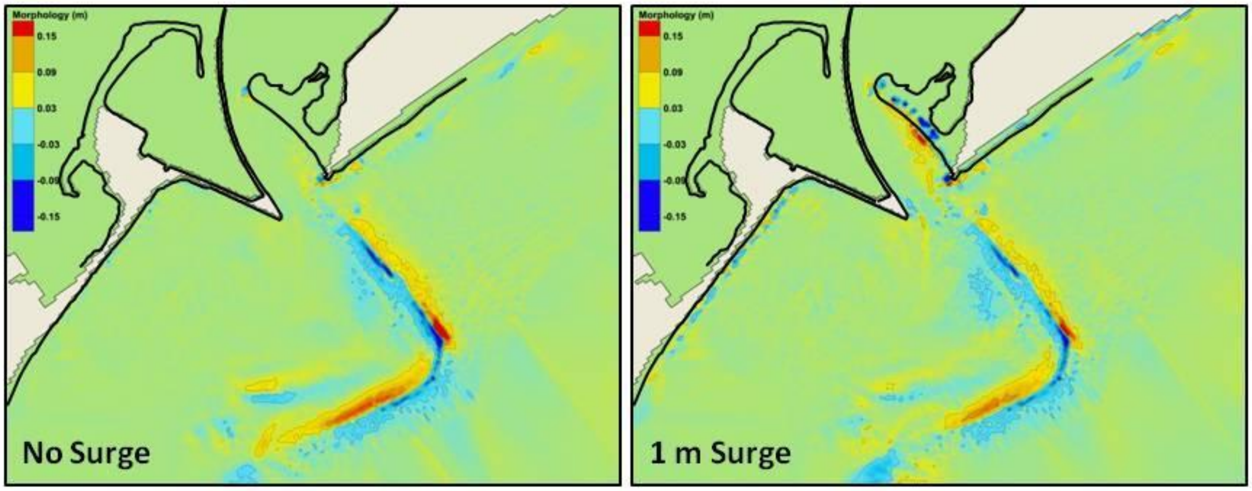

Figure 6.10: Morphology change after a 12 hour annual storm with waves from 330° during a maximum spring tide with no additional storm surge (left), and with 1 m storm surge (right).

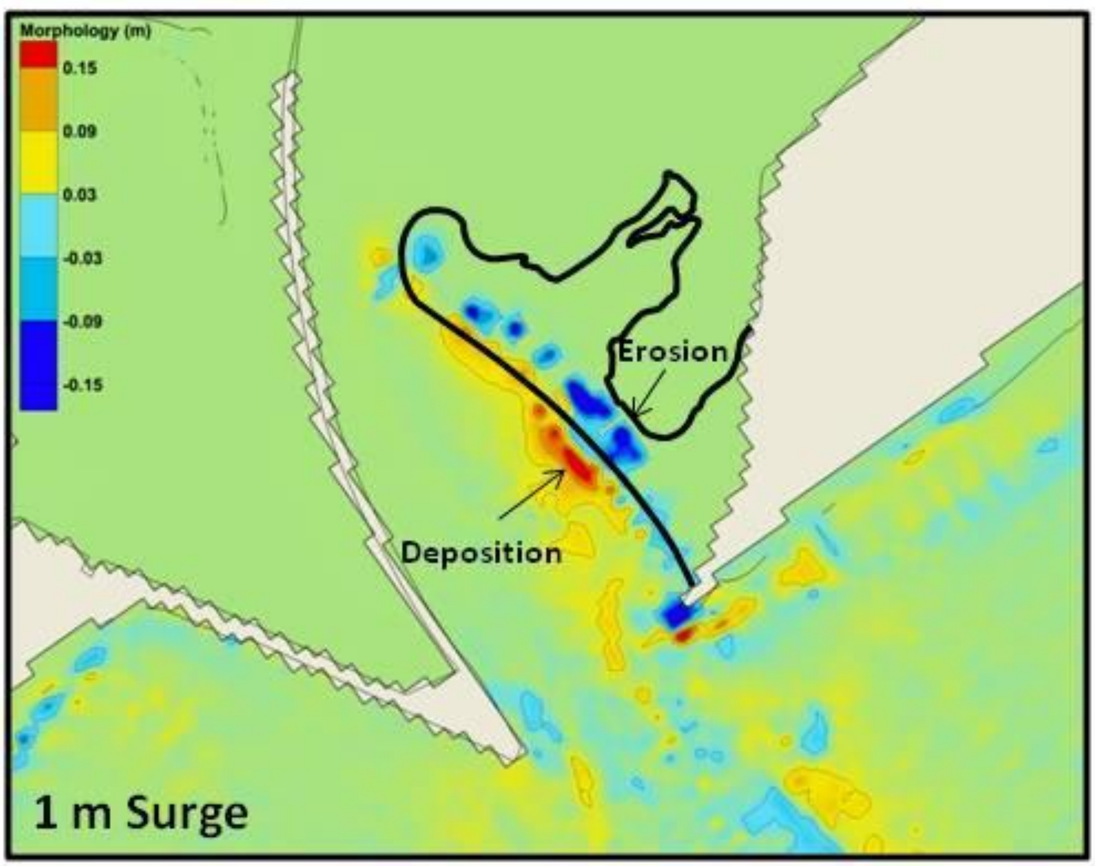

Figure 6.11: A closer view of predicted sediment deposition on the east side of the inlet for a 12 hour annual storm from 330° with 1 m of storm surge.

The erosion and deposition pattern observed in Figure 6.11 is a sign that the numerical model is doing a good job of simulating what really happens in nature. Large waves breaking on a beach face (particularly at higher than normal water levels) tend to erode the beach face above the waterline and deposit sediment just below the water line. This creates what is known as an S-shaped beach profile, a geometric property of beach faces which is often observed after a large storm event. This process is illustrated in Figure 6.12 below.

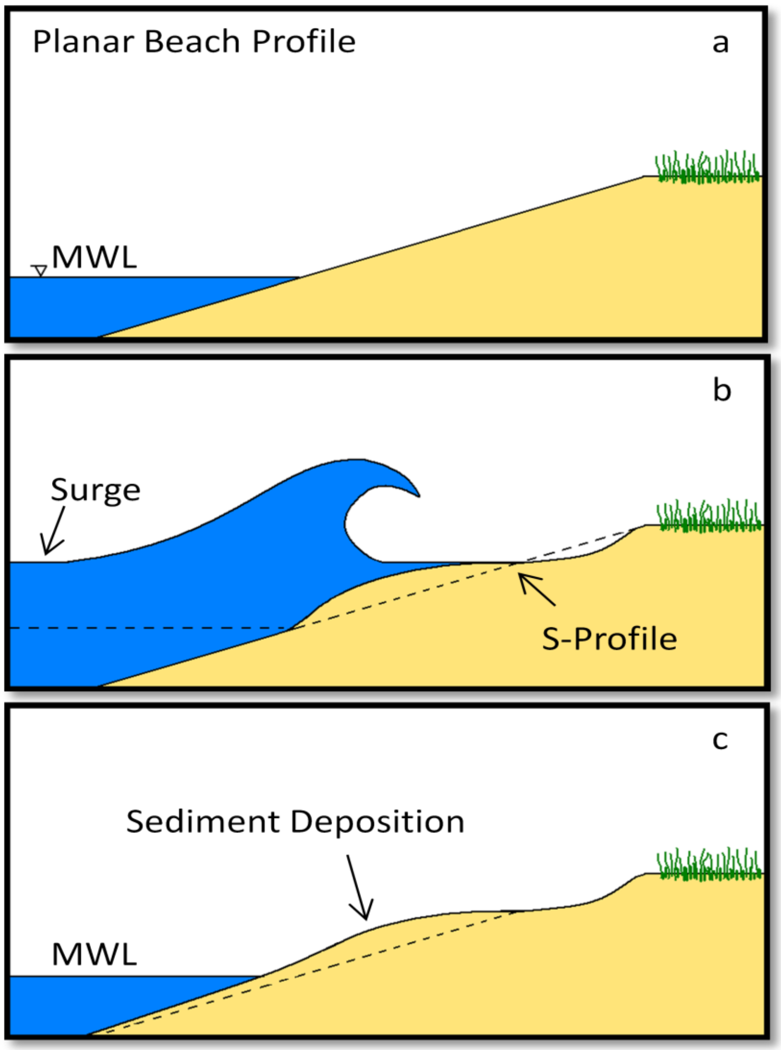

Figure 6.12: Illustration of the natural process in which a beach is eroded by wave attack and takes on what is known as an S-shape profile.

6.1.4 Summary of Morphological Processes

In the previous sections, the calibrated numerical model has been used to identify three separate sediment deposition zones within Shippagan Gully. Furthermore, coastal processes responsible for sediment deposition in each of the three zones have been determined. Sediment deposition at the inlet mouth and immediately offshore from the inlet mouth (particularly on the east side of the navigation channel) has been identified as wave-dominated deposition, created by waves propagating over water depths typical to the local tidal range. The source of this sediment is longshore transport, thus meaning that it arrives at the inlet from the northeast.

Sediment deposited well within Shippagan Gully along on the eastern bank of the navigation channel has been shown to cause a westerly migration of the navigation channel. This deposition is typically at depths of 1 to 4 meters and is accompanied by slight erosion on the opposite (west) bank. This morphologic trend has been shown to be tide-dominated and is more specifically due to the strong ebb-tide flows which are forced around a bend prior to exiting into the Gulf of St. Lawrence. This curvature of flow acts in the same manner as a river meander, promoting deposition along its inner bank while eroding radially outward.

Finally, sediment deposition at higher elevations on the east side of the navigation channel (as is apparent from aerial photographs) has been demonstrated to be sediment which is deposited during large storm events which are accompanied by an increase in local water levels (storm surge). A summary of these three deposition zones and the responsible coastal processes is presented in Figure 6.13 below.

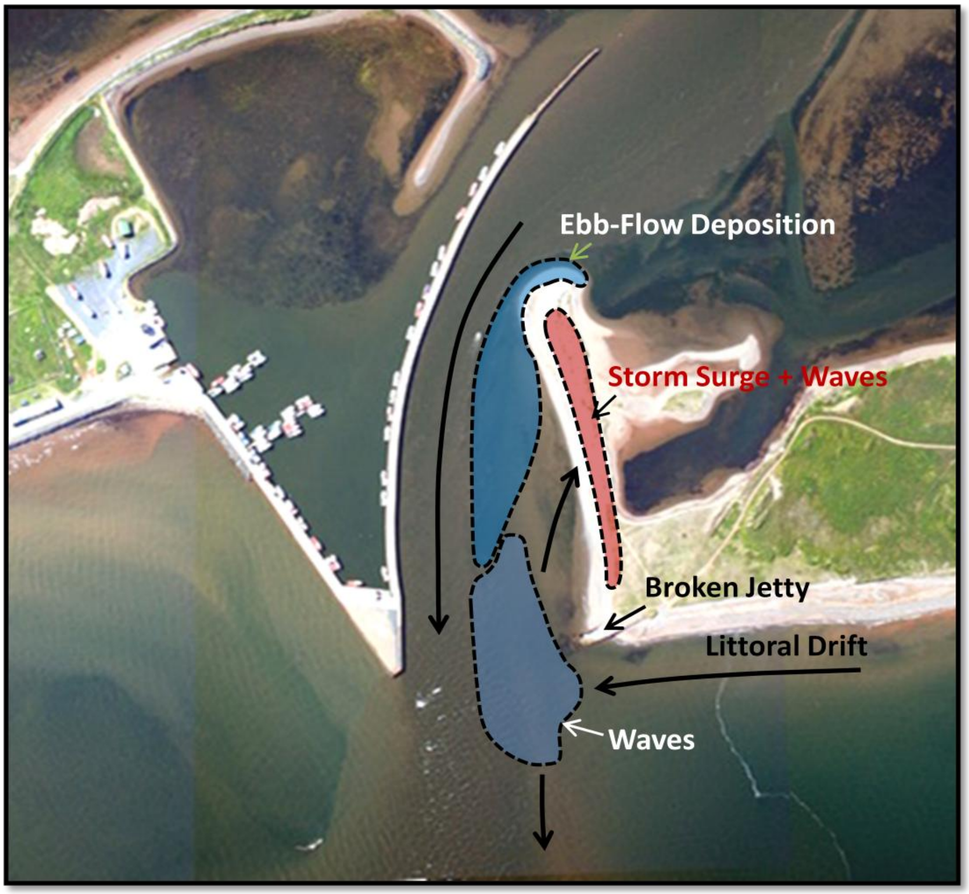

Figure 6.13: A summary of deposition zones and coastal processes responsible for each deposition zone, overlaid on a 2008 aerial photograph of Shippagan Gully.

6.2 Simulation and Assessment of Design Options

Based on the findings presented thus far, a number of alternative design options were formulated with the objective of improving the current situation at Shippagan Gully. The numerical model was first applied to assess what can be expected of Shippagan Gully if the status quo is maintained. Alternative design options were then modeled (each starting from 2010 bathymetry) and the results compared to that of the status quo, in order to determine if the current situation at Shippagan Gully can be improved upon. The major areas of interest in which improvements were sought, corresponded to the three deposition zones outlined in Section 6.1.4, which are:

- Wave-dominated deposition at the inlet mouth;
- Storm-wave and storm-surge dominated deposition on the east side of the inlet; and

- Ebb-tide dominated westerly migration of the navigation channel.

The ultimate objective of simulating alternative design options was to determine what options, if any, are available to improve current morphological trends in these three zones, ultimately improving the navigability of Shippagan Gully and reducing long term maintenance requirements. A complete list of the design options which were simulated at Shippagan Gully using the calibrated numerical model is presented in Table 6.1 below. The scenarios were developed in collaboration with PWGSC.

Table 6.1: Complete list of scenarios that simulated using the calibrated numerical model.

Simulation ID	Scenario Description	Simulation Duration
A	Status Quo	6 years
B1	70 m east jetty, perpandicular to shoreline, 140 m wide inlet	6 years
B2	140 m east jetty, perpandicular to shoreline, 140 m wide inlet	6 years
B3	140 m east jetty, elbow at 70 m, start perpandicular to shoreline, 140 m wide inlet	6 years
B4	70 m east jetty, perpandicular to shoreline, 80 m wide inlet	6 years
B5	140 m east jetty, perpandicular to shoreline, 80 m wide inlet	6 years
B6	140 m east jetty, elbow at 70 m, start perpandicular to shoreline, 80 m wide inlet	6 years
D	Amour west bank with scour blanket, 10 m width from toe of curved breakwater	6 years
E	Armour west bank with scour blanket, reduce curvature with 30 m width at center of curved breakwater, reducing to 10 m at both ends	6 years
H1-a	Training wall parallel to curved breakwater, 140 m wide through inlet, ending in B1 jetty	6 years
H1-b	Training wall parallel to curved breakwater, 140 m wide through inlet, ending in B2 jetty	6 years
H1-c	Training wall parallel to curved breakwater, 140 m wide through inlet, ending in B3 jetty	6 years
H2-a	Training wall parallel to curved breakwater, 80 m wide through inlet, ending in B4 jetty	6 years
H2-b	Training wall parallel to curved breakwater, 80 m wide through inlet, ending in B5 jetty	6 years
H2-c	Training wall parallel to curved breakwater, 80 m wide through inlet, ending in B6 jetty	6 years
I1	Status Quo with rubble removed at north limit of curved breakwater	5 days
I2	H1-a simulation with 100m shorter parallel wall at north limit	5 days
I3	H2-a simulation with 100m shorter parallel wall at north limit	5 days

It should be re-stated that all simulations were run using the 2010 calibrated d50 map which was discussed in Section 6.2.1 above. As was demonstrated in Section 6.2.1, modeled morphology is strongly influenced by this static dataset, thus resulting in a model limitation. However, since all simulations were run using the same d50 map, it is deemed acceptable to draw conclusions from their relative results (improvements). It should also be re-stated that all water levels and bottom elevations in the following sections are presented in metres above or below the Geodetic Datum (as per Table 4.2).

6.2.1 Status Quo

Figure 6.14: Aerial photograph taken in 2008 illustrating the Status Quo configuration of structures and morphologic features present at Shippagan Gully.

The calibrated numerical model was run using the most recent available bathymetry (2010) and the current configuration of structures. This included a representation of the current state of the east jetty, in which the outer 40 m of the structure lies just below the low water line (collapsed), while the remainder of the structure is intact at 2 m above LWL. The starting bathymetry (the same for all simulations presented hereafter), final bathymetry (after 6 years), morphology change over the 6 year simulation period and channel cross-sections are presented in Figure 6.15 through Figure 6.18 below.

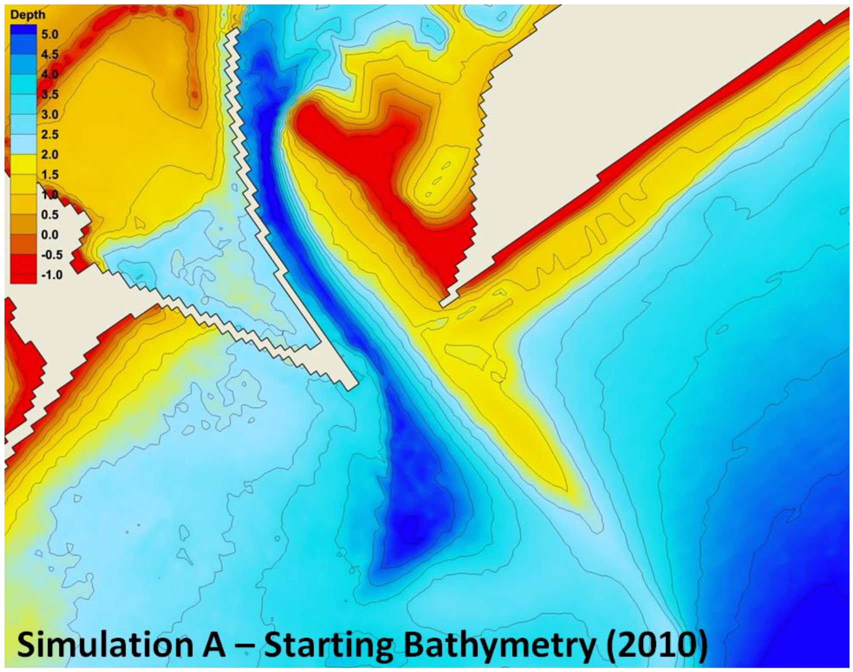

Figure 6.15: Initial bathymetry for simulation A (Status Quo), based on 2010 bathymetric surveys.

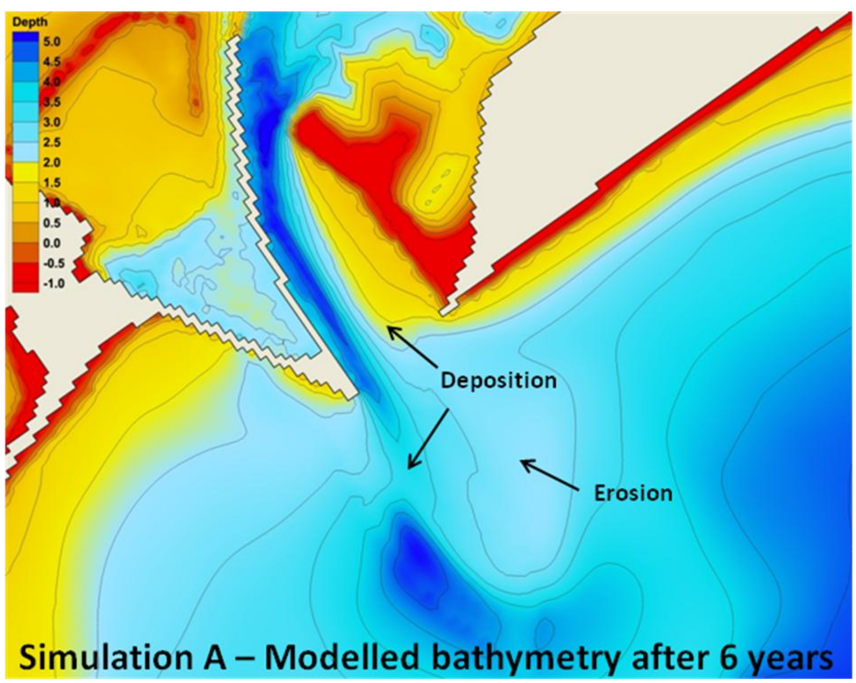

Figure 6.16: Modeled bathymetry after 6 years for simulation A (Status Quo).

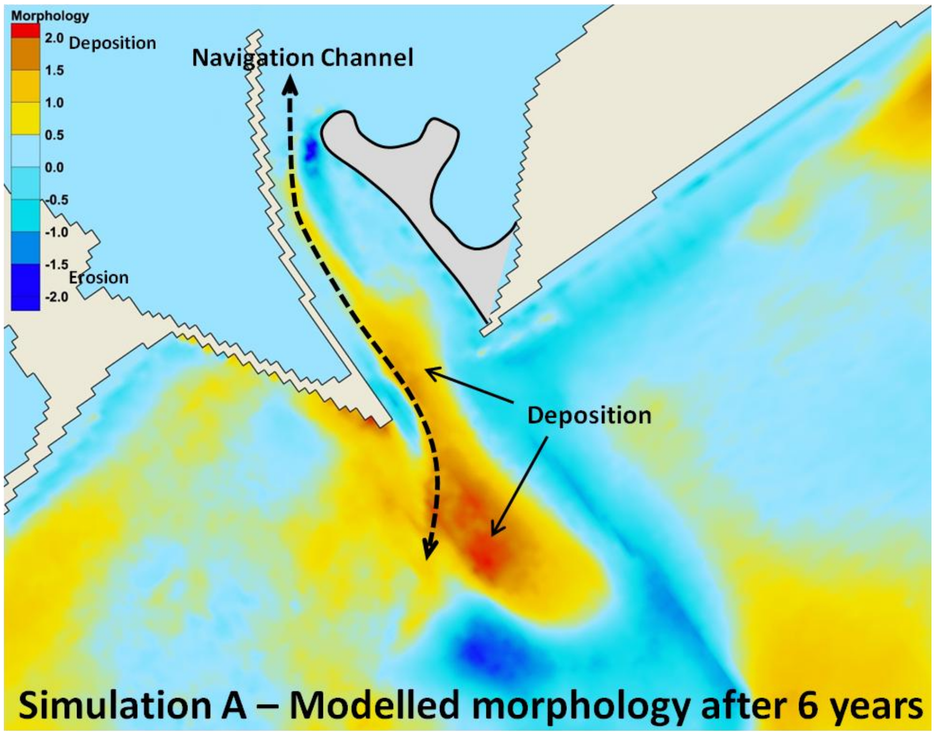

Figure 6.17: Modeled morphology change (erosion and deposition) after 6 years for simulation A (Status Quo). Erosion is negative (blue) and deposition is positive (red).

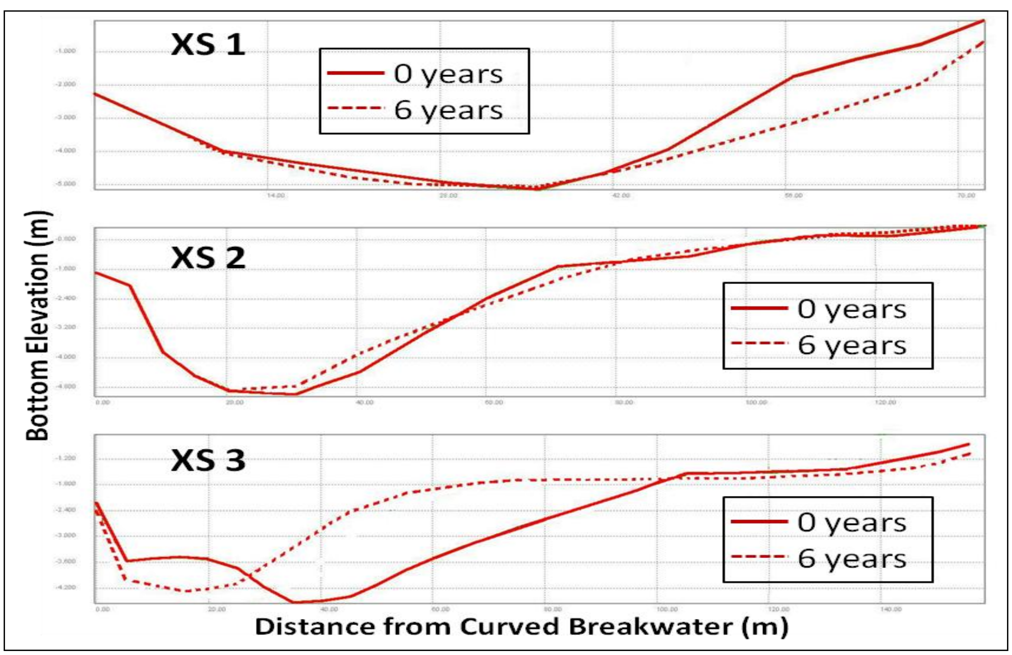

Figure 6.18: Channel cross-sections at three locations for simulation A (Status Quo) (locations denoted in Figure 4.12 above).

From Figure 6.15 through Figure 6.18, it can be seen that the numerical model indicates that if the status quo is maintained, significant deposition of sediment will continue at Shippagan Gully, particularly within and immediately offshore from the inlet mouth. This deposition is primarily wave-dominated and arrives at the inlet as longshore transport from the northeast, prior to being deposited near the inlet mouth and on the east side of the navigation channel (see XS 3 in Figure 6.18). Furthermore, the model results indicate that ebb-tide dominated sediment deposition will continue on the east side of the navigation channel, resulting in further westward migration of the channel (as seen in Figure 6.17). However, the numerical model also shows that this westward migration does not occur where the tip of the deposited spit on the east side of the inlet is only 70 m from the face of the curved breakwater. In fact, the model results indicate that this, the narrowest location in the channel, will actually undergo slight erosion in the coming years on its eastern bank (see XS 1 in Figure 6.18). These results must be interpreted with caution, as it is unlikely that the channel will become wider at this location, since it has been growing steadily narrower for many years. It is however likely that these numerical model results indicate that the navigation channel is approaching equilibrium at this particular location; the narrowest part of the inlet.

Although storm surge is not included in the long-term simulations, it can be assumed that deposition along the accumulated beach on the east side of the inlet will also continue, as large waves accompanied by storm surge will continue to propagate well into the inlet and break along the shoreline. This process is expected to result in continual reshaping of the beach profile and deposition of large amounts of sediment.

The numerical model shows substantial erosion of the shoal which is observed in Figure 6.15 immediately offshore from the east jetty. As was illustrated in Section 5.2, the numerical model has a tendency to smooth the bathymetry in this region to an approximate depth of 2.0 metres. This is not likely to occur in reality; it is an artefact of the numerical model which is common to all model results. Therefore, for the purpose of the comparison of multiple alternative scenarios, this smoothing of bathymetry to the east of Shippagan Gully is not relevant.

6.2.2 New East Jetty (B1, B2, B3, B4, B5 and B6)

Since the most substantial deposition indicated by the status quo simulations is found at or immediately offshore from the inlet mouth, and given the fact that this sediment is primarily arriving at the inlet from the northeast in the form of longshore sediment transport, several incarnations of a sediment-trapping jetty on the east side of the inlet were simulated. There are several possible purposes for placing a jetty on the east side of the inlet. Firstly, shore-perpendicular jetties are generally effective in trapping sediment on their updrift side and/or diverting sediment offshore when a strong net longshore transport exists. Secondly, a properly placed jetty can provide shelter to the inlet from incoming storm waves. Lastly, the width of the inlet mouth and subsequently the cross-sectional flow area at the inlet mouth can be adjusted depending on the placement of the jetty, thus influencing the hydrodynamic conditions at the inlet mouth.

Since each of these expected outcomes is highly sensitive to jetty orientation, location and length, several different jetty orientations and dimensions were simulated. The various jetty configurations which were simulated using the calibrated numerical model are illustrated in Figure 6.19 below.

Figure 6.19: Six east jetty configurations were evaluated using the calibrated numerical model.

Morphology change maps at the conclusion of the 6 year simulations are presented below, first for the status quo (repeated from Figure 6.17), and subsequently for each of the scenarios B1 - B6 (see Figure 6.21). The effects that the various jetties may have on the local patterns of deposition and erosion at Shippagan Gully can be assessed from these images.

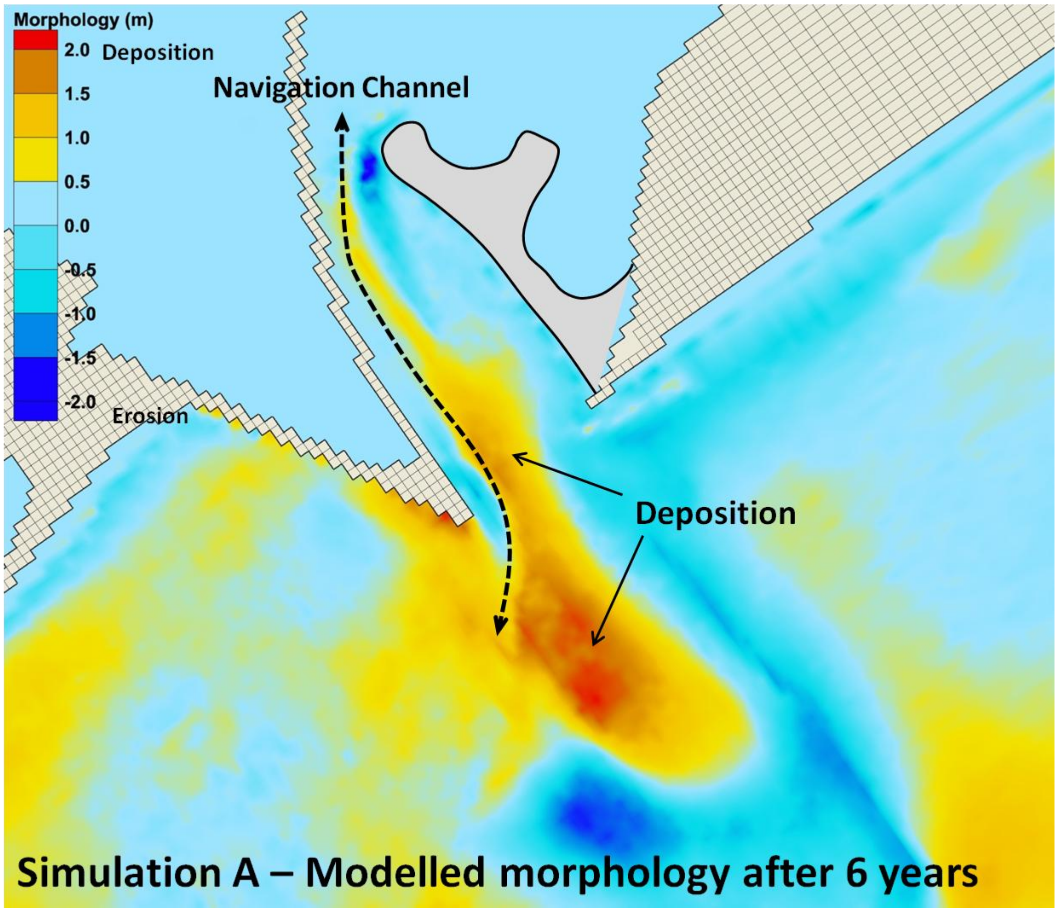

Figure 6.20: Modeled morphology change map after 6 years for scenario A (status quo) (repeated from Figure 6.17).

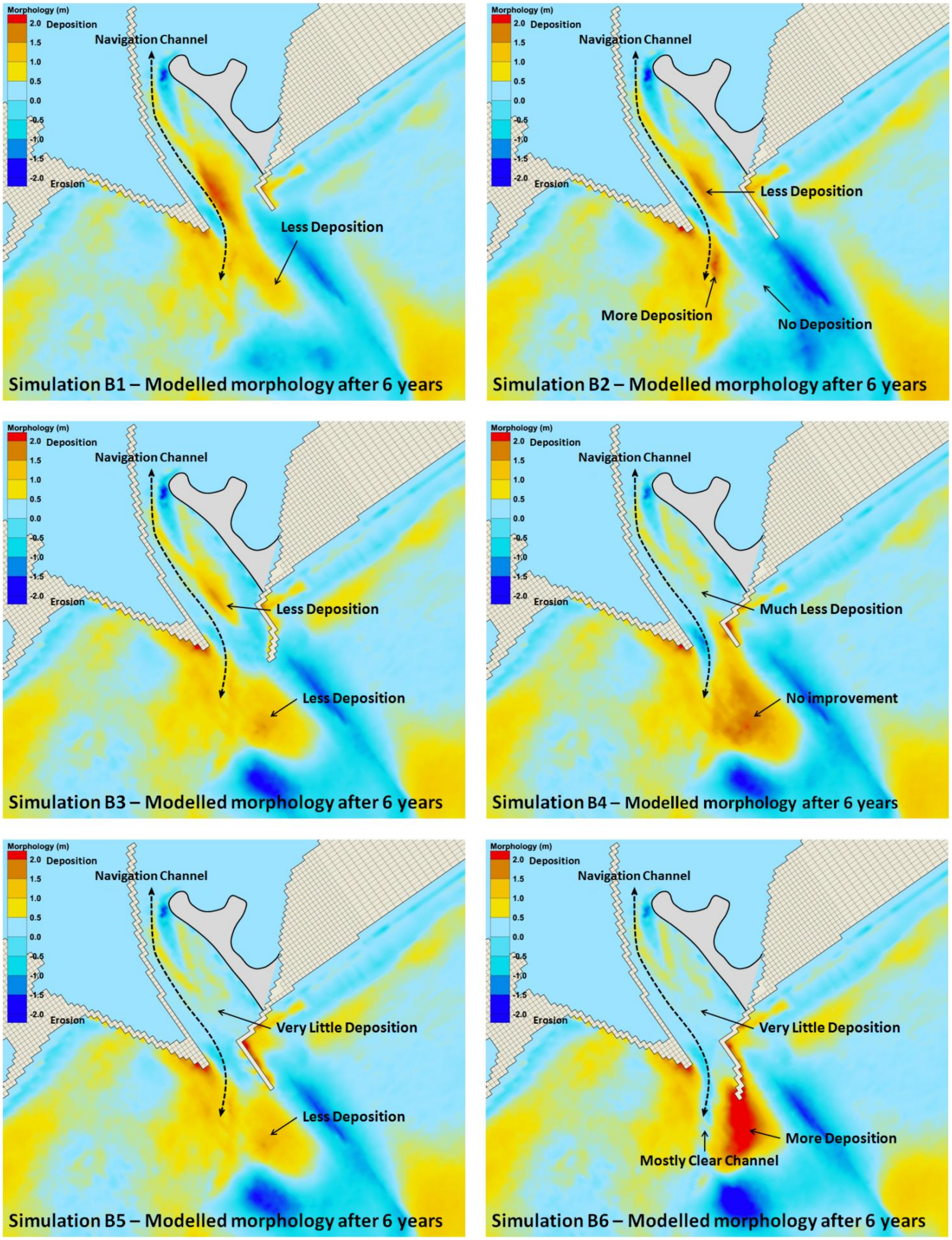

Figure 6.21: Modeled morphology change maps after 6 years for east jetty scenarios B1-B6.

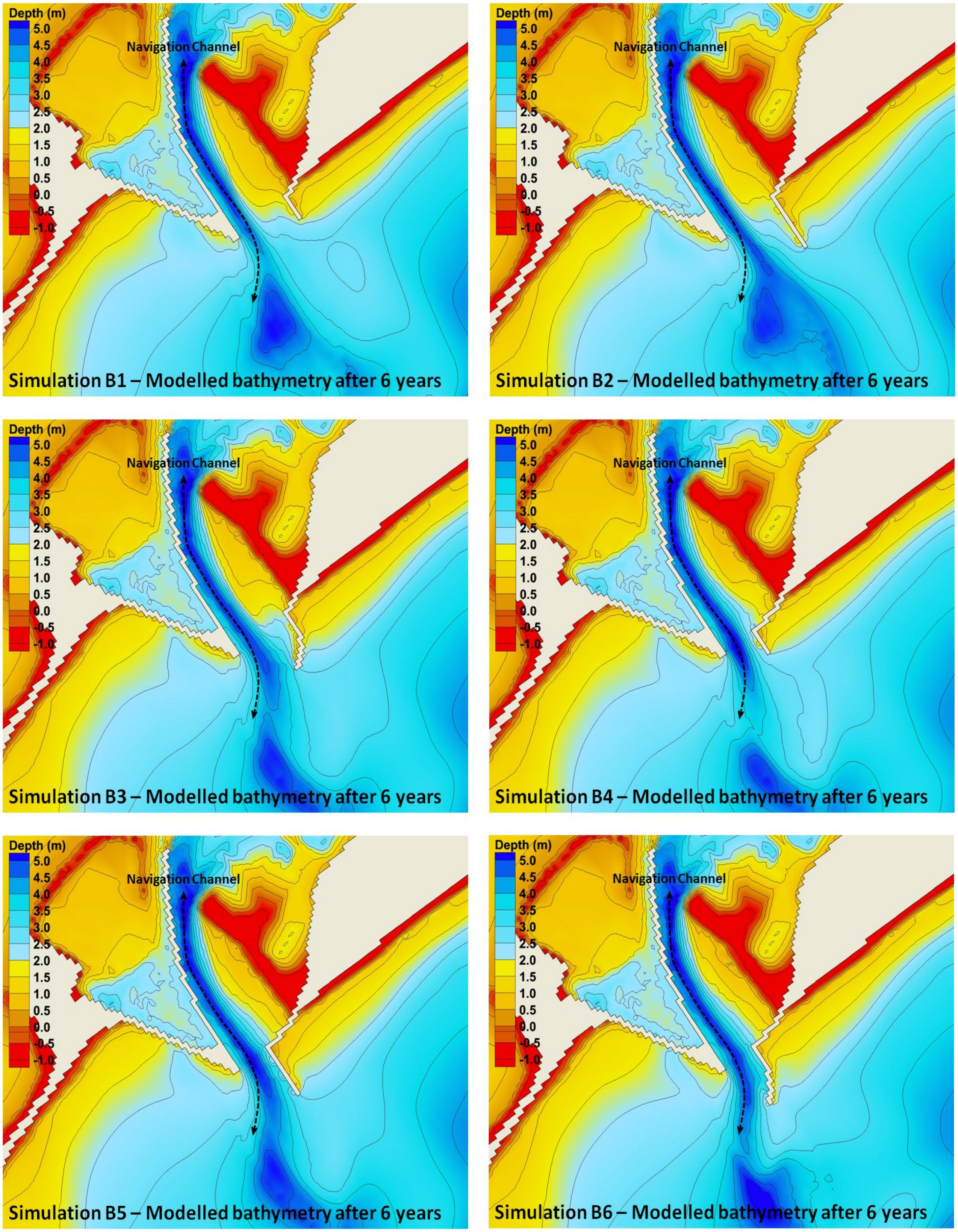

Figure 6.22: Modeled bathymetric contour maps after 6 years of simulation for east jetty scenarios B1 – B6.

From Figure 6.21 and Figure 6.22 it can be seen that all of the east jetty configurations offer an overall improvement compared with the status quo option with regards to deposition patterns and rates. Simulations B2 and B5 indicate that a relatively long jetty of 140m is effective in reducing sediment deposition immediately offshore from Shippagan Gully. These long structures trap or divert a large fraction of the net longshore transport which is approaching the inlet from the northeast, thus diminishing the deposition of longshore transport at the inlet mouth. More specifically, scenario B2 (140 m width across the inlet mouth), appears to do a better job of diverting sediment offshore along the ebb-shoal than placing the same length jetty further to the west as was simulated in scenario B5 (80 m width across the inlet mouth). This is likely because in scenario B2, the jetty is in line with the existing ebb shoal to the east of the inlet, and thus encourages sediment to follow this pathway.

It should be made clear that although using a long jetty to trap large volumes of sediment reduces the sedimentation at Shippagan Gully, it could have adverse effects down-drift from the project site where the sediment supply could be reduced. This reduction in sediment supply could lead to shoreline erosion down-drift (southwest) of the inlet. As such, care must be taken to maximize, as much as possible, the fraction of sediment diverted to the ebb-shoal (and ultimately bypassing the inlet), and minimize the fraction that is trapped permanently on the upstream side of the jetty.

Simulations B4, B5 and B6 (creating a narrower inlet entrance) result in a large improvement with regards to sediment deposition immediately inside the inlet. Sediment deposition in this zone is wave dominated, and all three of these jetty configurations provide a great deal of shelter to the inlet from wave attack, particularly from the east. Furthermore, although storm surge was not included in the long term simulations, it is expected that the additional shelter provided by scenarios B4, B5 and B6 would be highly effective in reducing the deposition on the east side of the inlet created by storm waves accompanied by surge (as was discussed in Section 6.1.3).

Simulations B3 and B6 indicate that a curved jetty (or a jetty with a bend or elbow) will be effective in sheltering Shippagan Gully from easterly waves and subsequently reducing deposition immediately inside the inlet. Both of these scenarios however show that an elbow jetty creates a great deal of deposition immediately off the tip of the jetty. For the case of configuration B3 in which the inlet mouth is wide, this deposition poses a threat to the navigable depths at the entrance to the navigation channel. The narrowing of the inlet mouth in simulation B6 however seems to focus and magnify the ebb-flow to a degree in which it is capable of scouring the inlet entrance and maintaining a channel.

From Figure 6.21 and Figure 6.22 it is clear that constructing a new jetty on the east side of the inlet, regardless of orientation or length, will not halt the westerly migration of the navigation channel further inside the inlet. As was previously discussed, this migration is due to deposition along the inner (east) bank and erosion on the outer (west) bank caused by the curved flow path followed by the strong ebb-current. Adding a jetty on the east side of the inlet mouth will not reduce this curvature nor alter the flow of the ebb-current inside the inlet, thus, the channel should continue to migrate westward.

6.2.3 Armouring the West Bank of the Navigation Channel (D and E)

In order to address the westerly migration of the navigation channel, focus was shifted to the strong ebb-current which is responsible for both deposition along the eastern bank and erosion of the west bank. A relatively simple solution to the problem of erosion is to place a layer of large riprap on the bed at the toe of the east breakwater to act as scour protection. Given the fact that continual erosion of the west bank could ultimately lead to undermining of the curved breakwater, some form of erosion protection may eventually be required. However, for the present study, focus was given to determining how the addition of scour protection at the base of the curved steel sheet pile breakwater would affect the deposition of sediment on the east bank, and subsequently the westerly migration and continual constriction of the navigation channel against the curved breakwater face.

Two separate scour-protection scenarios were simulated using the calibrated numerical model. For simulation D, a single grid cell of scour protection (10 m wide) was added to the cells immediately adjacent to the curved breakwater (in the inlet side), with the cells being given a reduced depth (to account for a scour protection layer 1 m thick) and the inability to erode. In addition to this scenario however, a second simulation (simulation E) was run in which scour protection just south of the narrowest part of the navigation channel (at approximately the centre of the curved breakwater) was extended 30m (3 cells) into the navigation channel. This width of scour protection was subsequently reduced in both directions along the length of the curved breakwater, from 30 m down to 10 m (1 cell) at each limit. By tapering the scour protection in this way, the curvature of the navigation channel as it flows through Shippagan Gully is slightly reduced. Schematics of both of these simulations are presented in Figure 6.23 and Figure 6.24 respectively.

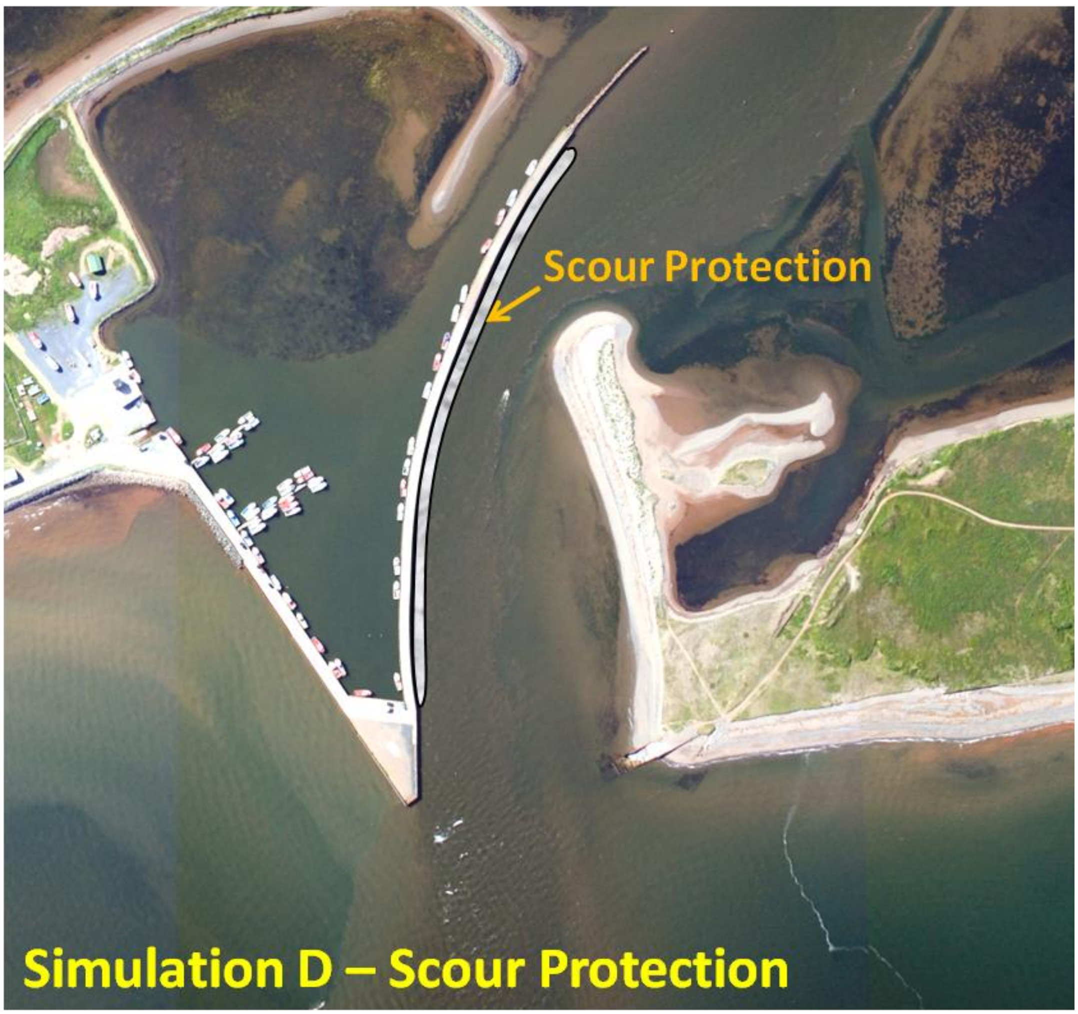

Figure 6.23: Aerial photograph of Shippagan Gully showing the location of scour protection simulated in scenario D.

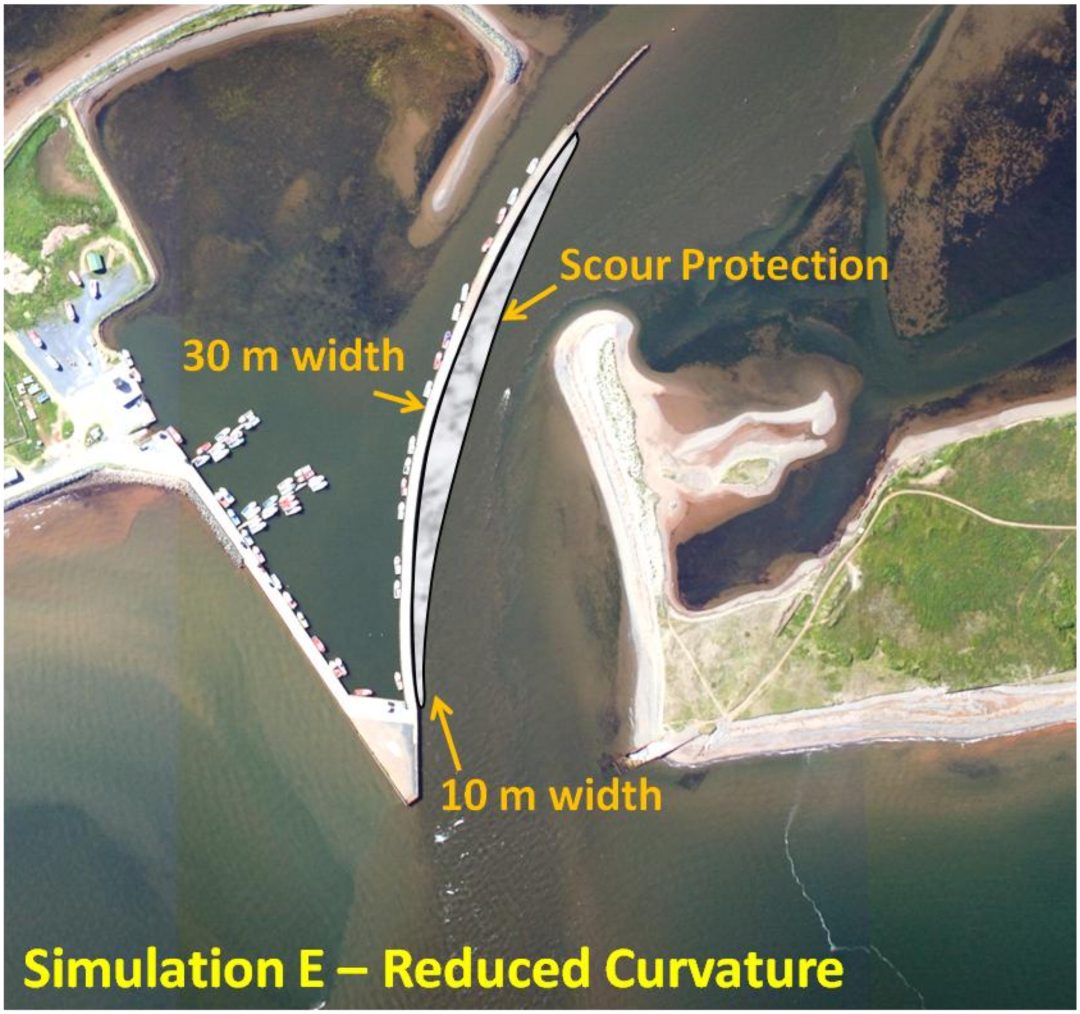

Figure 6.24: 2008 aerial photograph of Shippagan Gully showing the location of scour protection simulation in scenario E.

Morphology change maps showing erosion and deposition patterns after 6 years of simulation for both scenarios D and E are shown in Figure 6.25 below. From these maps it can be seen that, as is to be expected, the addition of scour protection on the west side of the navigation channel does not affect deposition patterns near and immediately offshore from the inlet entrance. The effects that these scenarios have on the navigation channel can be more easily discerned from the channel cross-sections, which are presented in Figure 6.26.

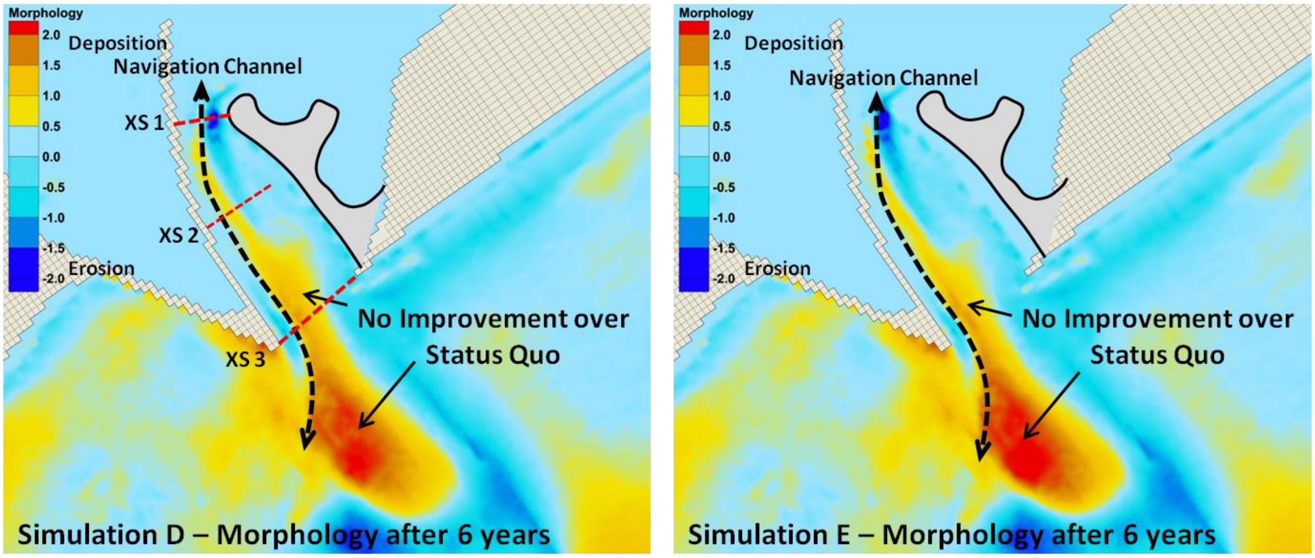

Figure 6.25: Modeled morphology change after 6 years of simulation for scenarios D and E. No significant improvement is noted compared to the status quo simulation, particularly with regards to deposition at and immediately offshore from the inlet mouth.

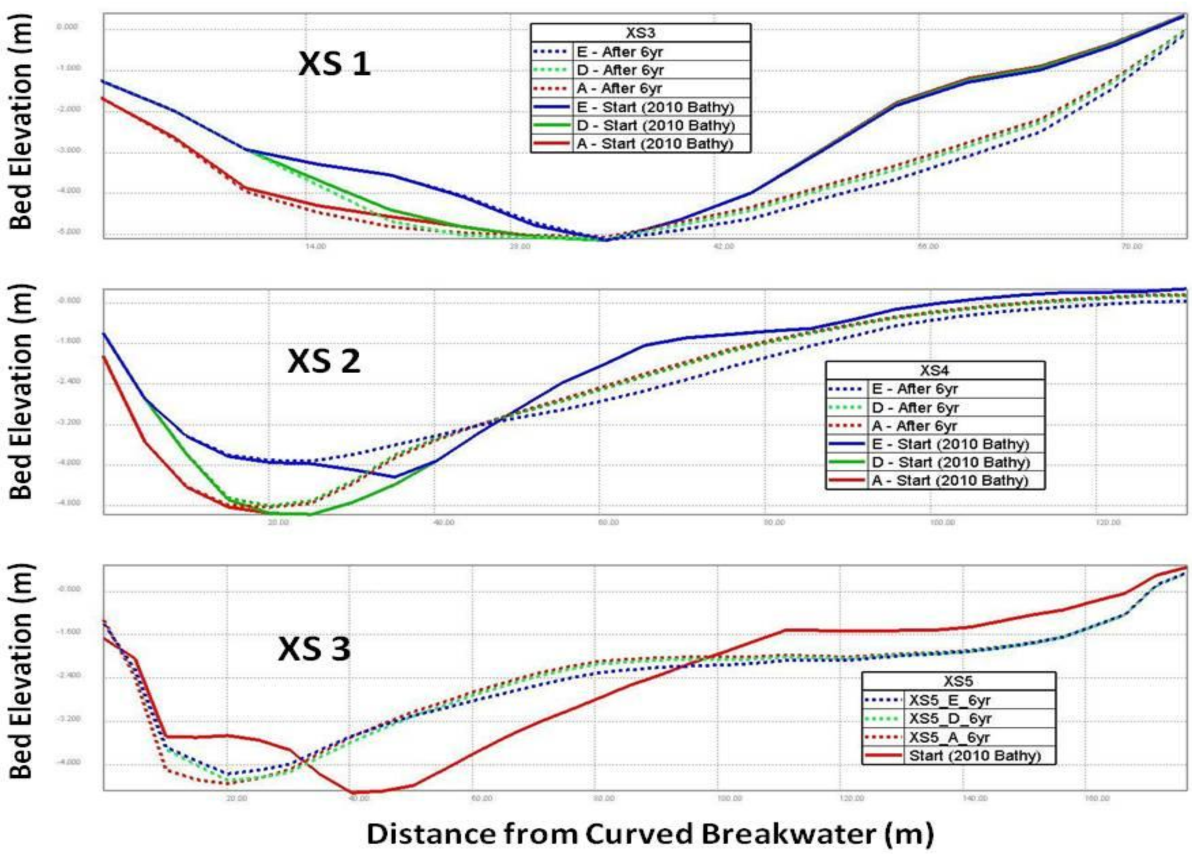

Figure 6.26: Modeled navigation channel cross-sections for scenarios A (status quo), D and E, at the beginning (solid lines) and end (dashed lines) of the 6 year simulations.

The model results presented in Figure 6.26 illustrate the effects of scenarios D and E on the navigation channel morphology. As previously mentioned, these scenarios are expected to have very little impact on the westward migration of the southern part of the channel near the inlet mouth (at cross-section 3). The model predicts that the southern part of the navigation channel (near the inlet mouth) will migrate approximately 20 m to the west over six years, for both the status quo situation (scenario A) and also for scenarios D and E. As such, scenarios D and E are unlikely to improve conditions at the inlet mouth.

The model results suggest that scenario D (10m wide revetment) has very little effect on the behaviour of the central part of the channel (cross-section 2) compared with the status quo. However, the results from scenario E indicate that reducing the curvature of the navigation channel with 30 m of scour protection at the centre of the curved breakwater would result in a widening of the channel by approximately 5 m after 6 years. However, the adverse effects of introducing a 30 m wide layer by 1 m thick layer of scour protection on the west bank (scenario E) can be clearly seen. The navigation channel already passes very close to the curved breakwater wall at this location, and armouring the seabed with riprap at this location would greatly infringe upon the channel and pose a significant threat to safe navigation through the inlet. This is due to the 1 m decrease in available depth on the west side of the channel which is clearly visible in cross-section 2 and the significant hardening of the bed which poses a greater danger to vessels. Hence, it is reasonable to conclude that implementing scenario E could degrade the navigability of the channel.

The trends in the northern part of the channel, at cross-section 3, are similar to those at cross-section 2. The model results suggest very little change in navigable depths on the east side of the channel for scenarios D or E, compared to the status quo. Moreover, the new riprap makes the western side of the channel shallower and harder, and thus less navigable. Hence, it is reasonable to conclude that scenarios D and E are unlikely to improve the navigability of the shipping channel through Shippagan Gully. However, it should be noted that if erosion of the west bank continues as is expected, undermining of the curved breakwater may become a structural issue. If this should occur, it may be necessary to install scour protection to prevent undermining and failure of the curved breakwater structure.

6.2.4 Parallel Training Wall (H1a, H1b, H1c, H2a, H2b and H2c)

Given the fact that scenarios D and E did not provide adequate improvement over the status quo with regards to the westerly migration of the navigation channel, an alternative approach was formulated. This new approach involved adding a second curved breakwater, also known as a training wall (a structure which guides flow), parallel to the existing curved breakwater but on the opposite side of the navigation channel. The goal of this configuration is to fix the position of the east side of the channel and regulate flow through the inlet by creating an approximately constant cross-sectional flow area by which the tide-induced currents can enter and exit the tidal lagoon. This technique of constructing parallel training walls at coastal inlets is not uncommon, and an example of this configuration of structures is shown in Figure 6.27 for a coastal inlet located on the Pacific coast in Oregon.

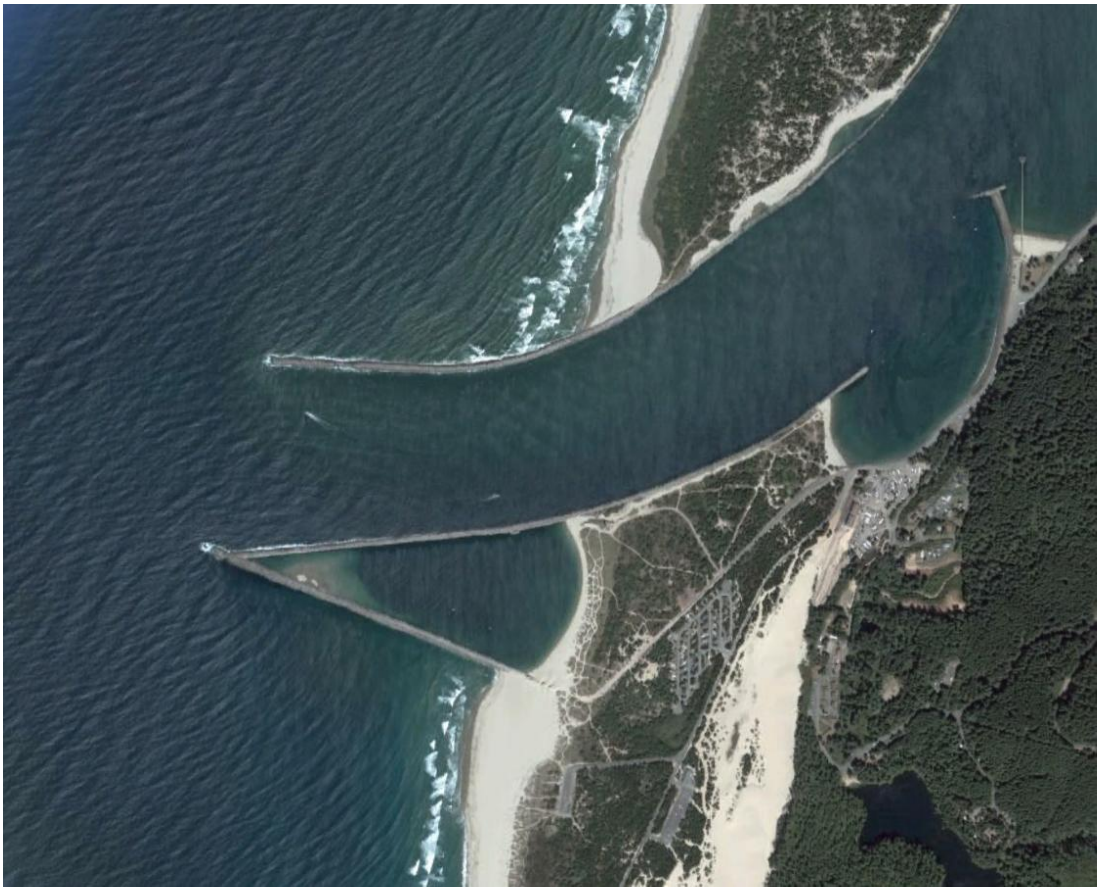

Figure 6.27: Umpqua River inlet in Oregon. An example of the use of parallel curved training walls to guide flow through a coastal inlet and stabilize its position for navigational purposes (Google Earth, 2011).

When assessing a parallel training wall configuration for Shippagan Gully, two key variables must be considered. First, the width of the navigation channel and subsequently the flow area will be controlled by the distance at which the parallel wall is placed from the existing curved breakwater. A wider channel creates a larger two-dimensional area in which to navigate, but may also promote slower velocities and increased siltation. A narrower channel on the other hand will promote higher flow velocities through the inlet, thus increasing the inlets ability to self-scour, a process which helps keep the channel clear of unwanted sediment deposition. A narrower channel therefore typically corresponds to a deeper channel, providing greater depths in which to navigate.

The second key parameter with regards to a parallel training wall configuration is the length at which the structure will extend in the offshore direction. At the inlet mouth, the parallel training wall becomes a shore-perpendicular jetty, as was previously simulated and discussed in Section 6.2.2. As such, its length and orientation can be manipulated depending on its desired effect with regards to entrapment and/or diversion of longshore sediment transport and sheltering from incoming waves.

Several different training wall configurations were simulated in order to investigate the influences that these parameters (channel width and training wall length) may have on the future patterns of morphology change at Shippagan Gully. In order to assess the effects of the channel width on hydrodynamic and sedimentary processes, two different widths were tested. In one case a parallel training wall was added 140 m away from the existing curved breakwater; while in the other case, the two structures were separated by 80 m. Both of these training walls were then simulated with three different configurations at their southern limit. These configurations corresponded to the orientations and dimensions that were tested and discussed in Section 6.2.2 above, where the jetty was simulated independently (70m jetty, 140m jetty and 140m elbow jetty). Figure 6.28 shows the various training wall scenarios that have been simulated.

Figure 6.28: Layout of parallel training wall configurations assessed using the calibrated numerical model.

The impacts of scenarios H1a through H2c were simulated for a period of 6 years (the same as the other long term simulations). The initial elevation of the seabed between the two curved walls was set to a minimum depth of 1.5 m, to ensure that there was flow across the entire width of the channel in the numerical model.

The results from each simulation were analysed and compared to both each other, and to the status quo situation (scenario A). A map of morphology change for the status quo situation (full 6 year simulation) and bathymetric contours at the beginning and end of the 6 year simulation for the status quo situation are repeated in Figure 6.29, Figure 6.30 and Figure 6.31 for reference. Similar maps of modeled morphology change and future bathymetric contours (after 6 years) for simulations H1a – H2c are presented below in Figure 6.32 and Figure 6.33.

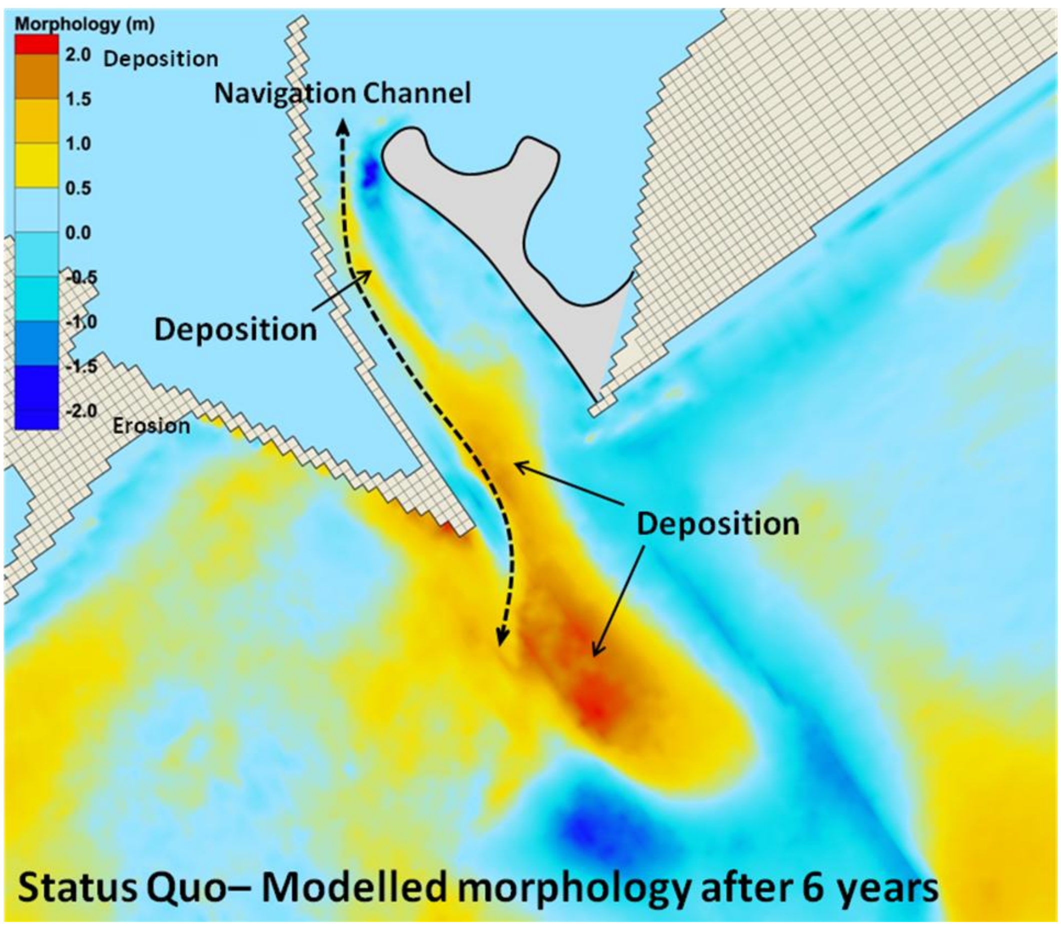

Figure 6.29: Modeled morphology change after 6 years for scenario A - status quo (repeated from Figure 6.17).

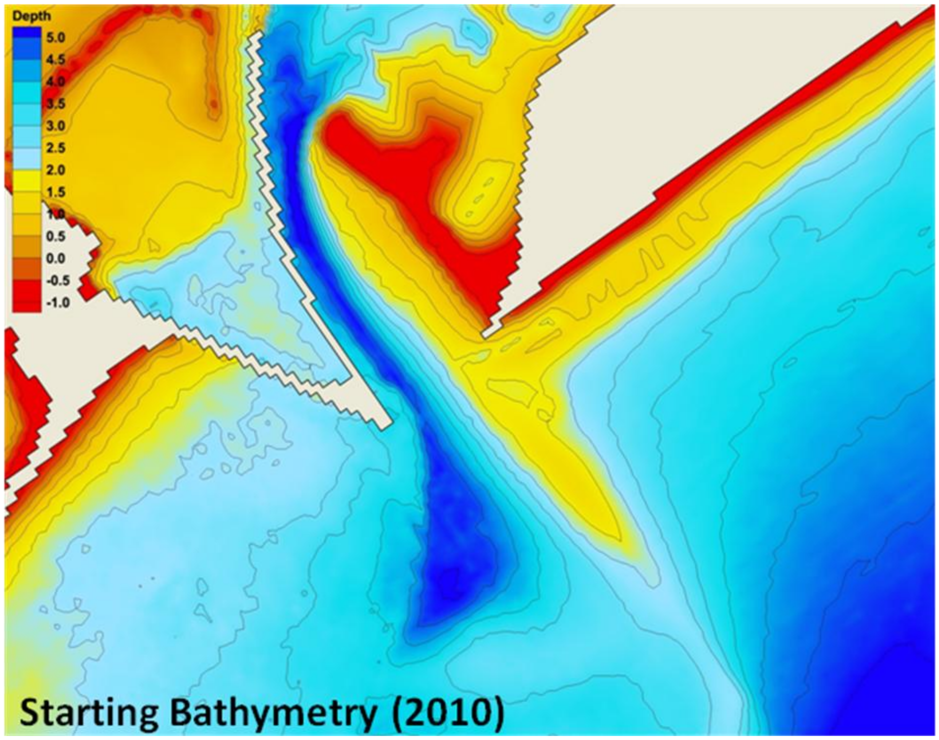

Figure 6.30: Initial bathymetry (repeated from Figure 6.15).

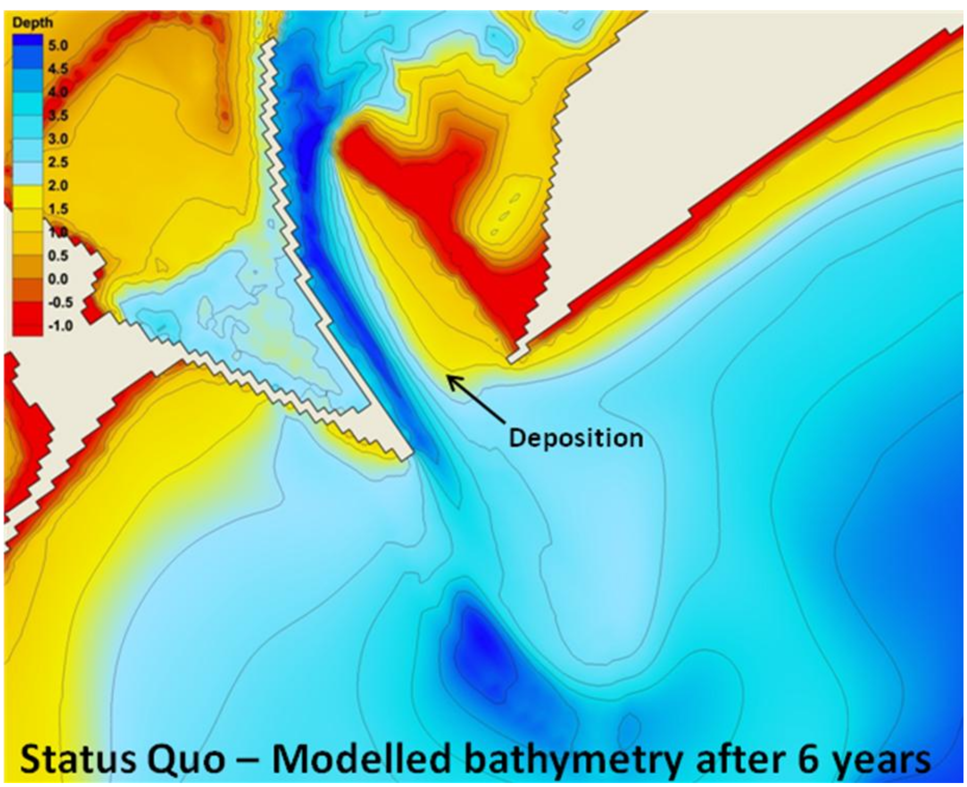

Figure 6.31: Modeled bathymetric contours after 6 years for the status quo scenario.

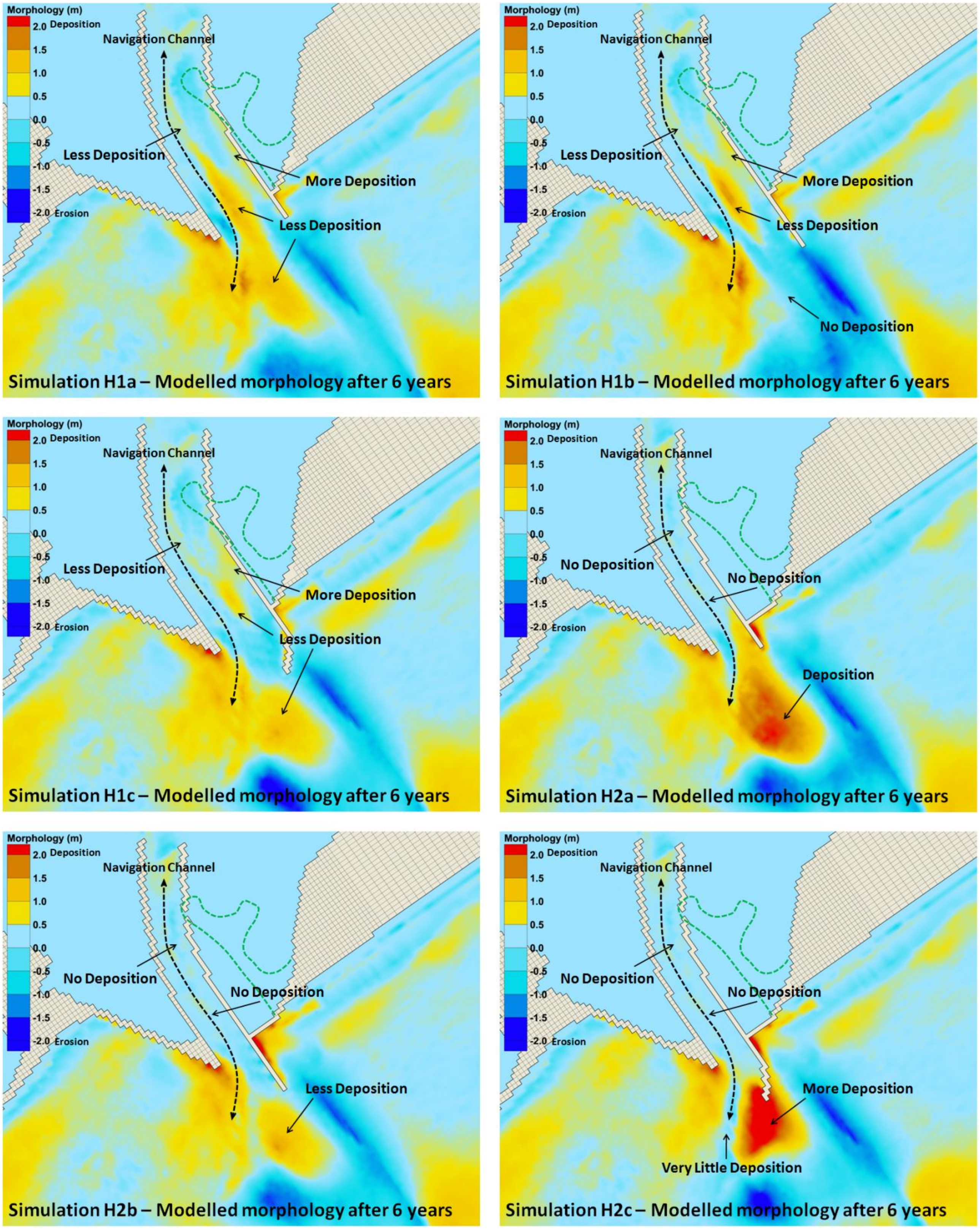

Figure 6.32: Modeled morphology change after 6 years for scenarios H1a – H2c.

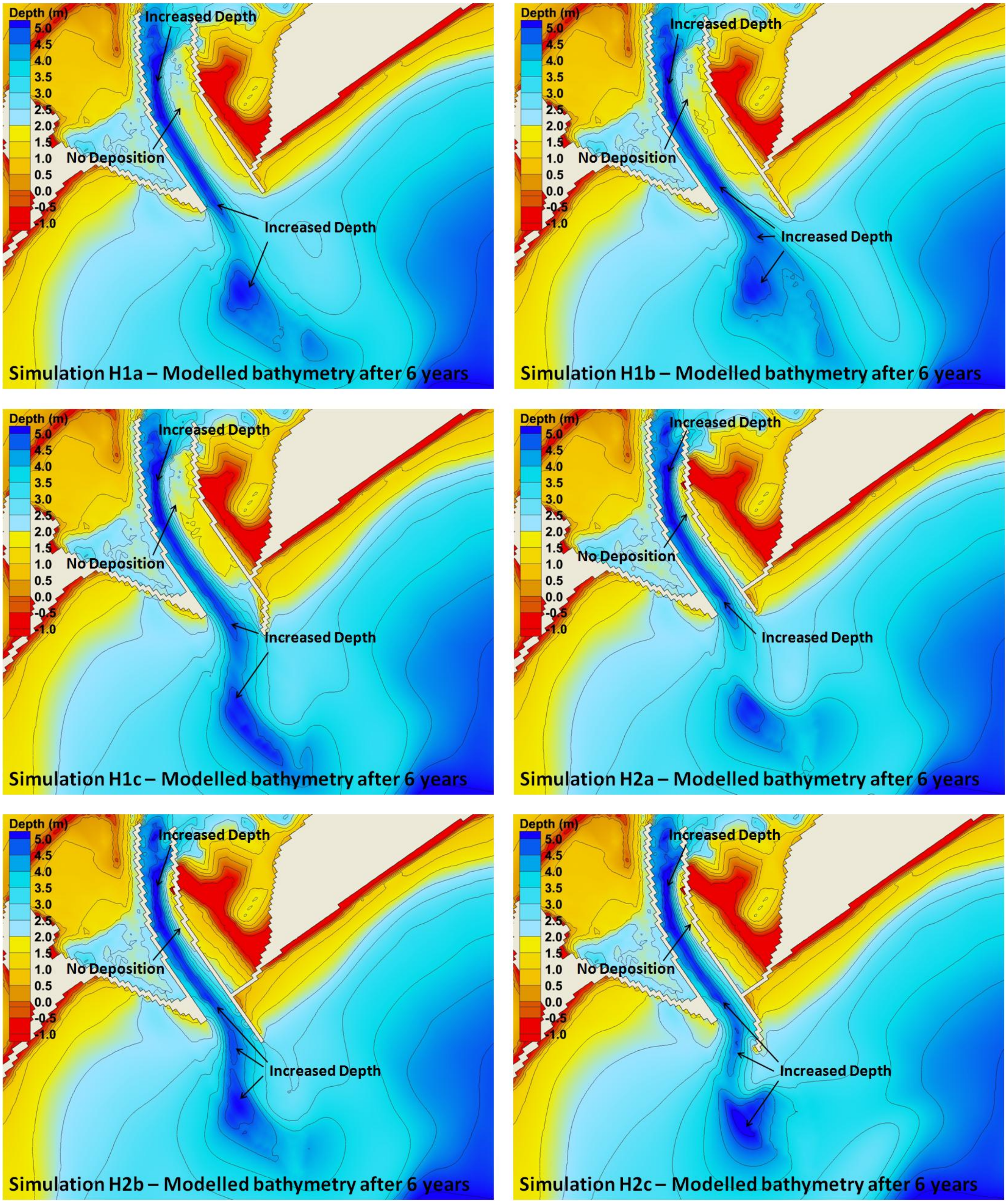

Figure 6.33: Modeled bathymetric contours after 6 years for scenarios H1a – H2c.

Several important observations can be made from the results presented in Figure 6.32 and Figure 6.33. First, in comparing the parallel training wall simulations H1a – H2c (with a minimum depth of -1.5m across the inlet) to the results from the status quo, it can be seen that with the exception of the offshore deposition denoted in simulations H2a and H2c, all six scenarios predict significantly less deposition within the inlet, at the inlet mouth and immediately offshore from the inlet mouth. Thus, regardless of the channel width or jetty configuration, the parallel training wall option appears to offer a general improvement over the status quo situation.

Comparing the H1 simulations (140 m wide channel) to the H2 simulations (80 m wide channel), it can be seen that although both scenarios reduce the deposition within the inlet (compared with the status quo), the reduction is greater when the channel is narrower (H2). The model predicts that very little sediment will be deposited within the 80 m wide channel, slightly more sediment will be deposited within the 140 m wide channel, and the most sediment will be deposited under the status quo situation. In fact, with the parallel training wall modeled at a distance of 80 m from the existing curved breakwater, the numerical model predicts that virtually no deposition will occur within the channel at all. As such, the model results indicate that a training wall placed in this location would create a self-scouring channel in which navigable depths can be maintained, and the migration of the channel would be halted.

In order to further illustrate this result, contour maps of depth-averaged current speed at peak ebb-tide flow are presented in Figure 6.34 below for the status quo situation (simulation A), for simulation H1b (140 m wide channel), and for simulation H2b (80 m wide channel). In Figure 6.34, areas of moderate velocity (speed < 0.75 m/s) are observed along the eastern edge of the navigation channel for scenarios A (status quo) and H1 (140 m wide channel). These zones with lower flow speeds are most prominent in the status quo simulation, although lower velocity zones persist in the H1 results as well. Deposition will likely outpace erosion in these areas. For the H2 configuration (narrower channel), higher flow velocities are maintained across the entire width and length of the channel. For this reason, the narrower channel provides the most favourable conditions for reducing deposition within the navigation channel.

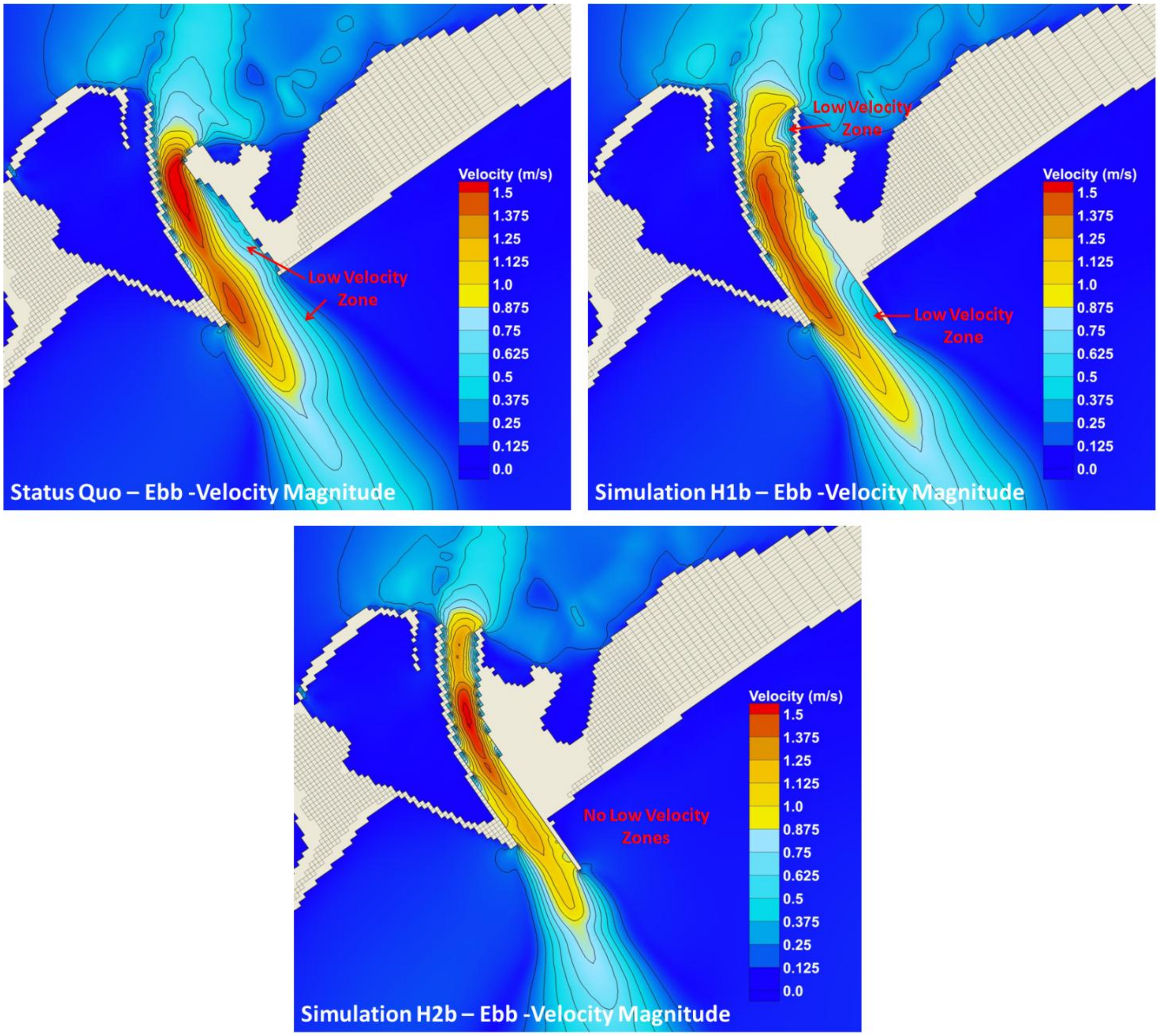

Figure 6.34: Contour maps of depth-averaged current speed at peak ebb-tide flow for simulations A (status quo), H1b (140 m wide channel) and H2b (80 m wide channel).

In addition to the reduced deposition well into the inlet, the numerical model indicates that deposition just inside the inlet mouth is reduced by all three H1 scenarios, and practically eliminated in the H2 scenarios. As was previously discussed, deposition in this zone is wave dominated. As such, the improvements in this area are likely due to the improved sheltering from waves provided by the east jetty. Furthermore, the narrower inlet mouth featured in scenarios H2a, b and c greatly decreases the wave energy inside the inlet. Thus, the H2 simulations (a,b and c) provide the most shelter to wave attack, and subsequently the least amount of sediment deposition immediately inside the inlet.

Deposition in the area immediately offshore from the inlet mouth is wave-dominated and is primarily controlled by the orientation and dimensions of the east jetty. This was discussed in detail in Section 6.2.2 above, and the same conclusions hold true for the parallel training wall simulations discussed here. However, another important factor in the offshore deposition is that sediment which was deposited in the inlet under status quo conditions is now being transported out of the inlet in the H1 and H2 simulations. As such, the numerical model indicates that the volume of sediment being deposited in the region immediately offshore from the inlet mouth is slightly larger with a parallel training wall in place. This increased deposition outside the inlet is an unfortunate trade-off of increased scouring inside the inlet.

As can be ascertained from Figure 6.33 above, the numerical model indicates that, of the scenarios studied, scenario H2b provides the best combination of decreased deposition within the inlet combined with increased depths immediately offshore from the inlet mouth. This scenario is, in essence, a combination of a narrower channel stabilized with a parallel training wall, and the 140 m jetty that was simulated in scenario B5. It should once again be cautioned however, that a long, straight jetty can be expected to trap a great deal of longshore sediment transport on its updrift side. As such, consideration must be given to the potential downdrift effects (beach erosion) which could be incurred should the natural sediment bypassing around Shippagan Gully be temporally or permanently interrupted.

6.2.4.1 Northern extent of Parallel Training Wall (I2 and I3)

An important consideration with regards to the potential implementation of a parallel training wall at Shippagan Gully, is the northern extent (within the tidal lagoon) at which the structure should end. Since waves have been shown to have no influence on the hydrodynamics at this location, a relatively simple numerical model analysis of ebb-tide currents can be undertaken in order to assess the appropriate length of the northernmost end of a parallel training wall. Short term hydrodynamic simulations were therefore run using the calibrated numerical model in order to address this topic. These short-term simulations excluded both waves and transport, and were run for a 5 day period that included the maximum spring tide.

Four separate simulations were completed in order to assess the effects of altering the northern configuration of the parallel training walls which were discussed in Section 6.2.4 above. The first two simulations (I2a and I2b) were based off of the H1 simulations (140 m wide channel) while the other two simulations (I3a and I3b) were based off of the H2 channel configuration (80 m wide channel). Schematics of these four scenarios are presented in Figure 6.35 below.

Figure 6.35: Definition sketch of layouts for scenarios I2-a, I2-b, I3-a and I3-b.

The relative performance of the 80 m wide and 140 m wide channels have been considered previously in Section 6.2.4. Hence, simulations I2 and I3 will be discussed separately below.

Figure 6.36 shows contour maps of modeled depth averaged velocity at the time of peak ebb flow (maximum spring tide) for scenarios I2-a and I2-b. The only difference between the two simulations is that the parallel training wall on the east side of the inlet is 100 m longer in scenario I2-b, with its northernmost end approximately opposite the end of the existing curved breakwater (not including the 100m of degraded sheet pile and rock at its end).

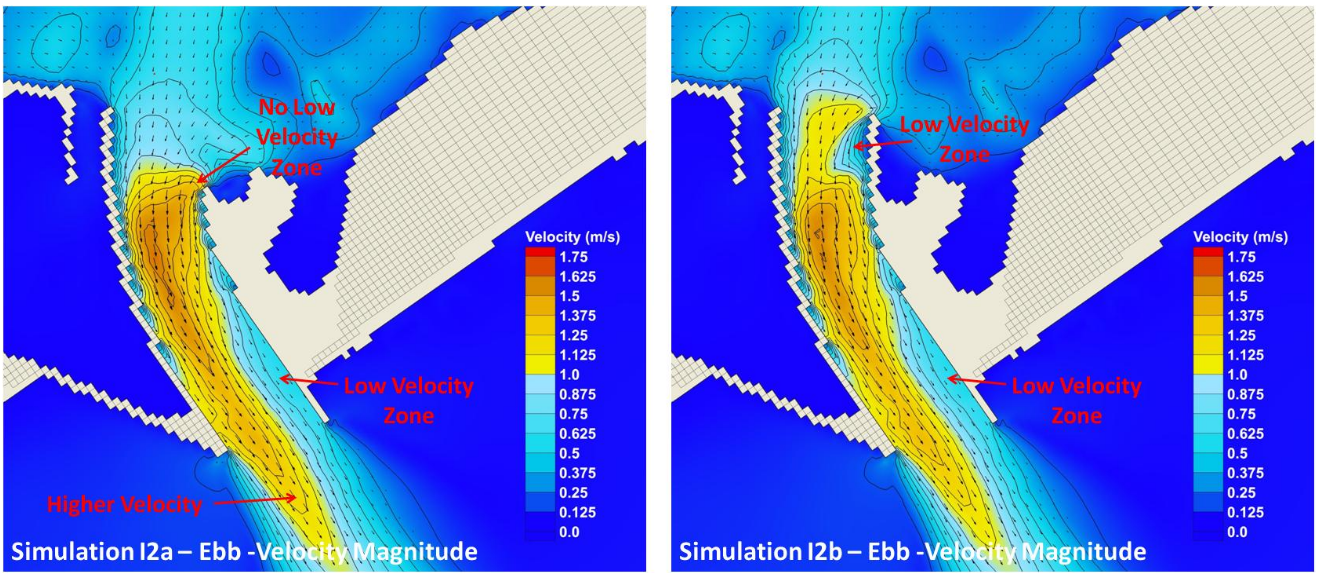

Figure 6.36: Modeled velocity contours at peak ebb-flow (maximum spring tide) for scenarios I2-a (left) and I2-b (right).

As can be seen in Figure 6.36, the training wall which extends further into the tidal lagoon (I2-b) creates an obstruction around which the secondary ebb-flow approaching from the eastern part of the tidal lagoon must flow. As this current passes around the northern tip of the parallel training wall and enters the main channel, it causes the main ebb flow to deviate from the training wall, thereby creating a calm area within the channel adjacent to the northern part of the training wall. This low velocity zone is in addition to the one located near the inlet mouth that was identified previously in Section 6.2.4. Both of these lower velocity zones can be clearly seen in Figure 6.36b (right). It is likely that sediments will tend to accumulate in these lower velocity zones.

In scenario I2-a on the other hand, where the training wall is 100 m shorter, the ebb-flow follows a less curved flow path; it approaches the inlet more directly and does not separate from the training wall. This is clearly a better flow condition for avoiding siltation. In addition to creating a northern entrance to the inlet which is less susceptible to sediment deposition, the numerical model indicates that the shorter parallel training wall actually promotes a slight increase in velocity inside the inlet and offshore from the inlet mouth. This increases the potential for self scouring and produces a more powerful ebb-jet capable of pushing sediment further offshore.

Figure 6.37 shows contour maps of modeled depth averaged velocity at the time of peak ebb flow (maximum spring tide) for scenarios I3-a and I3-b, in which the navigation cannel is only 80 m wide. Again, the difference between these two simulations is that the parallel training wall on the east side of the inlet is 100m longer in scenario I3-b, with its northernmost end approximately opposite the end of the existing curved breakwater (not including the 100m of degraded sheet pile and rock).

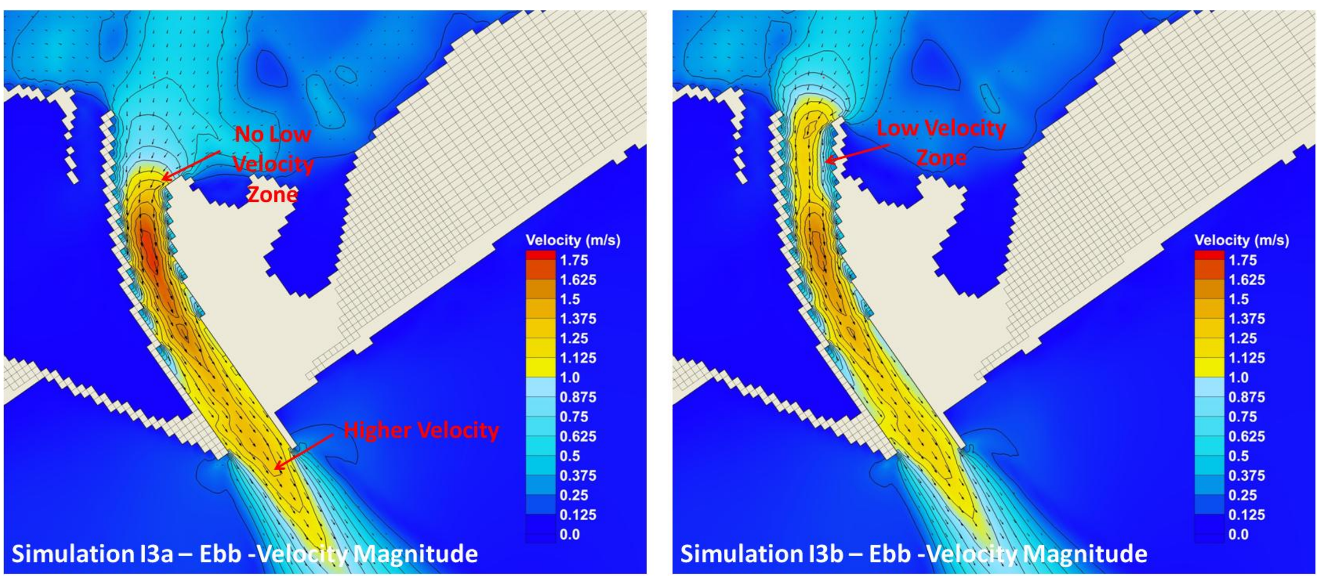

Figure 6.37: Modeled velocity contours at peak ebb-flow (maximum spring tide) for scenarios I3-a (left) and I3-b (right).

The results for these two scenarios are similar to those for scenarios I2-a and I2-b, discussed above. The results presented in Figure 6.37 illustrate that the shorter training wall helps create hydrodynamic conditions that are less likely to promote sediment deposition within the channel. As with the wider channel, the secondary ebb-flow which approaches the inlet from the east is forced around the tip of the longer parallel training wall, creating a low-velocity zone in its lee. This zone creates the potential for sediment deposition and should therefore be avoided.

Additionally, similar to the results for the I2 scenarios, the model results for the I3 scenarios indicate that the shorter parallel training wall promotes stronger ebb-current velocities through the inlet. This increase in velocity is likely to result in improved scouring of the inlet and will help promote a stronger ebb-jet capable of pushing sediment further offshore.

6.2.5 Northern Extent of Existing Curved Breakwater (I1)

A further consideration with regards to the configuration of structures at Shippagan Gully is the required length of the existing curved breakwater. Presently, the northernmost 100 m of this structure is composed of severely degraded (particularly above LWL) sheet pile and rubble. As such, a recent topic of discussion has been whether or not this portion of the breakwater should be replaced. At this location, nearly half a kilometre inside Shippagan Gully, the effects of waves have been shown to be insignificant. As such, ebb-tide currents govern the hydrodynamics in this region, and their flow paths must be examined in greater detail in order to address this consideration. Ebb-tide flow paths, as understood and described by locals, are presented in Figure 6.38 overlaid on a 2008 aerial photograph of Shippagan Gully.

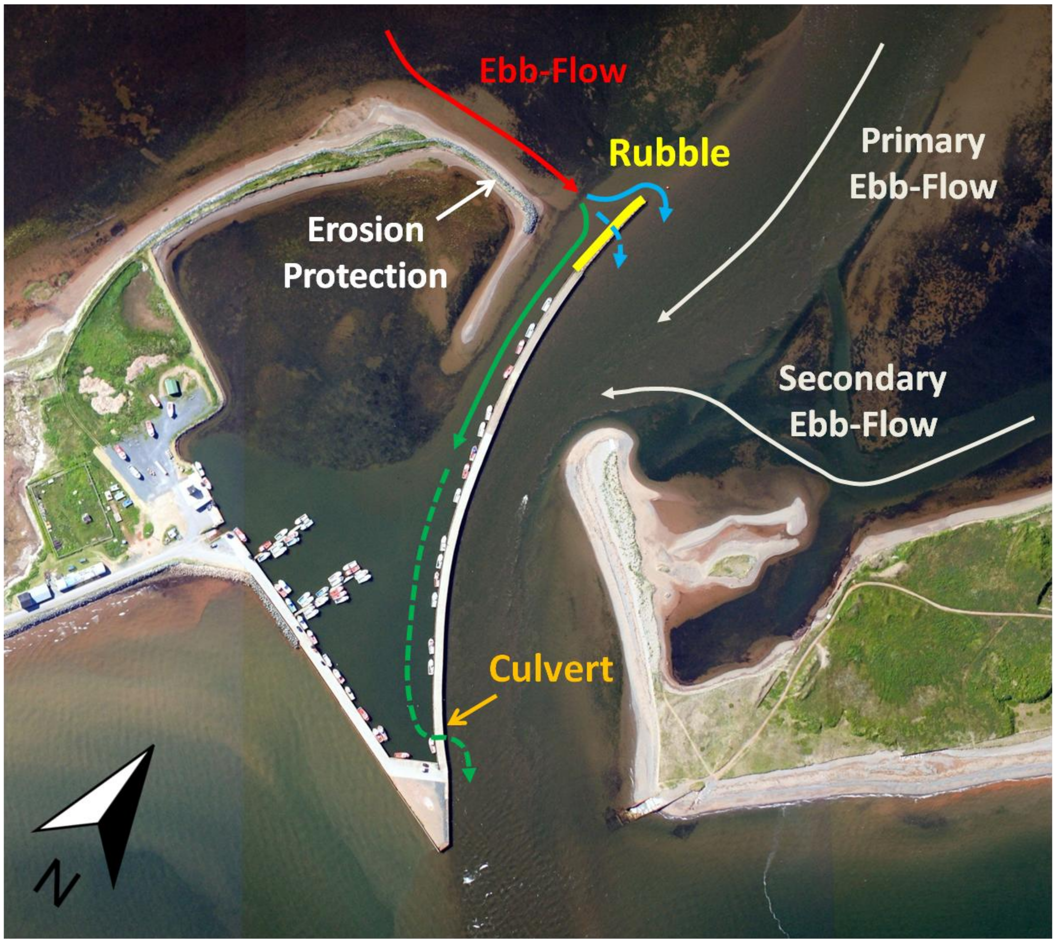

Figure 6.38: Ebb-tide flow paths at Shippagan Gully.

From Figure 6.38 it can be seen that in addition to the primary and secondary ebb-flow paths discussed in Section 4.3 (which approach Shippagan Gully from the north and east respectively), there is a third, weaker flow path by which ebb-currents arrive at the inlet from the northwest (shown in red in Figure 6.38). This third flow path approaches the inlet from the portion of the tidal lagoon to the northwest of Shippagan Gully which is separated from the small craft harbour by a narrow spit. According to locals, this spit has been severely eroded in the past by this tertiary current. Erosion along the spit progressed to a degree at which rock was placed on the beach in order to prevent the spit from being breached, which would compromise the integrity of the small craft harbour (see Figure 6.38).

As the tertiary flow path approaches the inlet from the northwest, it is obstructed by the 100 m of degraded breakwater at the northern end of the structure. In the numerical model, the cells over the degraded breakwater are represented as being approximately 0.5 m below the geodetic datum. As such, water will flow over the structure most of the time but at a much reduced depth (instances in which water is able to flow over the rubble mound in the numerical model can be assessed from Figure 4.17). Although some of flow may be forced through voids in the rubble and some likely passes around the northern end of the structure (shown as blue arrows in Figure 6.38), the vast majority of the flow is observed to enter the small craft harbour, where it follows the curvature of the curved breakwater on its leeward side. This, along with the natural configuration of the small craft harbour, causes the water level in the harbour to be slightly higher than in the inlet. This head gain is regulated by the presence of a culvert near the southern tip of the curved breakwater, which allows water to exit the harbour at its southern limit and join the primary flow path near the inlet mouth.

In light of the existence of this third flow path, the question has been posed as to whether or not removing the northernmost 100 m of degraded breakwater would in fact improve the hydrodynamics at Shippagan Gully. Unfortunately, since the primary focus of this study was to examine sediment deposition in the navigation channel and along the eastern side of the inlet with respect to various structural configurations, the area to the north east of the inlet and the small craft harbour were not represented in the numerical model with high resolution. Furthermore, no measured bathymetry was available for this region of the tidal lagoon. As such, the numerical model was not calibrated to simulate flows in this region, and could not be used to reliably investigate this question.

Engineering judgement and experience can however be applied to provide guidance on what *could* be expected to occur, should the northern 100 m of degraded breakwater be removed. If this obstruction were removed, the tertiary ebb-flow which approaches the inlet from the north-west would like rejoin the primary flow path at the northern end of the inlet. As such, the flow rate through the confines of the inlet would likely be slightly increased, relative to the portion of ebb-flow which follows this tertiary path. This would likely be beneficial to the inlet, as it would result in slightly higher scour potential through the channel during the ebb-tide. In addition to the added flow rate, the tertiary flow would enter the main channel of the inlet on a bend opposite to that which is followed by the primary flow path. Therefore, this additional flow would likely not contribute to additional ebb-tide induced deposition on the east side of the inlet (along the inside of the channel bend). In fact, a slight *reduction* in ebb-tide deposition may be incurred due to the fact that this introduction of flow from the west may slightly reduce the bend in the primary ebb-flow pathway at the inshore end of the inlet.

An additional potential benefit to removing the northern 100 m of degraded breakwater is that less flow will be diverted into the small craft harbour, subsequently resulting in a reduction in head gain relative to the navigation channel. It can therefore be expected that a reduction of flow into the sheltered harbour will result in a reduced potential for siltation.

It should be strongly noted that the points listed in the previous paragraphs are not based on data nor are they based on numerical model results. These remarks are educated speculations only and should therefore be treated accordingly.

7.0 Conclusions

The present study has been successful in identifying the governing coastal processes responsible for the complex morphology which is present at Shippagan Gully. A detailed and accurate knowledge of the local wave climate has been developed and a good understanding of the local water levels has been obtained. From this information, a coupled numerical model of the hydrodynamic and coastal processes at the inlet was developed using the numerical models CMS-Flow and CMS-Wave, accessed through the SMS user interface. With data measured during an August 2010 field investigation campaign supplemented by an understanding of historical morphology change obtained from an analysis of geo-referenced aerial photographs and dredging records, the numerical model was successfully calibrated with regards to both hydrodynamics and morphodynamic evolution. The calibrated model was therefore able to simulate the complex hydrodynamics at the site due to the combined effects of waves and tides with fairly good accuracy. However, due to the complexity of the site and the limitations of CMS-Flow (one of the most advanced coastal modeling tools available today), the long-term changes in morphology could only be modeled in an approximate manner.

Using the calibrated numerical model as a tool, simulated morphodynamic trends were analysed in order to determine where sediment was deposited, when the deposition occurred, and the coastal processes responsible for the deposition. It was determined that three inter-related processes were primarily responsible for the decreasing navigability of Shippagan Gully. The navigation channel has been shown to migrate further and further to the west each year, ultimately becoming narrower as it approaches the curved breakwater on the west side of the inlet. The numerical model indicates that this migration is caused by the strong ebb-tide currents which follow a curved flow path as they exit Shippagan Gully. This bend in flow causes outward erosion of the west bank, while depositing sediment along the east bank of the navigation channel.

A second morphological process identified at Shippagan Gully is the deposition of sediment at, and immediately offshore from the inlet mouth. This sediment has been shown to arrive at the inlet from the northeast as longshore transport (littoral drift). This net longshore transport is created by the local wave climate which is dominated by large easterly waves. Under certain wave conditions, the longshore transport has been shown to carry sediment along the extensive crescentric ebb-shoal which exists offshore from the inlet, subsequently returning sediment to the shoreline down-drift of Shippagan Gully (to the southwest). Some of the sediment arriving at the inlet is however deposited in the shallow waters in lee of the ebb-shoal and on the east side of the inlet mouth, where ebb-flow velocities and associated scour potential are small.

The third and final morphological process identified at Shippagan Gully is the above-LWL deposition of sediment along the eastern side of the inlet, and at elevations along the berm exceeding 2 m. The numerical model indicates that this deposition is caused by storm waves accompanied by storm surge, which allows larger, more energetic waves to propagate further into the inlet than would otherwise occur during the normal tidal range. These larger waves are capable of transporting sand from the ebb shoal into the inlet where the sediments are deposited along the east side of the inlet. The main sedimentary processes identified at Shippagan Gully are summarized in Figure 7.1.

Figure 7.1: Summary of identified deposition zones and responsible coastal processes, overlaid on a 2008 aerial photograph of Shippagan Gully.

The calibrated numerical model was successfully applied to study the possible effects of maintaining the status quo at Shippagan Gully. From these simulations it was determined that both sediment deposition and westerly migration of the navigation channel are likely to continue if no intervention is made. The model suggests that future deposition will be most significant at and immediately offshore from the inlet mouth. It also indicates that the narrowest part of the channel may be approaching a cross-sectional equilibrium state. It is important to note however that this is not sufficient to ensure the navigability of the system.

Several alternative human interventions (design scenarios) have been formulated in an attempt to seek improvements to the status quo. These scenarios were created based on the developed understanding of coastal and morphological processes discussed herein. Several east jetty configurations were proposed and tested, in order to analyse the effects of placing a new jetty on the east side of the inlet mouth. It was determined that an east jetty can be effective in trapping or partially diverting littoral drift approaching from the northeast, subsequently reducing deposition within and immediately offshore from the inlet mouth. The numerical model indicates that a long, shore-perpendicular jetty provides the best improvements in these regards. Furthermore, a jetty which provides protection from waves in general and easterly waves in particular has been shown to be highly effective in reducing sediment deposition inside Shippagan Gully. This can be achieved by locating the jetty further to the west (reducing the width of the inlet mouth), and/or by introducing a southerly bend in the jetty plan-form. However, care must be exercised in placing a jetty, particularly a long, shore-perpendicular jetty, at a coastal inlet such as Shippagan Gully where natural sediment bypassing has been shown to occur. The introduction of a sediment trapping structure could (temporarily) interrupt the natural bypassing of sediment, subsequently reducing the sediment supply to the down shore region and potentially creating erosion. Hence, the benefits of extending the existing jetty must be balanced against the potential for increased shoreline erosion southwest of the inlet.

In order to address the westerly migration of the navigation channel, several alternative scenarios were simulated and assessed. Armouring the west bank of the navigation channel has been shown to slow (or halt) erosion, providing a possible solution for protecting the curved breakwater from eventually being undermined. The armoured bank does not however result in a significant decrease in sediment deposition on the eastern bank, and subsequently does not appear to help stabilize or widen the navigation channel.

Additional armouring at the centre of the curved breakwater was investigated, in order to protect the bank against erosion while simultaneously reducing the curvature of the primary flow path through the inlet. However, the reduced navigational depths due to the addition of scour protection in the channel far offset the slight improvement in deposition patterns on the east side of the channel. As such, armouring the west bank of the navigation channel has not been shown to improve the navigability nor the morphodynamic trends at Shippagan Gully.

Several inlet configurations with parallel training walls were studied in which a curved structure is constructed on the east side of the navigation channel, parallel to the existing curved breakwater. The bathymetry in these scenarios was adjusted such that a minimum depth of 1.5 m was obtained between the parallel structures (in the channel). This was done in order to ensure flow across the entire newly defined channel. Numerical model results indicate that adding a parallel training wall is an effective means of reducing deposition within the channel. Of the two primary training wall configurations that were investigated, the configuration that creates an 80 m wide navigation channel performed better than the one that creates a 140 m wide channel (although the model indicates that both options offer an improvement over the status quo). Attention must be given to the northern limit of the parallel training walls, to ensure that low-velocity zones are not created within the channel during the ebb flow, caused by flow entering the channel at right angles to the channel axis. Low-velocity zones of this nature should be avoided as they will tend to act as sediment traps: calm areas in which transported sediments can be deposited.

Another viable option that was not investigated in the present study is to institute a program of mechanical dredging to maintain a channel with sufficient depth and width for safe navigation. Historical evidence suggests that dredging was used to maintain the navigation channel at Shippagan Gully throughout much of the 20th century. A cost benefit analysis would however have to be completed to assess this option, as both the present study and the extensive history of the site have shown that considerable mechanical dredging would have to be performed regularly in order to maintain adequate navigable depths.

Finally, the author would like to stress that Shippagan Gully is an immensely complicated coastal inlet, due to the asymmetry of tidal forcings, the numerous historical human interventions, the vast supply and mobility of coastal sediment, and the highly complex interaction of both hydrodynamic and morphodynamic coastal process. Based upon the findings of this study, a much better understanding of the complexities present at Shippagan

Gully has been achieved. Reasonable estimates of the changes to be expected in future for the status quo option and for a wide range of plausible human interventions have been determined. The level of confidence for these estimates however is limited by a lack of detailed field data and by the inherent limitations of the CMS-Flow model. In future, the level of confidence and precision of the numerical modeling could be improved significantly if it were supported with additional field data on sediment properties and spatial sediment distribution.

Despite the uncertainties, the knowledge and information generated by this study can be used by PWGSC to help make informed decisions concerning future human interventions at Shippagan Gully and their impacts.

7.1 Future Work

The present study has been successful in improving our understanding of the complex morphology at Shippagan Gully and has provided a good basis upon which future works can be assessed. This work is however only a stepping stone from which future work can and should be completed.

Throughout the course of this study, a number of topics have been encountered which would have been extremely interesting to pursue had the project time-line and scope of work permitted it. For example, a large portion of the sediment deposition within Shippagan Gully was shown to be a direct result of wave action. The relative magnitude of this wave action and subsequent sediment transport inside the inlet was further shown to be highly sensitive to changes in water level, with deposition being significantly more abundant under storm surge conditions. It would therefore be very interesting to assess the impacts of climate change on the inlet morphology at Shippagan Gully. This could be done by simply applying various water level changes to the model based on results from climate change forecasting models which are widely available.

In addition to assessing the impacts of climate change, it would be beneficial to look at individual storm events at a higher resolution, particularly where reliable measured wind and wave data exist. The present study modeled generic storms only based on idealized wave climates for statistical return period events. This analysis showed that storm-waves, particularly when accompanied by significant surge, are capable of transporting a great deal of sediment into Shippagan Gully and depositing it at elevations above the LWL on the east side of the inlet. If the coupled numerical model used in this study were applied at a higher temporal resolution to individual storm events, much more detail could be obtained regarding storm-induced morphology at Shippagan Gully. Furthermore, if reliable wind and wave data were obtained, a numerical estimate for storm surge could be computed by CMS-Wave, which was not done for the present study.

Much of the confidence attributed to numerical model results comes from the degree of certainty and accuracy obtained through the calibration process. In the case of the present study, morphological calibration was extremely difficult due in large part to a lack of information regarding sediment properties below the water level. Presently, properties of the bed material throughout the navigation channel were estimated based on a small amount of data obtained from the shoreline during the field investigation and adjusted throughout the calibration process. It is likely that a more accurate model which produces a greater level of confidence in its results could be obtained if the bed material present within Shippagan Gully was properly assessed.

Finally, in the relatively short amount of time that has elapsed since the present study was commenced, newer and improved numerical schemes have been developed whereby tidal inlet morphology could be better simulated. Throughout the course of the past year, USACE developers have been working on a newer version of CMS-Flow which is capable of simulating the simultaneous transport of multiple sediment sizes throughout the domain. This new release will be capable of sorting the transported sediment sizes based on the spatial hydrodynamics such that the model computes an appropriate d50 map for the domain. In other words, a gradation curve which accurately describes the entire study area can be input into the model, and the model will then sort out its spatial distribution appropriately. This technique would have proved to be extremely useful for Shippagan Gully, as it would have saved a great deal of time in the morphological calibration process and likely produced a d50 map which lends itself to a much higher degree of confidence in the final model results.

8.0 REFERENCES

Aquaveo. "Water Modeling Solutions, SMS 10.1". XMS Wiki. <http://xmswiki.com/xms/SMS:SMS>. (2011).

Bagnold, R.A. (1968). Deposition in the Process of Hydraulic Transport. *Sedimentology*, Vol. 10. Pp 45-56.

Bailard, J., (1981). An energetics total load transport model for a plane sloping beach. *J. Geophysical Research*, 86, C11, 10938-10954.

Battjes, J.A. and J. Janssen, (1978). Energy loss and set-up due to breaking of random waves. *Proceedings 16th International Conference Coastal Engineering*, ASCE, pp. 569-587.

Benoit, (2005). TOMAWAC software for finite element sea state modelling, release 5.5 User Manual, EDF-LNHE, France.

Bijker, E.W., (1968). Mechanics of sediment transport by the combination of waves and current. *Proc. 23rd Int. Conf. on Coastal Engineering*, 147-173.

Bruun, P. (1987). Sediment By-Passing Across Coastal Inlets by Natural Means, by R. Silvester. Discussion. *Coastal Engineering*, Vol. 11, pp. 175-181.

Bruun, P. (1990). Improvement of Bypassing and Backpassing at Tidal Inlets. *Journal of Waterway, Port, Coastal and Ocean Engineering*, ASCE, New York, NY, Vol. 116(4), pp. 494-501.

Bruun, P. (1995). The Development of Downdrift Erosion. *Journal of Coastal Research*, Vol. 11, No. 4, pp. 1242-1247.

Buttolph, A.M, C.W. Reed, N.C. Kraus, N. Ono, M. Larson, B. Camenen, H. Hanson, T. Wamsley and A.K. Zundel, (2006). Two-dimensional Depth-Averaged Circulation Model CMS-M2D: Version 3.0, Report 2, Sediment Transport and Morphology Change. USACE Report ERDC/CHL TR-06-9, 148p.

Buttolph, A.M., W.G. Grosskopf, G.P. Bass and N.C. Kraus, (2006). Natural Sand Bypassing and Response of Ebb Shoal to Jetty Rehabilitation, Ocean City Inlet, Maryland, USA. *Proceedings 30th Coastal Engineering Conference*, World Scientific Press, Vol. 3, pp. 3344-3356.

Camenen, B., Larson, M., (2005). A bedload sediment transport formula for the nearshore. *Estuarine, Coastal and Shelf Science*, Vol. 63, pp. 249-260.

Camenen, B., Larson, M., (2006). A suspended load sediment transport formula for the nearshore. *Journal of Coastal Research*. Pending publication.

Camenen, B., Larson, M., (2007). A Unified Sediment Transport Formulation for Coastal Inlet Application. USACE Report ERDC/CHL CR-07-1, 247p.

Chawla, A., and J.T. Kirby (2002). Monochromatic and random wave breaking at blocking points. *Journal of Geophysical Research*, Vol. 107, 10.1029/2001JC001042.

Collins, J.I. (1972). Prediction of shallow water spectra. *Journal of Geophysical Research*, Vol. 77(15), pp. 2693-2707.

Cooper A.J., (1996), Telemac Modelling System, Validation Document, Rapport Électricité de France-DER, HE-43/96/006/A.

Dabajnia, M. and Watanabe, A., (1992). Sheet flow under non-linear waves and currents. *Proc. Int. Conf. on Coastal Engineering*, 2015-2029.

D'Alpaos, A., S. Lanzoni, D. Marani and A. Rinaldo, (2010). On the tidal prism – channel area relations. *Journal of Geophysical Research*, Vol. 115, 2010.

Davis, R.E and D.M. FitzGerald, (2004). Beaches and Coasts, Blackwell Science Ltd, Oxford, UK (2004) 419 pp.

Davis Jr., R.A., Hayes, M.O., (1984). What is a Wave-dominated Coast? Hydrodynamics and Sedimentation in Wave-Dominated Coastal Environments. *Marine Geology* 60, 313–329.

Dean, R.G. and R.A. Dalrymple, (2002). Coastal Processes with Engineering Applications. Cambridge University Press, Cambridge, pp. 413-448

Demirbilek, Z. And V. Panchang, (1998). CGWAVE: A Coastal Surface Water Wave Model of the Mild Slope Equation. Technical Report CHL-98-XX, USACE, Vicksburg, MS.

Dronkers, J.J. (1964). Tidal Computations in Rivers and Coastal Waters. North Holland Publishing Company.

Einstein, H.A. (1942). Formulas for the Transport of Bed Sediment. *Trans. American Society of Civil Engineers*, Vol. 107. Pp. 561-574.

Einstein, H.A. (1950). The Bed-Load Function for Sediment Transportation in Open Channel Flows. Technical Bulletin No. 1026, U.S. Department of Agriculture, Soil Conservation Service, Washington D.C.

Einstein, H.A., N. Chien, (1954). Second Approximation to the Solution of the Suspended Load Theory. Qinghua University Press, Beijing, p. 30.

FitzGerald, D.M., N.C. Kraus and E.B. Hands, (2000). Natural Mechanisms of Sediment Bypassing at Tidal Inlets. USACE Report ERDC/CHL CHETN-IV-30, 10p.

Forrester, W.D. (1983). Canadian Tidal Manual, Canada Fisheries and Oceans, Ottawa.

Galvin, C. J., Jr. (1971), Wave climate and coastal processes, Water Environments and Human Needs, MIT Press, Cambridge, Mass. pp. 44-78

Goda, Y. (1970). A synthesis of breaker indices. *Transactions of the Japan Society of Civil Engineers*. Vol 13. pp. 227-230.

Goda, Y. (1985). Radom seas and design of maritime structures. Tokyo: Universiyt of Tokyo Press.

Goda, Y. (2006). Examination of the influence of several factors on longshore current computation with random waves. *Coastal Engineering*. Vol. 53, pp. 157-170.

Hervouet J.-M; Lang P.; (2000). Telemac-2D version 5.0, Validation Document, Rapport Électricité de France-DER, HP-73/2000/042/A.

Hervouet, J-M., (2007). Hydrodynamics of Free Surface Flows. John Wiley & Sons Press, 2007.

Josenhans, H., (2007). Atlas of the Marine Environment and Seabed Geology of the Gulf of St. Lawrence; Commission géologique du Canada, Dossier public 5346, 75 p.

Kamphuis, J.W. (2000). Introduction to Coastal Engineering and Management. World Scientific Publishing Co. Pte. Ltd., Singapore.

Kraus, N.C., (2008). Engineering of Tidal Inlets and Morphologic Consequences. In: Kim, Y. (editor), Handbook of Coastal Engineering, World Scientific Press, Singapore, 39 p.

Lin, L., Demirbilek, Z., Mase, H., Zheng, J., Yamada, F., (2008). CMS-Wave: A Nearshore Spectral Wave Process Model for Coastal Inlets and Navigation Projects. USACE Report ERDC/CHL CR-08-13, 131p.

Longuet-Higgins M.S. and R.W. Stewart, (1963). A Note on Wave Set-Up. *Journal of Marine Research*, Vol. 21, pp. 4-10.

Luettich, R., and J. Westerink, (2011). A (Parallel) Advanced Circulation Model for Oceanic, Coastal and Estuarine Waters. User's Manual v49. University of North Carolina at Chapel Hill, Institute of Marine Sciences, Morehead City, NC.

Mase, H. (2001). Multidirectional random wave transformation model based on energy balance equation. *Coastal Engineering Journal*, Vol. 43, pp. 317-337.

Mase, H., K.Oki, T.S. Hedges, and H.J.Li, (2005). Extended energy-balance-equation wave model for multidirectional random wave transformation. *Ocean Engineering*, Vol. 32, pp. 961-985.

Meyer-Peter, E., and R. Muller, (1948). Formulas for Bed-load Transport. Proc., International Association for Hydraulic Research, 2nd Meeting, Stockholm, Sweden, pp. 39-64.

Miche, M. (1951). Le pouvoir reflechissant des ouvrages maritimes exposes a l'action de la houle. Annals des Ponts et Chau.ssess. 121e Annee: pp. 285-319. (translated by Lincoln and Chevron, University of California, Berkeley, Wave Research Laboratory, Series 3, Issue, 363, June 1954).

Militello, A. And A.K. Zundel, (2003). USACE Report ERDC/CHL CHETN-IV-60, 14p.

Nishimura, H. (1988). Computation of nearshore current. Nearshore Dynamics and Coastal Processes, K. Horikawa, ed., University of Tokyo Press, Tokyo, Japan, 271-291.

Nwogu, O.G. and Z. Demirbilek, (2001). BOUSS-2D: A Boussinesq Wave Model for Coastal Regions and Harbors. ERDC/CHL TR-01-25, Coastal and Hydraulics Laboratoru, United States Army Corps of Engineers, Vicksburg, MS.

Olsen Associates, Inc. (2005). Inlet Morphology – Beaufort Inlet – Morehead City Harbor. Olsen Associates Technical Report, Section 4.0.

Pratt, T.C., T.L. Fagerburg and D.C. McVan, (2000). Field Data Collection at Coastal Inlets. USACE Technical Report ERDC/CHL CETN-IV-24, 12p.

Rattanapitikon, W. and T. Shibayama, (2000). Verification and Modification of Breaker Height Formulas. *Coastal Engineering Journal*, Vol 42-4, pp. 389-406. World Scientific.

Ris, R.C., (1997): Spectral modelling of wind waves in coastal areas, (Ph.D. Dissertation Delft University of Technology, Department of Civil Engineering), Communications on Hydraulic and Geotechnical Engineering, Report No. 97-4, Delft, The Netherlands

Rosati, J.D. (2005). Concepts in Sediment Budgets. *Journal of Coastal Research*, Vol. 21, No. 2, pp. 307-322.

Rosati, J.D. and N.C. Kraus, (1999). Formulation of Sediment Budgets at Inlets. USACE, Coastal Engineering Technical Note IV-15, Rev. September 2009. 20p.

Sankaranarayanan, S and D.F. McCay, (2003). Three-Dimensional Modeling of Tidal Circulation in the Bay of Fundy. *Journal of Waterway, Port, Coastal and Ocean Engineering*, ASCE, Vol. 129, No. 3, May 1, 2003.

Seabergh, W.C. and N.C. Kraus, (2003). Progress in Management of Sediment Bypassing at Coastal Inlets: Natural Bypassing, Weir Jetties, Jetty Spurs, and Engineering Aids in Design. *Coastal Engineering Journal*, Vol. 45, No. 4, pp. 533-563. World Scientific.

Sheng, Jinyu, (2001). Dynamics of a Buoyancy-Driven Coastal Jet: The Gaspé Current. *Journal of Physical Oceanography*. Vol. 31, pp 3146-3162.

Shields, A. (1936). Application of Similarity Principles and Turbulence Research to Bed-Load Movement. Communications of the Prussian Research Institute for Shipbuilding. Berlin, 1936.

Smith, J.M., A.R. Sherlock and D.T. Resio, (2001). STWAVE: Steady-State Spectral Wave Model - User's Manual for STWAVE, Version 3.0. ERDC/CHL SR-01-1, Coastal and Hydraulics Laboratory, United States Army Corps of Engineers, Vicksburg, MS.

Soulsby, R., (1997), Dynamics of Marine Sands. Thomas Telford Press.

Swail, V.R., V.J. Cardone, M. Ferguson, D.J. Gummer, E.L. Harris, E.A. Orelup and A.T. Cox, (2006). The MSC50 Wind and Wave Re-analysis. Environment Canada and Oceanwather Inc. 9th International Workshop on Wave Hindcasting and Forecasting, Sep 25-29, Victoria BC, Canada, 2006.

USACE, (1984). "Shore Protection Manual". United States Army Corps of Engineers, Coastal Engineering Laboratory, Vicksburgh, MS.

Van Rijn, L.C., (1984). Sediment Transport, Part I: Bed-Load Transport. ASCE, *Journal of Hydraulic Engineering*, Vol. 110, pp. 1431-1456.

Van Rijn, L.C., (1998). Principles of coastal morphology. Aqua Publications, Amsterdam, The Netherlands.

Villaret, C. (2004), SYSIPHE Software, release 5.4 User Manual, EDF-LNHE, France.

Watanabe, A., (1987). Three dimensional numerical model of beach evolution. *Proc. Coastal Sediments '87*. ASCE. 802-817.

Yalin, Y.S. (1963). An Expression for Bed-Load Transportation. Journal of Hydraulics. Div. ASCE Vol 89. Pp. 221-250.

Zarillo, G.A., N.C. Kraus and R.K. Hoeke. (2003). Morphological Analysis of Sebastian Inlet, Florida: Enhancements to the Tidal Inlet Reservoir Model". *Proceedings, Coastal Sediments 2003*, Clearwater Beach, Florida, USA.

Appendix A – Sediment Properties and Accretion Volumes

			Mass Trapped by Seive (g)																							
Sample	Mass 1 (g)		(mm) 12.5	9.50	6.30	4.00	2.00	1.70	1.40	1.18	1.00	0.850	0.600	0.500	0.300	0.180	0.125	Finer	Mass 2 (g)	Mass Lost (g)	Mass 3 (g)	Total Volume (ml)	Sediment Volume (ml)	Volume of Voids (ml)	Porosity	Density (g/ml)	d50 (mm)
A	805.00		0.00	0.00	0.00	0.00	0.45	0.30	0.15	0.40	0.45	0.85	11.00	22.45	439.60	292.65	35.20	2.00	805.50	-0.50	805.15	558	310	248	0.44	2.597	0.32
B	1330.45		262.20	197.30	248.80	160.55	90.60	11.75	10.85	9.60	9.00	8.75	32.35	27.15	142.45	94.20	18.15	2.55	1326.25	4.20	1324.35	710	505	205	0.29	2.622	6.90
C	689.85		0.00	0.00	0.00	0.00	0.00	0.00	0.00	0.00	0.00	0.10	0.35	1.85	420.25	258.45	8.65	0.25	689.90	-0.05	689.45	470	260	210	0.45	2.652	0.32
D	805.40		120.35	17.80	11.00	7.00	16.00	4.40	5.30	5.50	6.10	6.65	32.65	45.75	393.75	125.35	4.95	0.30	802.85	2.55	802.20	485	305	180	0.37	2.630	0.41
E	947.10		15.20	2.95	45.95	54.90	60.75	12.70	19.95	21.20	20.95	24.75	106.15	125.70	345.10	80.90	5.95	1.30	944.40	2.70	943.25	585	360	225	0.38	2.620	0.51
F	911.60		0.00	0.00	0.00	0.00	0.00	0.00	0.15	0.15	0.15	0.10	0.10	0.35	261.40	619.00	29.00	0.85	911.25	0.35	910.80	645	350	295	0.46	2.602	0.24
G	790.65		172.20	6.60	7.85	0.40	1.25	0.40	0.55	0.65	1.05	1.70	16.25	47.30	366.35	109.90	7.85	0.10	740.40	50.25	723.75	430	280	150	0.35	2.585	0.41
H																											
I	758.50		0.00	0.00	0.00	0.00	0.00	0.05	0.05	0.05	0.05	0.15	3.15	19.00	595.30	125.45	13.25	2.00	758.50	0.00	756.15	525	290	235	0.45	2.607	0.36
J	638.50		196.25	63.45	63.90	42.10	52.55	10.95	16.40	16.00	15.70	16.75	44.30	23.80	50.50	16.65	2.85	1.20	633.35	5.15	632.90	330	245	85	0.26	2.583	6.50
K	793.25		0.00	0.00	2.55	7.20	17.95	4.35	5.30	5.00	5.75	6.65	34.65	61.60	449.70	154.80	31.25	5.35	792.10	1.15	790.85	550	305	245	0.45	2.593	0.37
L	926.60		269.30	63.45	79.50	44.85	45.75	6.70	8.80	8.70	10.20	13.70	70.15	67.90	197.60	34.00	2.05	1.00	923.65	2.95	922.95	510	345	165	0.32	2.675	3.90

			% Finer by Mass																							
Sample	Mass 1 (g)	20.00	12.50	9.50	6.30	4.00	2.00	1.70	1.40	1.18	1.00	0.850	0.600	0.500	0.300	0.180	0.125	0.100	Mass 2 (g)	Mass Lost (g)	Mass 2 (g)	Total Volume (cm^3)	Sediment Volume (cm^3)	Volume of Voids (cm^3)	Porosity	Density (kg/m^3)	d50 (mm)
A	805.00	100.00%	100.00%	100.00%	100.00%	100.00%	99.94%	99.91%	99.89%	99.84%	99.78%	99.68%	98.31%	95.52%	40.95%	4.62%	0.25%	0.00%	805.50	-0.50	805.15	558	310	248	0.44	2597.26	0.32
B	1330.45	100.00%	80.23%	65.35%	46.59%	34.49%	27.66%	26.77%	25.95%	25.23%	24.55%	23.89%	21.45%	19.40%	8.66%	1.56%	0.19%	0.00%	1326.25	4.20	1324.35	710	505	205	0.29	2622.48	6.90
C	689.85	100.00%	100.00%	100.00%	100.00%	100.00%	100.00%	100.00%	100.00%	100.00%	100.00%	99.99%	99.93%	99.67%	38.75%	1.29%	0.04%	0.00%	689.90	-0.05	689.45	470	260	210	0.45	2651.73	0.32
D	805.40	100.00%	85.01%	82.79%	81.42%	80.55%	78.56%	78.01%	77.35%	76.66%	75.90%	75.08%	71.01%	65.31%	16.27%	0.65%	0.04%	0.00%	802.85	2.55	802.20	485	305	180	0.37	2630.16	0.41
E	947.10	100.00%	98.39%	98.08%	93.21%	87.40%	80.97%	79.62%	77.51%	75.26%	73.05%	70.43%	59.19%	45.88%	9.33%	0.77%	0.14%	0.00%	944.40	2.70	943.25	585	360	225	0.38	2620.14	0.51
F	911.60	100.00%	100.00%	100.00%	100.00%	100.00%	100.00%	100.00%	99.98%	99.97%	99.95%	99.94%	99.93%	99.89%	71.20%	3.28%	0.09%	0.00%	911.25	0.35	910.80	645	350	295	0.46	2602.29	0.24
G	790.65	100.00%	76.74%	75.85%	74.79%	74.74%	74.57%	74.51%	74.44%	74.35%	74.21%	73.98%	71.79%	65.40%	15.92%	1.07%	0.01%	0.00%	740.40	50.25	723.75	430	280	150	0.35	2584.82	0.41
H																											
I	758.50	100.00%	100.00%	100.00%	100.00%	100.00%	100.00%	99.99%	99.99%	99.98%	99.97%	99.95%	99.54%	97.03%	18.55%	2.01%	0.26%	0.00%	758.50	0.00	756.15	525	290	235	0.45	2607.41	0.36
J	638.50	100.00%	69.01%	59.00%	48.91%	42.26%	33.96%	32.23%	29.64%	27.12%	24.64%	21.99%	15.00%	11.24%	3.27%	0.64%	0.19%	0.00%	633.35	5.15	632.90	330	245	85	0.26	2583.27	6.50
K	793.25	100.00%	100.00%	100.00%	99.68%	98.77%	96.50%	95.95%	95.28%	94.65%	93.93%	93.09%	88.71%	80.94%	24.16%	4.62%	0.68%	0.00%	792.10	1.15	790.85	550	305	245	0.45	2592.95	0.37
L	926.60	100.00%	70.84%	63.97%	55.37%	50.51%	45.56%	44.83%	43.88%	42.94%	41.83%	40.35%	32.76%	25.40%	4.01%	0.33%	0.11%	0.00%	923.65	2.95	922.95	510	345	165	0.32	2675.22	3.90

			Percent Trapped by Seive (%)																							
Sample	Mass 1 (g)	20.00	12.50	9.50	6.30	4.00	2.00	1.70	1.40	1.18	1.00	0.850	0.600	0.500	0.300	0.180	0.125	0.100	Mass 2 (g)	Mass Lost (g)	Mass 2 (g)	Total Volume (cm3)	Sediment Volume (cm3)	Volume of Voids (cm3)	Porosity	Density (kg/m3)	d50 (mm)
A	805.00	0.00%	0.00%	0.00%	0.00%	0.00%	0.06%	0.04%	0.02%	0.05%	0.06%	0.11%	1.37%	2.79%	54.57%	36.33%	4.37%	0.25%	805.50	-0.50	805.15	558	310	248	0.44	2597.26	0.32
B	1330.45	0.00%	19.77%	14.88%	18.76%	12.11%	6.83%	0.89%	0.82%	0.72%	0.68%	0.66%	2.44%	2.05%	10.74%	7.10%	1.37%	0.19%	1326.25	4.20	1324.35	710	505	205	0.29	2622.48	6.90
C	689.85	0.00%	0.00%	0.00%	0.00%	0.00%	0.00%	0.00%	0.00%	0.00%	0.00%	0.01%	0.05%	0.27%	60.91%	37.46%	1.25%	0.04%	689.90	-0.05	689.45	470	260	210	0.45	2651.73	0.32
D	805.40	0.00%	14.99%	2.22%	1.37%	0.87%	1.99%	0.55%	0.66%	0.69%	0.76%	0.83%	4.07%	5.70%	49.04%	15.61%	0.62%	0.04%	802.85	2.55	802.20	485	305	180	0.37	2630.16	0.41
E	947.10	0.00%	1.61%	0.31%	4.87%	5.81%	6.43%	1.34%	2.11%	2.24%	2.22%	2.62%	11.24%	13.31%	36.54%	8.57%	0.63%	0.14%	944.40	2.70	943.25	585	360	225	0.38	2620.14	0.51
F	911.60	0.00%	0.00%	0.00%	0.00%	0.00%	0.00%	0.00%	0.02%	0.02%	0.02%	0.01%	0.01%	0.04%	28.69%	67.93%	3.18%	0.09%	911.25	0.35	910.80	645	350	295	0.46	2602.29	0.24
G	790.65	0.00%	23.26%	0.89%	1.06%	0.05%	0.17%	0.05%	0.07%	0.09%	0.14%	0.23%	2.19%	6.39%	49.48%	14.84%	1.06%	0.01%	740.40	50.25	723.75	430	280	150	0.35	2584.82	0.41
H																											
I	758.50	0.00%	0.00%	0.00%	0.00%	0.00%	0.00%	0.01%	0.01%	0.01%	0.01%	0.02%	0.42%	2.50%	78.48%	16.54%	1.75%	0.26%	758.50	0.00	756.15	525	290	235	0.45	2607.41	0.36
J	638.50	0.00%	30.99%	10.02%	10.09%	6.65%	8.30%	1.73%	2.59%	2.53%	2.48%	2.64%	6.99%	3.76%	7.97%	2.63%	0.45%	0.19%	633.35	5.15	632.90	330	245	85	0.26	2583.27	6.50
K	793.25	0.00%	0.00%	0.00%	0.32%	0.91%	2.27%	0.55%	0.67%	0.63%	0.73%	0.84%	4.37%	7.78%	56.77%	19.54%	3.95%	0.68%	792.10	1.15	790.85	550	305	245	0.45	2592.95	0.37
L	926.60	0.00%	29.16%	6.87%	8.61%	4.86%	4.95%	0.73%	0.95%	0.94%	1.10%	1.48%	7.59%	7.35%	21.39%	3.68%	0.22%	0.11%	923.65	2.95	922.95	510	345	165	0.32	2675.22	3.90

Accretion volume calculation within Shippagan Gully (Section 4.3.2.2)

Year	Total Area	Volume above LWL	Volume to -1m GD	Rate
1944	0 m^2			
1958	14168.771 m^2	11002.5 m^3	25804 m^3	
1964	12623.612 m^2	13167.5 m^3	26752.5 m^3	158 m^3/year
1966	15147.215 m^2	15793.75 m^3	30796 m^3	2022 m^3/year
1970	18661.571 m^2	14625 m^3	35161 m^3	1091 m^3/year
1980	23951.717 m^2	29928.75 m^3	53796.25 m^3	1864 m^3/year
1987	14495.451 m^2	21406.25 m^3	37140 m^3	dredged
2004	37811.686 m^2	49090.5 m^3	88098 m^3	2998 m^3/year
2007	41088.19 m^2	52265.25 m^3	93656 m^3	1853 m^3/year
2008	42770.114 m^2	55882.5 m^3	99063 m^3	5407 m^3/year
2010	46097.864 m^2			
			Average =	2199 m^3/year

***Volumes calculated by cross-sections

**New Jetty added (different boundary)

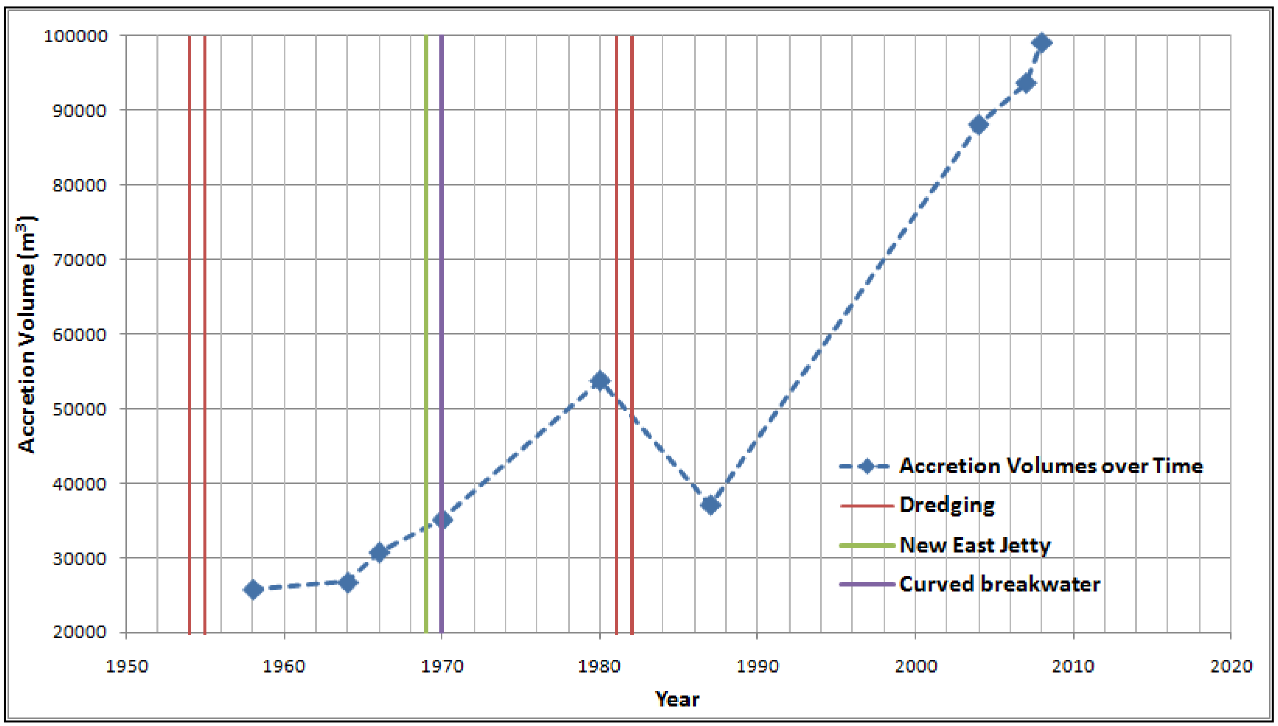

Appendix B – Shippagan Gully History

- **Relevant History**
- **Construction**
- **Dredging**
- **Morphologic Response**

1880-1900

- Dock shown in **1800s** drawings behind lighthouse belonged to William Fruing & Co., a shipping company that transported general cargo
    - Likely reason for damming the east outlet side of the estuary (access to mainland by road)
- Original East breakwater constructed approximately **1886**
    - Appears in **1882** drawings along with Dam at eastern end of estuary
    - East breakwater extended and repaired several times **1887-1916**
- Original West breakwater proposed in **1889**
    - Completed sometime before **1897**
- Rapidly retreating shingle beach is documented after west breakwater construction, west of the new structure. Shown in Figure 1.
    - Shingle beach was originally in line with east beach (channel likely flowed behind it and to the east)
    - Retreat (erosion) documented is 20 to 30m per year in late **1800s**
- Accretion apparent on east beach immediately east of the jetty
    - Accretion occurred prior to **1944**
    - Waterline 10-30m further seaward in **1944** then **1882**
- Shoal on east side of channel is documented in **1899** as: "Shoal made by littoral drift from eastward passing around E (jetty)"
    - This was the likely reason for numerous jetty extensions in late **1890s** and early **1900s**
- Shoal on east side of channel represents 1 fathom line in **1899** drawing (6ft)
- Direction of flow through the channel is documented in **1899** as :
        - Exiting – "Half flood to half ebb"
        - Entering – "Half ebb to half flood"

- Northern beach (behind harbor) became concave after construction of west breakwater
    - Likely due to flow re-circulation

1990-1944

- **1900** drawings report that the "channel reported deepened from 6 ft in **1895** to 9 ft in **1900**"
    - Deepening likely due to the construction of the west breakwater and east breakwater extensions
- Inner groyne proposed in **1909** for lobster hatchery access from water
    - Was built shortly thereafter
- "Pierhead" groyne at end of west breakwater was built **1904-1907**
- 2,633.5 cu. yds. dredged in **1912-1913**
- 25,662 cu. yds. dredged from 4 different sections of channel in **1917-1918**
- 18,557 cu. yds. Dredged from harbour (main channel at the time) in **1918-1919**
- West breakwater repaired and ice breaker block proposed in **1918-1919**
    - Steel sheet piles introduced sometime around then

No Records from **1919** to **1930**

- 30' by 20' ice breaker block shown in **1930** drawings
- "Pierhead" groyne at end of west breakwater was extended sometime between **1919** and **1930**
- Sheet pile walls added to breakwaters in **1938-1945**
    - Machinery shown on west breakwater in **1944** image

1944-1970

- **1944** Image shows no visible accretion within channel , although likely shallower than 1 fathom (from **1899** drawing)
    - Channel is very well defined
- 12,709 cu. Yds. removed from 2 areas in gully, **1954-1955**
- 28,623 cu. Yds. removed from shoals on either side of the channel, **1955-1956**
    - No more dredging for 25 years post **1955-1956**
- **1958** Inner shoal is clearly visible
    - A = 14,169 m^2

- $V = 25{,}804\ m^3$
- **1964** inner shoal as moved slightly further into estuary
  - $A = 12{,}624\ m^2$
  - $V = 26{,}752\ m^3$
- **1966** little change to inner shoal – slightly larger
  - $A = 15{,}147\ m^2$
  - $V = 30{,}796\ m^3$
- New eastern jetty proposed in **1965** and completed sometime before **1969**
- West training wall (first curved section) completed **1966-1970**
- Remainder of west breakwater (curved training wall) appears in **1970** drawings
  - Was likely constructed **1970-1971**
- **1970** significant change to shoals – split into less defined deposits, moved further south into channel and continued to increased in area and volume
  - $A = 18{,}662\ m^2$
  - $V = 35{,}161\ m^3$
    - Drastic change and temporary "confusion" likely due to the addition of new structures on both sides of channel

1970-1990

- 2 to 4 ton stone added to west beach and over 200 ft. of westernmost side of breakwater in **1976**
  - To prevent further erosion of west beach and protect harbour access road
- **1980** inner shoal continued to grow and was pushed back again to a more stable position and more unified form behind the new (1969) jetty
  - $A = 23{,}952\ m^2$
  - $V = 53{,}796\ m^3$
- 1,900 m^3 (CMTM) dredged in **1981-1982**
- 59,520 m^3 (CMPM) was dredged in channel entrance and harbour basin area **1982-1983**
- Appears from **1987** images that a large amount of dredged material was pumped/placed onto land west of lighthouse
  - Some was additionally placed in a pile behind the inner channel bar
- A new channel appears to have been dredged providing access to bay behind inner channel bar alongside where the dredged material was subsequently placed
- End of west breakwater filled and inner wharf reconstructed in **1983**
  - **1987** image shows that construction was still underway

- **1987** inner shoal is in same location but much smaller due to dredging
    - $A = 14,495\ m^2$
    - $V = 37,140\ m^3$
- $3,190\ m^3$ (CMTM) dredged from inside harbour **1988-1989**
- **1989** a channel appears to be cut through the inner shoal however image does not cover enough area to see

1990-2010

- **1992** Repairs to timber breastwork along west beach and addition of more 2 to 5 ton stone
- **1993** New land and dyke built within harbour at westernmost end
- **1997** Repairs completed along inner harbour wall of western breakwater
- **2001** Additional 2 to 4 ton stone added to western beach
    - Shore protection extended further west with an underplayed below the 2 to 4 ton stone
- **2004** inner shoal has taken up its approximately current position
    - $A = 37,812\ m^2$
    - $V = 88,098\ m^3$
- **2007** inner shoal shows continual accretion, in particular near northern end
    - $A = 41,088\ m^2$
    - $V = 93,656\ m^3$
- **2008** inner shoal shows additional accretion
    - $A = 42,770\ m^2$
    - $V = 99,063\ m^3$
- **2010** inner shoal shows significant accretion immediately behind jetty and at northern tip facing estuary
    - $A = 46,098\ m^2$

END OF WORKS

APPENDIX C – WAVE CLIMATE SUMMARY TABLES

240 Degrees

9.34%

Extreme Value Analysis

Weibull Distribution

Correlation:	0.994	0.993

Tr	Hs (m)	Tp (s)	
1	2.40	9.10	**
1.5	2.51	9.36	
2	2.63	9.58	
5	3.01	10.15	
10	3.30	10.51	
20	3.60	10.83	
25	3.70	10.92	
50	4.00	11.21	
100	4.30	11.47	
500	5.01	12.02	
1000	5.32	12.23	

Frequency Table

		Hs (m)						
	TOTAL	0 to 1	1 to 2	2 to 3	3 to 4	4 to 5	Total %	Cum. %
Tp (s)	0 to 2	9.30%	0.04%	0.00%	0.00%	0.00%	9.3%	9.3%
	2 to 4	19.13%	0.30%	0.00%	0.00%	0.00%	19.4%	28.8%
	4 to 6	41.89%	5.83%	0.04%	0.00%	0.00%	47.8%	76.5%
	6 to 8	9.12%	5.68%	1.46%	0.00%	0.00%	16.3%	92.8%
	8 to 10	3.04%	1.63%	0.36%	0.15%	0.01%	5.2%	98.0%
	10 to 12	1.15%	0.03%	0.01%	0.00%	0.00%	1.2%	99.2%
	12 to 14	0.47%	0.01%	0.00%	0.00%	0.00%	0.5%	99.6%
	14 to 16	0.26%	0.01%	0.00%	0.00%	0.00%	0.3%	99.9%
	16 to 18	0.05%	0.00%	0.00%	0.00%	0.00%	0.1%	100.0%
	18 to 20	0.03%	0.00%	0.00%	0.00%	0.00%	0.0%	100.0%
	20 to 22	0.00%	0.00%	0.00%	0.00%	0.00%	0.0%	100.0%
	22 to 24	0.00%	0.00%	0.00%	0.00%	0.00%	0.0%	100.0%
	Total %	84.4%	13.5%	1.9%	0.2%	0.0%	1.0000	
	Cum. %	84.4%	98.0%	99.8%	100.0%	100.0%		100.00%

270 Degrees

11.04%

Extreme Value Analysis

Weibull Distribution

Correlation:	0.993	0.990

Tr	Hs (m)	Tp (s)	
1	3.20	9.25	**
1.5	3.32	9.33	
2	3.50	9.55	
5	4.02	10.16	
10	4.37	10.55	
20	4.71	10.91	
25	4.81	11.01	
50	5.12	11.33	
100	5.42	11.63	
500	6.07	12.26	
1000	6.34	12.51	

Frequency Table

		Hs (m)							
	TOTAL	0 to 1	1 to 2	2 to 3	3 to 4	4 to 5	5 to 6	Total %	Cum. %
Tp (s)	0 to 2	7.54%	0.01%	0.00%	0.01%	0.02%	0.00%	0.0758	0.0758
	2 to 4	18.01%	0.38%	0.00%	0.00%	0.00%	0.00%	0.1839	0.2597
	4 to 6	35.62%	5.09%	0.03%	0.00%	0.00%	0.00%	0.4074	0.6672
	6 to 8	8.52%	9.66%	1.28%	0.02%	0.00%	0.00%	0.1947	0.8619
	8 to 10	2.75%	4.10%	1.92%	0.44%	0.04%	0.00%	0.0924	0.9543
	10 to 12	2.32%	0.11%	0.20%	0.13%	0.02%	0.00%	0.0277	0.9820
	12 to 14	0.98%	0.03%	0.00%	0.00%	0.00%	0.00%	0.0102	0.9922
	14 to 16	0.53%	0.04%	0.00%	0.00%	0.00%	0.00%	0.0057	0.9979
	16 to 18	0.17%	0.01%	0.00%	0.00%	0.00%	0.00%	0.0019	0.9998
	18 to 20	0.02%	0.00%	0.00%	0.00%	0.00%	0.00%	0.0002	0.9999
	20 to 22	0.00%	0.00%	0.00%	0.00%	0.00%	0.00%	0.0001	1.0000
	22 to 24	0.00%	0.00%	0.00%	0.00%	0.00%	0.00%	0.0000	1.0000
	Total %	0.7647	0.1943	0.0343	0.0060	0.0008	0.0000	1.0000	
	Cum. %	0.7647	0.9589	0.9933	0.9992	1.0000	1.0000		100.00%

300 Degrees

8.79%

Extreme Value Analysis

Weibull Distribution

Correlation:	0.996	0.989

Tr	Hs (m)	Tp (s)	
1	3.40	9.10	**
1.5	3.55	9.22	
2	3.71	9.43	
5	4.18	10.02	
10	4.50	10.42	
20	4.80	10.77	
25	4.89	10.88	
50	5.17	11.21	
100	5.43	11.51	
500	6.01	12.15	
1000	6.25	12.40	

Frequency Table

		Hs (m)							
	TOTAL	0 to 1	1 to 2	2 to 3	3 to 4	4 to 5	5 to 6	Total %	Cum. %
Tp (s)	0 to 2	11.35%	0.02%	0.00%	0.00%	0.02%	0.00%	0.1139	0.1139
	2 to 4	24.10%	0.42%	0.00%	0.00%	0.00%	0.00%	0.2452	0.3590
	4 to 6	30.59%	7.75%	0.08%	0.00%	0.00%	0.00%	0.3842	0.7433
	6 to 8	3.61%	11.50%	2.73%	0.09%	0.00%	0.00%	0.1793	0.9226
	8 to 10	1.30%	1.07%	2.34%	0.79%	0.09%	0.00%	0.0560	0.9785
	10 to 12	0.99%	0.04%	0.01%	0.09%	0.02%	0.00%	0.0115	0.9900
	12 to 14	0.53%	0.01%	0.00%	0.00%	0.00%	0.00%	0.0054	0.9954
	14 to 16	0.31%	0.00%	0.00%	0.00%	0.00%	0.00%	0.0031	0.9986
	16 to 18	0.10%	0.01%	0.00%	0.00%	0.00%	0.00%	0.0011	0.9997
	18 to 20	0.03%	0.00%	0.00%	0.00%	0.00%	0.00%	0.0003	1.0000
	20 to 22	0.00%	0.00%	0.00%	0.00%	0.00%	0.00%	0.0000	1.0000
	22 to 24	0.00%	0.00%	0.00%	0.00%	0.00%	0.00%	0.0000	1.0000
	Total %	0.7291	0.2081	0.0517	0.0097	0.0013	0.0000	1.0000	
	Cum. %	0.7291	0.9373	0.9890	0.9987	1.0000	1.0000		100.00%

330 Degrees

7.42%

Extreme Value Analysis

Weibull Distribution

Correlation:	0.996	0.994

Tr	Hs (m)	Tp (s)	
1	2.65	8.25	**
1.5	2.79	8.36	
2	2.91	8.60	
5	3.28	9.29	
10	3.54	9.74	
20	3.79	10.15	
25	3.87	10.28	
50	4.11	10.66	
100	4.34	11.01	
500	4.86	11.76	
1000	5.08	12.07	

Frequency Table

		Hs (m)						
	TOTAL	0 to 1	1 to 2	2 to 3	3 to 4	4 to 5	Total %	Cum. %
Tp (s)	0 to 2	16.27%	0.03%	0.00%	0.00%	0.00%	0.1629	0.1629
	2 to 4	24.82%	1.11%	0.12%	0.02%	0.00%	0.2608	0.4237
	4 to 6	32.78%	15.18%	0.28%	0.01%	0.00%	0.4825	0.9062
	6 to 8	1.38%	4.21%	1.97%	0.12%	0.00%	0.0769	0.9831
	8 to 10	0.42%	0.12%	0.31%	0.15%	0.01%	0.0101	0.9931
	10 to 12	0.34%	0.01%	0.00%	0.00%	0.00%	0.0036	0.9968
	12 to 14	0.16%	0.00%	0.00%	0.00%	0.00%	0.0016	0.9984
	14 to 16	0.09%	0.00%	0.00%	0.00%	0.00%	0.0009	0.9993
	16 to 18	0.05%	0.01%	0.00%	0.00%	0.00%	0.0006	0.9999
	18 to 20	0.01%	0.00%	0.00%	0.00%	0.00%	0.0001	1.0000
	20 to 22	0.00%	0.00%	0.00%	0.00%	0.00%	0.0000	1.0000
	22 to 24	0.00%	0.00%	0.00%	0.00%	0.00%	0.0000	1.0000
	Total %	0.7632	0.2069	0.0268	0.0030	0.0001	1.0000	
	Cum. %	0.7632	0.9701	0.9969	0.9999	1.0000		100.00%

360 Degrees

9.86%

Extreme Value Analysis

Weibull Distribution

Correlation:	0.995	0.976

Tr	Hs (m)	Tp (s)	
1	2.00	6.20	**
1.5	2.07	6.38	
2	2.18	6.86	
5	2.45	7.72	
10	2.63	8.20	
20	2.80	8.61	
25	2.85	8.74	
50	3.00	9.10	
100	3.15	9.44	
500	3.47	10.15	
1000	3.61	10.43	

Frequency Table

		Hs (m)						
	TOTAL	**0 to 1**	**1 to 2**	**2 to 3**	**3 to 4**	**4 to 5**	**Total %**	**Cum. %**
Tp (s)	**0 to 2**	17.56%	0.16%	0.00%	0.00%	0.00%	**0.1773**	**0.1773**
	2 to 4	40.08%	1.07%	0.06%	0.02%	0.01%	**0.4123**	**0.5896**
	4 to 6	23.75%	14.66%	0.47%	0.06%	0.01%	**0.3895**	**0.9791**
	6 to 8	0.07%	1.04%	0.58%	0.02%	0.00%	**0.0171**	**0.9962**
	8 to 10	0.08%	0.01%	0.06%	0.02%	0.00%	**0.0017**	**0.9979**
	10 to 12	0.12%	0.01%	0.00%	0.00%	0.00%	**0.0013**	**0.9992**
	12 to 14	0.03%	0.01%	0.00%	0.00%	0.00%	**0.0004**	**0.9995**
	14 to 16	0.02%	0.00%	0.00%	0.00%	0.00%	**0.0002**	**0.9997**
	16 to 18	0.02%	0.00%	0.00%	0.00%	0.00%	**0.0002**	**1.0000**
	18 to 20	0.00%	0.00%	0.00%	0.00%	0.00%	**0.0000**	**1.0000**
	20 to 22	0.00%	0.00%	0.00%	0.00%	0.00%	**0.0000**	**1.0000**
	22 to 24	0.00%	0.00%	0.00%	0.00%	0.00%	**0.0000**	**1.0000**
	Total %	**0.8173**	**0.1698**	**0.0117**	**0.0011**	**0.0002**	**1.0000**	
	Cum. %	**0.8173**	**0.9871**	**0.9987**	**0.9998**	**1.0000**		**100.00%**

APPENDIX D – HYDRODYNAMIC CALIBRATION

		Measured	Surface k = 0.85			Telemac		n_SJL_0.050Ent_All	
Date	Time	Velocity (m/s)	Adjusted (m/s)	bad	good	Velocity (m/s)	err	Velocity (m/s)	err
12/08/2010	8:16	1.18	1.18			1.40	0.22	1.04	0.14
12/08/2010	8:18	1.50	1.50			1.05	0.45	0.64	0.86
12/08/2010	8:18	0.69	0.69			0.60	0.09	0.96	0.27
12/08/2010	8:19	1.43	1.43			1.30	0.13	0.67	0.76
12/08/2010	8:30	1.50	1.50			0.95	0.55	0.57	0.93
12/08/2010	8:33	1.19	1.19			1.05	0.14	0.76	0.43
12/08/2010	8:35	1.29	1.29			1.05	0.24	0.76	0.53
12/08/2010	8:37	0.30	0.30			0.18	0.12	0.88	0.58
12/08/2010	8:42	1.19	1.19			1.24	0.05	1.19	0.01
12/08/2010	8:43	1.16	1.16			0.75	0.41	1.03	0.13
12/08/2010	8:44	0.68	0.68					0.73	0.05
12/08/2010	8:51	0.82	0.82			0.84	0.02	0.97	0.15
12/08/2010	8:55	0.78	0.78			0.71	0.07	0.73	0.05
12/08/2010	8:56	0.74	0.74					0.73	0.01
12/08/2010	8:58	0.38	0.38					0.34	0.04
12/08/2010	8:58	0.56	0.56					0.40	0.15
12/08/2010	9:33	0.49	0.49					0.26	0.23
12/08/2010	9:33	0.26	0.26					0.26	0.00
12/08/2010	15:35	-0.94	-0.94			-0.68	0.26	-0.57	0.37
12/08/2010	15:36	-0.96	-0.96					-0.57	0.38
12/08/2010	15:38	-0.63	-0.63			-0.59	0.04	-0.54	0.09
12/08/2010	15:40	-0.50	-0.50			-0.61	0.11	-0.67	0.16
12/08/2010	15:42	-0.46	-0.46			-0.78	0.32	-0.66	0.19
12/08/2010	15:45	-0.86	-0.86			-0.98	0.12	-0.86	0.01
12/08/2010	15:49	-0.29	-0.29			-0.71	0.42	-0.63	0.35
12/08/2010	15:49	-0.52	-0.52					-0.63	0.12
12/08/2010	15:49	-0.60	-0.60					-0.63	0.04
12/08/2010	15:52	-0.68	-0.68			-0.44	0.24	-0.26	0.42
12/08/2010	15:53	-0.78	-0.78			-0.47	0.31	-0.38	0.40
12/08/2010	15:54	-0.27	-0.27			-0.62	0.35	-0.26	0.00
12/08/2010	15:55	-0.46	-0.46			-0.60	0.14	-0.31	0.16
12/08/2010	16:15	1.05	1.05					0.95	0.11
12/08/2010	16:18	0.80	0.80					0.99	0.19
12/08/2010	16:38	0.41	0.41			0.60	0.19	0.66	0.25
12/08/2010	16:38	0.36	0.36			0.60	0.24	0.66	0.30
12/08/2010	18:35	1.94	1.65			1.55	0.10	1.48	0.17
12/08/2010	18:45	1.83	1.56			1.61	0.05	1.52	0.03
12/08/2010	19:00	2.00	1.70			1.68	0.02	1.57	0.13
12/08/2010	19:15	1.98	1.68			1.75	0.07	1.62	0.06
12/08/2010	19:30	1.86	1.58			1.79	0.21	1.63	0.04
12/08/2010	19:36	1.91	1.62			1.80	0.18	1.62	0.00
12/08/2010	19:45	1.96	1.67			1.81	0.14	1.64	0.03
12/08/2010	20:00	1.79	1.52			1.80	0.28	1.59	0.07

MEAN ABSOLUTE ERROR

	Telemac err	n_SJL_0.050Ent_All err
All points =	0.20	0.22
All good points =	0.15	0.15
Morning (All) =	0.21	0.30
Morning (Good) =	0.19	0.33
Afternoon (All) =	0.23	0.21
Afternoon (Good) =	0.15	0.08
Evening (All) =	0.13	0.07

n_0.06-0.015_0.035_0.075	A	n_0.06-0.015_0.020_035_0.075	B	n_0.06-0.020_035_0.075	C	n_0.06-0.025_035_0.075	D	
Velocity (m/s)	err	Velocity (m/s)	err	Velocity (m/s)	err	Velocity (m/s)	err	err
1.39	0.21	1.31	0.13	1.30	0.12	1.20	0.02	0.02
1.25	0.25	1.16	0.34	1.16	0.34	1.06	0.44	-0.44
0.63	0.06	0.77	0.08	0.75	0.06	0.83	0.14	0.14
1.30	0.13	1.22	0.21	1.24	0.19	1.12	0.31	-0.31
1.31	0.19	1.13	0.37	1.13	0.37	1.03	0.47	-0.47
1.19	0.00	1.13	0.06	1.13	0.06	1.06	0.13	-0.13
1.17	0.12	1.11	0.18	1.11	0.18	1.04	0.25	-0.25
0.22	0.08	0.39	0.10	0.39	0.10	0.50	0.21	0.21
1.14	0.05	1.12	0.07	1.12	0.07	1.09	0.10	-0.10
1.04	0.12	1.03	0.13	1.03	0.13	1.01	0.15	-0.15
0.97	0.29	0.95	0.27	0.95	0.27	0.93	0.25	0.25
1.06	0.24	1.05	0.23	1.05	0.23	1.03	0.21	0.21
0.85	0.07	0.88	0.10	0.85	0.07	0.84	0.06	0.06
0.85	0.11	0.88	0.14	0.85	0.11	0.84	0.10	0.10
0.42	0.04	0.42	0.04	0.40	0.02	0.40	0.02	0.02
0.41	0.15	0.40	0.16	0.40	0.16	0.40	0.16	-0.16
0.50	0.01	0.44	0.05	0.46	0.03	0.42	0.07	-0.07
0.50	0.24	0.44	0.18	0.46	0.20	0.42	0.16	0.16
-0.56	0.38	-0.54	0.40	-0.54	0.40	-0.52	0.42	0.42
-0.56	0.40	-0.54	0.42	-0.54	0.42	-0.52	0.44	0.44
-0.54	0.09	-0.51	0.12	-0.50	0.13	-0.47	0.16	0.16
-0.58	0.08	-0.44	0.06	-0.52	0.02	-0.48	0.02	0.02
-0.52	0.06	-0.51	0.05	-0.54	0.08	-0.51	0.05	-0.05
-0.62	0.24	-0.60	0.26	-0.61	0.25	-0.60	0.26	0.26
-0.50	0.21	-0.49	0.20	-0.50	0.21	-0.50	0.21	-0.21
-0.50	0.02	-0.49	0.03	-0.50	0.02	-0.50	0.02	0.02
-0.50	0.10	-0.49	0.11	-0.50	0.10	-0.50	0.10	0.10
-0.35	0.33	-0.34	0.34	-0.34	0.34	-0.34	0.34	0.34
-0.33	0.45	-0.32	0.46	-0.33	0.45	-0.34	0.44	0.44
-0.29	0.02	-0.26	0.01	-0.25	0.02	-0.22	0.05	0.05
-0.26	0.20	-0.23	0.23	-0.23	0.23	-0.20	0.26	0.26
0.90	0.15	0.91	0.14	0.90	0.15	0.90	0.15	-0.15
0.83	0.03	0.84	0.04	0.83	0.03	0.83	0.03	0.03
0.75	0.34	0.71	0.30	0.69	0.28	0.63	0.22	0.22
0.75	0.39	0.71	0.35	0.69	0.33	0.63	0.27	0.27
1.79	0.14	1.86	0.21	1.84	0.19	1.68	0.03	0.03
1.83	0.27	1.90	0.34	1.89	0.33	1.73	0.17	0.17
1.90	0.20	1.97	0.27	1.95	0.25	1.79	0.09	0.09
1.94	0.26	2.01	0.33	2.00	0.32	1.84	0.16	0.16
1.95	0.37	2.03	0.45	2.01	0.43	1.84	0.26	0.26
1.95	0.33	2.01	0.39	2.01	0.39	1.84	0.22	0.22
1.95	0.28	2.02	0.35	2.01	0.34	1.85	0.18	0.18
1.90	0.38	1.98	0.46	1.97	0.45	1.81	0.29	0.29
	0.19		0.21		0.21		0.19	0.07
	0.16		0.19		0.18		0.16	0.05
	0.13		0.16		0.15		0.18	-0.05
	0.11		0.14		0.13		0.16	-0.05
	0.20		0.21		0.20		0.20	0.15
	0.13		0.13		0.13		0.13	0.12
	0.28		0.35		0.34		0.18	0.18

n_0.06-0.015_0.025B_0.035_0.075	F		n_0.06-0.025_0.035_0.070	G		n_0.06-0.030_0.035_0.075	H	
Velocity (m/s)	err	err	Velocity (m/s)	err	err	Velocity (m/s)	err	err
1.20	0.02	0.02	1.20	0.02	0.02	1.09	0.09	-0.09
1.06	0.44	-0.44	1.06	0.44	-0.44	0.95	0.55	-0.55
0.83	0.14	0.14	0.82	0.13	0.13	0.81	0.12	0.12
1.12	0.31	-0.31	1.11	0.32	-0.32	1.00	0.43	-0.43
1.03	0.47	-0.47	1.03	0.47	-0.47	0.92	0.58	-0.58
1.06	0.13	-0.13	1.05	0.14	-0.14	0.98	0.21	-0.21
1.04	0.25	-0.25	1.04	0.25	-0.25	0.97	0.32	-0.32
0.50	0.21	0.21	0.49	0.20	0.20	0.56	0.27	0.27
1.09	0.10	-0.10	1.08	0.11	-0.11	1.06	0.13	-0.13
1.01	0.15	-0.15	1.01	0.15	-0.15	0.98	0.18	-0.18
0.93	0.25	0.25	0.92	0.24	0.24	0.90	0.22	0.22
1.04	0.22	0.22	1.02	0.20	0.20	1.01	0.19	0.19
0.84	0.06	0.06	0.82	0.04	0.04	0.82	0.04	0.04
0.84	0.10	0.10	0.82	0.08	0.08	0.82	0.08	0.08
0.40	0.02	0.02	0.39	0.01	0.01	0.39	0.01	0.01
0.39	0.17	-0.17	0.39	0.17	-0.17	0.39	0.17	-0.17
0.40	0.09	-0.09	0.40	0.09	-0.09	0.37	0.12	-0.12
0.40	0.14	0.14	0.40	0.14	0.14	0.37	0.11	0.11
-0.52	0.42	0.42	-0.50	0.44	0.44	-0.50	0.44	0.44
-0.52	0.44	0.44	-0.50	0.46	0.46	-0.50	0.46	0.46
-0.47	0.16	0.16	-0.45	0.18	0.18	-0.44	0.19	0.19
-0.47	0.03	0.03	-0.45	0.05	0.05	-0.44	0.06	0.06
-0.50	0.04	-0.04	-0.48	0.02	-0.02	-0.50	0.04	-0.04
-0.58	0.28	0.28	-0.56	0.30	0.30	-0.59	0.27	0.27
-0.48	0.19	-0.19	-0.45	0.16	-0.16	-0.51	0.22	-0.22
-0.48	0.04	0.04	-0.45	0.07	0.07	-0.51	0.01	0.01
-0.48	0.12	0.12	-0.45	0.15	0.15	-0.51	0.09	0.09
-0.32	0.36	0.36	-0.30	0.38	0.38	-0.34	0.34	0.34
-0.31	0.47	0.47	-0.29	0.49	0.49	-0.35	0.43	0.43
-0.22	0.05	0.05	-0.20	0.07	0.07	-0.20	0.07	0.07
-0.19	0.27	0.27	-0.17	0.29	0.29	-0.18	0.28	0.28
0.92	0.13	-0.13	0.93	0.12	-0.12	0.82	0.23	-0.23
0.84	0.04	0.04	0.86	0.06	0.06	0.82	0.02	0.02
0.67	0.26	0.26	0.66	0.25	0.25	0.57	0.16	0.16
0.67	0.31	0.31	0.66	0.30	0.30	0.57	0.21	0.21
1.72	0.07	0.07	1.73	0.08	0.08	1.50	0.15	-0.15
1.76	0.20	0.20	1.77	0.21	0.21	1.55	0.01	-0.01
1.82	0.12	0.12	1.83	0.13	0.13	1.60	0.10	-0.10
1.86	0.18	0.18	1.87	0.19	0.19	1.65	0.03	-0.03
1.87	0.29	0.29	1.87	0.29	0.29	1.65	0.07	0.07
1.86	0.24	0.24	1.87	0.25	0.25	1.66	0.04	0.04
1.87	0.20	0.20	1.86	0.19	0.19	1.66	0.01	-0.01
1.82	0.30	0.30	1.82	0.30	0.30	1.62	0.10	0.10
	0.20	0.08		0.20	0.09		0.18	0.02
	0.17	0.06		0.17	0.06		0.14	-0.02
	0.18	-0.05		0.18	-0.06		0.21	-0.10
	0.16	-0.05		0.16	-0.06		0.19	-0.09
	0.21	0.17		0.22	0.19		0.21	0.15
	0.14	0.13		0.15	0.15		0.13	0.13
	0.20	0.20		0.21	0.21		0.06	-0.01

n_0.06-0.027_0.035_0.075	I				Northing	Easting	
Velocity (m/s)	err	err	good	Node #	UTM Zone 20 NAD 83		Notes
1.16	0.02	-0.02		26296	5286367	375030	Substantial seaweed buildup on velocity meter
1.03	0.47	-0.47		26092	5286349	375003	Difficult to keep boat in same location for 10 second period
0.81	0.12	0.12		25691	5286366	375072	Switched to 5 second averages
1.08	0.35	-0.35		25687	5286337	375030	
1.00	0.50	-0.50		25484	5286318	375031	
1.04	0.15	-0.15		27514	5286403	374975	Moved further into channel
1.02	0.27	-0.27		27514	5286403	374973	
0.52	0.23	0.23		27113	5286426	375040	Likely 3 metres depth at this location
1.08	0.11	-0.11		30764	5286558	374916	Close to red buoy
1.00	0.16	-0.16		30967	5286552	374893	Close to red buoy
0.92	0.24	0.24		30560	5286549	374897	Substantial seaweed buildup on velocity meter
1.02	0.20	0.20		32190	5286648	374920	Off point of inner bar
0.83	0.05	0.05		32391	5286639	374880	
0.83	0.09	0.09		32391	5286639	374880	
0.39	0.01	0.01		34633	5286784	374906	Further up channel into estuary
0.39	0.17	-0.17		34634	5286781	374912	
0.41	0.08	-0.08		25484	5286324	375031	Back in main channel approximately 5 m from breakwater
0.41	0.15	0.15		25484	5286324	375031	
-0.51	0.43	0.43		25484	5286324	375042	
-0.51	0.45	0.45		25484	5286324	375042	
-0.46	0.17	0.17		25691	5286366	375082	Moved closer to east jetty
-0.46	0.04	0.04		28330	5286470	375008	
-0.50	0.04	-0.04		28935	5286471	374941	
-0.60	0.26	0.26		31375	5286595	374921	
-0.50	0.21	-0.21		31578	5286599	374894	
-0.50	0.02	0.02		31578	5286599	374894	
-0.50	0.10	0.10		31578	5286599	374894	
-0.34	0.34	0.34		33206	5286695	374881	Moved further up channel
-0.34	0.44	0.44		32799	5286676	374881	
-0.21	0.06	0.06		35860	5286882	374943	In line with estuary end of breakwater (harbour entrance)
-0.19	0.27	0.27		35861	5286888	374950	In line with estuary end of breakwater (harbour entrance)
0.90	0.15	-0.15		61213	5289739	372798	Under easternmost bridge span at shippagan - current switched direction
0.82	0.02	0.02		61203	5289638	372719	Under main bridge span - current switched direction
0.60	0.19	0.19		29950	5286515	374923	Back in channel - current now exiting
0.60	0.24	0.24		29950	5286515	374923	Back in channel - current now exiting
1.61	0.04	-0.04		26297			
1.65	0.09	0.09		26297			
1.71	0.01	0.01		26297			
1.76	0.08	0.08		26297			
1.77	0.19	0.19		26297			
1.77	0.15	0.15		26297			
1.77	0.10	0.10		26297			
1.73	0.21	0.21		26297			

0.18	0.05	
0.14	0.03	BEST RUN
0.19	-0.07	
0.16	-0.06	
0.20	0.15	
0.13	0.12	
0.11	0.10	

APPENDIX E – MEASURED MORPHOLOGY MAPS (1990'S)

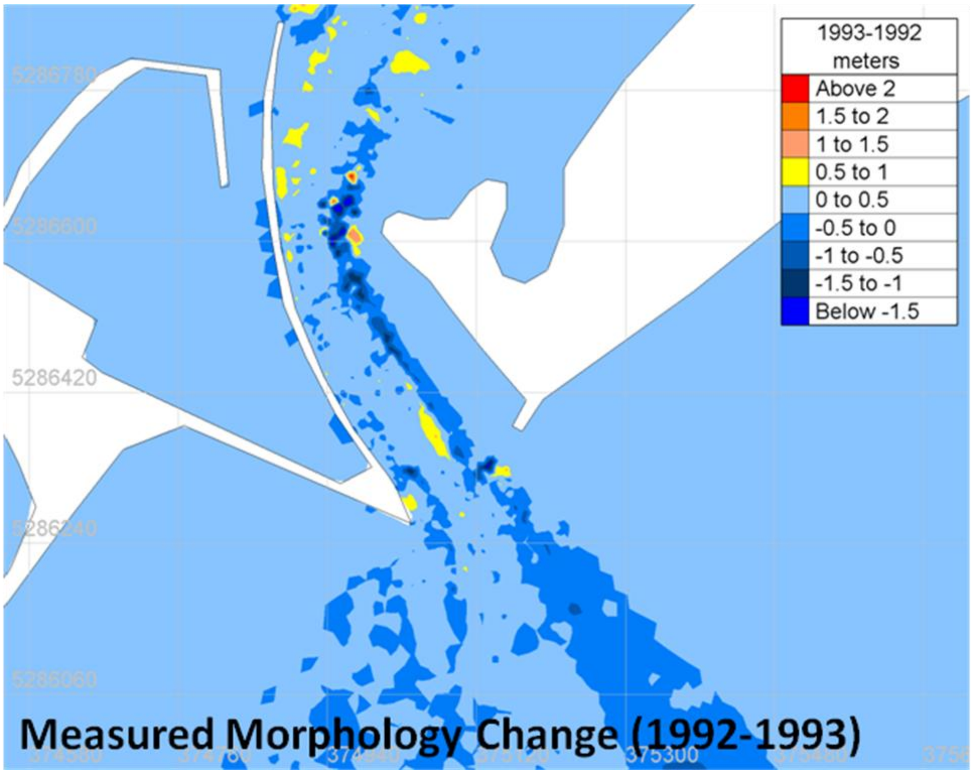

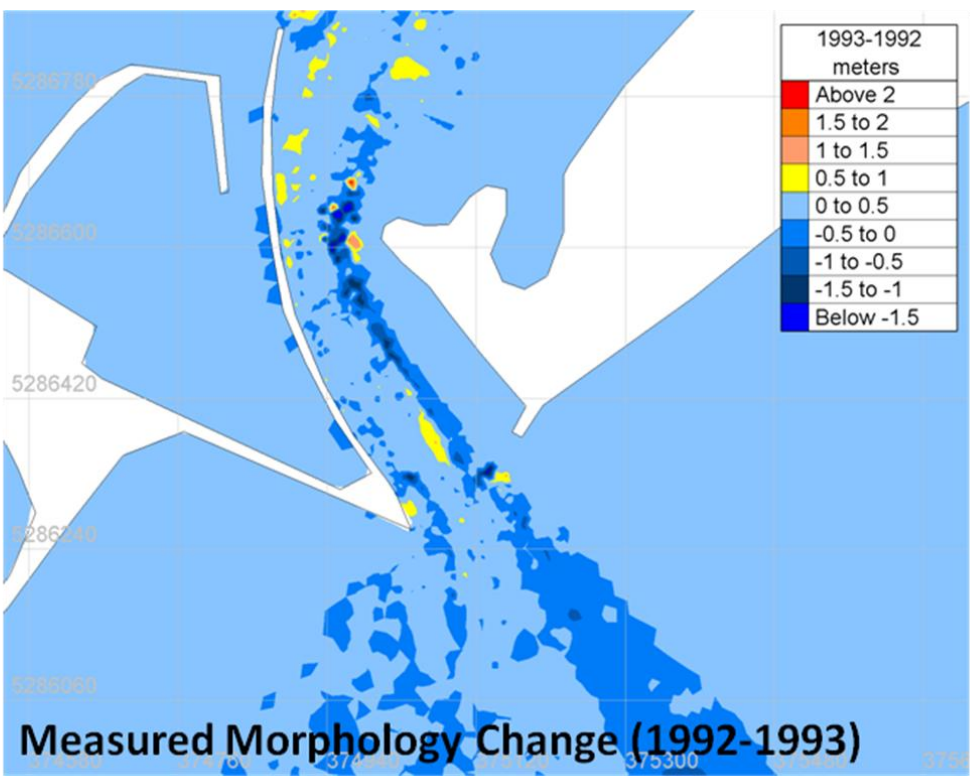

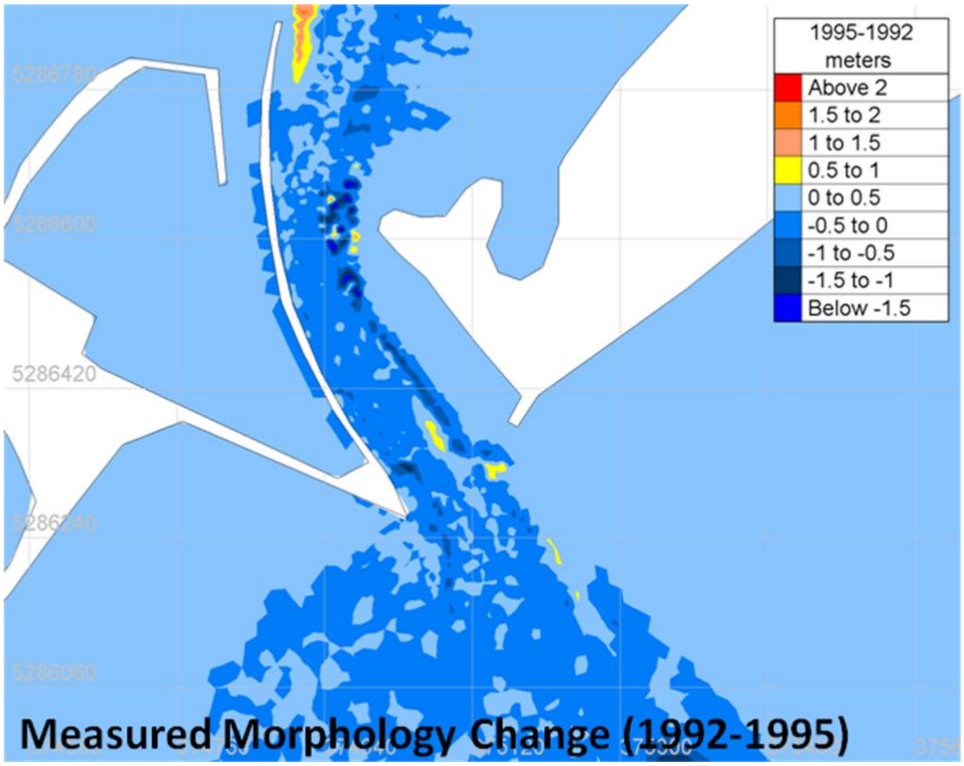
1995-1992
meters
Above 2
1.5 to 2
1 to 1.5
0.5 to 1
0 to 0.5
-0.5 to 0
-1 to -0.5
-1.5 to -1
Below -1.5
5286780
5286600
5286420
5286240
5286060
Measured Morphology Change (1992-1995)

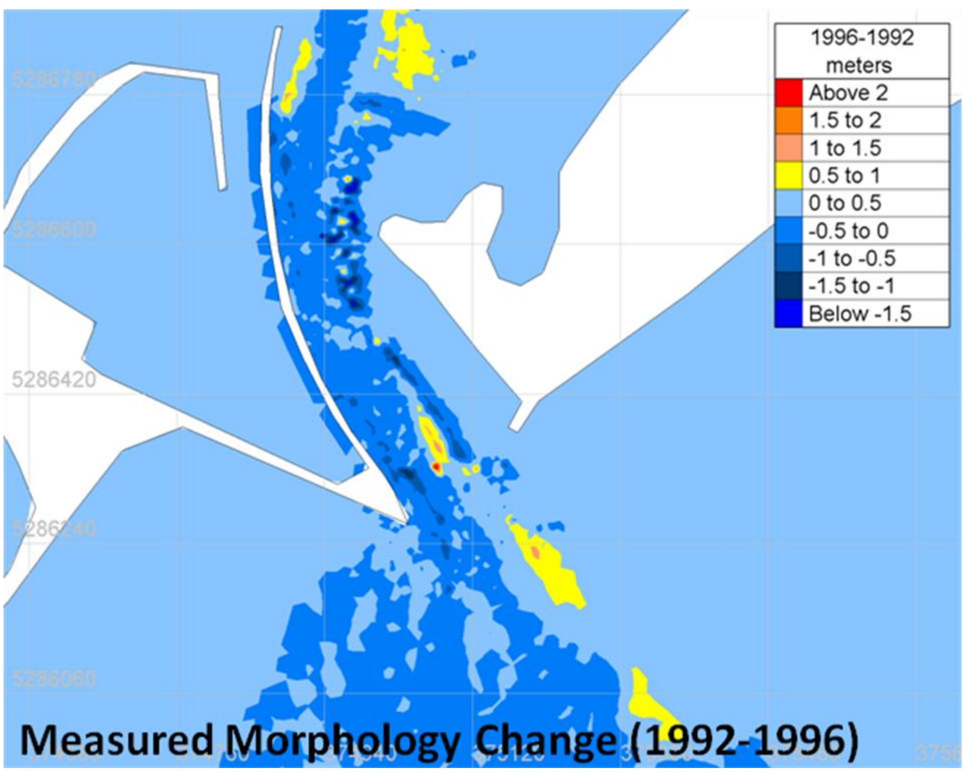
1996-1992
meters
Above 2
1.5 to 2
1 to 1.5
0.5 to 1
0 to 0.5
-0.5 to 0
-1 to -0.5
-1.5 to -1
Below -1.5
5286780
5286600
5286420
5286240
5286060
Measured Morphology Change (1992-1996)

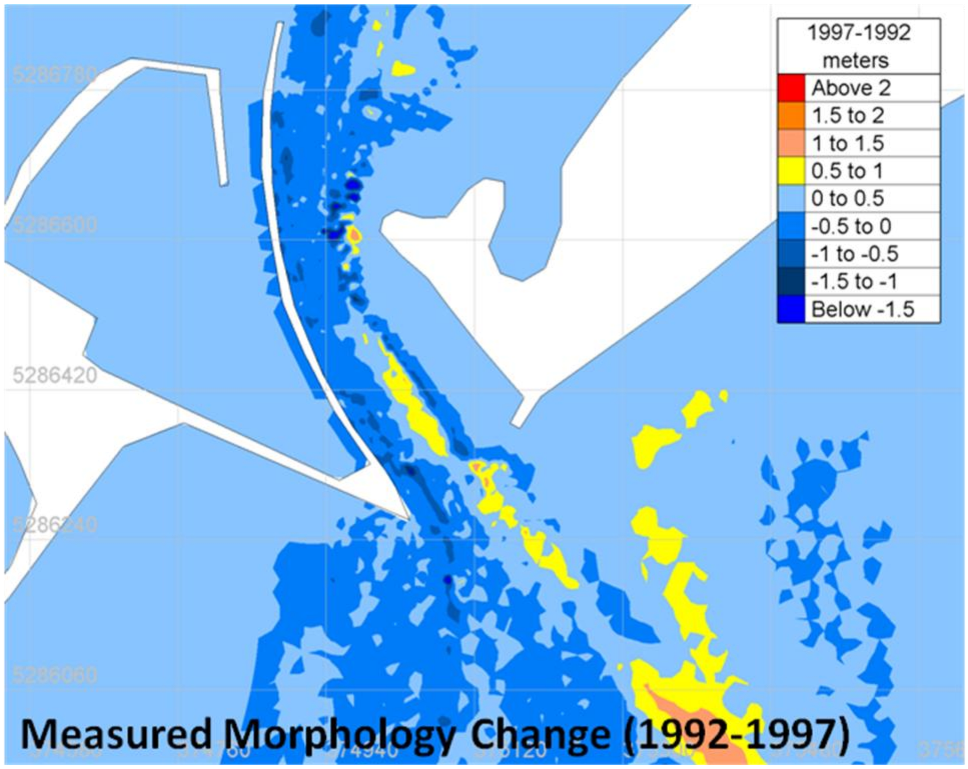
1997-1992
meters
Above 2
1.5 to 2
1 to 1.5
0.5 to 1
0 to 0.5
-0.5 to 0
-1 to -0.5
-1.5 to -1
Below -1.5
5286420
Measured Morphology Change (1992-1997)

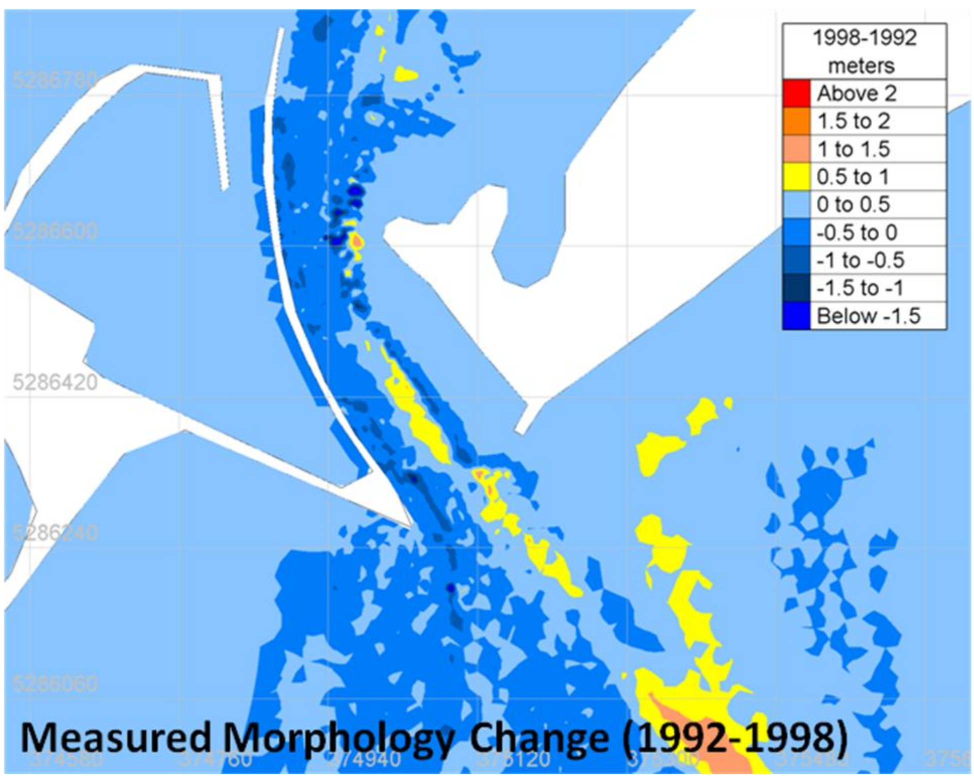
1998-1992
meters
Above 2
1.5 to 2
1 to 1.5
0.5 to 1
0 to 0.5
-0.5 to 0
-1 to -0.5
-1.5 to -1
Below -1.5
5286420
Measured Morphology Change (1992-1998)

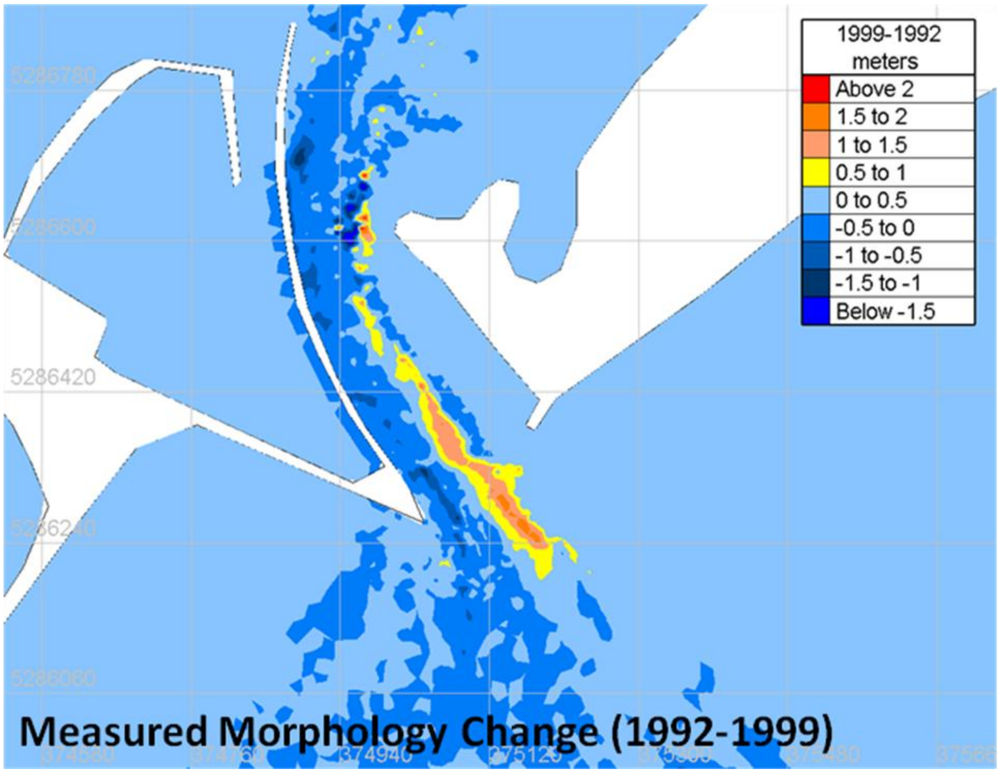
1999-1992
meters
Above 2
1.5 to 2
1 to 1.5
0.5 to 1
0 to 0.5
-0.5 to 0
-1 to -0.5
-1.5 to -1
Below -1.5
5286780
5286600
5286420
5286240
5286060
374940
Measured Morphology Change (1992-1999)